University of Nottingham
UK | CHINA | MALAYSIA

GPS/Galileo Precise Point Positioning and its integration with Inertial Navigation System

Lei Zhao

Thesis submitted to the University of Nottingham
for the degree of Doctor of Philosophy

February 2023

To my parents.

Three Proverbs from Christianism, Confucianism and Buddhism:

"But I tell you, love your enemies and pray for those who persecute you" — Matthew 5:44

"四海之內皆兄弟也。" —《論語》

"於諸眾生。視若自己。拯濟負荷。皆度彼岸。" —《佛說大乘無量壽莊嚴清淨平等覺經》

Abstract

The GNSS (Global Navigation Satellite System) Precise Point Positioning (PPP) technique that emerges in the late 1990s is well known for its flexibility of single receiver and capability of high accuracy around the globe. It can obtain centimeter-level accuracy as the classical real-time kinematic (RTK) technique but it requires a convergence process of tens of minutes to reach this level of accuracy.

The carrier-phase ambiguity resolution (AR) of PPP can accelerate the convergence time and further improve the positioning accuracy. PPP AR requires an additional layer of bias correction to recover the integer nature of the phase ambiguity, which are traditionally represented in a combined form: the widelane (WL) /narrowlane (NL) uncalibrated Phase Delays (UPDs) or the WL Satellite Biases (WSB) plus the 'integer' phase clocks (or the 'decoupled' clock model). As GNSS evolves, this PPP AR strategy is difficult to be extended to the multi-frequency case since there are many more possible combinations, which causes much inconvenience at the user side on PPP modelling. Another latest form of bias is uncombined, which complies with the Radio Technical Commission for Maritime Services (RTCM) state space representation (SSR) for code bias. It can be extended to the multi-frequency case very easily and GNSS PPP users can achieve AR of their preferable models using these uncombined bias products without referring to the parameter estimation methods at the network side. With the transition of the bias form from combined to uncombined, many IGS (International GNSS Service) analysis centers are starting issuing the uncombined bias products routinely to the GNSS community for free.

The Inertial Navigation System (INS) is an autonomous dead-reckoning system and an effective complementary technique to GNSS in case of signal outage. GNSS INS integration takes advantage of properties of each system and improves the system resilience in Navigation.

In order to validate the flexibility of the uncombined bias products in PPP applications at a user side, this thesis investigates the performance of GPS/Galileo zero-differenced PPP AR using uncombined bias products and its integration with INS based on our in-house software POINT (Position Orientation Integration).

Two different PPP models: the ionosphere-free (IF) and the ionosphere-estimated (IE) models are used first to assess the effect of phase AR with the correction of the uncombined biases. The CNES (Centre National d'Etudes Spatiales) uncombined bias products are applied to correct the raw code and phase measurements from the International GNSS Service (IGS) stations. In both of the IF and IE models, the east error component after AR is less than 1 *cm* with a significant improvement of 45%, and 63% respectively compared with the ambiguity-float solutions. The PPP convergence time after AR is also shortened by 23% for 3D error below 5 *cm* in the IF model and by 17% for 2D error below 5 *cm* in the IE model.

The PPP/INS LCI (Loosely Coupled Integration) and TCI (Tightly Coupled Integration) experiments are then carried out in a train positioning test and two van positioning tests. A tactical-grade IMU are equipped in the tests.

The train test is on the roof of NGB (Nottingham Geospatial Building) and has good satellite observability. The van tests are run on a complex road and around Nottingham city center respectively, where signal interruptions happen frequently due to bridges, vegetation,and city canyons. CNES real-time orbit, clock and the uncombined bias products are used. In the train positioning test, ambiguity-float PPP has almost identical performance with LCI and TCI with an accuracy of 8.5, 5.7 and 4.9 cm in the north (N), east (E) and up (U) direction respectively. After AR, all the solutions achieve significant improvements in all components, which are around 9%, 9% and 7% for the North component, 47%, 40% and 38% for the East component and 14%. 12% and 4% for the height component, for PPP-AR, PPP-AR/INS LCI and PPP-AR/INS TCI respectively. For the two van tests, due to the frequent signal interruptions, ionosphere-free AR is not feasible though uncombined phase biases are corrected. TCI achieves the highest accuracy, which can be 32, 29, 41 *cm* for the N E U component and also effectively eliminates the solution re-convergence in PPP.

This work has demonstrated that the uncombined satellite bias products are flexible for phase AR of different PPP modelling at the user end and can also be applied easily to PPP/INS integration to obtain better positioning performance. It is anticipated that more efficient methods for uncombined bias estimation would be developed to facilitate real-time PPP-AR or its integration with other types of sensors, which could greatly benefit the navigation in harsh signal reception environment.

Acknowledgements

This research is funded by the The University of Nottingham (for tuition fee) in partnership with the China Scholarship Council (CSC) (for stipend). Many thanks to my sponsors for providing me such a great chance to live and study in the UK for four years.

This research is based on the Nottingham Geospatial Institute (NGI). My academic supervisors are Professor Terry Moore, Dr Chris Hill, Dr Paul Blunt and Dr Lei Yang. I am thankful to the first two supervisors for helping me choose a good software platform (the NGI POINT software) at the beginning and to the second two supervisors for regulating the outcome of my research work. In particular, I am grateful to my new primary supervisor Dr Paul Blunt my new second supervisor Dr Leon for their support and guidance since the third year of my study. Paul also held many interesting activities in our spare time which I really enjoyed and Leon gave me an important hand as a driver when collecting the data of my second experiment.

Also many thanks to Sean Ince and Norma Oldfield who helped access the NGI facilities and data. I would also appreciate the help of Denis Laurichesse from the French CNES, who provided many instructions on the use of their uncombined bias products and the open source reference software PPPWizard.

I would also like to give many thanks to my research fellows at NGI including Dr Brian Weaver, Dr Francesco Basile, Dr Matthew Alcock, Dr Anna Klimkowska, Dr Cristina VRINCEANU, Dr Qiyi He and the visiting student Alex Schofield. I really had a memorable time with them during my study and it is my great luck to be friends with them.

I would be also very grateful to the supports and understandings from my parents and my fiancee. Despite a separation with them for more than three years due to the outbreak of the pandemic COVID 19, I can always feel the love from them which encouraged me to continue my study with my full courage.

Finally I would thank the great examples set by JESUS, Buddha and Confucius who teach me wisdom and love to overcome all the difficulties in my life.

List of Publications

Publications during this study:

Zhao L, Blunt P, Yang L. Performance Analysis of Zero-Difference GPS L1/L2/L5 and Galileo E1/E5a/E5b/E6 Point Positioning Using CNES Uncombined Bias Products. **Remote Sensing**. 2022; 14(3):650. https://doi.org/10.3390/rs14030650

Zhao L, Blunt P, Yang L, Ince S. Performance Analysis of Real-Time GPS/Galileo Precise Point Positioning Integrated with Inertial Navigation System. **Sensors**. 2023; 23(5):2396. https://doi.org/10.3390/s23052396

Publications at the beginning of this study:

Zhao L., Zhu K., Zhang S. (2019). Study on integrated cycle slip handling using GPS / Galileo combined observations. GPS Solutions, 1–12. https://doi.org/10.1007/s10291-019-0867-6

Contents

List of Tables

List of Figures

List of Acronyms

2D 2 Dimensional

3D 3 Dimensional

ANTEX ANTenna EXchange format

AR Ambiguity Resolution

ARP Antenna Reference Point

BIE Best Integer Equivariant

BKG Bundesamt für Kartographie und Geodäsie

CDDIS Crustal Dynamics Data Information System

CDMA Code Division Multiple Access

CLS Collecte Localisation Satellites

CNES Centre National d'Etudes Spatials

CS Commercial Service

CSC Cycle Slip Correction

DCB Differential Code Bias

DCM Direction Cosine Matrix

DD Double Difference

DFIF Dual-Frequency Ionosphere-Free

ECEF Earth-centered Earth-Fixed

EOP Earth Orientation Parameter

EWL Extra-Wide Lane

FCB Fractional Cycle Biases

FDMA Frequency Division Multiple Access

FOC Full Operational Capability

GF Geometry-Free

GFZ GeoForschungsZentrum Potsdam

GGTO GPS Galileo Time Offset

GIM Global Ionospheric Map

GNSS Global Navigation Satellite System

GPST GPS Time

GRGS Groupe de Recherche de Géodésie Spatiale

GTRF Galileo Terrestrial Reference Frame

IAC Information and Analysis Center

IB Integer Bootstrapping

IE Ionosphere-Estimated

IE Inertial Explorer

IF Ionosphere Free

IFCB Inter Frequency Clock Bias

IGS International GNSS Service

ILS Integer Least Square

IMU Inertial Measurement Unit

INS Inertial Navigation System

ISB Inter System Bias

ITRF International Terrestrial Reference Frame

ITRS International Terrestrial Reference System

JAXA Japan Aerospace Exploration Agency

LAMBDA Least squares AMBiguity Decorrelation Adjustment

LCI Loosely Coupled Integration

MEMS Micro-Electro-Mechanical System

MEO Medium Earth Orbit

MFIE Multi-Frequency Ionosphere-Estimated

MGEX Muti-GNSS Experiment

MJD Modified Julian Date

MW Melbourne-Wübbena

NGI Nottingham Geospatial Institute

NL Narrowlane

OEUFS Optimal Estimation using Uncombined Four-frequency Signals

OS Open Service

OSB Observable-Specific Bias

OSR Observation Space Representation

PAR Partial Ambiguity Resolution

PCO Phase Center Offset

PCV Phase Center Variation

PNT Positioning Navigation and Timing

POINT Position Orientation and INTegration

PPP Precise Point Positioning

PPPWIZARD PPP With Integer and Zero-difference Ambiguity Resolution Demonstrator

PRS Public Regulated Service

PVT Positioning Velocity and Timing

RINEX Receiver INdependent EXchange format

RNSS Regional navigation satellite systems

RTCM Radio Technical Commission for Maritime Services

RTK Real-Time Kinematic

SAR Search and Rescue

SBAS Satellite-Based Augmentation Systems

SD Single Difference

SGG School of Geodesy and Geomatics

SHAO Shanghai Observatory

SINEX Solution (Software/technique) INdependent EXchange format

SPP Single Point Positioning

SSR State Space Representation

TCI Tightly Coupled Integration

TEC Total Electron Content

TECU TEC unit

TF Triple Frequency

TUG The Graz University of Technology

UPD Uncalibrated Phase Delay

UTC Universal Time Coordinated

WAR Widelane Ambiguity Resolution

WGS World Geodetic System

WL Widelane

WSB Widelane Satellite Bias

ZD Zero Difference

ZTD Zenith Tropospheric Delay

Chapter 1

Introduction

1.1 Overview

The Global Navigation Satellite System (GNSS) is a radio-based positioning system, which uses the distance measurements between signal transmitter (satellites) and signal receiver (user) as well as the known positions of transmitters to determine a user position. This positioning method is a kind of spatial distance backward intersection in terms of geomatics, which is illustrated in Figure 1.1.

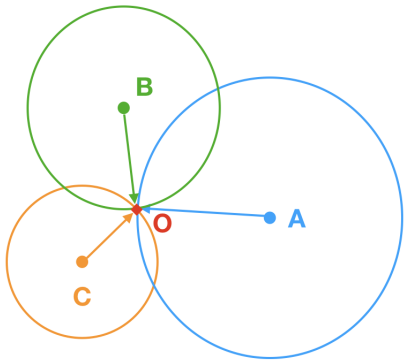

Figure 1.1: *Concept of backward intersection of distance measurements. The observer is at the unkonwn position O*

The GNSS distance measurement is known as pseudorange. It is obtained by multiplying the signal travel time with the speed of radio wave. GNSS satellites transmit ranging codes on its signals and a code replica is also generated at the receiver. By code correlation technique the signal travel time can be

determined when maximum correlation is identified inside receiver. In case of GPS two well-known ranging codes are modulated over the L1/L2 carriers: the civilian code and the precision code. The civilian code has a chipping rate of 1.023 Mbps and thus means a width of 293.1 m. The chipping rate of precision code is 10.23 Mbps, which leads to a width of 29.31 m and is ten times precise than the civilian code. The determination of signal travel time is based on clocks, which are the key components of GNSS. The GNSS satellites are equipped with atomic oscillators with high daily stability (frequency change ratio) $\Delta f/f \approx 10^{-13}$ to 10^{-14} (Subirana et al., 2013). The receiver clock is usually quartz clock with a poorer stability of 10^{-9} (Subirana et al., 2013) and much cheaper. The satellite clock offset over time along with its orbit information is broadcast to users in the navigation message modulated in the signal. The receiver clock offset is usually modelled as white noise and estimated together with coordinates in a filter at the user end.

The GNSS broadcast ephemerides and clocks modulated on carriers are in the meter-level accuracy, leading to a code-based single point positioning (SPP) of similar accuracy. However in relative positioning or differential positioning between a base and a rover e.g. RTK (Real-time Kinematic), the use of precise carrier-phase measurements enables an accuracy of centimeter level. The Precise Point Positioning (PPP) also benefits from carrier-phase measurements besides the precise satellite orbit and clock products but usually requires a certain period of time to reach centimeter-level accuracy.

The carrier-phase measurements from a receiver measures the instantaneous fractional beat phase (Hofmann-Wellenhof et al., 2001), which is the phase difference between a received signal and the generated signal at receiver, and the integer number of carrier-phase cycles between satellite and receiver is unknown. This unknown integer multiple is also called ambiguity. Without loss of lock, this ambiguity remains constant. Due to the existence of signal hardware delays at both transmitter and receiver, the standard PPP uses a float ambiguity which is contaminated by code and phase biases. To recover

the integer nature, an additional layer of bias correction is needed. PPP after ambiguity resolution (AR) has higher accuracy and more rapid convergence. In the last decade, the bias products has been transitioned from the combined widelane/narrowlane form to the uncombined form, which can be applied to the raw code and phase measurements directly and the phase ambiguity or its combinations can still conserve the integer nature. This uncombined bias products facilitate the PPP AR process at user end and can be extended to multi-frequency easily. Figure 1.2 shows the different levels of GNSS point positioning.

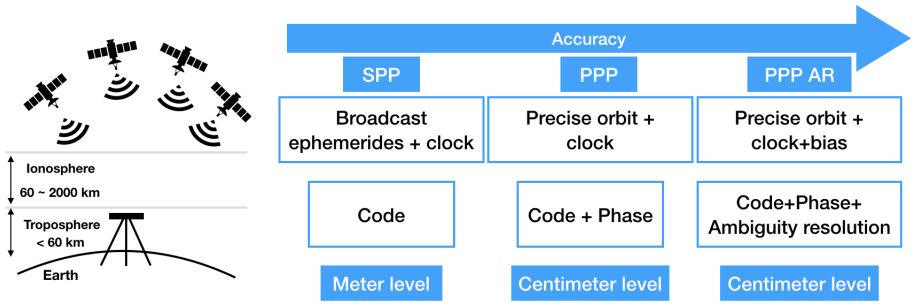

Figure 1.2: *Concept of GNSS point positioning*

The Inertial Navigation System (INS) measures the acceleration and rotation rate of a moving object and can provide precise position, velocity and attitude solution within a short interval. Its inertial measurement unit (IMU) consists of accelerometer triad and gyro triad. Different grades of IMU could greatly affect the INS performance. INS is an autonomous dead-reckoning system and its navigation process is shown in Figure 1.3.

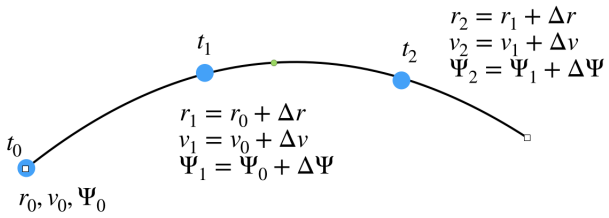

Figure 1.3: *INS is a dead-reckoning system. r, v and Ψ denote position, velocity and attitude respectively.*

It is an effective complementary technique to GNSS in case of signal outage.

GNSS PPP/INS integration takes advantage of properties of each system and improves the system resilience in Navigation.

1.2 Aims and Objectives

The research question being addressed in this study is:

To what effect can the application of GNSS uncombined bias products to PPP and PPP/INS integration improve the positioning performance?

The uncombined bias products for multi-constellation and multi-frequency PPP have been issued routinely at some IGS (International GNSS Service) anasis centers. There are already many studies demonstrating the use of this bias form, which simplifies the PPP modelling and allows independent AR method at user end. However as of the time of writing, the application of this uncombined bias products to the PPP/INS integration especially for the tightly-coupled integration has not been widely demonstrated.

Based on the above perception, the aim of this study is:

Aim: To investigate the performance of the integration of GPS/Galileo Precise Point Positioning using uncombined bias products and Inertial Navigation System (INS).

The corresponding **objectives** are organised as follows:

1. To implement and evaluate GPS/Galileo dual-frequency ionosphere-free PPP and PPP AR using uncombined bias products.
2. To implement and evaluate GPS/Galileo multi-frequency ionosphere-estimated PPP and PPP AR using uncombined bias products.
3. To implement and evaluate GPS/Galileo PPP/INS and PPP-AR/INS loosely coupled integration with the uncombined bias correction for AR.
4. To implement and evaluate GPS/Galileo PPP/INS and PPP-AR/INS tightly coupled integration with the uncombined bias correction for AR.

1.3 Innovation of this work

This thesis makes contribution to the validation of the flexibility of the GNSS uncombined bias products in PPP ambiguity resolution. Furthermore, the application of the uncombined bias is extended to the real-time PPP/INS integration and the integrated positioning performance is evaluated. Parts of the work are published in a journal paper presented in the 'List of Publications'. The majority of this work is involved with programming based on our in-house software POINT (Hide, 2003) and the contribution is made in the following steps:

1. The review of the source code of POINT in preparation for developing new algorithms.

2. The review of literature on GNSS PPP AR using uncombined bias products, especially the uncombined bias formulation proposed in Laurichesse (2012).

3. The development and evaluation of GPS/Galileo dual-frequency ionosphere-free PPP AR using CNES uncombined bias products based on POINT.

4. The development and evaluation of GPS L1/L2/L5 Galileo E1/E5a/E5b/E6 ionosphere-estimated PPP AR using CNES uncombined bias products based on POINT.

5. The development and evaluation of GPS/Galileo PPP AR/INS LCI using CNES uncombined bias products based on POINT.

6. The development and evaluation of GPS/Galileo PPP AR/INS TCI using CNES uncombined bias products based on POINT.

1.4 Outline

The organization of this thesis is as below:

Chapter 2 mainly reviews the literature on GNSS PPP AR. It is shown that

the uncombined bias products for PPP AR can be extended to the multi-frequency case easily and allows users to establish their own PPP model and resolve phase ambiguities.

Chapter 3 presents mathematical basics of GNSS PPP modelling. Especially, PPP AR modelling using CNES uncombined bias products are presented.

Chapter 4 gives a detailed description of the software tool: POINT and new features developed on this software. Data sources and test settings are also presented.

Chapter 5 presents the global GPS/Galileo PPP AR test results using CNES uncombined bias products including dual-frequency and multi-frequency model.

Chapter 6 presents INS basics and modeling of PPP/INS integration with the uncombined bias correction.

Chapter 7 presents the INS module in POINT and newly developed structure of TCI and LCI with PPP using uncombined bias correction.

Chapter 8 gives GPS/Galileo PPP-AR/INS results with observation data from a train positioning test.

Chapter 9 gives GPS/Galileo PPP-AR/INS results with observation data from two van positioning tests.

Chapter 10 summarises the entire thesis and gives limitations of this research and also points prospective work in the PPP/INS integrated navigation in the future.

Figure 1.4 shows the highlights of each chapter, which are classified by objectives of this research.

Objective 1 & 2		Objective 3 & 4	
Chap. 2	GNSS PPP literature review	**Chap. 6**	PPP/INS integration model
	Standard PPP and PPP AR		INS navigation equation
	Multi-constellation PPP AR		PPP/INS review
	Multi-frequency PPP AR		LCI with uncombined bias
	Uncombined bias products		TCI with uncombined bias
Chap. 3	GNSS PPP mathematical basis	**Chap. 7**	PPP/INS integration methodology
	Basic obs. functional model		Software tool: POINT — INS mechanization
	Kalman filter		Software tool: POINT — New feature
	Standard PPP model		NGI test train
	Uncombined bias formulation		NGI test van
Chap. 4	GNSS PPP methodology	**Chap. 8**	Train positioning test
	Data sources		PPP model comparison
	Software tool: POINT		PPP/INS LCI and TCI results
	Newly developed features		Gap analysis
	Test config		
Chap. 5	Global GNSS PPP test	**Chap. 9**	Van positioning test
	GPS/Galileo dural-frequency PPP AR with uncombined bias		PPP model comparison
	GPS/Galileo multi-frequency PPP AR with uncombined bias		PPP/INS LCI and TCI results

Figure 1.4: *Highlights of each chapter in this research*

Chapter 2

Background and literature review

2.1 Introduction

GNSS has already turned out to be an indispensable technology in our daily life. GNSS applications for position, navigation and timing (PNT) can be found from an individual travelling to massive scientific projects and military actions. Currently it mainly consists of GPS (USA), GLONASS (Russia), Galileo (EU), and BeiDou (China) satnavs. Other two regional navigation satellite systems (RNSS) are QZSS (Japan) and NavIC (India). In addition, the Satellite-Based Augmentation Systems (SBAS) is designed to improve the GNSS service.

GNSS Precise Point Positioning (PPP) has been an increasingly popular technique over the last decade for its high accuracy and flexibility around the globe. As GNSS evolves, PPP modelling at a user end also demonstrates great variety, especially for the carrier-phase ambiguity resolution (AR). In the multi-GNSS multi-frequency case, uncombined bias formulation gradually becomes the mainstream for PPP AR.

This chapter is organised as follows: Section 2.2 gives a brief review of GPS and Galileo status; Section 2.3 reviews the standard GPS dual-frequency PPP,

followed by the development of PPP under multi-GNSS scenario in Section 2.4; next description of uncombined PPP formulation is presented in Section 2.5; finally Section 2.6 gives a brief summary.

2.2 GPS and Galileo status

A GNSS basically comprises the space segment, the control segment and the user segment. The space segment or satellites mainly generate and transmit navigation signals driven by the precise atomic clocks onboard, and also broadcast navigation messages uploaded by the control segment, which is composed of a network of stations and maintains the GNSS constellation status and the corresponding GNSS time system. The user segment receives the GNSS signals, processes the signals and computes coordinates. The GNSS user equipment can be divided into four parts: the antenna, receiver hardware, ranging processor, and navigation processor (Groves, 2013). More information about these three segments can be found in the GNSS-related interface control documents (Dunn, 2021; European Union, 2021) and many GNSS textbooks (Hofmann-Wellenhof et al., 2001; Groves, 2013; Subirana et al., 2013; Morton et al., 2020).

In this section, GPS and Galileo status are briefly reviewed and presented for the coherence with the GNSS precise point positioning (PPP) in the subsequent chapters.

2.2.1 Constellation configuration

Both GPS and Galileo satellites circulates around the earth in a Medium Earth Orbit (MEO) orbit. The nominal GPS constellation consists of 24 slots in six orbital planes with four satellites per plane ensuring there are at least four satellites in view from virtually any point on the planet. The total number of operational satellites is typically 30 or 31 over the past 15 years (Morton et al., 2020). The Galileo constellation in the Full Operational Capability (FOC) phase consists of 24 MEO satellites in three orbital planes allowing global users to have 6 to 11 Galileo satellites in view at any time. Parts of

other constellation parameters are listed in Table 2.1.

Table 2.1: Partial GPS & Galileo constellation parameters

Configurations	GPS	Galileo
# of operational sats	30	24
# of orbital planes	6	3
Orbital altitude (km)	20 200	23 222 km
Inclination (°)	55	56
Orbital period	$11^h58^m02^s$	$14^h04^m42^s$
Ground track repeats (sidereal days)	1	10

Figure 2.1 and Figure 2.2 show the first-launched year of GPS block satellites and the deployment phase of Galileo satellites repectively. It has been reported that an inter-frequency clock bias (IFCB) exits for the GPS IIF satellites (Montenbruck et al., 2012) but can be neglected for the new generation systems including Galileo (Li et al., 2020b).

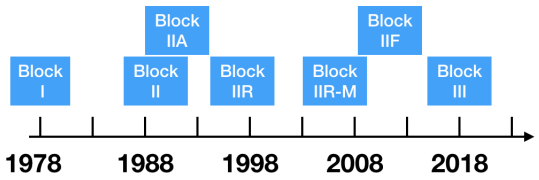

Figure 2.1: *First launched year of GPS satellite blocks*

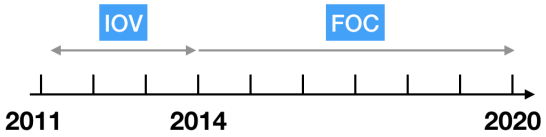

Figure 2.2: *Galileo launch plan. (IOV stands for in-orbit validation)*

2.2.2 Coordinate and time reference frames

Both GPS and Galileo have their own independent geodetic reference frame for coordinates and time reference frame, which are listed in Table 2.2. The coordinate reference frame used by GPS is World Geodetic System (WGS) 84 while for Galileo is Galileo's Terrestrial Reference Frame (GTRF). Those two geodetic frames are aligned to international reference standards such as the

International Terrestrial Reference Frame (ITRF) by which the International Terrestrial Reference System (ITRS) is realised. The time reference frame for GPS is GPS Time (GPST) starting at midnight UTC (Universal Time Coordinated) on 6 January 1980. The initial epoch for Galileo System Time (GST) is defined at 00:00 UTC on Sunday, 22 August 1999. Both of the time frames are maintained by their own control segment on the basis of a set of atomic clocks. Therefore, GPST and GST are continuous and not adjusted by the leap seconds. The GPS Galileo Time Offset (GGTO) is broadcast via Galileo's navigation message allowing hybrid-system positioning, velocity and timing (PVT) as long as at least four satellites from any of the two constellations are available to a receiver (Morton et al., 2020).

Table 2.2: Geodetic and time reference frames of GPS and Galileo

Reference frame	GPS	Galileo
Coordinate	WGS84	GTRF
Time	GPST	GST

2.2.3 Signal configuration

Frequency Plan

The frequency plan of GPS and Galileo signals is presented in Figure 2.3. The Galileo E6 signal is open to public as a result of the free offering of its commercial service (CS) by the European Union in 2018 (Laurichesse and Banville, 2018). This greatly promotes the PPP technique at a user end allowing instantaneous centimeter-level positioning performance (Laurichesse and Banville, 2018).

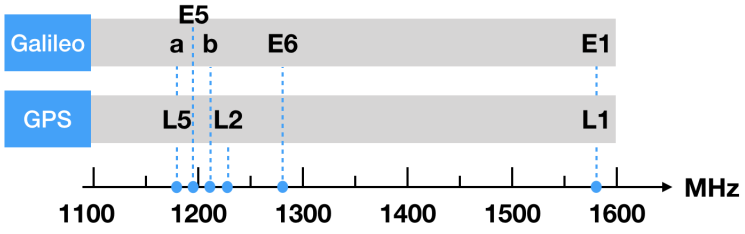

Figure 2.3: *GPS & Galileo frequency plan*

Signal structure

The GPS and Galileo navigation signal structures are listed in Table 2.3 and Table 2.4. The same frequency is shared by all the GPS or Galileo satellites and the signal access technique uses code division multiple access (CDMA). Pilot channels are data-less signals helping the track of signals (Subirana et al., 2013). Different channels correspond to different signal hardware delays, which is key to the PPP carrier-phase ambiguity resolution. Galileo signals provide more types of services including the Public Regulated Service (PRS), The Commercial Service (CS), The Open Service (OS) and Search and Rescue (SAR). It is noted that the navigation message is also modulated on the carriers but not presented here.

Table 2.3: GPS navigation signals

Band/Frequency (MHz)	Channel or code	Sat block	Services
L1/154×10.23	C/A	All	Civil
	P	All	Military
	M	IIR-M and After	Military
	L1C-I data	GPS III and After	Civil
	L1C-Q pilot		
L2/120×10.23	P	All	Military
	L2C M	IIR-M and After	Civil
	L2C L		
	M	IIR-M and After	Military
L5/115×10.23	L5-I data	IIF and After	Civil
	L5-Q pilot		

Table 2.4: Galileo navigation signals

Band/Freqquency (MHz)	Channel or code	Services
E1/1575.42	E1-A Data+PilotTime Mux	PRS
	E1-B Data	OS/SAR
	E1-C Pilot	OS
E6/1278.75	E6-A Data+Pilot Time Mux	PRS
	E6-B Data	CS
	E6-C Pilot	CS
E5/1191.795 E5a/1176.450	E5a-I Data	OS
	E5a-Q Pilot	OS
E5b/1207.140	E5b-I Data	OS
	E5b-Q Pilot	OS

2.3 Conventional GPS dual-frequency Precise Point Positioning (PPP)

2.3.1 RTK versus PPP

GNSS real-time kinematic or differential baseline positioning is already well established and a standard technique for high-precision surveying. GNSS PPP is relatively new but also has many applications in both scientific and industrial communities (Choy et al., 2016). Table 2.5 lists the general characteristics of PPP and RTK.

Table 2.5: General characteristics of RTK and PPP

RTK	**PPP**
Base stations and rovers	Single receiver
Double-difference	Zero- or single-difference positioning
Errors are eliminated or reduced	Errors: precise products, model, estimate
Phase ambiguity is integer-valued	Integer ambiguity requires bias correction
Centimeter-level or higher accuracy	
Single-epoch positioning ability	Convergence process (around 30 min)

Compared to RTK, PPP is well-known for its flexibility of single receiver and comparable high-precision positioning ability. Errors in short baseline RTK can be eliminated (e.g. satellite and receiver clock bias) or mostly reduced (e.g. atmospheric delays) after double-difference operation. PPP is an absolute positioning technique and delivers global coordinates directly e.g. WGS84 ellipsoid, and the errors are handled by using precise satellite orbit and clock products, precise models such like earth solid tide effect and parameter estimation e.g. zenith tropospheric wet delay. It can be zero-difference or between-satellite single-difference. In RTK the carrier-phase ambiguity is already integer-valued since the satellite/receiver hardware delays are also eliminated via thedoubled-ifference but for PPP, code and phase biases are required to be corrected to recover the carrier-phase integer property. RTK is capable of single-epoch positioning while the conventional dual-frequency PPP takes around half an hour to converge to centimeter-level accuracy. Nevertheless, Laurichesse and

Banville (2018) shows that GPS L1/L2 and Galileo E1/E5a/E5b/E6 PPP can achieve instantaneous centimeter-level accuracy and it is anticipated that PPP might become a practical alternative to RTK in the near feature.

2.3.2 GPS dual-frequency PPP

Ambiguity-float solutions

GNSS Precise Point Positioning (PPP) emerges in the late 1990s and is originally for analysing GPS data from large networks (Zumberge et al., 1997). It first determines the precise satellite positions and clock corrections from a globally distributed network of GPS receivers. The quality of these computed transmitter parameters is a few centimeters or better. Then receiver data from local network are processed by estimating receiver-specific parameters with satellite parameters fixed at the determined values in the global solutions. Both carrier phase and pseudorange are used as raw data. Héroux and Kouba (2001) and Kouba (2009) provide guidance on establishing GPS dual-frequency ionosphere-free PPP model and parameter adjustment procedure at a user end using IGS satellite orbit and clock products. They also listed additional correction terms that are significant for PPP including satellite/receiver antenna phase center offset (PCO) and phase center variation (PCV), phase wind-up effect, and the impact from solid earth tides, pole tides, ocean loading. Figure 2.4 shows the conceptual chart. With the external clock/orbit product that are generated from a sparse global station network, PPP can achieve centimeter-level positioning accuracy at anywhere in the world without the need of nearby base stations. However, it requires a convergence process to obtain such high accuracy as the carrier-phase ambiguity parametersconverge to constant values. This convergence time depends on the observational conditions of specific station e.g. satellite signal availability, atmospheric activity, receiver state. A typical value for the convergence time is 30 minutes but it can vary from tens of minutes to hours (Bisnath and Gao, 2008).

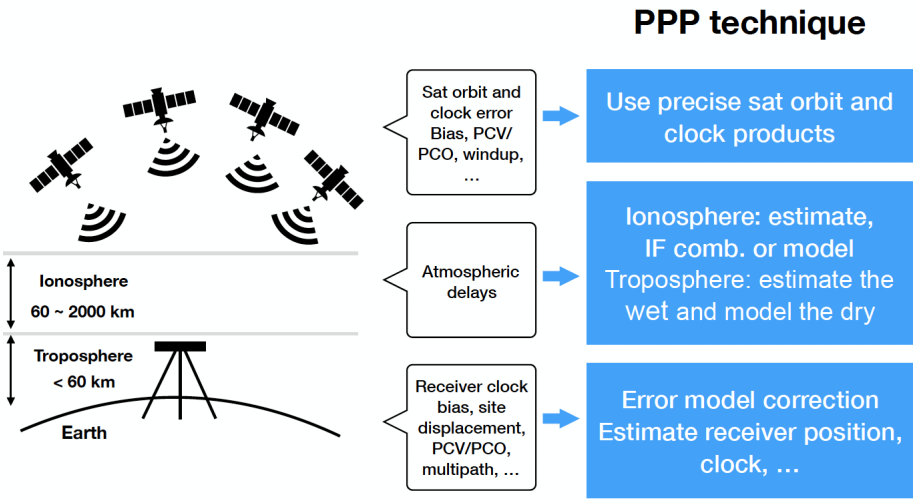

Figure 2.4: *PPP conceptual chart*

Ambiguity-fixed solutions

The carrier-phase ambiguity resolution in PPP is then exploited to accelerate the convergence time and improve the positioning accuracy in the case of the GPS legacy L1/L2 frequencies. This technique requires the computation of satellite phase biases from a network of stations, which are then disseminated as correction stream to a user side to enable PPP ambiguity resolution. The satellite phase biases are usually represented in a combined form: the Wide-Lane (WL) Uncalibrated Phase Delays (UPDs) and the Narrow-Lane (NL) UPD (Ge et al., 2008) or the WL Satellite Biases (WSB) and the 'integer' phase clocks (Laurichesse et al., 2009) or the 'decoupled' clock model (Collins et al., 2010). This bias form assumes that the phase ionosphere-free (IF) combination is used at the user end, and after having this bias applied, the Narrow-Lane (NL) ambiguity with a wavelength around 10 *cm* can be resolved. The following Figure 2.5 shows the comparison of PPP AR procedures at a user side using UPD products (Ge et al., 2008) and WSB and 'integer' phase clock (Laurichesse et al., 2009).

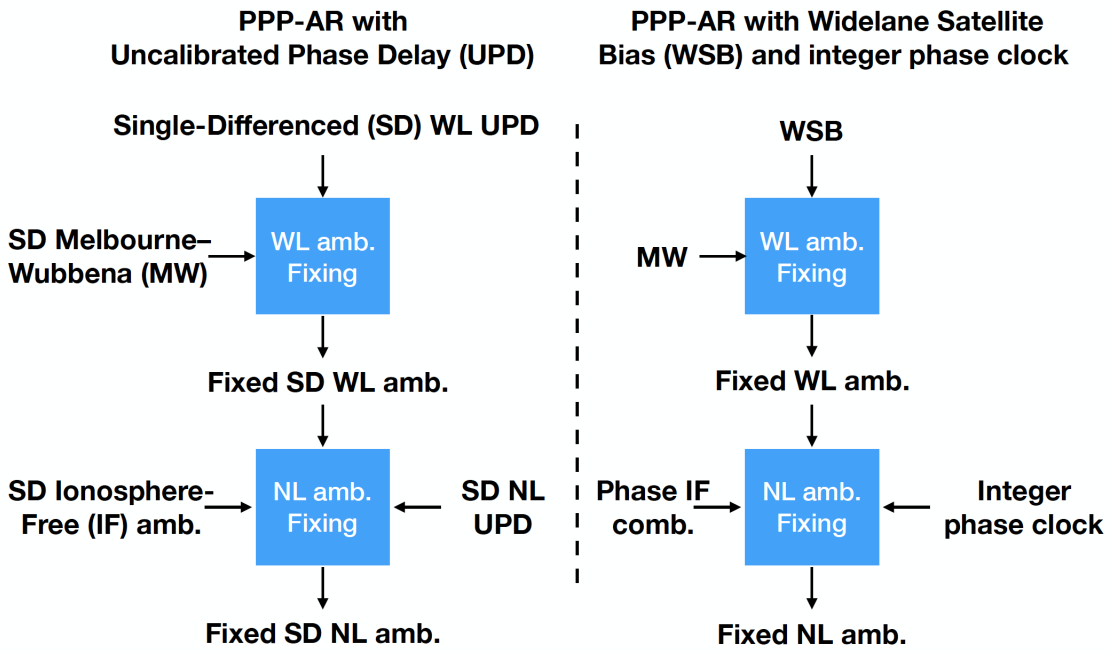

Figure 2.5: *Comparison of PPP-AR procedures using UPD and WSB, 'integer' phase clock*

The UPD method (Ge et al., 2008) operates on the basis of between-satellite single-differenced (SD) modelling which eliminates the common error sources at the receiver end, e.g. receiver clock bias. The SD Melbourne–Wübbena (MW) combination (Melbourne, 1985; Wübbena, 1985) first corrected by the SD UPD products is used to estimate the WL ambiguity. The MW combination is a linear combination of dual-frequency code and phase measurements and usually smoothed or averaged with a moving window to mitigate the code noise effect and improve the precision of the WL ambiguity estimates. Since the WL ambiguity has a wavelength of around 86 *cm*, it can be fixed very easily using the simplest integer rounding method. Then the fixed SD WL ambiguity is subtracted from the estimated SD IF ambiguity to obtain float NL ambiguity, which is then corrected by the SD NL UPD for the integer resolution. The NL ambiguity has a wavelength of around 10 *cm* and in this step the LAMBDA ((Least squares AMBiguity Decorrelation Adjustment) method (Teunissen, 1995) is usually used for the NL AR, which takes into account the correlations between the NL ambiguity estimates.

The WSB and 'integer' phase clock method (Laurichesse et al., 2009) is based

on the undifferenced modelling. The WSB is applied to the MW combination to estimate the WL ambiguity. A WL ambiguity datum needs to be fixed first to update receiver WL bias, which is accountable for the common fractional parts of the corrected WL ambiguities. Then the fixed WL ambiguity is removed from the decomposed phase IF combination, which is used together with the integer phase clock to estimate the NL ambiguity. As with the WL AR, a NL datum is also needed. The phase IF combination is not geometry-free and usually the code IF combination is used to calibrate the phase range. Note that the code measurement is modelled with the code clock e.g. the IGS clock products instead of the phase clock (Laurichesse, 2011).

Both of these two PPP-AR procedures work with combined biases. The equivalence of this combined formulation is demonstrated in Geng et al. (2010) and Shi and Gao (2014). Li et al. (2013) proposed a GPS dual-frequency ionosphere-estimated UPD scheme in which UPD on each frequency are generated and broadcast to user station. Cheng et al. (2017) further showed that the fractional cycle biases (FCBs), which are the fractional part of UPDs, can be estimated with high consistency using IF PPP model and ionosphere-estimated PPP model. Similar PPP AR performance is achieved with these two PPP models in their study. This equivalence is also confirmed in Wang et al. (2019), indicating the feasibility of the application of the FCB products to different PPP user model in the dual-frequecy case. The ionosphere-estimated PPP model has the advantage of constraining the ionospheric parameters using external precise ionosphere information, allowing for instantaneous PPP ambiguity fixing (Wabbena et al., 2005; Li et al., 2011; Juan et al., 2012).

2.4 GNSS multi-constellation multi-frequency PPP

2.4.1 GNSS multi-constellation dual-frequency PPP

Ambiguity-float solutions

As GNSS evolves, including the modernization of GPS and GLONASS and the newly deployed Galileo and BeiDou, PPP with multiple constellations improves the geometric strength of the solution as well as its reliability and has shown better accuracy and more rapid convergence (Tegedor et al., 2014b; Li et al., 2015; Choy et al., 2016). An additional Inter System Bias (ISB) or a separated receiver clock bias is usually estimated when incorporating measurements from another system since different system are referenced to their own time frame. Choy et al. (2016) reported that GPS/GLONASS/BeiDou kinematic PPP achieves a significant accuracy improvements of 20 and 30 % in the horizontal and vertical components, respectively compared to the GPS-only solution, and the convergence time is shortened by about 20 %. More importantly, multi-GNSS PPP shows a stable time series and experiences fewer fluctuation compared to single constellation and could provide better positioning results in the GNSS-challenged environments.

Ambiguity resolution with combined phase biases

The PPP-AR methods for GPS: UPD or WSB and 'integer' phase clock are naturally extended to other constellations. Pan et al. (2017) achieves GPS/BeiDou dual-frequency PPP AR using their estimated WL and NL FCB products. Tegedor et al. (2014a) computes the Galileo WL and NL UPDs for Galileo PPP-AR. Li et al. (2018) estimates WL and NL UPDs for GPS, GLONASS, Galileo, and BeiDou and assesses quadruple-constellation PPP with AR. However, as pointed in Banville et al. (2016), GLONASS satelltes uses the frequency division multiple access (FDMA) technology, calibration of code biases for widelane ambiguity resolution can be realized to some extent

by defining stations with similar equipment. Recently the WSB and 'integer' phase clock products from CNES are also available for Galileo E1/E5a measurements enabling millimeter-level ambiguity-resolved kinematic PPP solutions (Katsigianni et al., 2019a,b).

2.4.2 GNSS multi-constellation multi-frequency PPP

The prerequisite precise satellite clock products for PPP are conventionally referenced to the P1/P2 or L1/L2 ionosphere-free combinations in the GPS case. Applying these clock estimates directly to the modelling of the measurements on the third L5 frequency will inevitably result in extra clock bias due to the presence of the observable- and frequency-specific hardware delays. This inter frequency clock bias (IFCB) between the L1/L2 and the L1/L5 clock offset can vary with peak-to-peak amplitudes of 10–40 cm (Montenbruck et al., 2012). Many studies therefore have investigated the estimation of IFCB for its compensation in GPS triple-frequency (TF) PPP (Pan et al., 2017, 2019). Ambiguity-resolved GPS TF PPP with the correction of the estimated IFCB is further demonstrated in Li et al. (2020a). In Guo and Geng (2018) a separated satellite clock parameter is proposed for the L5 frequency to account for the IFCB effect instead of an explicit estimation and GPS TF PPP with ambiguity resolution based on the clock-separated model is also achieved in Geng et al. (2020). For Galileo E1/E5a/E5b PPP, it is found that the magnitude of the time-varying IFCB is negligible and the ambiguity-fixed solutions are also presented in many studies (Li et al., 2019; Geng et al., 2020; Li et al., 2020a). In Li et al. (2020b), Galileo five-frequency PPP with AR through using pairs of classical ionosphere-free combinations on different frequencies is even showed. The ambiguity resolution (AR) process for multi-constellation and multi-frequency PPP in the above studies compute the uncalibrated phase delays (UPDs) (Ge et al., 2008) or the fractional cycle biases (FCB) first using a network of reference stations. These satellite UPDs are generated in the

form of extra-wide lane (EWL), wide lane (WL) and narrow lane (NL) or L1 in the triple-frequency case. Then the integer nature of ambiguity estimates at a PPP user end could be recovered with the correction of these UPDs and ambiguity-fixed solution is then obtained. It is noted that these UPD products in the above studies are dedicated to their TF PPP models and the applicability of their bias products to different TF PPP models is not presented. The characteristics of multiple types of EWL UPD for Galileo five-frequency ionosphere-free PPP AR are also studied in Li et al. (2020b).

2.5 Uncombined bias products

2.5.1 Limitations of combined bias products

Though UPDs or the WSB plus 'integer' phase clocks provide a solution for dual-frequency PPP ambiguity resolution (AR), Laurichesse (2012) and Laurichesse and Langley (2015) listed major drawbacks of this combined form of biases, which are summarised as below:

- These bias products are just one type of solutions for accounting for the code and phase hardware delays in dual-frequency PPP AR. Different methods of handling these delays or biases will lead to different representations e.g. UPD products, despite the same physical signal delay fact. These combined bias products are now available from many IGS (International GNSS Service) analysis centers such like Centre National d'Etudes Spatials (CNES) (Loyer et al., 2012), School of Geodesy and Geomatics (SGG) (Li et al., 2016). As a result, PPP users have to establish consistent model as the server end when applying the bias products in order for AR.

- These combined bias formulations are limited to dual-frequency case and inconvenient to be extended to the triple-frequency case since there are many more possible combinations instead of only two WSB and 'integer' phase clock quantities. Li et al. (2020b) applied the UPD methods to

compute Galileo five-frequency PPP AR. Five pairs of EWL UPDs are computed first: E5a/E5b, E5a/E5, E5a/E6, E5/E5b, E5/E6. Then two pairs of WL UPDs are computed: E1/E5a and E1/E5. Multiple NL UPDs are also generated for frequency combinations of E1/E5a/E5b, E1/E5a/E5, E1/E5a/E6, E1/E5/E5b and E1/E5/E6. Their AR procedures follow the cascading scheme: extral widelane (EWL), WL and NL ambiguities. It's evident that combined bias representations for multi-frequency PPP AR are not a convenient choice.

2.5.2 Uncombined bias products

State space messages for code biases

The Radio Technical Commission for Maritime Services (RTCM) standard (https://www.rtcm.org) uses state space representation (SSR) to provide information on the status of individual GNSS error sources. Its SSR messages basically consist of satellite orbit errors, satellite clock errors, satellite signal biases, ionospheric delay parameters. tropospheric delay parameters. These SSR messages can be disseminated to users and used together with individual tracked observation data to obtain precise positioning. This SSR is different from observation space representation (OSR) for differential positioning.

In particular, the code biases reported in the SSR signal bias messages are in uncombined form and must be added directly to the corresponding pseudorange measurements instead of the combined form differential code biases (DCB).

CNES uncombined bias products

Laurichesse (2012) proposed a new uncombined phase bias representation which uses the same adding convention as the existing RTCM standard for the code biases. Advantages of this new uncombined phase bias is summarised as follows:

- Its modelling follows the basic GNSS observation equations for satellite and receiver signal biases and is closer to the physical nature of the

hardware delays, and thus it is independent of the methods used at the server or network side to estimate these biases. The unity of this uncombined form allows great flexibility of the implemented algorithms and simplicity of the application at user end.

- It can be extended to the multi-frequency code and phase observations very naturally and easily. All the uncombined phase bias products are referenced to the same clock datum as the code biases. The definition of the clock datum can be arbitrary but in the IGS convention the ionosphere-free P1-P2 combination is used in the GPS case.

- The most delicate property is that the phase ambiguity can still preserve the integer property after adding these uncombined biases to the raw code and phase observables. No assumptions are made on ambiguity resolution methods at the network or user level.

It also takes into account the inter frequency clock bias (Laurichesse, 2012) and in Laurichesse (2014) it is showed that various combined phase ambiguities in the GPS triple-frequency context can conserve their integer property.

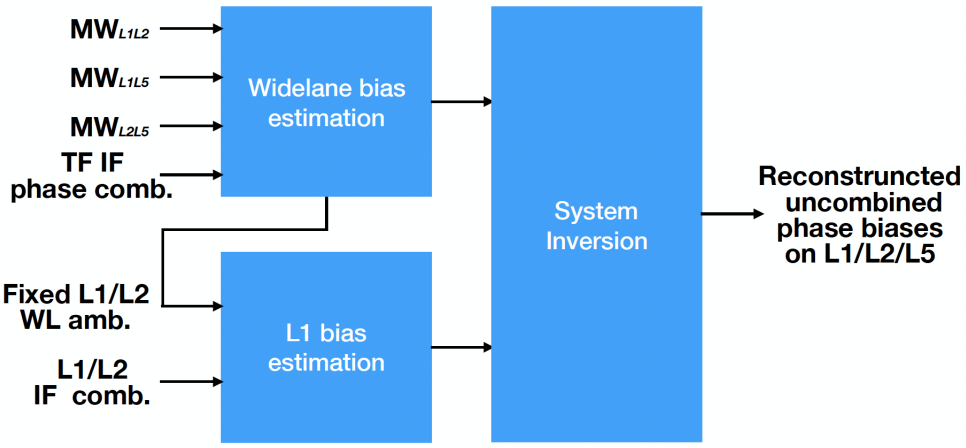

Figure 2.6: *Uncombined phase bias estimation at CNES*

In the dual-frequency case, with the defined RTCM uncombined code biases, the uncombined phase biases can be obtained by a unique linear transformation from the conventional WSB and 'integer' phase clock products. But in

the multi-frequency case, this transformation is not unique any more since there are more possible frequency pairs for combinations instead of two. Laurichesse (2014) extends their WL methods for dual-frequency bias estimation to the multi-frequency cases, which is explained in the following Figure 2.6. The MW combinations on different frequency pairs as for the WSB generation are used for the WL bias estimation. In addition, the triple-frequency phase ionosphere-free widelane-only combination is also used, which is much more accurate than the MW combination and will improve the accuracy of the estimated WL biases. Then the remaining biases on L1 are computed using the fixed L1/L2 widelane and the L1/L2 ionosphere-free combinations. After an inverse transformation the uncombined phase biases on each frequency can be reconstructed. It is clear that this uncombined phase biases are not the true phase hardware delays. It is also noted that this estimation method works on the combinations first, more investigation is needed on the bias estimation from the multi-frequency raw uncombined observation equations, which should also conserve the integer property of phase ambiguity for all possible phase and code combinations.

Since September 15 2014, CNES has started broadcasting these uncombined phase bias products on the IGS (International GNSS Service) CLK93 real-time data stream. Currently code and phase biases for GPS L1/L2/L5, Galileo E1/E5a/E5b/E6 and BeiDou-2 B1/B2/B3 signals are issued routinely while only code biases for GLONASS G1/G2 are available. An open source PPP client software PPP-WIZARD (With Integer And Zero-Difference Ambiguity Resolution) (Laurichesse and Privat, 2015) from CNES also demonstrates the use of their real-time bias products for GPS/Galileo/BeiDou-2 TF PPP with AR in a zero-differenced ambiguity-combined model. More detailed assessment of GPS/Galileo triple-frequency PPP based on the software is presented in Liu et al. (2020). In Duong et al. (2020) the bias stream is applied to a between-satellite single-difference PPP model and the performance after AR with the inclusion of Galileo E6 signal is assessed. In Laurichesse and Banville (2018),

an OEUFS (Optimal Estimation using Uncombined Four-frequency Signals) strategy is showed in which GPS L1/L2 and Galileo E1/E5a/E5b/E6 signals allows for instantaneous centimeter-level positioning with ionospheric information from the global ionospheric map (GIM) model. They remarked that this strategy is a generalization of the widelaning technique. CNES now also generates post-processed daily uncombined phase biases for validating their OEUFS strategy. Some other studies have also explored the single-epoch precise positioning ability with fixed widelane ambiguities (Geng and Guo, 2020a; Li et al., 2020b).

Uncombined bias products from other institutions

The Center for Orbit Determination in Europe (CODE) also provides uncombined bias products in the Solution (Software/technique) INdependent EXchange format (SINEX) (Schaer, 2016). These bias products are applied to the raw observations before making any combinations (Glaner and Weber, 2021). The Graz University of Technology (TUG) estimates the uncombined bias products using an uncombined formulation Strasser et al. (2019), which simplifies the parametrization of these time-variable biases. Geng and Guo (2020b) from Wuhan University also implemented satellite- and frequency-specific phase bias estimation and applied them directly to raw carrier-phase observations enabling wide-lane AR for single-epoch point positioning beyond three frequencies. Their estimation method is still based on between-satellite single-difference processing. Banville et al. (2020) from Natural Resources Canada achieved a combination of PPP AR products from six analysis centers by transforming them into a common observable-specific bias (OSB) representation. They remarked the combined OSB products provide better or equivalent results than the individual analysis center for both static and kinematic state. Geng et al. (2022) estimated phase OSBs with ambiguity-fixed, satellite clocks to enable PPP-AR over any frequency choices and possible observable combinations at the user end. Li et al. (2022a) also demonstrates the use of the OSBs for multi-cobstellation and multi-frequency PPP AR. These studies

clearly show that the uncombined phase bias formulation is widely accepted as a convenient way for multi-constellation multi-frequency PPP AR. It is necessary to validate the flexibility of these uncombined bias products with different PPP models at user end, especially for ambiguity resolution, which is addressed in this study.

2.6 Summary

This chapter presents the current development of GNSS PPP techniques. The standard dual-frequency GPS PPP can achieve centimeter-level positioning accuracy but a convergence process of around half a hour is required. Ambiguity-fixed PPP can obtain better accuracy and more rapid convergence. Multi-constellation multi-frequency PPP AR has further improvement but the conventional combined bias products for AR is not convenient and difficult for standardization. This leads to the recent uncombined bias formulation, which uses the RTCM SSR adding convention for code biases on raw measurments and is independent of PPP modelling at server or user end.

It is anticipated that more institution would use uncombined bias representation for PPP and work is needed for more effective estimation of these uncombined biases.

Chapter 3

GNSS Precise Point Positioning

3.1 Introduction

In this chapter, the PPP models using the CNES uncombined bias products are derived. Two models are evaluated in this study: ionosphere-estimated and ionosphere-free models. Thanks to the uncombined biases, the phase ambiguity resolution is allowed in both models.

This chapter is organised as follows: the basic GNSS observation models as well as the positioning error sources are reviewed in Section 3.2 and Section 3.3; then the discrete Kalman filter for parameter estimation is briefly presented in Section 3.4; then the conventional dual-frequency PPP including ambiguity-float and ambiguity-fixed models is given in Section 3.5; next the CNES uncombined formulation and uncombined biases are presented in Section 3.6; then the PPP models evaluated in this study with the correction of the CNES uncombined biases are given in Section 3.7. Finally a short summary of this chapter is in Section 3.8.

3.2 GNSS positioning error sources

The GNSS positioning errors are typically classified into three groups which are corresponding to the satellite (transmitter), the signal transmission path and the receiver respectively, as listed in Table 3.1.

Table 3.1: Typical GNSS positioning errors

	Error Sources	Comment
Satellite	Orbit and clock	Precise products accuracy: centimeter-level; Broadcast: meter-level (Montenbruck et al., 2015)
	Relativistic effect	Range domain: up to > 10 m Shapiro effect (secondary): < 2 cm (Subirana et al., 2013)
	Antenna PCO and PCV	PCO effect on height up to >10 cm PCV usually in mm level
	Instrumental delays	DCB effect on range up to tens of cm
	Phase wind-up effect	range effect up to > 10 cm
	Eclipse	Satellite in earth shadow with a random yaw angle
Transmission	Ionospheric delay	Range domain effect: up to tens of meter
	Tropospheric delay	Range effect: ten-meter level (Subirana et al., 2013)
Receiver	Clock	Estimated as white noise
	Instrumental delays	Usually coupled with clock bias
	Phase wind-up effect	The same as the satellite part
	Phase cycle slip	Phase ambiguity reinitialization
	Antenna PCO and PCV	The same as the satellite part
	Site displacement	e.g. Pole tide, solid tide, ocean load Range domain effect: Centimeter-level

PCO: Phase Center Offset; PCV: Phase Center Variation
DCB: Differential Code Bias

These errors are already well explained in many GNSS textbooks (Hofmann-Wellenhof et al., 2001; Subirana et al., 2013). A brief review over these errors are given in this section for the integrity of this thesis.

- GNSS ephemerides

  The broadcast ephemerides are included in the GNSS satellite navigation message. A typical 16 quasi-Keplerian parameters consists of six orbital elements, three rate parameters, three pairs of sinusoidal corrections and the reference ephemeris epoch. Noted that the GLONASS broadcast ephemerides contain initial conditions of position and velocity and gravitational acceleration perturbations of moon and sun instead of the keplerian orbital parameters (Subirana et al., 2013).

  The precise satellite orbit and clock products can be downloaded freely from IGS website in both real-time and post-processed mode. These precise products are usually determined using a priori constraints from broadcast ephemerides and clocks (Takasu et al., 2005).

- Computation of satellite coordinates

The signal emission time is computed first to retrieve correct satellite position from the provided ephemerides. This computation is usually an iterative process of the following equation:

$$t_{emission} = t_{reception} - dt_{travel} - (dt^{sat} + dt_{relativity}) \tag{3.1}$$

where dt_{travel} is the signal travel time; dt^{sat} is the satellite clock bias and $dt_{relativity}$ is the relativistic effect on satellite clock. Due to the earth's rotation during the signal transmission time, the satellite position at signal emission time needs to be transformed to be used at signal reception time or in navigation:

$$\mathbf{r}^{sat}_{t_{reception}} = \mathbf{R}(\omega \cdot dt_{travel}) \cdot \mathbf{r}^{sat}_{t_{emission}} \tag{3.2}$$

where $\mathbf{r}^{sat}$ is the satellite position vector in the ECEF (earth-centered earth-fixed) frame; R is a rotation matrix around the earth axis; ω is the earth rotation rate.

- Satellite antenna PCO & PCV correction

  Satellite antenna PCO & PCV correction is required when the satellite ephemerides information are from the precise satellite orbit and clock products, which are referred to the satellite mass center instead of the satellite antenna phase center. In the IGS ANTEX (Antenna Exchange Format) file, these phase center offsets are given in a satellite-fixed frame, which is defined by the following three orthogonal unit vectors (Subirana et al., 2013):

$$\begin{aligned} \mathbf{k} &= -\frac{\mathbf{r}^{sat}}{||\mathbf{r}^{sat}||} \\ \mathbf{j} &= \mathbf{k} \times \mathbf{e},\ \mathbf{e} = \frac{\mathbf{r}^{sun} - \mathbf{r}^{sat}}{||\mathbf{r}^{sun} - \mathbf{r}^{sat}||} \\ \mathbf{i} &= \mathbf{j} \times \mathbf{k} \end{aligned} \tag{3.3}$$

  where $\mathbf{r}^{sat}$ is the satellite position referred to the earth mass center.

Assume the antenna phase center offset is (x, y, z)^T, which is frequency dependent, then the phase center correction would be:

$$\Delta_{phase\,center} = x \cdot \mathbf{i} + y \cdot \mathbf{j} + z \cdot \mathbf{k} \tag{3.4}$$

- Ionospheric delay

  The ionosphere layer extending from about 60 km to more than 2000 km above the earth surface is a dispersive medium which causes frequency-dependent delay as signal goes through. In specific, the GNSS code measurements are delayed while the carrier phases are advanced. By cutting off the series expansion of the refractive index after the quadratic term, the ionospheric delay or refraction for code measurement at frequency f can be expressed as:

  $$\Delta^{Iono} = \frac{40.3}{f^2} TEC \tag{3.5}$$

  where TEC is the total electron content along the signal transmission path. The influence on the carrier phase has the same magnitude but reverse sign. TEC is usually given in TEC units (TECU):

  $$1\,TECU = 10^{16}\,electrons\,per\,m^2 \tag{3.6}$$

  The GPS code ionospheric delay is about 0.16 m if one TECU is substituted.

- Tropospheric delay

  The troposphere layer with a height of about 60 km from earth surface is a nondispersive medium for GNSS signals, thus its effect is frequency independent. The tropospheric delay depends on the temperature, pressure and humidity of a local receiver. This delay can be usually divided into hydrostatic or dry and wet components. The hydrostatic effect varying with local temperature and atmospheric pressure is caused by

dry gases (mainly N_2 and Q_2) and can be precisely predicted (Subirana et al., 2013). The wet delay is relevant to the water vapour of local weather and changes faster. Its effect is difficult to model and usually estimated in the navigation filter together with receiver coordinates in precise point positioning. The tropospheric delay is often expressed as zenith delay multiplied by an elevation-dependent mapping function for both dry and wet components as follows:

$$Trop = M_{dry}Z_{dry} + M_{wet}Z_{wet} \tag{3.7}$$

where M is mapping function and Z is the zenith tropospheric delay.

- Phase wind-up effect

  GNSS signals are right circularly polarized and an relative orientation change between satellite and receiver antenna will cause a shift in the received phase measurements up to one cycle. This effect is only considered in precise point positioning. Its correction corresponds to two effective dipoles for the receiver and satellite (Wu et al., 1993):

$$\begin{aligned} \mathbf{d} &= \mathbf{a} - \boldsymbol{\rho}(\boldsymbol{\rho} \cdot \boldsymbol{a}) + \boldsymbol{\rho} \times \boldsymbol{b} \\ \boldsymbol{d}' &= \boldsymbol{a}' - \boldsymbol{\rho}(\boldsymbol{\rho} \cdot \boldsymbol{a}') - \boldsymbol{\rho} \times \boldsymbol{b}' \end{aligned} \tag{3.8}$$

  where $\boldsymbol{\rho}$ is the satellite to receiver unit vector; $\boldsymbol{a}$ and $\boldsymbol{b}$ are unit vectors of local receiver; $\boldsymbol{a}'$ and $\boldsymbol{b}'$ are unit vectors of a satellite-fixed frame. It is noted that the satellite body frame defined in Equation (3.3) can be used for simplicity. However a satellite body frame involves the yaw angle is more realistic especially during the satellite eclipse periods.

3.3 Basic functional model of GNSS measurement

This section gives basic functional models of GNSS code, phase and doppler measurements. These are the fundamental equations that will be used to derive

PPP models in the following sections.

3.3.1 Code measurement

For a specific GNSS satellite j, the code measurement C (meters) on band k with frequency f_k tracked at a receiver i may be modelled as:

$$C_k = \rho + c(dt_i - dt^j) + T + \gamma_k I + K_{C_k,i} - K^j_{C_k} + \varepsilon_{C_k} \tag{3.9}$$

where:

ρ is the geometric propagation distance of the GNSS radio wave between satellite j and receiver i antenna phase centers including phase centre correction on frequency f_k, relativistic effects.

c is the speed of light.

dt_i and dt^j are the clock offset at receiver i and satellite j.

T is the slant troposeric delay, see Equation (3.7).

I is the slant ionospheric delay at a reference frequency; Higher-order effect is ignored, see Equation (3.5); γ is a constant ratio, e.g. $\gamma_k = f_1^2/f_k^2$ in the GPS case, which is referenced to band L_1.

K_i and K^j are the instrumental delays at receiver i and satellite j. This delay is dependent on observable type, frequency and tracking code.

ε groups multipath and other unmodeled errors.

Noted that in accordance with the conventional notations related to the GPS legacy L1/L2 frequencies, f_k with k = 1,2,5 are still used for the frequency of the GPS L_k carrier. Likewise P_1, P_2 and C_5 are for the GPS code measurements.

3.3.2 Carrier-phase measurement

The carrier-phase measurement L (cycles) on frequency k may also be modeled as:

$$\lambda_k L_k = \rho + c(dt_i - dt^j) + T - \gamma_k I + K_{L_k,i} - K^j_{L_k} + \lambda_k N_k + \lambda_k W + \varepsilon_{L_k} \tag{3.10}$$

where:

$\lambda_k = c/f_k$ is the wavelength of signal.

I has the same magnitude as it in the code model but is inversely corrected in the phase case.

N is the carrier-phase integer ambiguity (cycle).

W is the phase wind-up effect (cycle).

3.3.3 Doppler measurement

The Doppler measurement D (Hz) on band k may be expressed as:

$$-\lambda_k D_k = \dot{\rho} + \dot{dt}_i - \dot{dt}^j + \varepsilon_{D_k} \tag{3.11}$$

where: $\dot{\rho}$ is the range rate between satellite j and receiver i.

$\dot{dt}_i$ and $\dot{dt}^j$ are the clock bias drift for receiver i and satellite j.

Given satellite and receiver velocity $\boldsymbol{v^j}$, $\boldsymbol{v_i}$ and position $\boldsymbol{r^j}$, $\boldsymbol{r_i}$, the range rate $\dot{\rho}$ is computed as:

$$\dot{\rho} = (\boldsymbol{v^j} - \boldsymbol{v_i}) \cdot \frac{\boldsymbol{r^j} - \boldsymbol{r_i}}{||\boldsymbol{r^j} - \boldsymbol{r_i}||} \tag{3.12}$$

3.4 Kalman filter

Kalman filtering can be regarded as synonymous with recursive minimum variance and/or least squares estimation (Bierman, 1975). This section presents key equations in prediction and measurement update of a discrete Kalman filter.

3.4.1 Prediction

The estimated states $\hat{x}_{t-1}^{(+)}$ from Kalman filter at previous epoch is predicted to current epoch $\hat{x}_t^{(-)}$ by multiplying by the state transition matrix Φ :

$$\hat{x}_t^{(-)} = \Phi \hat{x}_{t-1}^{(+)} + w_{t-1} \tag{3.13}$$

where w is the system noise or driving noise. This is assumed to be a zero mean and uncorrelated sequence (Hide, 2003). Φ is computed as:

$$\begin{aligned}\Phi &= e^{F\Delta t} \\ &= I + F\Delta t + \frac{(F\Delta t)^2}{2!} + ...\end{aligned} \tag{3.14}$$

where I is the identity matrix; Δt is the prediction interval; F is the dynamics matrix. For standard PPP model, the identity matrix is usually used as the transition matrix. When the inertial measurements are available, the dynamic model is formed using the error dynamics of the inertial system, see Chapter 6. The corresponding covariance matrix $P_{t-1}^{(+)}$ at previous epoch is also propagated to $P_t^{(-)}$ with:

$$P_t^{(-)} = \Phi P_{t-1}^{(+)} \Phi^T + Q_{t-1} \tag{3.15}$$

where Q_{t-1} is termed the process noise matrix and approximated using:

$$Q_t \approx GQG^T \Delta t \tag{3.16}$$

where G maps the disturbing forces to the states in INS and is simply an identity matrix in PPP; Q is the spectral density matrix. Noted that this approximation does not account for any of the correlations between the components of the driving noise w_t (Shin, 2001).

3.4.2 Measurement update

With new measurements z_t and the above predicted states, an innovation vector is formed by their difference:

$$v_t^{(-)} = z_t - H_t \hat{x}_t^{(-)} \tag{3.17}$$

where H_t is the design matrix. In POINT H_t is linearised at the predicted states, which is also known as Extended Kalman filter. The linearisation of H_t can also be evaluated at a coarse point at each epoch (Laurichesse and Privat,

2015).

Then the innovation vector weighed by the Kalman gain K_t is added to the predicted states to yield the measurement updated states:

$$\hat{x}_t^{(+)} = \hat{x}_t^{(-)} + K_t v_t^{(-)} \tag{3.18}$$

where K_t is computed as:

$$K_t = P_t^{(-)} H_t^T (H_t P_t^{(-)} H_t^T + R_t)^{-1} \tag{3.19}$$

where R_t is the measurement noise matrix.

The measurement updated covariance matrix is then expressed as:

$$P_t^{(+)} = (I - K_t H_t) P_t^{(-)} (I - K_t H_t)^T + K_t R_t K_t^T \tag{3.20}$$

3.5 Standard GNSS dual-frequency ionosphere-free PPP

3.5.1 Ambiguity-float PPP

The conventional dual-frequency (DF) ionosphere-free (IF) code and phase measurements in the GPS case may be expressed as follows:

$$\begin{aligned} P_{IF} &= \alpha \cdot P_1 + \beta \cdot P_2 \\ &= \rho + c \cdot \Delta dt + T + \Delta K_{P_{IF}} + \varepsilon_{P_{IF}} \\ \lambda_{IF} L_{IF} &= \alpha \cdot \lambda_1 L_1 + \beta \cdot \lambda_2 L_2 \\ &= \rho + c \cdot \Delta dt + T + \Delta K_{L_{IF}} + \lambda_{IF} N_{IF} + \lambda_{IF} W + \varepsilon_{L_{IF}} \end{aligned} \tag{3.21}$$

with:

$$\begin{aligned} \alpha &= \frac{\gamma_2}{\gamma_2 - 1} = \frac{f_1^2}{f_1^2 - f_2^2} \\ \beta &= 1 - \alpha = -\frac{1}{\gamma_2 - 1} = -\frac{f_2^2}{f_1^2 - f_2^2} \end{aligned} \tag{3.22}$$

where:

$\Delta(*) = (*)_i - (*)^j$ denotes the difference operation between receiver i and satellite j. $\Delta dt = dt_i - dt^j$; $\Delta K = K_i - K^j$.

$(*)_{P_{IF}} = \alpha \cdot (*)_{P_1} + \beta \cdot (*)_{P_2}$ denotes the IF combination of error term $(*)$ for code on frequency f_1 and f_2; $(*)_{L_{IF}} = \alpha \cdot (*)_{L_1} + \beta \cdot (*)_{L_2}$ is the IF combination of error term $(*)$ for phase; $\Delta K_{P_{IF}} = \alpha \cdot \Delta K_{P_1} + \beta \cdot \Delta K_{P_2} = \alpha(K_{P_1,i} - K^j_{P_1}) + \beta(K_{P_2,i} - K^j_{P_2})$; $\Delta K_{L_{IF}} = \alpha \cdot \Delta K_{L_1} + \beta \cdot \Delta K_{L_2} = \alpha(K_{L_1,i} - K^j_{L_1}) + \beta(K_{L_2,i} - K^j_{L_2})$.

$\lambda_{IF} N_{IF} = \alpha \cdot \lambda_1 N_1 + \beta \cdot \lambda_2 N_2 = \frac{c}{f_1^2 - f_2^2}(f_1 N_1 - f_2 N_2)$ denotes the IF combined ambiguity. $N_{IF} = 77N_1 - 60N_2$ with $\lambda_{IF} \approx 6\,mm$ after substituting the values of the GPS f_1 and f_2 frequencies (Collins et al., 2010).

The IF ambiguity can also be decomposed as:

$$\lambda_{IF} N_{IF} = \lambda_{NL}(N_1 + \frac{\lambda_{WL}}{\lambda_2} N_{WL}) \tag{3.23}$$

where $\lambda_{NL} = \frac{c}{f_1 + f_2} \approx 11\ cm$ is the narrow-lane (NL) wavelength; $\lambda_{WL} = \frac{c}{f_1 - f_2} \approx 86\ cm$ is the wide-lane (WL) wavelength. This decomposition is frequently used for resolving the NL ambiguity N_1.

The precise satellite clock product from IGS are referenced to the P_1/P_2 ionosphere-free (IF) combination in the GPS case. It may be modeled as:

$$dt^j_{P_{IF}} = dt^j + \alpha K^j_{P_1} + \beta K^j_{P_2} = dt^j + K^j_{P_{IF}} \tag{3.24}$$

Rewriting the receiver clock offset with the same format:

$$dt_{P_{IF},i} = dt_i + \alpha K_{P_1,i} + \beta K_{P_2,i} = dt_i + K_{P_{IF},i} \tag{3.25}$$

and substituting Equation (3.24) and Equation (3.25) into Equation (3.21), it

follows that:

$$\begin{aligned} P_{IF} &= \rho + c \cdot \Delta dt_{P_{IF}} + T + \varepsilon_{P_{IF}} \\ \lambda_{IF} L_{IF} &= \rho + c \cdot \Delta dt_{P_{IF}} + T + A_{IF} + \lambda_{IF} W + \varepsilon_{L_{IF}} \end{aligned} \tag{3.26}$$

where $A_{IF} = \lambda_{IF} N_{IF} + \Delta K_{L_{IF}} - \Delta K_{P_{IF}}$ is the float ambiguity which also includes the code hardware delays. When the IGS satellite clock products are used, $dt^j_{P_{IF}}$ is regarded as known value and can be eliminated from Equation (3.26). Therefore a further reduced form can be obtained as below:

$$\begin{aligned} P_{IF} &= \rho + c \cdot dt_{P_{IF},i} + T + \varepsilon_{P_{IF}} \\ \lambda_{IF} L_{IF} &= \rho + c \cdot dt_{P_{IF},i} + T + A_{IF} + \lambda_{IF} W + \varepsilon_{L_{IF}} \end{aligned} \tag{3.27}$$

This equation is the standard dual-frequency ionosphere-free ambiguity-float PPP model.

3.5.2 Ambiguity resolution

In order to resolve the ambiguity in Equation (3.27) with Equation (3.23), the hardware biases have to be corrected first. The manner of these biases correction varies with the definition of applied bias products. Ge et al. (2008) formed a between-satellite single-difference (SD) PPP model , in which the common receiver clock and hardware biases are eliminated, then computed the SD WL and NL uncalibrated phase delays (UPD) for correction. Another form of bias representation is the undifferenced 'decoupled' code and phase clock model presented in Laurichesse et al. (2009) and Collins et al. (2010). This undifferenced model also resolves the satellite WL ambiguity first with the WL satellite biases (WSB) products. The Melbourne–Wübbena (MW) combination (Melbourne, 1985; Wübbena, 1985) is usually constructed for the WL ambiguity estimation:

$$MW = L_1 - L_2 + \alpha_1 P_1 + \alpha_2 P_2 = N_{WL} + \mu_i - \mu^j \tag{3.28}$$

where $\alpha_1 = \frac{\lambda_1-\lambda_2}{(\lambda_1+\lambda_2)\lambda_1}$; $\alpha_2 = \frac{\lambda_1-\lambda_2}{(\lambda_1+\lambda_2)\lambda_2}$; μ_i is the receiver WL delays; μ^j is the satellite WL delays, which can be corrected by applying the WSB products. This combination is usually averaged to smooth the effect from the code noises and then the WL ambiguity N_{WL} can be identified easily due to its long wavelength. With the fixed N_{WL}, the phase IF combination in Equation (3.26) can be expressed as:

$$\frac{\gamma_2\lambda_1 L_1 - \lambda_2(L_2 + N_{WL})}{\gamma_2 - 1} = \rho + dt_{L_{IF},i} - dt^j_{L_{IF}} + T + \lambda_{NL}N_1 + \lambda_{NL}W + \epsilon \tag{3.29}$$

where $dt_{L_{IF},i} = dt_i + K_{L_{IF},i}$; $dt^j_{L_{IF}} = dt^j + K^j_{L_{IF}}$.

Then the satellite phase clocks products are used to eliminate $dt^j_{L_{IF}}$ and fix the remaining N_1 ambiguities with wavelength around $11cm$. This phase clock is also called 'integer' phase clock as it allows the direct fixing of N_1, however it is different from the IGS clock products in Equation (3.24).

3.5.3 Integer estimator

Integer estimator is used to compute the integer-valued ambiguities from their real-valued or float estimates and covariance. The simplest way is a direct integer-rounding to their nearest integers ignoring their correlations. In GNSS data processing, three other integer estimators are commonly used: integer bootstrapping (IB), integer least square (ILS) and best integer equivariant (BIE).

Integer Bootstrapping

The integer bootstrapping makes use of integer rounding but it also takes some of the correlation between the ambiguities into account. Its computation follows a sequential conditional least-square adjust. The condition comes from the fixed ambiguities in previous steps prior to rounding in current step. More discussion can be found in Teunissen (1999) and Verhagen et al. (2013). This estimator enables partial ambiguity resolution (PAR) and could still benefit the estimated states when the ambiguity set has different levels of accuracy. See Figure 8.10 for an example.

Integer Least-Square

The integer least-squares refer to the estimation of ambiguities in a least square sense with additional integer constraint. It consists two steps: Z-transformation decorrelation and integer search. This procecedure is well mechanized in the LAMBDA ((Least squares AMBiguity Decorrelation Adjustment) method (Teunissen, 1995). This estimator has higher success rate than IB but works on an ambiguity vector instead of a separate ambiguity. See Figure 5.2 for an example.

Best Integer Equivariant

The best integer equivariant estimator (Teunissen, 2003; Odolinski and Teunissen, 2020) may be expressed as

$$\bar{a} = \sum_{z\in\mathbb{Z}} z \frac{exp(-\frac{1}{2}||\hat{a}-z||^2_{Q_{\hat{a}\hat{a}}})}{\sum_{z\in\mathbb{Z}} exp(-\frac{1}{2}||\hat{a}-z||^2_{Q_{\hat{a}\hat{a}}})} \tag{3.30}$$

where $\hat{a}$ is a vector of float ambiguities with its covariance matrix $Q_{\hat{a}\hat{a}}$; $z \in \mathbb{Z}$ is an integer candidate; $||\cdot||^2_{Q_{\hat{a}\hat{a}}} = (\cdot)^T Q^{-1}_{\hat{a}\hat{a}}(\cdot)$. Therefore the output solution $\bar{a}$ is a weighted average of integer candidates, which could mitigate the effect of wrong fixing although $\bar{a}$ is non-integer. The decorrelation and search procedures of the conventional LAMBDA method can still be used for finding integer candidates. See Figure 5.11 for an example.

3.6 CNES uncombined bias representation

The CNES uncombined bias formulation can be extended to multi-frequency measurements easily without explicit estimation of the IFCB for the GPS Block IIF satellites (Laurichesse, 2012) and the integer nature of phase ambiguity and its combinations is also preserved. In this section, two PPP models: ionosphere-float and ionosphere-free models are formulated with the CNES uncombined biases correction on the raw GNSS measurements.

3.6.1 CNES undifference and uncombined model

Laurichesse (2012) extended the definition of code biases in the Radio Technical Commission for Maritime Services (RTCM) framework, which can be directly added to the raw code measurements, to the phase biases and the general model for uncombined code and phase biases in the GPS triple-frequency case is expressed as (Laurichesse and Langley, 2015):

$$\begin{aligned}
P_1^{'} &= P_1 + \Delta b_{P_1} = \rho + \Delta h + I + T \\
P_2^{'} &= P_2 + \Delta b_{P_2} = \rho + \Delta h + \gamma_2 I + T \\
C_5^{'} &= C_5 + \Delta b_{C_5} = \rho + \Delta h + \gamma_5 I + T \\
\lambda_1 L_1^{'} &= \lambda_1 (L_1 + \Delta b_{L_1}) = \rho + \Delta h - I + T + \lambda_1 W + \lambda_1 N_1 \\
\lambda_2 L_2^{'} &= \lambda_2 (L_2 + \Delta b_{L_2}) = \rho + \Delta h - \gamma_2 I + T + \lambda_2 W + \lambda_2 N_2 \\
\lambda_5 L_5^{'} &= \lambda_5 (L_5 + \Delta b_{L_5}) = \rho + \Delta h - \gamma_5 I + T + \lambda_5 W + \lambda_5 N_5
\end{aligned} \tag{3.31}$$

where $\Delta h = h_i - h^j$ is the clock difference between receiver i and satellite j; $\Delta b_P = b_{P,i} - b_P^j$ and $\Delta b_L = b_{L,i} - b_L^j$ denote the bias difference between i and j for code and phase, respectively.

This model reflects that the code or phase bias is inherent to each frequency and the estimated phase ambiguity has integer property. Hence it allows for zero-differenced ambiguity resolution after the phase bias correction. It is also independent of the method of bias estimation on the network side and user can implement the ambiguity resolution method of his choice (Laurichesse, 2012). This uncombined biases Δb_P and Δb_L are referenced to the same clock Δh while Δh is arbitrary and can follow any definition (Laurichesse and Privat, 2015). The convention chosen for the standard is the same as the one used by IGS, namely:

$$\Delta h = \Delta dt_{P_{IF}} \tag{3.32}$$

With this standard, the relationship between the uncombined and undifferenced biases b_P, b_L and the original hardware delays K_P, K_L can be obtained

as follows:

$$\begin{aligned}
\Delta b_{P_1} &= -\beta(\Delta K_{P_1} - \Delta K_{P_2}) \\
\Delta b_{P_2} &= \alpha(\Delta K_{P_1} - \Delta K_{P_2}) \\
\Delta b_{C_5} &= \Delta K_{P_{IF}} - \Delta K_{C_5} \\
\lambda_1 \Delta b_{L_1} &= \Delta K_{P_{IF}} - \Delta K_{L1} \\
\lambda_2 \Delta b_{L_2} &= \Delta K_{P_{IF}} - \Delta K_{L2} \\
\lambda_5 \Delta b_{L_5} &= \Delta K_{P_{IF}} - \Delta K_{L5}
\end{aligned} \tag{3.33}$$

It can be seen that the code and phase biases b_P, b_L are not true signal hardware delays but just can be added to the raw measurements with respect to the defined clock.

3.6.2 Estimation of uncombined phase bias

In the dual-frequency case, b_{L_1} and b_{L_2} can be uniquely determined by the previous WSB μ and the 'integer' phase clock $dt_{L_{IF}}$ when $dt_{P_{IF}}$ is introduced. Laurichesse and Langley (2015) gave the mathmatical transformation as below:

$$\begin{bmatrix} b_{L_1} \\ b_{L_2} \end{bmatrix} = \frac{1}{\gamma_2\lambda_1 - \lambda_2} \begin{bmatrix} -\lambda_2 & 1 \\ -\gamma_2\lambda_1 & 1 \end{bmatrix} \begin{bmatrix} \mu - \alpha_1 b_{P_1} - \alpha_2 b_{P_2} \\ (\gamma_2 - 1)(dt_{L_{IF}} - dt_{P_{IF}}) \end{bmatrix} \tag{3.34}$$

In the triple-frequency case, however, different sets of μ and $dt_{L_{IF}}$ could be generated depending on the the used frequency pair. It is difficult to use three uncombined phase biases b_{L1}, b_{L_2} and b_L5 to keep the integer nature of all viable combinations. Laurichesse and Langley (2015) proposed to work with combinations of biases and adpot the traditionaled WL/NL GPS scheme. The WL biases $b_{L_i} - b_{L_j}$ are computed first. The classical MW combinations and the triple-frequency widelane-only ionosphere-free combinations are used to identify all the $b_{L_i} - b_{L_j}$ and the remaining b_{L_1} is estimated using the ionosphere-free phase combination of L1 and L2.

3.7 PPP models using CNES uncombined biases

3.7.1 GPS/Galileo multi-frequency ionosphere-estimated PPP

Functional model

In Equation (3.31), after applying precise satellite clock products and the CNES bias products, the terms h^j, b_P^j and b_L^j can be eliminated. As a consequence, one receiver clock per observable can be reparameterized at a user end. Alternatively, a common receiver clock offset with additional receiver clock biases may be defined in these equations as:

$$\begin{aligned} P_1 &= \rho + dt^G + I + T \\ P_2 &= \rho + dt^G + b_{P_2} + \gamma_2 I + T \\ C_5 &= \rho + dt^G + b_{C_5} + \gamma_5 I + T \\ \lambda_1 L_1 &= \rho + dt^G + b_{L_1} - I + T + \lambda_1 W + \lambda_1 N_1 \\ \lambda_1 L_2 &= \rho + dt^G + b_{L_2} - \gamma_2 I + T + \lambda_2 W + \lambda_2 N_2 \\ \lambda_1 L_5 &= \rho + dt^G + b_{L_5} - \gamma_5 I + T + \lambda_5 W + \lambda_5 N_5 \end{aligned} \tag{3.35}$$

Where dt^G is the common GPS receiver clock offset and we omit the subscript i of b. It is noted that for simplicity no change is marked in the bias terms but they should be different from those in Equation (3.31).

Similarly, Galileo E1/E5a/E5b/E6 code and phase measurements are expressed as:

$$
\begin{aligned}
C_{E1} &= \rho + dt^E + I + T \\
C_{E5a} &= \rho + dt^E + b_{C_{E5a}} + \gamma_{E5a} I + T \\
C_{E5b} &= \rho + dt^E + b_{C_{E5b}} + \gamma_{E5b} I + T \\
C_{E6} &= \rho + dt^E + b_{C_{E6}} + \gamma_{E6} I + T \\
\lambda_{E1} L_{E1} &= \rho + dt^E + b_{L_{E1}} - I + T + \lambda_{E1} W + \lambda_{E1} N_{E1} \\
\lambda_{E5a} L_{E5a} &= \rho + dt^E + b_{L_{E5a}} - \gamma_{E5a} I + T + \lambda_{E5a} W + \lambda_{E5a} N_{E5a} \\
\lambda_{E5b} L_{E5b} &= \rho + dt^E + b_{L_{E5b}} - \gamma_{E5b} I + T + \lambda_{E5b} W + \lambda_{E5b} N_{E5b} \\
\lambda_{E6} L_{E6} &= \rho + dt^E + b_{L_{E6}} - \gamma_{E6} I + T + \lambda_{E6} W + \lambda_{E6} N_{E6}
\end{aligned}
\tag{3.36}
$$

where dt^E is the Galileo receiver clock offset.

Instead of the usual method of converting the float ambiguity estimates to their widelane combinations or using the Melbourne–Wüebbena (MW) combination (Melbourne, 1985; Wübbena, 1985) to achieve the ambiguity resolution, an explicit widelane-nested model is presented in Laurichesse and Privat (2015) for GPS carrier-phase measurements in which the individual ambiguities are configured as follows:

$$
\begin{aligned}
\lambda_1 N_1 &= \lambda_1 N_1 \\
\lambda_2 N_2 &= \lambda_2 (N_1 + N_{WL}) \\
\lambda_5 N_5 &= \lambda_5 (N_1 + N_{WL} + N_{EWL})
\end{aligned}
\tag{3.37}
$$

where N_{WL} and N_{EWL} are the GPS well-known widelane and extra-widelane ambiguities. Likewise, the Galileo quadruple-frequency phase ambiguities in Equation (3.36) can also be rearranged as:

$$
\begin{aligned}
\lambda_{E1} N_{E1} &= \lambda_{E1} N_{E1} \\
\lambda_{E5a} N_{E5a} &= \lambda_{E5a} (N_{E1} + N_{WL,E1E5a}) \\
\lambda_{E5b} N_{E5b} &= \lambda_{E5b} (N_{E1} + N_{WL,E1E5a} + N_{WL,E5aE5b}) \\
\lambda_{E6} N_{E6} &= \lambda_{E6} (N_{E1} + N_{WL,E1E5a} + N_{WL,E5aE5b} + N_{WL,E5bE6})
\end{aligned}
\tag{3.38}
$$

where the subscript Galileo frequency pair indicates the used frequencies for forming the widelane observation. These widelane ambiguities with long wavelength (meter level) can be resolved more easily and thus the resolution is usually performed in a cascading manner according to their wavelengths.

Implementation in Kalman filter

Assuming m GPS satellites $(p1, ..., pm)$ and n Galileo satellites $(q1, ..., qn)$ are observed at an epoch, the states to be estimated in the above models Equation (3.35) and Equation (3.36) are:

$$\begin{aligned} x = \big[& \varphi \quad \lambda \quad h \quad ZTD \quad dt^G \quad b_{P_2} \quad b_{C_5} \quad b_{L_1} \quad b_{L_2} \quad b_{L_5} \\ & dt^E \quad b_{C_{E5a}} \quad b_{C_{E5b}} \quad b_{C_{E6}} \quad b_{L_{E1}} \quad b_{L_{E5a}} \quad b_{L_{E5b}} \quad b_{L_{E6}} \\ & I^{p1} \quad N_1^{p1} \quad N_2^{p1} \quad N_5^{p1} \quad ... \quad I^{pm} \quad N_1^{pm} \quad N_2^{pm} \quad N_5^{pm} \\ & I^{q1} \quad N_{E1}^{q1} \quad N_{E5a}^{q1} \quad N_{E5b}^{q1} \quad N_{E6}^{q1} \quad ... \quad I^{qn} \quad N_{E1}^{qn} \quad N_{E5a}^{qn} \quad N_{E5b}^{qn} \quad N_{E6}^{qn} \big]^T \end{aligned} \tag{3.39}$$

where φ is latitude; λ is longitude; h is the geodetic height with reference to the WGS84 ellipsoid surface; ZTD is the zenith tropospheric delay on the wet component. p and q denote a specific GPS and Galileo satellite respectively. The transition matrix of states in Equation (3.14) is set as identity. The G matrix in Equation (3.16) with position spectral densities in the north east and up directions is as follows:

$$G = \begin{bmatrix} \frac{1}{RN+h} & 0 & 0 & \\ 0 & \frac{1}{(RE+h)cos(\varphi)} & 0 & \mathbf{0} \\ 0 & 0 & 1 & \\ & \mathbf{0} & & \mathbf{I} \end{bmatrix} \tag{3.40}$$

where RN and RE are the radii of curvature in the meridian and prime vertical. Assume the measurement vector is arranged as :

$$
\begin{aligned}
z = \big[& P_1^{p1} \quad P_2^{p1} \quad C_5^{p1} \quad \lambda_1 L_1^{p1} \quad \lambda_2 L_2^{p1} \quad \lambda_5 L_5^{p1} \quad ... \\
& P_1^{pm} \quad P_2^{pm} \quad C_5^{pm} \quad \lambda_1 L_1^{pm} \quad \lambda_2 L_2^{pm} \quad \lambda_5 L_5^{pm} \\
& C_{E1}^{q1} \quad C_{E5a}^{q1} \quad C_{E5b}^{q1} \quad C_{E6}^{q1} \quad \lambda_{E1} L_{E1}^{q1} \quad \lambda_{E5a} L_{E5a}^{q1} \quad \lambda_{E5b} L_{E5b}^{q1} \quad \lambda_{E6} L_{E6}^{q1} \quad ... \\
& C_{E1}^{qn} \quad C_{E5a}^{qn} \quad C_{E5b}^{qn} \quad C_{E6}^{qn} \quad \lambda_{E1} L_{E1}^{qn} \quad \lambda_{E5a} L_{E5a}^{qn} \quad \lambda_{E5b} L_{E5b}^{qn} \quad \lambda_{E6} L_{E6}^{qn} \big]^T
\end{aligned}
\tag{3.41}
$$

$$
H = \begin{bmatrix}
H_{r,T}^{p1} & H_{clk}^{p1} & \mathbf{0} & H_{I,amb}^{p1} & \mathbf{...} & \mathbf{0} & \mathbf{0} & \mathbf{...} & \mathbf{0} \\
\vdots & \vdots & \vdots & \vdots & \vdots & \vdots & \vdots & \vdots & \vdots \\
H_{r,T}^{pm} & H_{clk}^{pm} & \mathbf{0} & \mathbf{0} & \mathbf{...} & H_{I,amb}^{pm} & \mathbf{0} & \mathbf{...} & \mathbf{0} \\
H_{r,T}^{q1} & \mathbf{0} & H_{clk}^{q1} & \mathbf{0} & \mathbf{...} & \mathbf{0} & H_{I,amb}^{q1} & \mathbf{...} & \mathbf{0} \\
\vdots & \vdots & \vdots & \vdots & \vdots & \vdots & \vdots & \vdots & \vdots \\
H_{r,T}^{qn} & \mathbf{0} & H_{clk}^{qn} & \mathbf{0} & \mathbf{...} & \mathbf{0} & \mathbf{0} & \mathbf{...} & H_{I,amb}^{qn}
\end{bmatrix}
\tag{3.42}
$$

with:

$$
H_{r,T}^{p} = \begin{bmatrix}
H_{\varphi}^{p} & H_{\lambda}^{p} & H_{h}^{p} & m_w \\
H_{\varphi}^{p} & H_{\lambda}^{p} & H_{h}^{p} & m_w \\
H_{\varphi}^{p} & H_{\lambda}^{p} & H_{h}^{p} & m_w \\
H_{\varphi}^{p} & H_{\lambda}^{p} & H_{h}^{p} & m_w \\
H_{\varphi}^{p} & H_{\lambda}^{p} & H_{h}^{p} & m_w \\
H_{\varphi}^{p} & H_{\lambda}^{p} & H_{h}^{p} & m_w
\end{bmatrix}, H_{clk}^{p} = \begin{bmatrix}
1 & 0 & 0 & 0 & 0 & 0 \\
1 & 1 & 0 & 0 & 0 & 0 \\
1 & 0 & 1 & 0 & 0 & 0 \\
1 & 0 & 0 & 1 & 0 & 0 \\
1 & 0 & 0 & 0 & 1 & 0 \\
1 & 0 & 0 & 1 & 0 & 1
\end{bmatrix}
$$

$$
H_{I,amb}^{p} = \begin{bmatrix}
1 & 0 & 0 & 0 \\
\gamma_2 & 0 & 0 & 0 \\
\gamma_5 & 0 & 0 & 0 \\
-1 & \lambda_1 & 0 & 0 \\
-\gamma_2 & 0 & \lambda_2 & 0 \\
-\gamma_5 & 0 & 0 & \lambda_5
\end{bmatrix}, H_{r,T}^{q} = \begin{bmatrix}
H_{\varphi}^{q} & H_{\lambda}^{q} & H_{h}^{q} & m_w \\
H_{\varphi}^{q} & H_{\lambda}^{q} & H_{h}^{q} & m_w \\
H_{\varphi}^{q} & H_{\lambda}^{q} & H_{h}^{q} & m_w \\
H_{\varphi}^{q} & H_{\lambda}^{q} & H_{h}^{q} & m_w \\
H_{\varphi}^{q} & H_{\lambda}^{q} & H_{h}^{q} & m_w \\
H_{\varphi}^{q} & H_{\lambda}^{q} & H_{h}^{q} & m_w \\
H_{\varphi}^{q} & H_{\lambda}^{q} & H_{h}^{q} & m_w \\
H_{\varphi}^{q} & H_{\lambda}^{q} & H_{h}^{q} & m_w
\end{bmatrix}
$$

$$
H_{clk}^{q} = \begin{bmatrix}
1 & 0 & 0 & 0 & 0 & 0 & 0 & 0 \\
1 & 1 & 0 & 0 & 0 & 0 & 0 & 0 \\
1 & 0 & 1 & 0 & 0 & 0 & 0 & 0 \\
1 & 0 & 0 & 1 & 0 & 0 & 0 & 0 \\
1 & 0 & 0 & 0 & 1 & 0 & 0 & 0 \\
1 & 0 & 0 & 0 & 0 & 1 & 0 & 0 \\
1 & 0 & 0 & 0 & 0 & 0 & 1 & 0 \\
1 & 0 & 0 & 0 & 0 & 0 & 0 & 1
\end{bmatrix}, H_{I,amb}^{q} = \begin{bmatrix}
1 & 0 & 0 & 0 & 0 \\
\gamma_{E5a} & 0 & 0 & 0 & 0 \\
\gamma_{E5b} & 0 & 0 & 0 & 0 \\
\gamma_{E6} & 0 & 0 & 0 & 0 \\
-1 & \lambda_{E1} & 0 & 0 & 0 \\
-\gamma_{E5a} & 0 & \lambda_{E5a} & 0 & 0 \\
-\gamma_{E5b} & 0 & 0 & \lambda_{E5b} & 0 \\
-\gamma_{E6} & 0 & 0 & 0 & \lambda_{E6}
\end{bmatrix}
\tag{3.43}
$$

where m_w is the tropospheric mapping function for the wet component; H_r^p and H_r^q are the partial derivatives of ρ^p and ρ^q with respect to receiver position $r = [\varphi\ \lambda\ h]^T$. The line-of-sight vector $[H_\varphi^p\ H_\lambda^p; H_h^p]^T$ can be computed as:

$$\begin{bmatrix} H_\varphi^p \\ H_\lambda^p \\ H_h^p \end{bmatrix} = \begin{bmatrix} RN+h & 0 & 0 \\ 0 & (RE+h)cos\varphi & 0 \\ 0 & 0 & 1 \end{bmatrix} C_e^n \begin{bmatrix} \frac{\partial \rho^p}{\partial r_X} \\ \frac{\partial \rho^p}{\partial r_Y} \\ \frac{\partial \rho^p}{\partial r_Z} \end{bmatrix} \tag{3.44}$$

where $[r_X\ r_Y\ r_Z]^T$ is the receiver coordinate vector in the Cartesian form. C_e^n is the rotation matrix that transform coordinates from earth frame to a local navigation frame.

The measurement noise matrix R in Equation (3.19) is usually diagonal and weighted according to the elevation angles of satellites.

3.7.2 GPS/Galileo dual-frequency ionosphere-free PPP

Functional model

Equation (3.35) shows the undifferenced and uncombined GPS observation model with the corrections of precise satellite clock products and CNES uncombined code and phase biases. Applying the traditional ionosphere-free (IF) combination on the first two frequencies, the IF code and phase observation equations would be:

$$\begin{aligned} P_{IF} &= \alpha P_1 + \beta P_2 = \rho + dt_P^G + T \\ \lambda_{IF} L_{IF} &= \alpha \lambda_1 L_1 + \beta \lambda_2 L_2 = \rho + dt_L^G + T + \lambda_{IF} W + B_{IF} \end{aligned} \tag{3.45}$$

where $dt_P^G = dt^G + \beta b_{P_2}$; $dt_L^G = dt^G + (\alpha b_{L_1} + \beta b_{L_2})$; $B_{IF} = \lambda_{IF} N_{IF} = \alpha \lambda_1 N_1 + \beta \lambda_2 N_2$, which can be decomposed as WL ambiguity and narrow ambiguity, see Equation (3.23). The WL ambiguity can still be estimated from the MW combination but with the uncombined biases instead of using the WSB in

Equation (3.28) as below:

$$\begin{aligned} MW_{L_1L_2} &= (L_1 - b^p_{L_1}) - (L_2 - b^p_{L_2}) + \alpha_1(P_1 - b^p_{P_1}) + \alpha_2(P_2 - b^p_{P_2}) \\ &= N_{WL_{L1L2}} + \mu^G_i \end{aligned} \tag{3.46}$$

where $\mu^G_i = \frac{b_{L_1}}{\lambda 1} - \frac{b_{L_2}}{\lambda 2} + \alpha_2 b_{P_2}$ is the receiver WL bias. After the WL ambiguity is fixed, the remaining N_1 can also be resolved using Equation (3.23) with the eatimated B_{IF}.

Similarly the Galileo E1/E5a IF model can be expressed as:

$$\begin{aligned} C_{IF_{E_1E_{5a}}} &= \alpha_{E_1E_{5a}} C_{E_1} + \beta_{E_1E_{5a}} C_{E_{5a}} = \rho + dt^E_C + T \\ \lambda_{IF_{E_1E_{5a}}} L_{IF_{E_1E_{5a}}} &= \alpha_{E_1E_{5a}} \lambda_{E_1} L_{E_1} + \beta_{E_1E_{5a}} \lambda_{E_{5a}} L_{E_{5a}} \\ &= \rho + dt^E_L + T + \lambda_{IF_{E_1E_{5a}}} W + B_{IF_{E_1E_{5a}}} \\ B_{IF_{E_1E_{5a}}} &= \lambda_{NL_{E_1E_{5a}}} (N_{E_1} + \frac{\lambda_{WL_{E_1E_{5a}}}}{\lambda_{E_{5a}}} N_{WL_{E_1E_{5a}}}) \\ MW_{E_1E_{5a}} &= (L_{E_1} - b^q_{L_{E_1}}) - (L_{E_{5a}} - b^q_{L_{E_{5a}}}) \\ &\quad + \alpha 1_{E_1E_{5a}} (C_{E_1} - b^q_{C_{E_1}}) + \alpha 2_{E_1E_{5a}} (C_{E_{5a}} - b^q_{C_{E_{5a}}}) \\ &= N_{WL_{E_1E_{5a}}} + \mu^E_i \end{aligned} \tag{3.47}$$

where $\alpha_{E_1E_{5a}} = \frac{\gamma_{E_{5a}}}{\gamma_{E_{5a}} - 1} = \frac{E_1^2}{E_1^2 - E_{5a}^2}$; $\beta_{E_1E_{5a}} = 1 - \alpha_{E_1E_{5a}} = -\frac{1}{\gamma_{E_{5a}} - 1} = -\frac{E_1^2}{E_1^2 - E_{5a}^2}$; $\alpha 1_{E_1E_{5a}} = \frac{\lambda_{E_1} - \lambda_{E_{5a}}}{(\lambda_{E_1} + \lambda_{E_{5a}})\lambda_{E_1}}$; $\alpha 2_{E_1E_{5a}} = \frac{\lambda_{E_1} - \lambda_{E_{5a}}}{(\lambda_{E_1} + \lambda_{E_{5a}})\lambda_{E_{5a}}}$.

Implementation in Kalman filter

Assuming m GPS satellites (p1, ..., pm) and n Galileo satellites (q1, ..., qn) are observed at an epoch, the states to be estimated in the above models Equation (3.45), Equation (3.46) and Equation (3.47) are:

$$\begin{aligned} x = \big[& \varphi \quad \lambda \quad h \quad ZTD \quad dt^G_P \quad dt^G_L \quad dt^E_C \quad dt^E_L \\ & N^{p1}_{IF} \quad \ldots \quad N^{pm}_{IF} \quad N^{q1}_{IF_{E_1E_{5a}}} \quad \ldots \quad N^{qn}_{IF_{E_1E_{5a}}} \big]^T \end{aligned} \tag{3.48}$$

Assume the measurement vector is arranged as:

$$\begin{aligned} z = \big[& P_{IF}^{p1} \quad \lambda_{IF} L_{IF}^{p1} \quad ... \quad P_{IF}^{pm} \quad \lambda_{IF} L_{IF}^{pm} \\ & C_{IF_{E_1E_{5a}}}^{q1} \quad \lambda_{IF_{E_1E_{5a}}} L_{IF_{E_1E_{5a}}}^{q1} ... \quad C_{IF_{E_1E_{5a}}}^{qn} \quad \lambda_{IF_{E_1E_{5a}}} L_{IF_{E_1E_{5a}}}^{qn} \big]^T \end{aligned} \tag{3.49}$$

and the design matrix will be:

$$H = \begin{bmatrix} H_{r,T}^{p1} & H_{clk}^{p1} & \mathbf{0} & H_{amb}^{p1} & \mathbf{...} & \mathbf{0} & \mathbf{0} & \mathbf{0} & \mathbf{0} \\ \vdots & \vdots & \vdots & \vdots & \vdots & \vdots & \vdots & \vdots & \vdots \\ H_{r,T}^{pm} & H_{clk}^{pm} & \mathbf{0} & \mathbf{0} & \mathbf{...} & H_{amb}^{pm} & \mathbf{0} & \mathbf{0} & \mathbf{0} \\ H_{r,T}^{q1} & \mathbf{0} & H_{clk}^{q1} & \mathbf{0} & \mathbf{0} & \mathbf{0} & H_{amb}^{q1} & \mathbf{...} & \mathbf{0} \\ \vdots & \vdots & \vdots & \vdots & \vdots & \vdots & \vdots & \vdots & \vdots \\ H_{r,T}^{qn} & \mathbf{0} & H_{clk}^{qn} & \mathbf{0} & \mathbf{0} & \mathbf{0} & \mathbf{0} & \mathbf{...} & H_{amb}^{qn} \end{bmatrix} \tag{3.50}$$

with:

$$H_{clk}^{p} = \begin{bmatrix} 1 & 0 \\ 0 & 1 \end{bmatrix}, H_{amb}^{p} = \begin{bmatrix} 0 \\ 1 \end{bmatrix}, H_{clk}^{q} = \begin{bmatrix} 1 & 0 \\ 0 & 1 \end{bmatrix}, H_{amb}^{q} = \begin{bmatrix} 0 \\ 1 \end{bmatrix} \tag{3.51}$$

The components of the measurement matrix R are also elevation-dependent but are propagated from the standard deviations of original measurements through IF combination.

3.8 Summary

This chapter formulates two PPP models using CNES uncombined bias products at a user side. The integer nature of the phase ambiguities in both of the models can be preserved after applying the uncombined biases on the raw code and phase measurements, which allows users to resolve phase ambiguities in undifferenced mode. This flexibility of uncombined bias products simplify the ambiguity resolution process and is more inherent to physical nature of GNSS biases.

The current generation of CNES bias products are transformed from the WL combined biases, which requires the computation of all possible WL ambigui-

ties first. The direct estimation of these uncombined biases from uncombined observation models is to be investigated.

In the next chapter, the methodology for assessing the two PPP models is presented.

Chapter 4

Methodology for GNSS Precise Point Positioning evaluation

4.1 Introduction

In this chapter, the methodology of GPS/Galileo PPP using CNES uncombined bias products is presented. The internal software tool POINT developed at Nottingham Geospatial Institute is introduced, which is mainly utilized to perform analysis in this thesis.

This chapter is organised as follows: Section 4.2 gives the data sources used in the PPP evaluation, including precise products and observation data; then the POINT software tool used for PPP processing is introduced in Section 4.3, with emphasis on newly developed features and comparison with external PPP software; Section 4.4 presents the basic settings of POINT for PPP computation including ionosphere-free and ionosphere-estimated models, followed by the positioning accuracy assessment manner; last this chapter is recapped in Section 4.5.

4.2 Data sources

The International GNSS Service (IGS) has set up a Multi-GNSS Experiment (MGEX) nearly a decade a ago (Steigenberger et al., 2013; Montenbruck and Et.al, 2014) to track, collate and analyze all available GNSS signals. For ex-

ample, it includes signals from modernized GPS and GLONASS satellites, the relatively new BeiDou, Galileo, QZSS and space-based augmentation system (SBAS). Since 2016, IGS has decided to terminate the experimental phase of MGEX and pursue the IGS multi-GNSS activities as a pilot project with the term 'MGEX' retained.

As of summer 2022, there are around 365 IGS multi-GNSS stations globally distributed. With the existing network of the IGS GPS/GLONASS reference stations, more than 500 stations in total are available,

Observation data of these stations and the precise products such like orbit, clock and signal bias for the new constellations are archived in the IGS data centers and the analysis centers respectively. In the following, the IGS multi-GNSS products from analysis centers GeoForschungsZentrum Potsdam (GFZ) and Centre National d'Etudes Spatiales (CNES) used in the study are briefly introduced, followed by the information of the selected station data.

4.2.1 IGS multi-GNSS products

The IGS multi-GNSS products usually include precise ephemerides, clocks, earth orientation parameters (EOPs), site coordinates, atmosphere and combined and uncombined biases. Currently seven IGS analysis centers (ACs) are contributing dedicated multi-GNSS products routinely, which are Centre National d'Etudes Spatiales (CNES), Collecte Localisation Satellites (CLS), Groupe de Recherche de Géodésie Spatiale (GRGS); Center for Orbit Determination in Europe (CODE); GeoForschungsZentrum Potsdam (GFZ); Information and Analysis Center (IAC); Shanghai Observatory (SHAO); Wuhan University; Japan Aerospace Exploration Agency (JAXA).

Products from GFZ and CNES

Table 4.1 summarises the products from GFZ and CNES. It is noted that the GFZ products have three modes: ultra-rapid (latency 3-9h; GPS, GLONASS, Galileo), rapid (latency 1 day; GPS, GLONASS, Galileo), and final (latency two weeks; GPS and GLONASS) while CNES/CLS only provides final-mode

products. Both of these two analysis centers provide dual-frequency code and phase uncombined bias products in the SINEX form and CNES/CLS also generates its conventional dual-frequency WSB and integer phase-clock products for GPS and Galileo.

Table 4.1: Products of two IGS analysis centers: GFZ and CNES/CLS. The time information are the sampling intervals of the products; the same below.

Products	GFZ	CNES/CLS
Constellation	GPS(G)/GLONASS(R)/ Galileo(E)/BeiDou(C)/QZSS(J)	G/R/E
Satellite orbit	5 min; *.SP3	
Satellite and station clocks	30 s;*.CLK	
Site coordinates	None	1 d, *.SNX
EOPs	1 d, *.ERP	None
Bias	1 d, *.BIA; Dual frequency; Code and phase	
Satellite attitude	30 s;*.OBX	

CNES products in the PPPWIZARD project

Thanks to the CNES PPPWIZARD (Precise Point Positioning With Integer and Zero-difference Ambiguity Resolution Demonstrator) project (Laurichesse, 2010), multi-constellation and multi-frequency code and phase bias products are available for outside users for multi-frequency PPP with ambiguity resolution and archived in their daily products portal. These products are issued in both real-time and post-processed modes. Noted their post-processed bias products have to be used with the GFZ MGEX rapid orbit and clock products for consistency reasons. Table 4.2 lists the CNES products in the PPP-WIZARD project. It can be seen that the tracking channels of bias types in real-time and post-processed mode are not exactly the same.

Table 4.2: CNES products in the PPPWIZARD project. The bias types are referenced to the bias file headers, which are also consistent with the RINEX document (Gurtner and Estey, 2006).

Products	Real-time	Post-processed
Constellation	G/R/E/C	
Satellite orbit	5 min, *.sp3	-
Satellite clock	5 s, *.clk	-
Bias	30 s, *.bia Used with the above orbit and clock	30 s, *.BIA Used with GFZ MEGX rapid orbit and clock
G code:	C1P	C2C
	C1C, C1W, C2S, C2L, C2X, C2W	
	C5Q, C5X	
G phase:	L1C, L2W, L5I	
R code:	C1C, C1P, C2C, C2P	
E code:	C1C, C5Q, C7Q,C6C	C1X, C5X, C7X, C6X, C8X
E phase:	L1C, L5Q, L7Q, L6C	L1X, L5X, L7X, L6X
C code:	C5P	C1X, C5X, C7Z, C8X
	C1P, C7I, C2I C6I	
C phase:	-	L7I
	L2I, L6I	

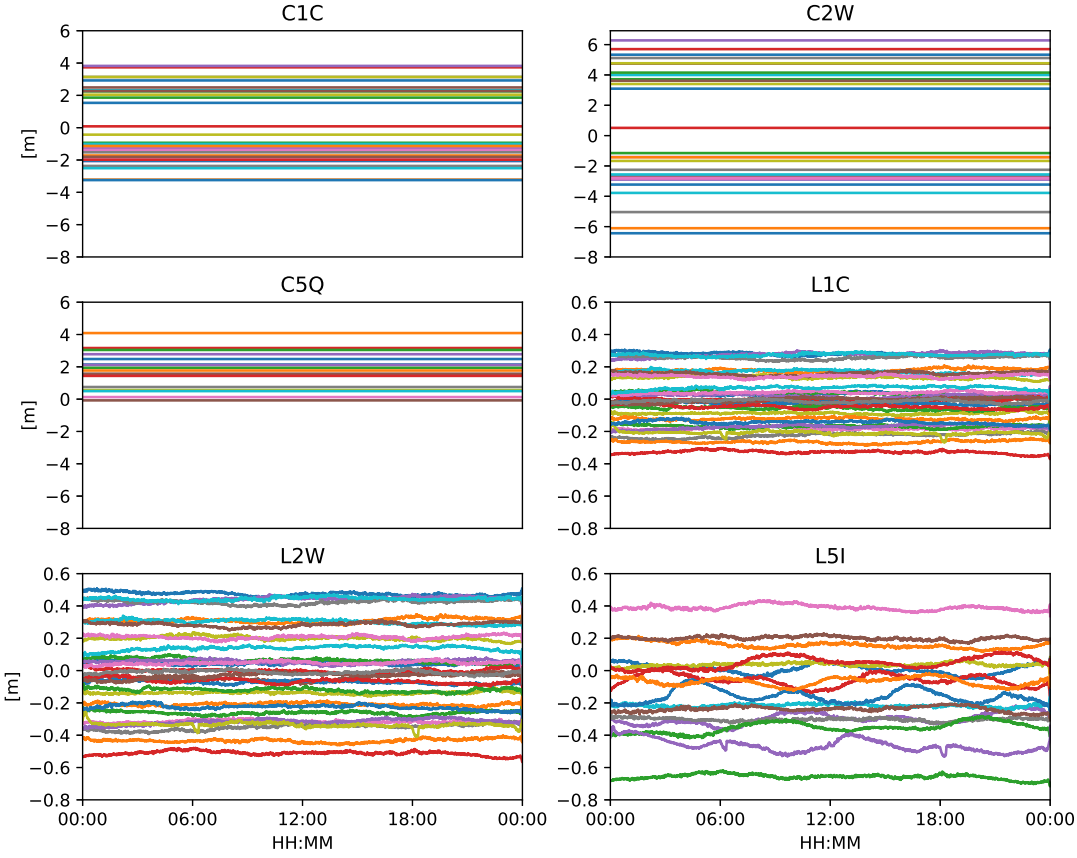

Figure 4.1: *Uncombined GPS satellite code and phase bias products generated at CNES on 01/05/2021. Different color represents different satellite, the same below.*

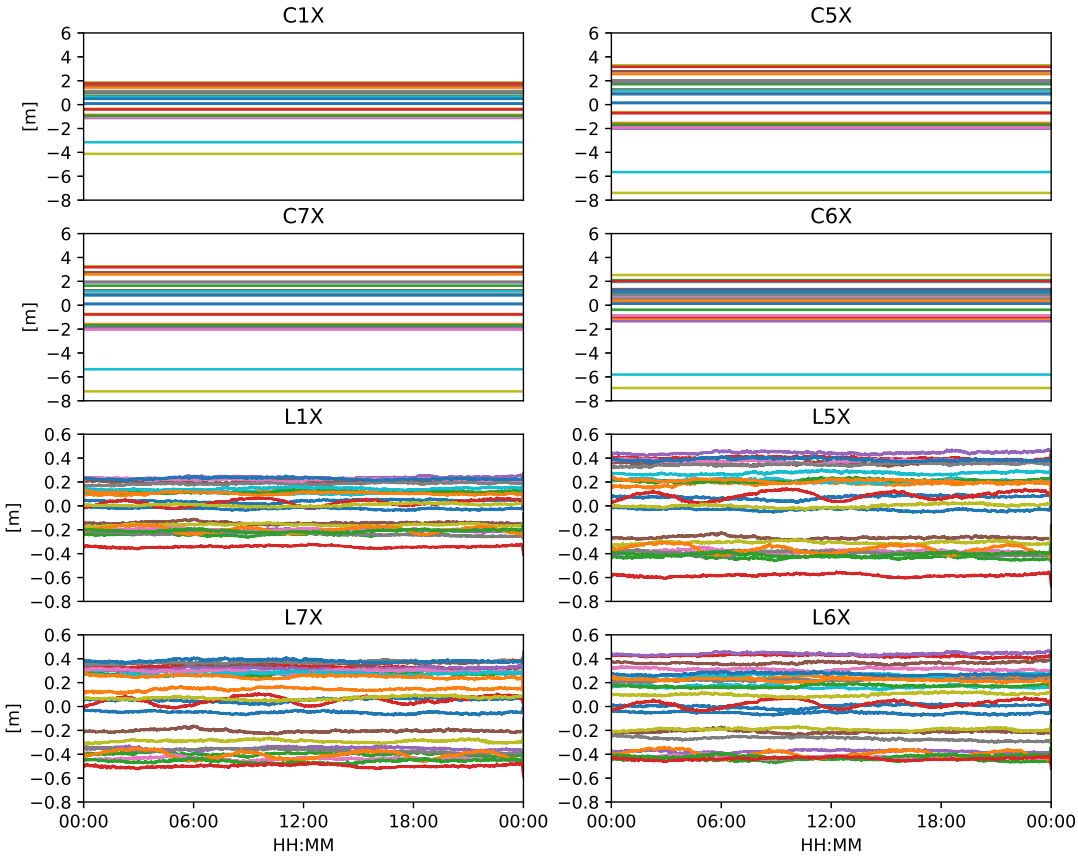

Figure 4.2: *Uncombined Galileo satellite code and phase bias products generated at CNES on 01/05/2021*

Figure 4.1 and Figure 4.2 demonstrate the CNES post-processed code and phase bias products on 01/05/2021. These products are not only relevant to the observable types and frequencies but also to the tracking modes or channels as indicated by the third character in the titles of the subplots (namely the C, W, Q, C, W, I modes in the types C1C, C2W, C5Q, L1C, L2W and L5I for GPS). These tracking modes should be considered when applying the CNES bias products at a user side. It can be seen that the code biases are constant values over the 24-hour period and the phase biases are relatively stable on most of the frequencies despite some small variations (a few centimeters) for specific satellites. The GPS L5 phase biases fluctuate more significantly because of the inclusion of the IFCB for the GPS IIF satellites (Liu et al., 2020).

4.2.2 IGS multi-GNSS observation data

The observation data of the IGS multi-GNSS stations are archived in RINEX3 format and can be downloaded freely from IGS global data centers: Crustal Dynamics Data Information System (CDDIS), Institut Géographique National (IGN) and Bundesamt für Kartographie und Geodäsie (BKG). The daily RINEX files are at 30 s update rate and the high-rate (1 Hz) data are also available at selected stations.

The following Table 4.3 lists the information of the stations used in the PPP evaluation. These selected stations are globally and evenly distributed and routinely report both GPS and Galileo multi-frequency code and phase measurements.

Table 4.3: General information of the stations used in the PPP test

Site	Country	Receiver Firmware	Antenna Radome	Constellation
BRST	France	TRIMBLE ALLOY 5.45	TRM57971.00 NONE	GPS,GLO,GAL, BDS,SBAS
BSHM	Israel	SEPT POLARX5 5.4.0	TRM59800.00 SCIS	GPS,GLO,GAL, BDS,QZSS,IRNSS
POL2	Kyrgyzstan	JAVAD TRE_3 DELTA 4.1.01	TPSCR.G3 NONE	GPS,GLO,GAL, BDS,QZSS
CUSV	Thailand	JAVAD TRE_3 DELTA 4.1.01	JAVRINGANT _DM NONE	GPS,GLO,GAL, BDS,QZSS
PERT	Australia	TRIMBLE ALLOY 5.45	TRM59800.00 NONE	GPS,GLO,GAL, BDS,QZSS
ZAMB	Zambia	JAVAD TRE_3 DELTA 4.1.01	AOAD/M_T NONE	GPS,GLO,GAL, BDS
BOGT	Colombia	JAVAD TRE_3 DELTA 4.1.01	JAVRINGANT _DM NONE	GPS,GLO,GAL, BDS
QUIN	USA	JAVAD TRE_3 DELTA 4.1.01	ASH701945E_M SNOW	GPS,GLO,GAL, BDS,QZSS
CEDU	Australia	SEPT POLARX5 5.4.0	AOAD/M_T NONE	GPS,GLO,GAL, BDS,QZSS,IRNSS
TID1	Australia	SEPT POLARX5 5.4.0	AOAD/M_T NONE	GPS,GLO,GAL, BDS,QZSS

4.3 The POINT software tool

The POINT (Position Orientation and INTegration) software (Hide et al., 2007) was initially developed at Nottingham Geospatial Institute (NGI) for the integration of real-time kinematic (RTK) and Inertial Navigation System

(INS). It is coded in standard C++ computer language and can be installed on any supported environments. In this section, the GNSS-related modules in POINT are presented first, including POINT features and POINT architecture. Then the newly developed features based on POINT are given, followed by a comparison with the CNES PPPWIZARD software.

4.3.1 General features of POINT

POINT provides a number of C++ libraries that can be assembled for multiple GNSS applications apart from RTK or PPP. Three groups of features can be summarised as: basic geodesy functions, file handling and GNSS error modelling, which are listed in Table 4.4, Table 4.5 and Table 4.6 respectively.

Geodesy functions

Table 4.4: Basic geodesy functions in POINT

Time system conversion	UTC $\Longleftrightarrow$ GPST $\Longleftrightarrow$ MJD
Coordinate system conversion	ECEF $\Longleftrightarrow$ Local NEU $\Longleftrightarrow$ Body frame
Earth radii of curvature	RN, RE
Parameter estimation	Least-square, Kalman filter

UTC: Universal Time Coordinated; MJD: Modified Julian Date

File handling

Table 4.5: File handling in POINT

GNSS observation	RINEX2 & RINEX3
GNSS ephemerides	Broadcast ephemerides; Precise orbit and clocks
Bias products	CNES WSB products and phase integer clocks CODE DCB products
Sun moon position	NASA SPICE files
Earth orientation data	EOP 14 C04 (IAU2000A) (1962-now)
Antenna PCO/PCV	IGS ANTEX file

GNSS error modelling

Table 4.6: GNSS error modelling in POINT

Antenna PCO/PCV correction	Both satellite and receiver
Phase wind-up effect	Satellite yaw angle not considered
Phase cycle slip	Detected and marked as lock time gap Ambiguity states are reset
Site displacement correction	Pole tide, Solid tide, Ocean loading
Relativistic effect Earth rotation effect	Compacted in the signal $t_{emission}$
Tropospheric delay	Model: EGNOS, Saastamoinen ... Mapping function: EGNOS, Saastamoinen, Neil ...
Ionospheric delay	Ionosphere-free combination Slant ionospheric delay estimation Higher order modelling

It is noted that POINT uses L_1 PCO/PCV correction for L_5.

For the PPP module in POINT, the specific features are listed in Table 4.7.

Table 4.7: POINT PPP features

Constellation	GPS, GLONASS, Galileo, and BeiDou-2
Frequencies	L1/L2/L5, G1/G2, E1/E5a/E5b/E6, B1/B2
Ionosphere	Ionosphere-free & ionosphere-estimated
Troposphere	Wet ZTD estimation
Ambiguity resolution	Single-difference and zero-difference IF combined ambiguity
Integer estimator	Integer rounding, LAMBDA, Bootstraping

4.3.2 The POINT structure

The POINT software can be divided into the modules as shown in Figure 4.3.

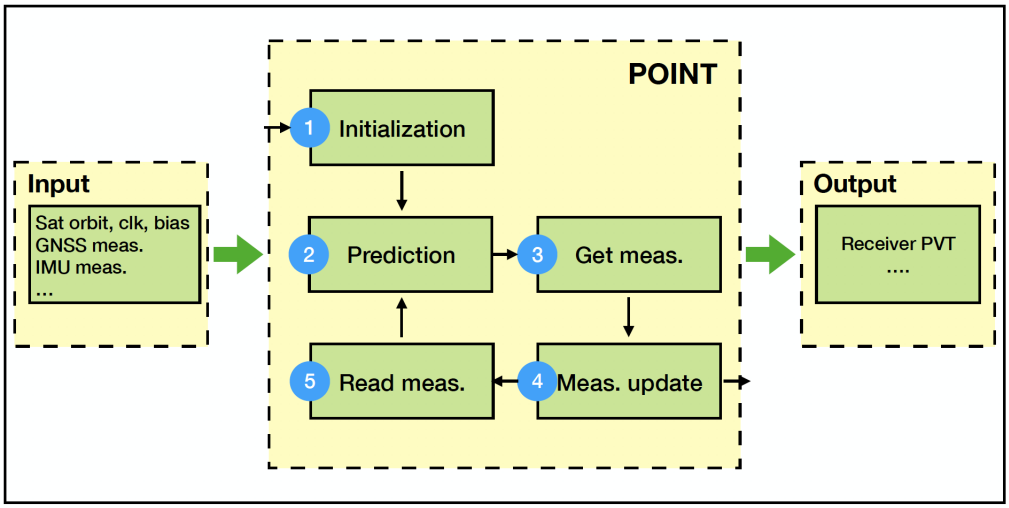

Figure 4.3: *Structure of the POINT software. Meas. is measurement. The same below.*

POINT has flexible design of data structure that allows for convenient variable configuration in the initialisation stage. The loop in the center is driven by input measurements and a process of kalman filtering including prediction and update. The navigation output of POINT has multiple format and is compatible with the Google earth XML for trajectory demonstration.

The following Figure 4.4 is the POINT initialisation module. Different positioning models can be configured such as ionosphere-free/ionosphere-estimated PPP, PPP/INS integration etc. Different model corresponds to different parameters to be estimated, of which the initial values and constraints are set. The spectral densities of the estimated parameters are also specified at this step. Other configurations are also specified at this stage. This could be satellite orbit/clock/bias products, error correction models, variable spectral densities, output files etc.

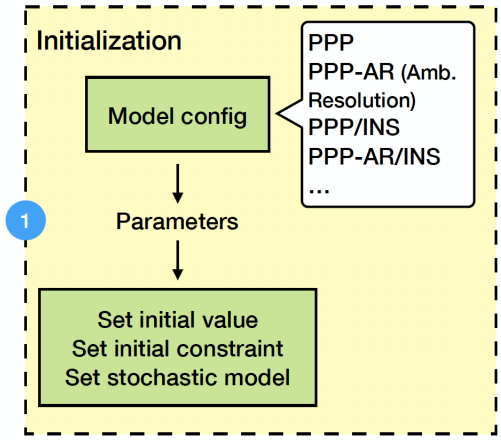

Figure 4.4: *POINT Initialisation*

The prediction module is shown in Figure 4.5. The dynamic model computes state transition matrix. For PPP, this matrix is simply an identity matrix but for PPP/INS fusion the acceleration and rotation of IMU will be involved. Then the process noise for each variable is computed. With the state transition matrix and process noise matrix, POINT is ready for prediction, which computes the predicted state and its covariance matrix. When the kalman filter is configured to reset with centain time interval, the reinitialisation process is followed.

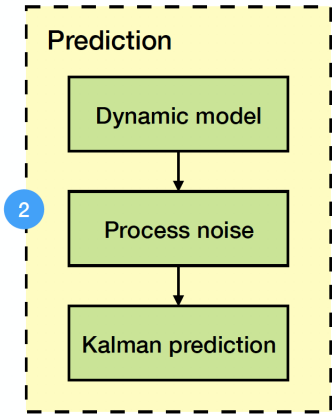

Figure 4.5: *POINT prediction*

When prediction is finished, POINT preprocesses the measurements from different sensors. For a typical GNSS receiver with POINT zero-difference configuration, the satellite measurements of different constellations are classified as range, range rate, MW combinations etc. as shown in Figure 4.6. Error

correction models for different types of measurements are then applied for each satellite. If the combined measurements are configured such like dual-frequency ionosphere-free combination, the linear combination is then computed as well as the related measurement noise matrix after combination. Currently, POINT supports the combination of triple-frequency either code or phase measurements with arbitrary coefficients. The combination between code and phase like MW is not supported, which is the reason that the MW combination is enumerated along with range and range rate and needs to be improved.

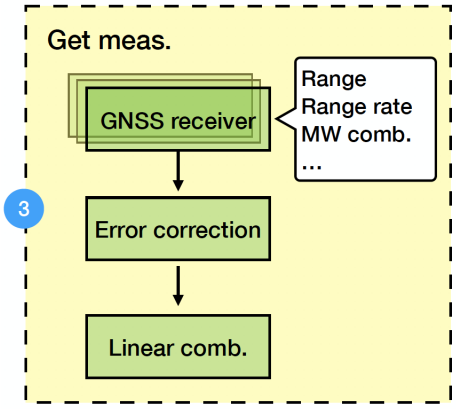

Figure 4.6: *GNSS measurement retrieval in POINT. comb. is for combination*

Figure 4.7 is the real Kalman update module in POINT. POINT supports multiple types of measurements as are listed and each type of measurement follows the same route. First compute the prefit residuals or innovation vector; then form the design matrix for a specific measurement type. Thanks to the data structure of POINT, the implementation of a new measurement model can be carried out easily in this part.

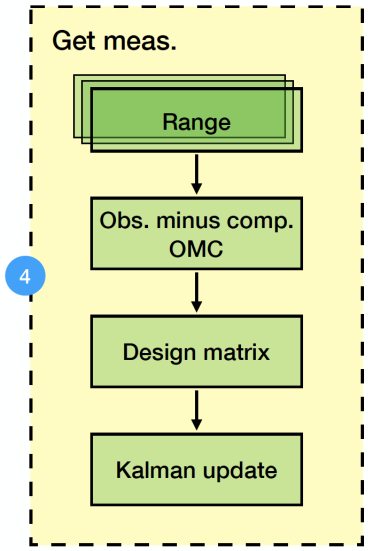

Figure 4.7: *Measurement update in POINT. Obs. is observation; comp. is computation.*

Figure 4.8 is a typical process for the reading of GNSS RINEX format data including parsing the header and record.

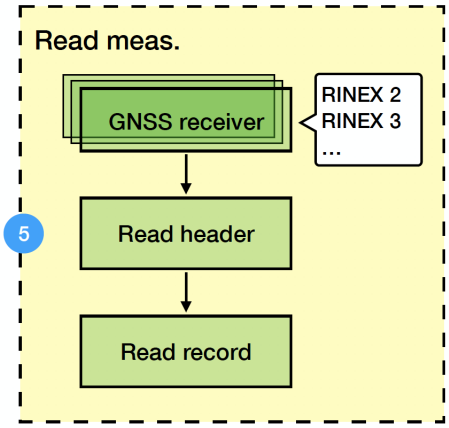

Figure 4.8: *The module of reading GNSS measurements in POINT. RINEX stands for Receiver INdependent EXchange GNSS measurement format.*

Figure 4.9 shows the POINT output. The navigation solution position, velocity and attitudes are printed to specified files. The Byproducts after each GNSS measurement update are also yielded including atmosphere, receiver clock bias/drift, phase ambiguity etc.

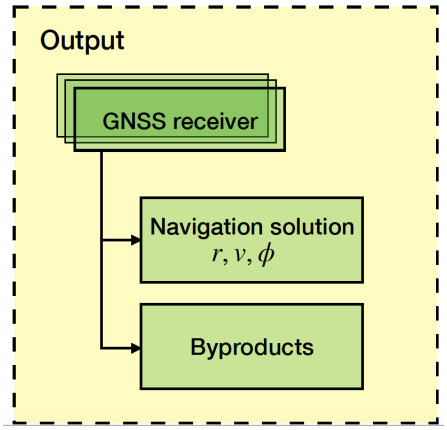

Figure 4.9: *The output module of POINT*

4.3.3 Newly developed features

Thanks to the POINT features and structure, new applications can be appended easily. The PPP models with the CNES biases corrections in Section 3.7 are implemented in POINT in this study and the newly developed features are listed in Table 4.8.

Table 4.8: Newly developed PPP features in POINT

CNES uncombined bias reading	SINEX format
CNES uncombined bias correction	Simple linear interpolation Indexed by $t_{emission}$
MW combination smoothing	Both GPS and Galileo
Galileo DFIF PPP with AR	b_L^E added IF NL AR: Bootstrapping; Partial AR
Multi-frequency ionosphere-float PPP	$b_{P_2}, b_{C_5}, b_{L_1}, b_{L_2}, b_{L_5}$ $b_{C_{E5a}}, b_{C_{E5b}}, b_{C_{E_6}}, b_{L_{E_1}}, b_{L_{E_{5a}}}, b_{L_{E_{5b}}}, b_{L_{E_6}}$ N_1, N_2, N_5, I_1 $N_{E_1}, N_{E_{5a}}, N_{E_{5b}}, N_{E_6}, I_{E_1}$ added AR: combined WL ambiguities See Equation (3.37) and Equation (3.38) BIE, independent AR

The key new features: CNES uncombined bias correction, Multi-frequency ionosphere-float PPP and Independent ambiguity resolution are expalined in the following:

CNES uncombined bias correction

The CNES uncombined bias products are applied to GNSS raw code and phase measurements with the same observation codes or types. These observation codes for each constellation are listed in the header of a RINEX file.

However, the codes in the RINEX2 file format only contains observation types (code/phase/doppler) and frequencies. The channel or tracking mode attribute of signal is not specified. In the RINEX3 format, all of these three elements are included. The CNES bias products uses the observation codes compatible with the RINEX3 format and thus the channel information has to be recorded when reading the GNSS measurements. With the recorded observation codes, the CNES uncombined biases can be matched and corrected to the GNSS measurements. This correction process for GPS PRN01 codes L1C is shown as an example in the following error correction module Figure 4.10 which is a sub-module of Figure 4.6. It is noted that the signal emission time should be computed first to index the bias products and a simple linear interpolation is used for time tags that are not exactly matched.

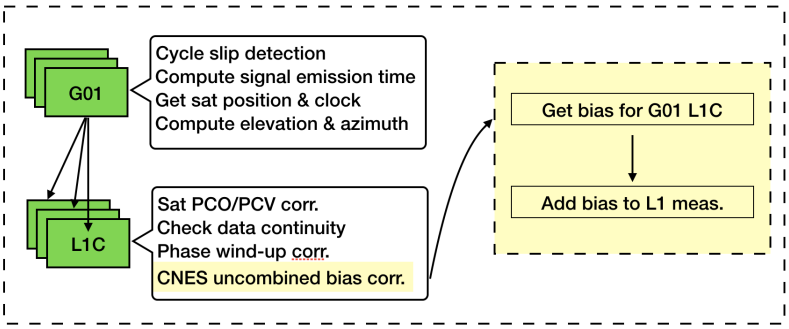

Figure 4.10: *The process of CNES uncombined bias correction in POINT.*

Multi-frequency ionosphere-float PPP

With the CNES uncombined bias corrections, multi-frequency ionosphere-float model can be established. At the receiver side, new receiver clock bias parameters apart from the original receiver clocks for each system are needed to be configured. Undifferenced phase ambiguities on each frequency and slant ionospheric delay are also estimated, see Table 4.8.

Figure 4.11 shows the new variable registration in POINT, in which four specific classes (see Appendix A) are used to handle the new parameters.

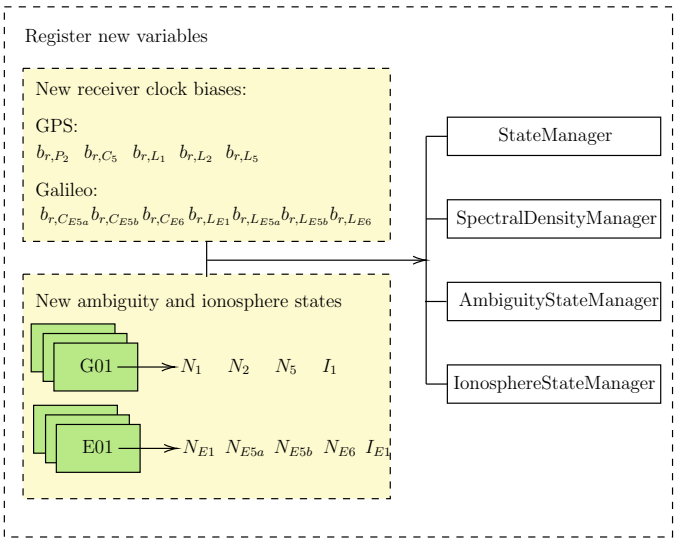

Figure 4.11: *New parameter registration in POINT*

However, when adding or removing parameters, the consistence between these classes is vital as it could cause severe index problem in the subsequent estimation.

After adding the variables, the prefit residuals or innovation vector and design matrix need to be computed and filled due to the contribution of new parameters. This is shown in Figure 4.12 and Figure 4.13 by an example of GPS PRN01 phase measurement on L2.

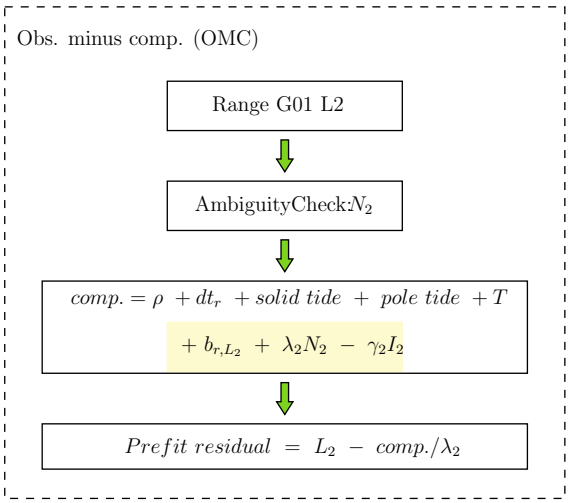

Figure 4.12: *Innovation vector computation in POINT*

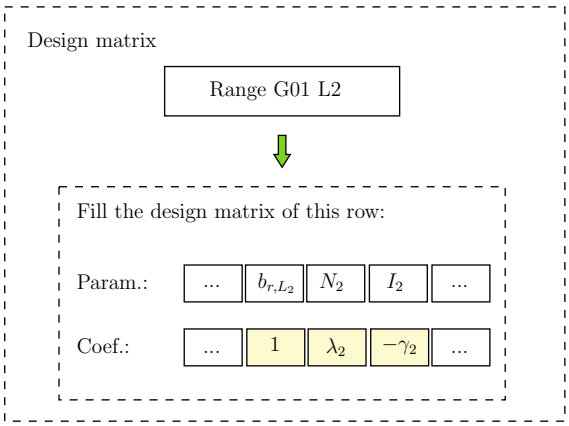

Figure 4.13: *Design matrix filling in POINT*

The highlighted parts are related to the new variables for the L_2 measurement modelling. These two figures are sub-modules of Figure 4.7. The carrier-phase ambiguity is reset when cycle slip is marked in the step 'AmbiguityCheck'.

Independent ambiguity resolution

An independent AR module is added in POINT as Figure 4.14. The ambiguities are fixed at each epoch instead of being held from the fixed epoch. The float states are assigned back for subsequent Kalman filtering.

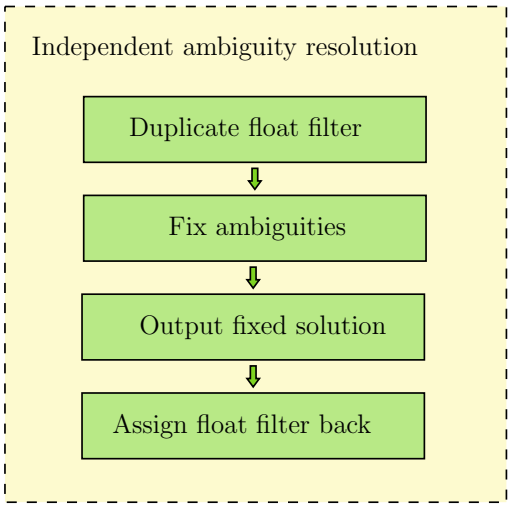

Figure 4.14: *Independent ambiguity resolution in POINT*

4.3.4 Comparison with the PPPWIZARD software

The PPPWIZARD (Precise Point Positioning With Integer and Zero-difference Ambiguity Resolution Demonstrator) software is an open source PPP client software that is released by the CNES (Laurichesse, 2011; Laurichesse and Privat, 2015). It originally demonstrates the use of their widelane biases (WSB)

and 'integer' phase clock products for GPS legacy L1/L2 ionosphere-free ambiguity resolution (Laurichesse, 2011). As the uncombined phase bias products are pushed forward (Laurichesse, 2012), an updated version are published for the demonstration of multi-constellation multi-frequency PPP AR using their uncombined bias products (Laurichesse and Privat, 2015). This software is also programmed in C++ and dedicated to ionosphere-estimated PPP in the current version. It supports triple-frequency GPS/Galileo/BeiDou-2 PPP with AR. At the time of writing, an online PPP service (Laurichesse, 2010) is running and the PPPWIZARD package is not available currently.

The PPPWIZARD software is referenced for the implementation of uncombined bias correction in the multi-frequency PPP model in this study. This section presents the features and structure of PPPWIZARD, followed by a comparison with POINT.

General feature

PPPWIZARD is a specific PPP processing software with features as listed in Table 4.9.

Table 4.9: PPPWIZARD PPP features

Constellation	GPS, GLONASS, Galileo, and BeiDou-2
Frequencies	L1/L2/L5, G1/G2, E1/E5a/E5b, B1/B2/B3
Ionosphere	Slant ionospheric delay estimation
Troposphere	Wet ZTD estimation
Ambiguity resolution	Zero-difference WL combined and N_1 ambiguity
Integer estimator	Bootstraping

It is not a completely independent software but employs libraries from RTKLIB (Takasu, 2009) for reading data like satellite orbits, clocks and observations.

PPPWIZARD structure

Figure 4.15 shows the top leves of PPPWIZARD, which consists two modules: generateLowlevel and processLowlevel. The generateLowlevel outputs a satellite-indexed table with all the orbit, clocks, biases, and observations. The ProcessLowlevel loads the table and computes PPP solutions. This separated

design facilitates the debugging process in PPP as the data is not read from the raw input files.

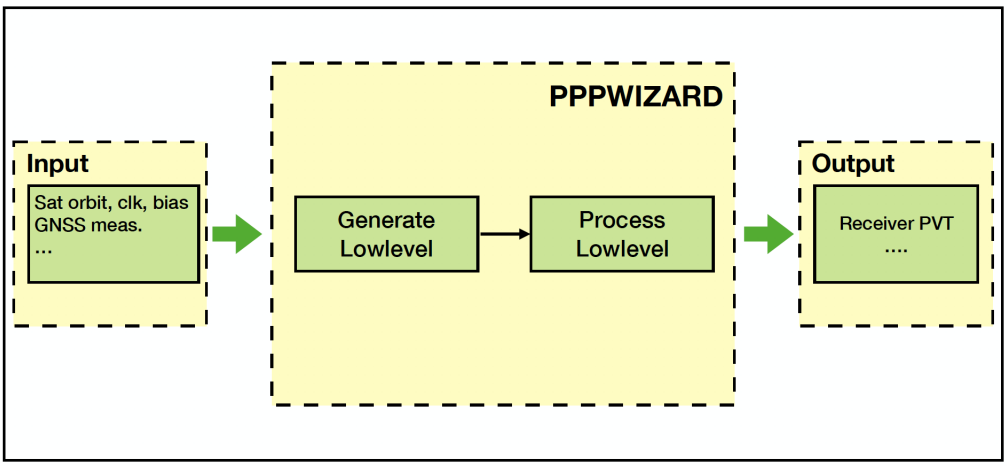

Figure 4.15: *The structure of the PPPWIZARD software*

The internal structure of the processLowlevel is shown in Figure 4.16. As in Figure 4.3, the core parts of this modules are Kalman prediction and measurement updates.

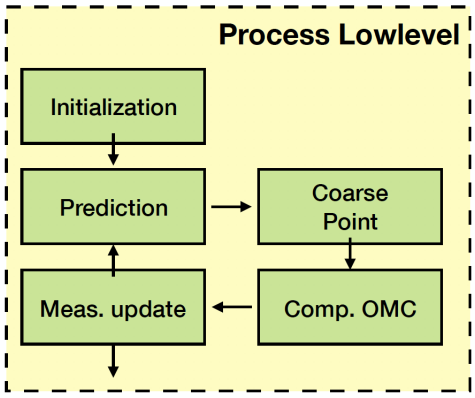

Figure 4.16: *The structure of the PPPWIZARD ProcessLowlevel module*

Comparison between PPPWIZARD and POINT

Table 4.10 lists the properties of POINT and PPPWIZARD. POINT linearises the geometric distance between satellite and receiver at predicted receiver coordinates while the linearisation in PPPWIZARD is evaluated at receiver coordinates based on code measurements. Moreover, the computation of Kalman filtering in PPPWIZARD is directly in numerical form following algorithms of covariance decomposition, which completes computing task more efficiently

than the traditional vector/matrix form. PPPWIZARD does not include any cycle slip detection method; instead, it estimates combined phase cyle slips together with ambiguity parameters, hence supporting the cycle slip correction as well.

Table 4.10: Comparison between POINT and PPPWIZARD

	POINT	PPPWIZARD
Real-time data stream	No	Yes
Constellations	GPS, GLONASS, Galileo and BeiDou	
Frequencies	L1/L2/L5, G1/G2 E1/E5a/E5b/E6, B1/B2	L1/L2/L5, G1/G2 E1/E5a/E5b, B1/B2/B3
Sun, moon, earth position	IERS, NASA SPICE files	Internal models
Observation model	Ionosphere-free/-estimated	Ionosphere-estimated
Linearisation	At predicted states	At receiver coordinates based on code measurements
Kalman filter	Vector/Matrix form See Section 3.4	UDU^T decomposition Bierman (1975) Thornton and Bierman (1975)
Sat-dependent param.	Specific data structure	A pass indicator
Phase cycle slip	Detected using observation linear combinations	Estimated together with ambiguities

PPP results using real data

Figure 4.17 and Figure 4.18 show the PPP results of POINT and PPPWIZARD using real data. The purpose of this comparison is mainly to justify the POINT multi-frequency ionosphere-estimated PPP results with external reference software PPPWIZARD. Table 4.11 is the related statistical results.

Table 4.11: RMS of PPP errors (after one hour) computed from PPPWIZARD and POINT at station BRST on 10/09/2020. Unit: *cm*

Software	High rate			30-s rate		
	N	E	U	N	E	U
PPPWIZARD	2.69	4.40	9.78	3.78	5.05	10.76
POINT	2.03	4.39	3.92	1.84	2.20	4.34

It can be seen that POINT obtains a better converged positioning accuracy for both high-rate (Figure 4.17) and 30-s sampling rate data (Figure 4.18).

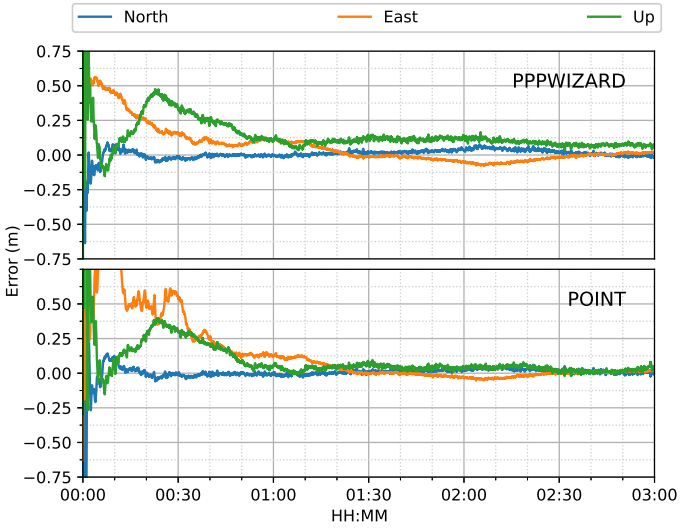

Figure 4.17: *GPS triple-frequency ionosphere-estimated PPP results using high-rate data at IGS station BRST*

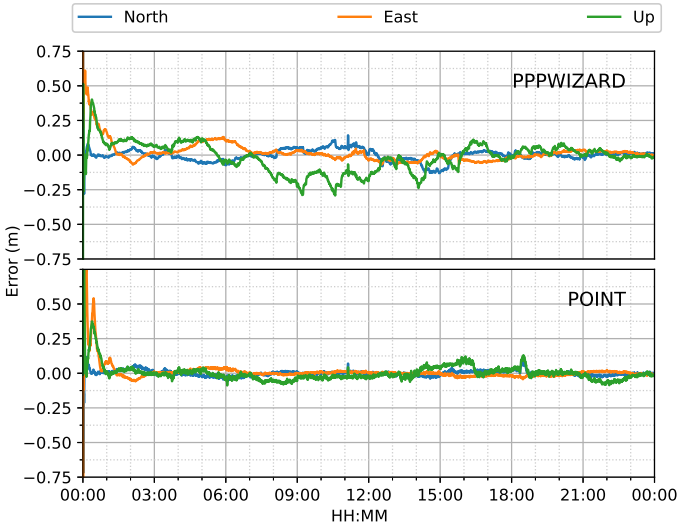

Figure 4.18: *GPS triple-frequency ionosphere-estimated PPP results using data with 30 s sampling rate at IGS station BRST*

4.4 Test configuration

4.4.1 POINT PPP settings

Table 4.12 is the settings of the POINT software for computing ionosphere-free and ionosphere-estimated PPP solutions. The model noise values are empirical, which are referenced from Laurichesse and Privat (2015).

Table 4.12: POINT PPP settings

	PPP ionosphere-estimated	PPP ionosphere-free
Constellation	GPS & Galileo	
Frequency	L1/L2/L5 E1/E5a/E5b/E6	L1/L2 E1/E5a
Meas. noise	Code: 0.3 m; Phase: 0.01 *cycle*	
Parameter estimation	Extended Kalman Filter	
Orbit and clocks	GFZ rapid products	
Biases	CNES post-processed uncombined products	
Elevation cut-off	7°	
Weighting function	$\frac{1.001}{\sqrt{0.002001+sin^2\theta}}$ where θ is the elevation angle (radian)	
Antenna PCO/PCV correction	igs14.atx	
Site displacement	Pole tides and solid earth tides corrections Earth orientation parameters: IERS EOP 14 C04 (IAU2000A); Solar system body ephemerides: NASA NAIF SPICE files	
Phase windup	Wu et al. (1993)	
Phase cycle slip detection	Liu (2011)	
Ionosphere	Higher-order terms are ignored Estimation of slant ionospheric delay on L1 Initial value and Std.: 0, 10 m Model noise 2 mm/s	Ionosphere-free combination
Troposphere	Saastamoinen model for the hydrostatic delay Niell mapping function Estimation on the zenith wet delay Initial variance: 0.5 m; Model noise: 0.005 mm/s	
Receiver code clock	Initial value and Std.: 0,1000 m; Model noise 1000 m/s	-
Receiver phase clock	-	Initial value and Std.: 0, 0 m; Model noise 1000 m/s
Receiver state	Model noise: 100 m/s	
Additional receiver clock bias	Initial value and Std.: 0,0 m; Model noise 1 mm/s	-
Output format	Geodetic latitude, longitude and height	

4.4.2 Results evaluation

Accuracy

The IGS site coordinate products are used as reference to compute the positioning errors of all the selected stations during the testing periods. There are transformed to a local NEU frame and the errors are demonstrated in the following three forms:

- Typical repeatability

For all the sessions of a testing day of a individual station, the superimposed positioning errors are depicted to show the typical performance of PPP repeatability in the timeline. See Figure 5.2 for an example.

- Accuracy representative

  The the 68th percentile (Banville et al., 2020) of the absolute positioning errors after half an hour is computed for the accuracy assessment instead of the RMS error to mitigate the impact from possible wrong ambiguity fixing or outliers. See Figure 5.4 for an example.

- Error distribution histogram

  All the positioning errors after half an hour are also counted in the conventional frequency histogram with defined bin width. This histogram reflects the distribution property of errors. See Figure 5.5 for an example.

Convergence Time

The convergence time for each session is defined as the time interval which the 2 dimensional (2D) or 3 dimensional (3D) positional error takes to reach a certain accuracy (5cm) for at least 10 or 20 successive epochs. These are represented in a conventional frequency histogram with a defined bin width of 10 min, i.e. where 10 denotes 5-15 min, 20 denotes 15-25 min, 30 denotes 25-35 min, etc. See Figure 5.6 for an example.

4.5 Summary

This chapter provides the information regarding the data sources, software tool and results assessment manner for the GPS/Galileo PPP evaluation.

The POINT software tool with the newly developed features supports the processing of GPS/Galileo ionosphere-free and ionosphere-estimated PPP. Multiple frequencies and phase ambiguity resolution are also supported. According to the results compared with the external CNES PPPWIZARD software, POINT can be used as a precise tool for GNSS PPP application.

Nevertheless, POINT still needs to be improved for real-time data stream processing and phase cycle slip correction under signal blockage conditions.

Chapter 5

Global PPP performance analysis

5.1 Introduction

In this chapter, GPS/Galileo PPP using CNES uncombined bias products is evaluated. Two PPP models: the ionosphere-free (IF) and the ionosphere-estimated are tested with real IGS global observation data respectively. For both cases, the uncombined code and phase biases are added to the raw measurements, which keeps the integer property of phase ambiguities, thus allowing ambiguity resolution. All the tests are computed using the POINT software. The ionosphere-estimated PPP results have been published in the journal *Remote Sensing* in early 2022 (Zhao et al., 2022).

This chapter is organised as follows: Section 5.2 presents the ionosphere-free PPP ambiguity-float and ambiguity-fixed results; Similarly Section 5.3 presents the ionosphere-estimated results. Section 5.4 summarises the PPP performance of all the tests and lists other potential research points regarding the application of the CNES uncombined bias products.

5.2 GPS/Galileo dual-frequency ionosphere-free PPP

5.2.1 Test description

The PPP model in Section 3.7.2 is implemented in the POINT software (see Section 4.3) and is applied to real GNSS measurements with a 30-s sampling interval collected at eight IGS MGEX stations (see Table 4.3) from 19 to 21 May 2020. GPS L1/L2 and Galileo E1/E5a IF float PPP and ambiguity-fixed PPP are configured and GFZ MGEX rapid precise orbit and clock products and the CNES post-processed uncombined bias products are used (see Table 4.1 and Table 4.2). Figure 5.1 shows the distribution of the eight selected stations. The Kalman filter is reset with an interval of three hours for each day at each station, thus there are 192 testing sessions in total. A minimum time for NL AR is set to half an hour in order to reach a reliable ambiguity resolution. The LAMBDA (Least-squares AMBiguity Decorrelation Adjustment) method (Teunissen, 1995) is used to search for the optimal integer ambiguity candidates and the ratio test is used for validation of fixed solution. All the following positioning tests are in the simulated kinematic mode which assigns a process noise of 100 m/s for the coordinate estimates (see Table 4.12).

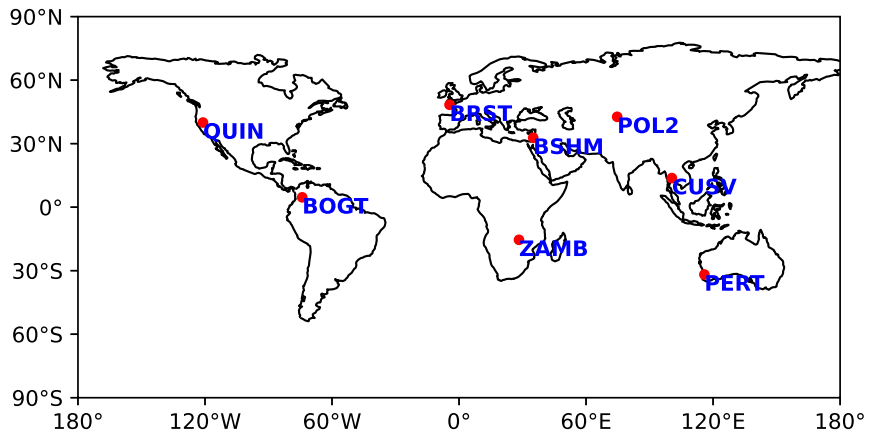

Figure 5.1: *Selected IGS stations for GPS/Galileo dual-frequency IF PPP test*

5.2.2 PPP results evaluation

Positioning accuracy

The PPP results of station BRST on 19/05/2020 are shown in Figure 5.2, eight sessions are superimposed in each of the sub-plot. It clearly shows that therepeatability on the three positioning error components are all improved in the fixed setting (the three sub-plots on the right side), especially in the east direction.

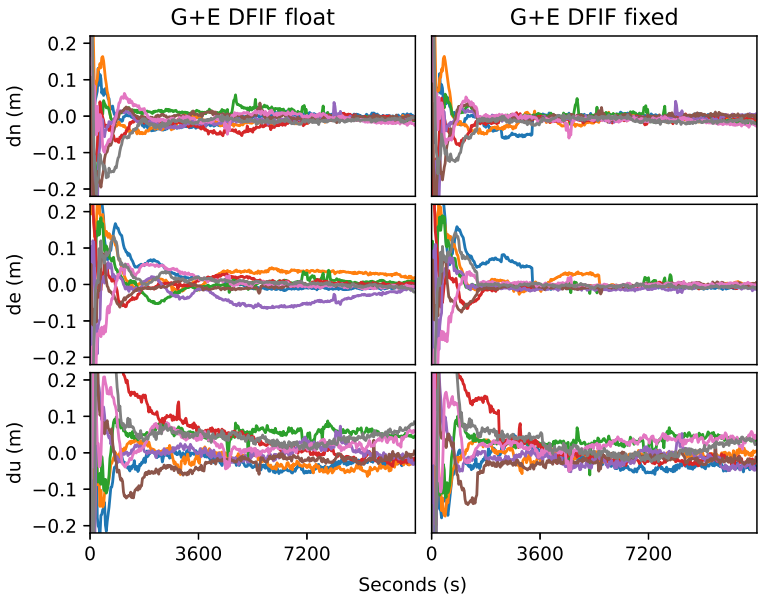

Figure 5.2: *GPS L1/L2 and Galileo E1/E5a ionosphere-free float (left) and fixed (right) PPP results on 19/05/2020 at station BRST. (Different color represents different session; dN, dE dU stand for positioning error in the north, east and up direction respectively; G and E denote for GPS and Galileo; DFIF is dual-frequency ionosphere-free, the same below)*

From the ambiguity fixing rates in Figure 5.3, it can be seen that both GPS and Galileo WL ambiguities have high fixing rates. It also shows that GPS achieves higher NL-ambiguity fixing rate than Galileo, which could be caused by the relatively less satellite number of Galileo system.

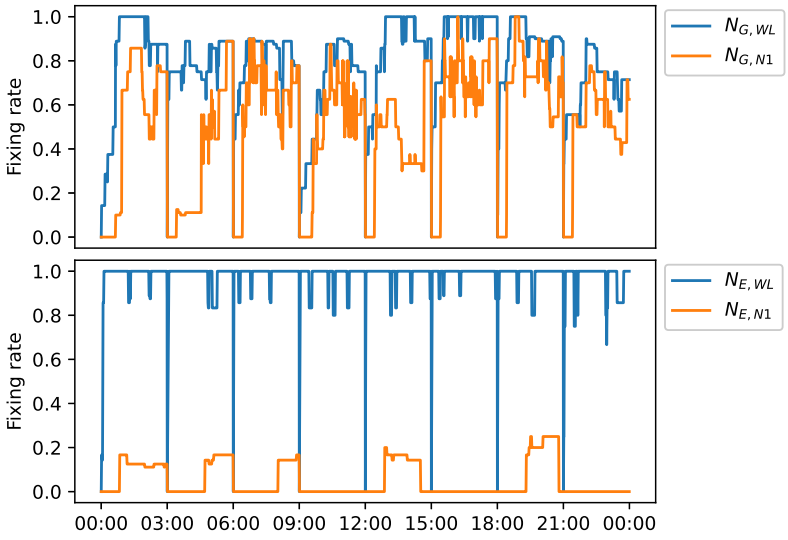

Figure 5.3: *Ambiguity-fixing rate of GPS L1/L2 and Galileo E1/E5a ionosphere-free PPP fixed solutions on 19/05/2020 at station BRST. The LAMBDA method is used for ambiguity resolution and the ratio test for validation.*

The 24-h positioning statistic error for both the ambiguity-float and ambiguity-fixed solutions in this DFIF setting for all the selected stations are also compared in Figure 5.4. Overall, comparing between the float and the fixed solutions, a noticeable improvement in the east component for all the stations could be found; the north and the up components also have slight improvements for most of the stations and exhibit some exceptions, which could be caused by improper setting of conditions for ambiguity resolutions.

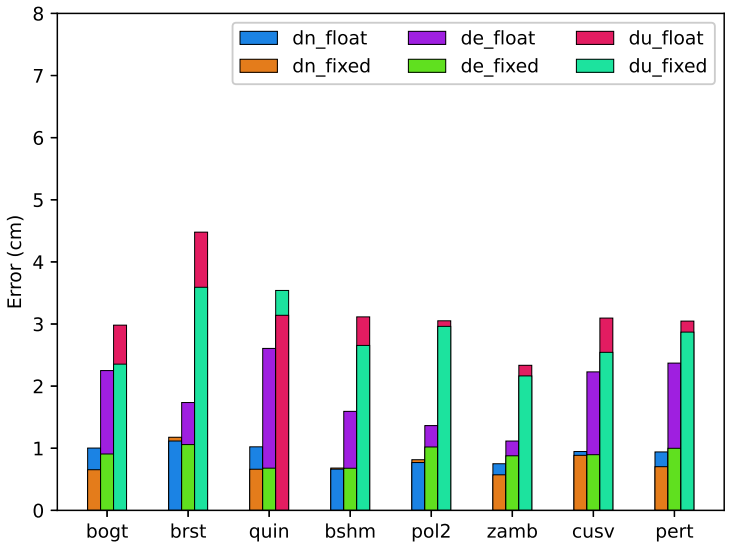

Figure 5.4: *The 68th percentile of GPS/Galileo DFIF PPP solutions from selected stations on 20/05/2020*

For all the 192 sessions the positioning errors (after half an hour within a session) are counted in the histogram of Figure 5.5. It can be seen that the east error distribution of the fixed solution has significantly higher frequency around zero. The north component also shows slight accuracy improvement while the improvement in the up direction is marginal.

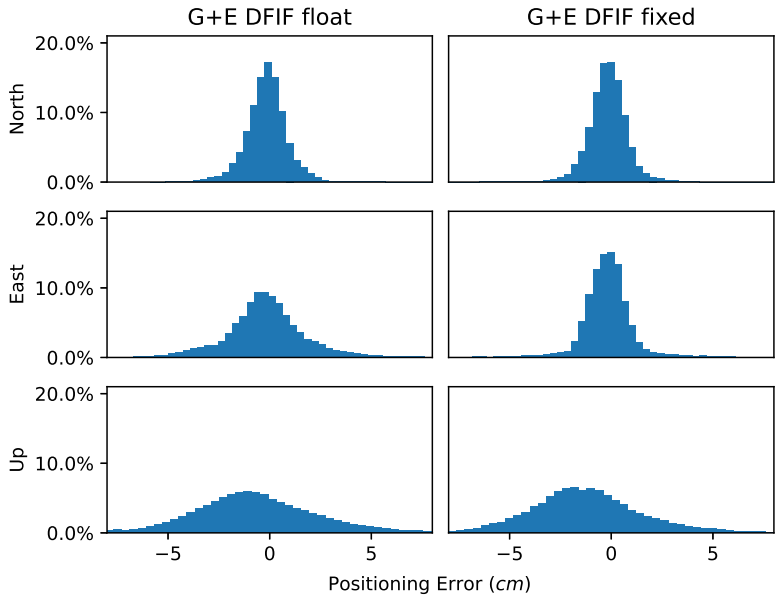

Figure 5.5: *Histogram of GPS L1/L2 and Galileo E1/E5a ionosphere-free float (left) and fixed (right) PPP errors (after half an hour) for all the 192 testing sessions of the eight selected stations from 19/05/2020 to 21/05/2020*

The 68th percentile (Banville et al., 2020) of the positioning errors is computed instead of the root mean square (RMS) to mitigate the impact from possible wrong fixing or outliers and listed in Table 5.1. The east component achieves an improvement of 45% on accuracy. Ge et al. (2008) also reported marked accuracy improvement on the east component of about 27% after AR for GPS PPP, which is further improved by computing the NL FCB with ambiguity-fixed GPS network solutions (Geng et al., 2012).

Table 5.1: The 68th percentile of positioning errors and convergence time average of GPS L1/L2 and Galileo E1/E5a ionosphere-free PPP for all the 192 testing sessions of the eight selected stations from 19/05/2020 to 21/05/2020

PPP model	North (cm)	East (cm)	Up (cm)	Convergence time (3D<5cm)(min)
Float	0.87	1.73	3.12	45.1
Fixed	0.82	0.96	3.04	34.7

Table 5.2 also lists the convergence time averages under different conditions. It can be seen that the horizontal convergence is more rapid requiring about 20 *min* and longer successive condition requires a longer convergence time.

Table 5.2: The convergence time average of GPS L1/L2 and Galileo E1/E5a ionosphere-free ambiguity-float and ambiguity-fixed PPP solutions for all the 192 testing sessions of the eight selected stations from 19/05/2020 to 21/05/2020. Unit: *min*

Convergence condition	Float	Fixed
3D<10*cm*, 20 epochs	45.1	34.7
3D<5*cm*, 10 epochs	42.0	33
2D<5*cm*, 10 epochs	22.5	21.6
2D<5*cm*, 20 epochs	25.4	24.2

Convergence time

Figure 5.6 shows the convergence time distribution for all the testing sessions. It clearly shows that the fixed solution achieves substantial improvement with most sessions less than 100 min and many more sessions in the 25-35 min bin, indicating the benefit of AR on accelerating the PPP convergence. Noted that the convergence time here is defined as the time interval which the three-dimensional (3D) positioning error takes to reach 5 cm accuracy for at least 20 successive epochs (10 min). It is also found that both float and fixed solutions can obtain 3D error less than 10 cm in about 20 min on average. Table 5.1 also lists the averaged convergence time for all the sessions. An improvement of 23% is achieved after AR. This convergence time acceleration is also confirmed in many studies (Pan et al., 2017; Nadarajah et al., 2018; Glaner and Weber, 2021) for the dual-frequency PPP AR though the adopted constellations and convergence definition vary.

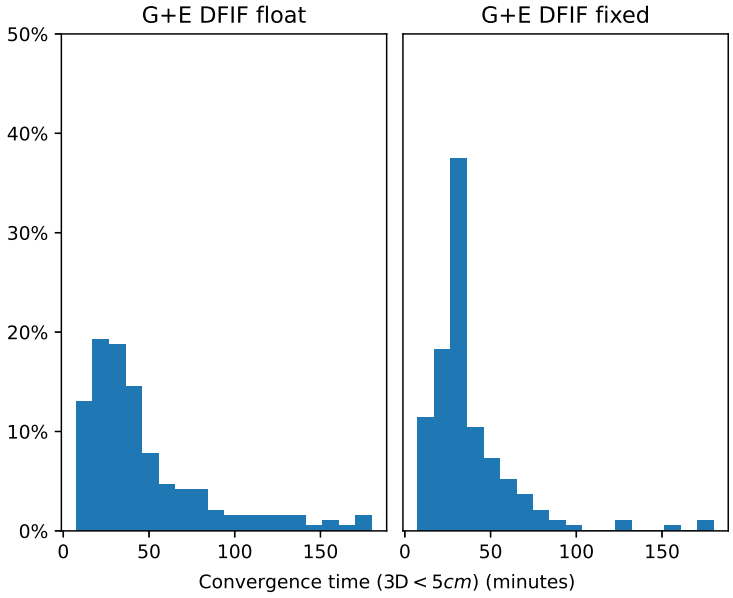

Figure 5.6: *Histogram of GPS L1/L2 and Galileo E1/E5a ionosphere-free float (left) and fixed (right) PPP convergence time (3D positioning error less than 5 cm) for all the 192 testing sessions of the eight selected stations from 19/05/2020 to 21/05/2020*

More detailed PPP results of each selected station during the testing days are presented in Appendix B.

5.3 GPS/Galileo multi-frequency ionosphere-estimated PPP

5.3.1 Test Description

The GPS/Galileo multi-frequency positioning models in Equation (3.35) and Equation (3.36) have been applied to real data collected from 1 to 10 May 2021 with a 30-s sampling interval at nine globally distributed IGS (International GNSS Service) MGEX (Multi-GNSS Experiment) stations. GPS L1/L2/L5 and Galileo E1/E5a/E5b/E6 code and carrier-phase observations are routinely collected at these sites as shown in Figure 5.7.

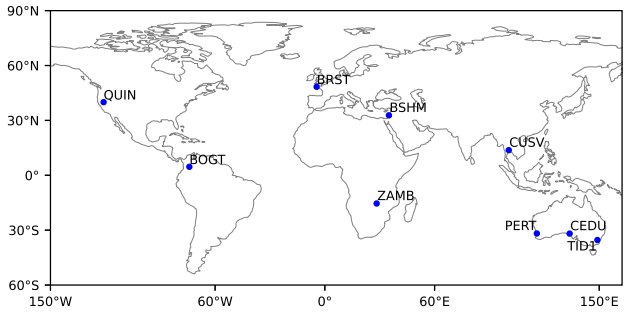

Figure 5.7: *Selected IGS stations for GPS/Galileo multi-frequency ionosphere-estimated PPP test*

The POINT software was used for PPP implementation and results evaluation. A common configuration of POINT for all the following tests is listed in Table 4.12. Noted that the additional receiver clock bias refers to the terms b_{P_2}, b_{C_5}, b_{L_1}, b_{L_2} and b_{L5} in Equation (3.35) for GPS and the same for the terms in Equation (3.36) of Galileo.

Cycle slip detection is still indispensable in our implementation. Because when fixing the undifferenced ambiguities, an ambiguity datum is needed to be selected first. But when this selection happens on an ambiguity which has unidentified cycle slip , a spike in the positioning error series is observed in our results. For single-epoch processing, the cycle slip detection is not necessary as the ambiguity is reset at each epoch. The classical geometry-free (GF) and MW combinations (Blewitt, 1990; Liu, 2011) are used for cycle slip detection. But this method suffers from high ionospheric activity and code measurement noises Banville and Langley (2013).

The best integer equivariant (BIE) estimator (Teunissen, 2003; Odolinski and Teunissen, 2020) is used for ambiguity resolution, see Section 3.5.3. The open-source software goGPS (Herrera et al., 2016) is referenced for the implementation of this estimator. To mitigate the effect of wrong ambiguity fixing, the ambiguities are resolved independently at each epoch.

5.3.2 Stochastic analysis

As shown in the multi-frequency model in Section 3.7, a series of widelane ambiguities are configured to be estimated and resolved. Laurichesse and Banville

(2018) evaluates the benefit of the Widelane Ambiguity Resolution (WAR) to the range estimates through a Galileo single-satellite quadruple-frequency model. In their analysis, the range precision can reach around 19 centimeters after WAR with a priori 3 millimeters and 30 centimeters for the phase and code standard deviation respectively. However, the advantage of the WAR on the estimation of the remaining narrow-lane ambiguity is not presented. Further more, with additional constraints provided from other satellite system on the range parameter and the external ionospheric information, the effect of the WAR on the resolution of the narrow-lane ambiguity is not clear. To further explore the stochastic characteristics of the estimates with fixed widelanes, we extended their model with the inclusion of pseudo measurements for the range and the ionospheric parameters as below:

$$
\begin{aligned}
E\{y_s\} &= E\left\{\begin{bmatrix} C_{E1} \\ C_{E5a} \\ \lambda_{E1}L_{E1} \\ \lambda_{E5a}L_{E5a} \\ \lambda_{E5b}L_{E5b} \\ \lambda_{E6}L_{E6} \\ \rho_0 \\ I_0 \end{bmatrix}\right\} = \begin{bmatrix} 1 & 1 & 0 & 0 & 0 & 0 \\ 1 & \gamma_{E5a} & 0 & 0 & 0 & 0 \\ 1 & -1 & \lambda_{E1} & 0 & 0 & 0 \\ 1 & -\gamma_{E5a} & \lambda_{E5a} & \lambda_{E5a} & 0 & 0 \\ 1 & -\gamma_{E5b} & \lambda_{E5b} & \lambda_{E5b} & \lambda_{E5b} & 0 \\ 1 & -\gamma_{E6} & \lambda_{E6} & \lambda_{E6} & \lambda_{E6} & \lambda_{E6} \\ 1 & 0 & 0 & 0 & 0 & 0 \\ 0 & 1 & 0 & 0 & 0 & 0 \end{bmatrix} \begin{bmatrix} \rho \\ I \\ N_{E1} \\ N_{WL,E1E5a} \\ N_{WL,E5aE5b} \\ N_{WL,E5bE6} \end{bmatrix} \\
&= A_s\hat{x}_s \\
D\{y_s\} &= Q_{y_s}
\end{aligned}
\tag{5.1}
$$

where E $\{\cdot\}$ and D $\{\cdot\}$ are the expectation and dispersion operation. Q_{y_s} is diagonal and consists of the noise of the measurements. Then the covariance matrix of

$\hat{x}_s$ will be:

$$Q_{\hat{x}_s} = (A_s^T Q_{y_s}^{-1} A_s)^{-1} \tag{5.2}$$

When the float widelane ambiguities in $\hat{x}_s$ are fixed, $Q_{\hat{x}_s}$ will be updated as:

$$Q_{\check{b}\check{b}} = Q_{\hat{b}\hat{b}} - Q_{\hat{b}\hat{a}} Q_{\hat{a}\hat{a}}^{-1} Q_{\hat{b}\hat{a}}^T \tag{5.3}$$

where $\hat{a}$ is the ambiguity states to be fixed; $\hat{b}$ is the remaining states of $\hat{x}_s$ and $\check{b}$ is the updated states.

Figure 5.8 shows the possible values of $\sigma_{\hat{\rho}}$ under different σ_{code} and σ_{phase}

with a loose constraint of 100 m for both σ_{ρ_0} and σ_{I_0}. It can be clearly seen that the range precision after fixing the three widelanes in Equation (5.1) is substantially dependent on the variation of σ_{phase} while keeps nearly constant over the specified range of σ_{code}. For the precision of the estimated $\hat{N}_{E1}$, similar pattern is also observed in Figure 5.9. In particular, at coordinate (0.3, 0.003), $\sigma_{\hat{N}_{E1}}$ is still larger than one cycle which indicates the difficulty of resolving the remaining $\hat{N}_{E1}$ instantaneously. Figure 5.10 displays that only when the range

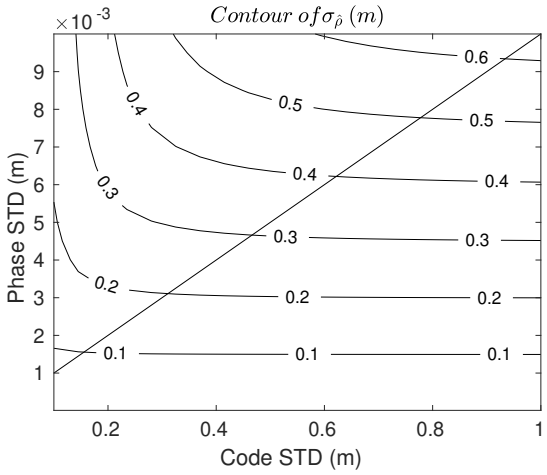

Figure 5.8: *Contour of $\sigma_{code}, \sigma_{phase}$, and $\sigma_{\hat{\rho}}$; The diagonal line has a slope of $\frac{1}{100}$, the same below*

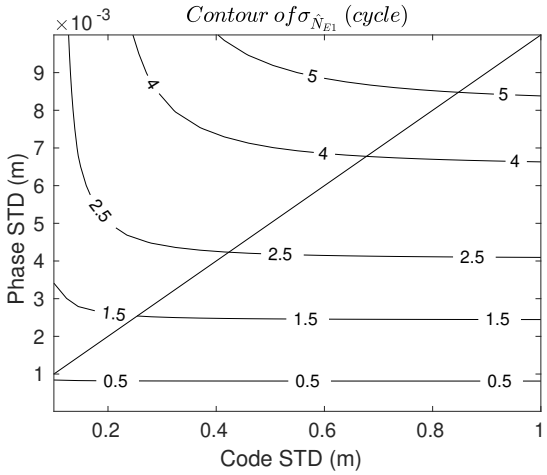

Figure 5.9: *Contour of $\sigma_{code}, \sigma_{phase}$, and $\sigma_{\hat{N}_{E1}}$*

is sufficiently precise would the resolution of $\hat{N}_{E1}$ be possible. which is mainly due to its short wavelength($\approx 20cm$); In the mean time, the contribution of the precision of ionosphere is not significant.

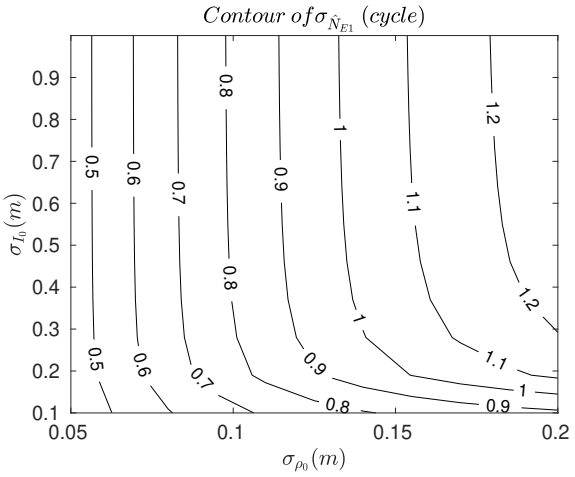

Figure 5.10: *Contour of* σ_{ρ_0} σ_{I_0} *and* $\sigma_{\hat{N}_{E1}}$

5.3.3 Multiple−epoch filtered positioning

The conventional PPP solution of the above model is first assessed with the filter reset every three hours. The code and phase measurements noise is set to 20 *cm* and 0.01 *cycles* at zenith respectively. The ambiguity resolution process is performed independently at each epoch and the float states and its covariance matrix are delivered to Kalman filter for next measurement update instead of using the fixed states. This process is designed to mitigate the impact of possible wrong fixing and it is also easy to study the difference between the float and fixed solutions, see Section 4.3.3. After resolving the extra-widelane, widelane and the remaining ambiguities sequentially, the ambiguity-fixed positioning solutions are more centered around zero and achieve more rapid convergence, especially on the east component as displayed in Figure 5.11.

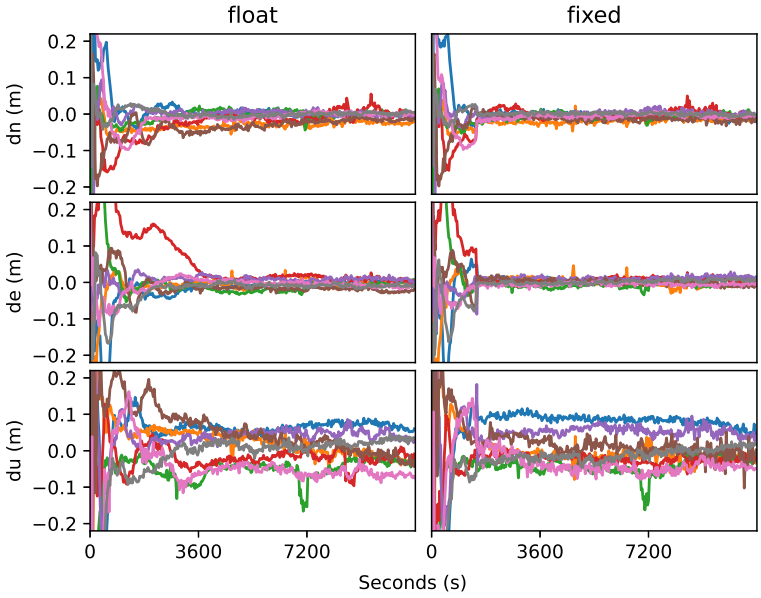

Figure 5.11: *Superimposed GPS L1/L2/L5 + Galileo E1/E5a/E5b/E6 ambiguity-float (left) and ambiguity-fixed (right) PPP solutions at station BRST on 01/05/2021 (Different color represents different sessions; dn, de, du stand for positioning errors in the north east and up direction respectively; Each session has a length of 3 hours or 10800 seconds as shown in the ticks of the horizontal axis.)*

Obtaining these more aggregated fixed solutions still requires a certain period of time (roughly half an hour) mainly caused by the slow convergence of N_1 and N_{E1} ambiguities. These ambiguities are difficult to be fixed due to short wavelengths and normally have lower fixing rate among all ambiguities.

For each session in Figure 5.11, the 68th percentile (Banville et al., 2020) of the absolute positioning errors after half an hour is computed instead of the RMS error to mitigate the impact from possible wrong fixing or outliers.

Figure 5.12 and Figure 5.13 show the ambiguity fixing rates of two integer estimators. It can be seen that the both GPS and Galileo could achieve high fixing rates for different kinds of ambiguities.

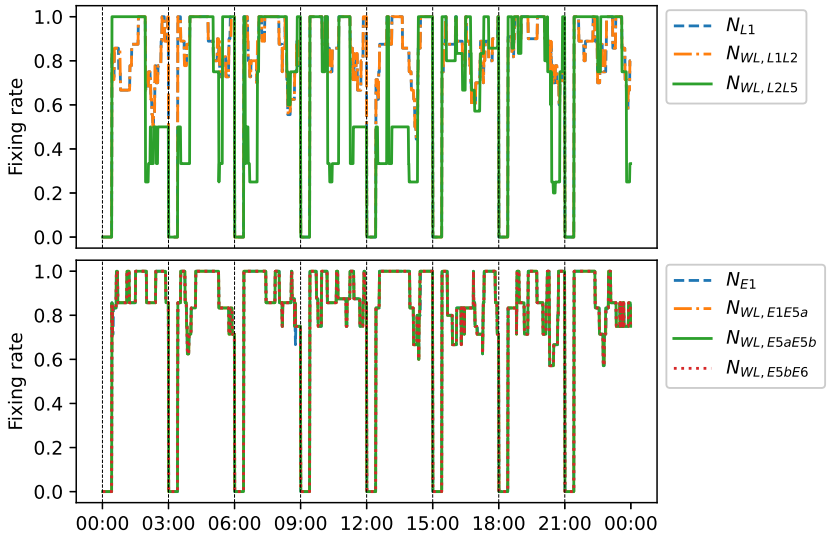

Figure 5.12: *Ambiguity fixing rates of GPS L1/L2/L5 + Galileo E1/E5a/E5b/E6 PPP fixed solutions at station BRST on 01/05/2021. The BIE estimator is used for ambiguity resolution.*

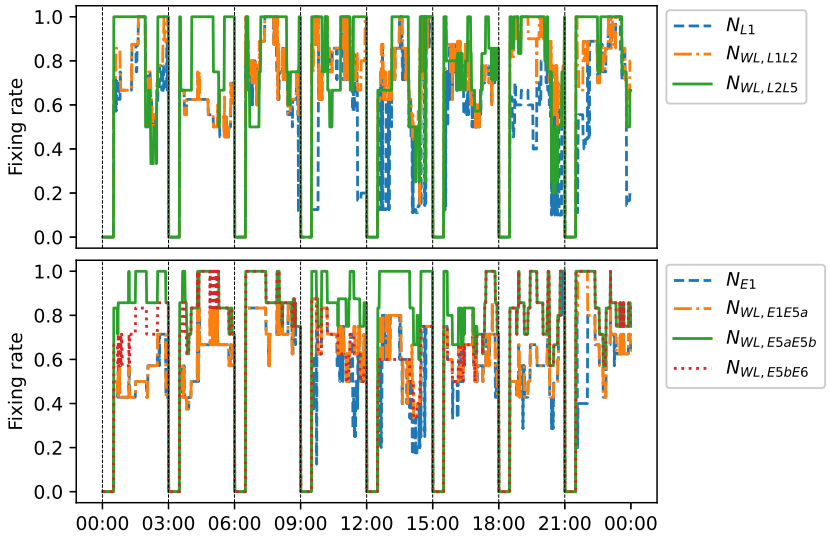

Figure 5.13: *Ambiguity fixing rates of GPS L1/L2/L5 + Galileo E1/E5a/E5b/E6 PPP fixed solutions at station BRST on 01/05/2021. The LAMBDA method is used for ambiguity resolution and ratio test for validation. Partial ambiguity resolution is used.*

The 68th percentile of positioning errors from all the eight sessions on 01/05/2021 for each station is displayed in Figure 5.14. It can be seen that the east component achieves substantial improvement from float to fixed solutions for all the stations. The height component degrades at some stations after AR. It was found that when using the BIE estimator, it is critical to set proper standard deviations (STD) for code and phase measurements. This is illustrated

in Figure 5.15. It shows that the ambiguity-fixed height solutions are more sensitive to the setting of code and phase STD. Figure 5.16 is another example of fixed solutions at station BOGT with different seting of phase STD. Therefore improper STD configuration could deteriorate the height accuracy when evaluating as in Figure 5.14. However proper setting of STD for specific station requires to check its postfit code and phase residuals. Moreover, currently no validation measure for the fixed solution from the BIE estimator is implemented in this study and an effective method could be applied in the future to check the difference between the fixed and the float solution to avoid poor results for user output. Figure 5.17 shows the ambiguity-fixed solutions using the LAMBDA method. It shows that output of this estimator could also be affected by different setting of phase STD.

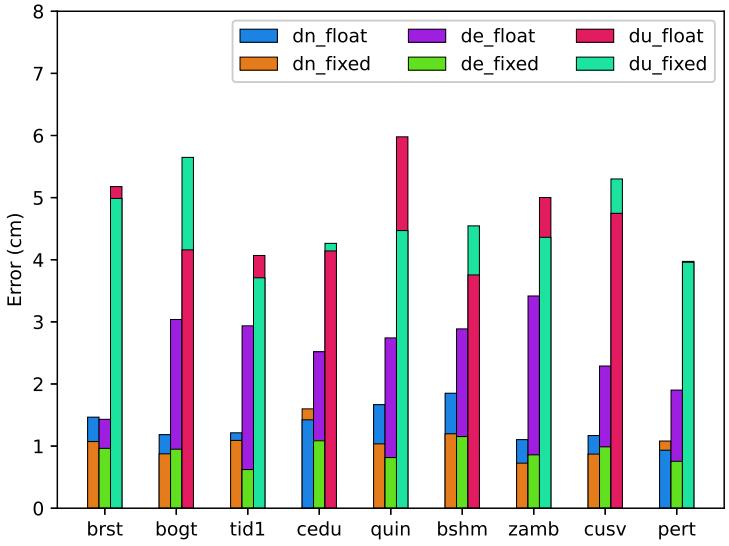

Figure 5.14: *The 68th percentile of GPS L1/L2/L5 + Galileo E1/E5a/E5b/E6 ambiguity-float and ambiguity-fixed PPP solution errors at all the selected stations on 01/05/2021*

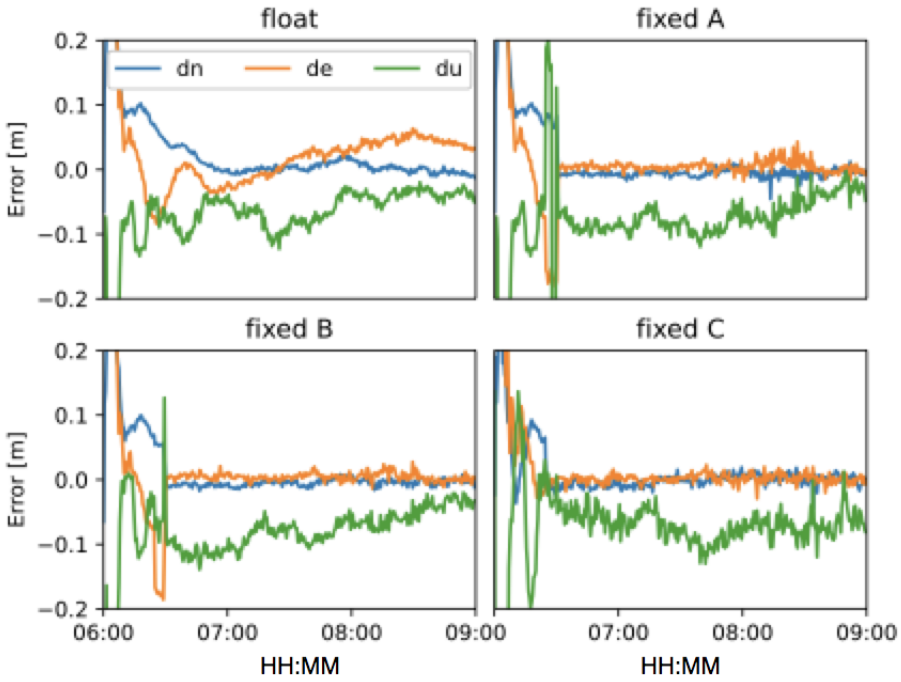

Figure 5.15: *One session of PPP solutions with different settings of zenithal code and phase STD at station bogt on 01/05/2021: float:* $\sigma_{code} = 0.2\ m, \sigma_{phase} = 0.01$ *cycles for both GPS and Galileo; fixed A:* $\sigma_{code} = 0.2\ m, \sigma_{phase} = 0.01$ *cycles for both GPS and Galileo; fixed B:* $\sigma_{code\_GPS} = 0.1\ m, \sigma_{phase\_GPS} = 0.015$ *cycles,* $\sigma_{code\_Galileo} = 0.2\ m, \sigma_{phase\_Galileo} = 0.015$ *cycles ; fixed C:* $\sigma_{code\_GPS} = 0.1\ m, \sigma_{phase\_GPS} = 0.015$ *cycles,* $\sigma_{code\_Galileo} = 0.2\ m, \sigma_{phase\_Galileo} = 0.035$ *cycles; dn de and du denote the error components in the north, east and up direction, the same below.*

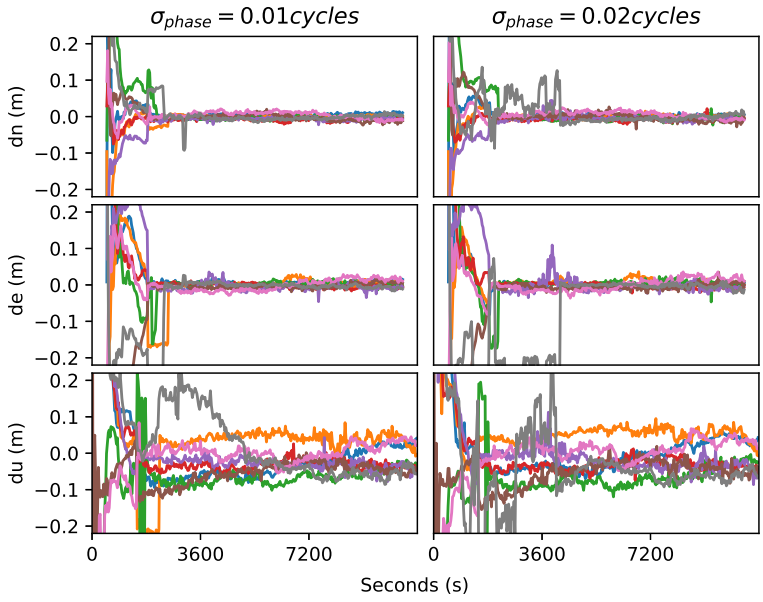

Figure 5.16: *Superimposed GPS L1/L2/L5 + Galileo E1/E5a/E5b/E6 ambiguity-fixed PPP solutions with different settings of phase STD at station BOGT on 01/05/2021. The BIE estimator is used for ambiguity resolution*

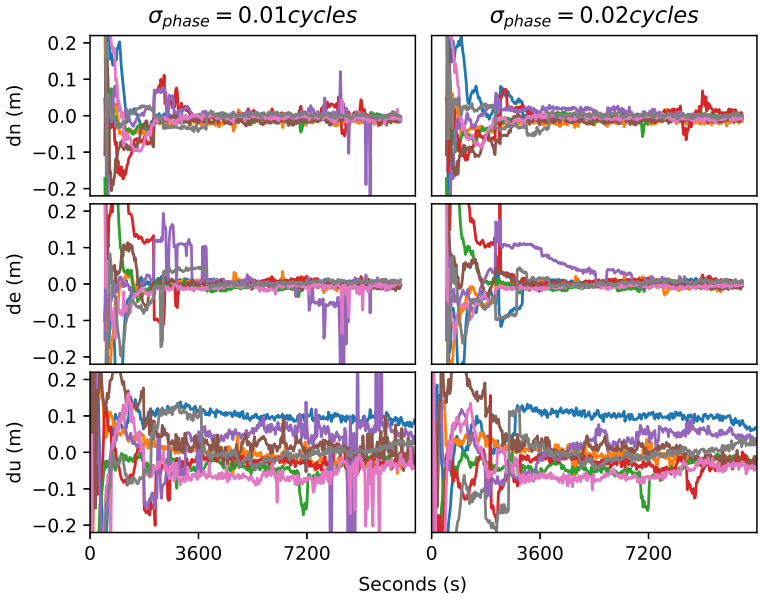

Figure 5.17: *Superimposed GPS L1/L2/L5 + Galileo E1/E5a/E5b/E6 ambiguity-fixed PPP solutions with different settings of phase STD at station BRST on 01/05/2021. The LAMBDA method is used for ambiguity resolution and ratio test for validation.*

Figure 5.18 is the distribution of the positioning errors accumulated from all the sessions (after half an hour for each session) over the ten testing days of the selected stations. It clearly shows that significant accuracy improvement on the east component is observed after AR. The fixed north error components are also more precise, while for the up direction no apparent improvement is found. As shown in Table 5.3 , an improvement of 63% is obtained in the east direction of the fixed solutions. However, the height solution after AR has a marginal improvement. It is noted that current functional model is based on the widelane combinations, and this strategy excludes the measurements if the required frequencies for the widelane combination are not complete or valid in the observation file. It is not uncommon when the receiver misses the measurements on a specific frequency, and thus this widelane-nested solution will be weakened due to reduced measurements. In order to assess this effect, the error statistics of the ambiguity-float solutions based on the separated frequencies were computed as listed in Table 5.3, which outperforms the widelane-nested float solutions in both the north and especially the height components. In

this study, all the 'float' solutions presented refer to the widelane-nested or -combined model.

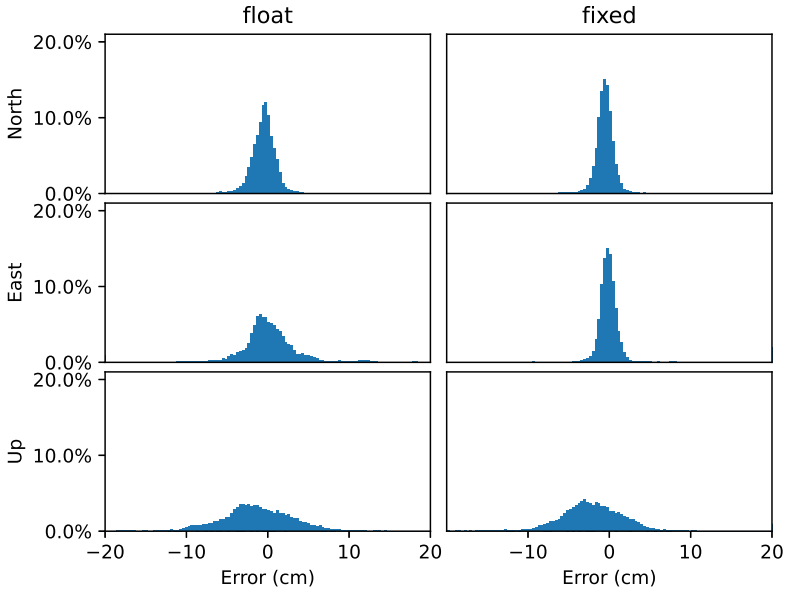

Figure 5.18: *Histogram of GPS L1/L2/L5 + Galileo E1/E5a/E5b/E6 PPP float (left) and fixed (right) errors at all the testing stations from 01/05/2021 to 10/05/2021. All types of ambiguities are resolved in the fixed solutions*

Table 5.3: The 68th percentile of GPS L1/L2/L5 + Galileo E1/E5a/E5b/E6 PPP errors at all the testing stations from 01/05/2021 to 10/05/2021 (unit: *cm*). Float* stands for the float solution based on the frequency-separated model; The Float and Fixed solutions are from the widelane-combined model.

Model	North	East	Up
Float*	1.3	2.64	4.34
Float	1.37	2.63	4.48
Fixed	1.16	0.98	4.44

The convergence time is also evaluated statistically from all the sessions. Here it is defined as the time it takes to converge below 5 cm for at least 10 consecutive epochs in the horizontal plane. Higher peak at around 25 *min* of the fixed solutions is clearly shown in the histogram of convergence time of Figure 5.19. From Table 5.4 the averaged convergence time is expedited by 17% after AR. It is also noted that in Figure 5.19 and Figure 5.6 the percentage of float PPP are slightly better than that of PPP-AR, which is also reported in Choy et al. (2016) showing that a specific time period is first required for the float solution to converge to then ensure correct ambiguity fixing.

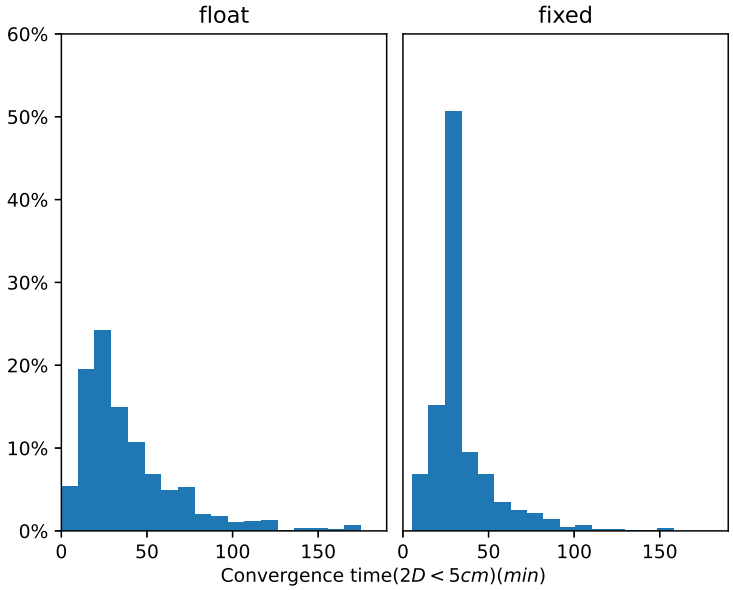

Figure 5.19: *Convergence time (2D<5cm) histogram of GPS L1/L2/L5 + Galileo E1/E5a/E5b/E6 PPP float (left) and fixed (right) solutions for all the testing stations from 01/05/2021 to 10/05/2021*

Table 5.4: Statistics of convergence time (2D<5cm) of GPS L1/L2/L5 + Galileo E1/E5a/E5b/E6 PPP float and fixed solutions for all the testing stations from 01/05/2021 to 10/05/2021 (unit: *min*)

	Float	Fixed
Average	35.1	29.2
Std.	25.3	14.4
68th percentile	37.1	29.6
median	28	25

Table 5.5 lists the statistic results of PPP fixed solutions with different settings of minimum time for AR. It can be seen that this minimum value could affect the statistic convergence time to some degree but this time period is still in the vicinity of 30 *min* for these cases.

Table 5.5: Statistics of convergence time (2D<5cm) (*min*) and positioning errors (the 68th percentile) (*cm*) of GPS L1/L2/L5 + Galileo E1/E5a/E5b/E6 PPP fixed solutions with different settings of minimum time for ambiguity resolution for all the testing stations from 01/05/2021 to 10/05/2021

Convergence time	Min. AR time = 600 *s*	Min. AR time = 1200 *s*
Average	38.9	36.7
Std.	23.5	23.9
68th percentile	44	42
median	34	31
Error		
North	1.23	1.23
East	1.19	1.21
Up	4.73	4.78

More detailed PPP results of each selected station during the testing days are presented in Appendix B.

5.3.4 Single−epoch positioning

In this section, the single-epoch positioning results of the GPS/Galileo multi-frequency model is studied. The filter is reset at each epoch for the ten testing days of all stations. Only the widelane ambiguities are fixed in this test since the remaining estimated ambiguity may still have noise level exceeding one cycle as discussed in 5.3.2. As shown in Figure 5.20, the widelane-fixed solutions have less dispersion than the float or code-only results. This improvement is due to the instantaneously fixed widelane ambiguities. The float solutions are completely determined by the code measurements since the phase ambiguities are reset at each instant. Figure 5.21 is the related fixing rate and it shows high fixing rates at each epoch for both GPS and Galileo.

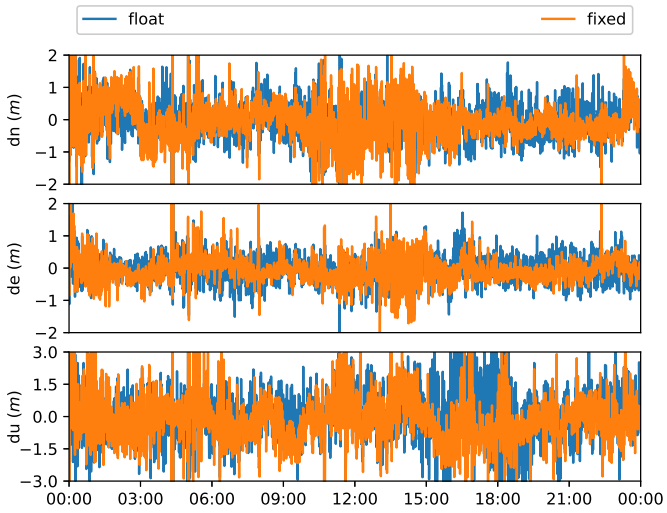

Figure 5.20: *GPS L1/L2/L5 + Galileo E1/E5a/E5b/E6 single-epoch float and fixed solution errors at station BRST on 01/05/2021; The float solution here means that the filter is reset at each epoch and the phase measurements does not contribute to the solution; The fixed solution only has the widelane ambiguities resolved(the same below)*

The 68th percentile of positioning error is still used for results evaluation. Figure 5.23 shows the percentile error for each station on 01/05/2021. It can be seen that horizontal precision improvement is achieved for all the testing stations while the height solutions from seven of them are negatively impacted

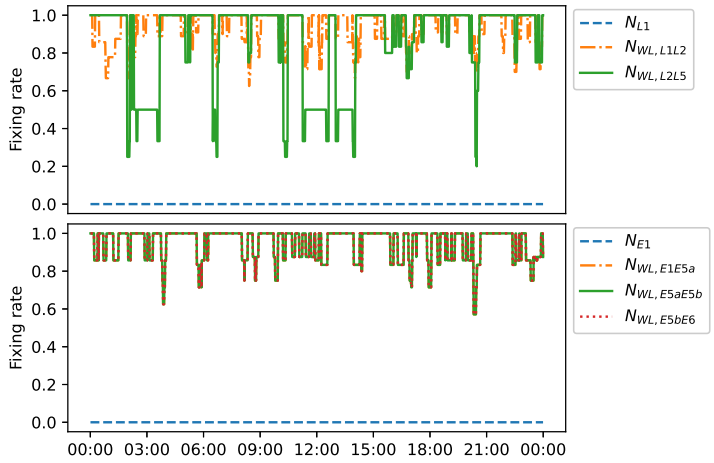

Figure 5.21: *Ambiguity fixing rates of GPS L1/L2/L5 + Galileo E1/E5a/E5b/E6 single-epoch fixed solution at station BRST on 01/05/2021. The filter is reset at each epoch. The fixed solution only has the widelane ambiguities resolved and the BIE estimator is used for ambiguity resolution.*

by AR. It is found that the empirical standard deviations of the phase measurements can significantly affect the height precision of the fixed solutions as illustrated in Figure 5.22. Proper configuration of the GPS and Galileo measurements standard deviations would help to achieve a better accuracy in the up direction when using the BIE estimator and this requires further investigation.

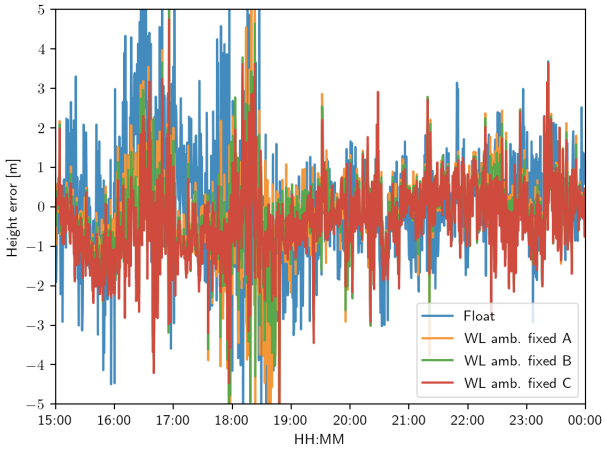

Figure 5.22: *GPS L1/L2/L5 + Galileo E1/E5a/E5b/E6 single-epoch solutions at station BRST on 01/05/2021. fixed A:* $\sigma_{phase\_GPS} = 0.02$ *cycles* $\sigma_{phase\_Galileo} = 0.03$ *cycles; fixed B:* $\sigma_{phase\_GPS} = 0.015$ *cycles* $\sigma_{phase\_Galileo} = 0.03$ *cycles;fixed C:* $\sigma_{phase\_GPS} = 0.01$ *cycles* $\sigma_{phase\_Galileo} = 0.03$ *cycles*

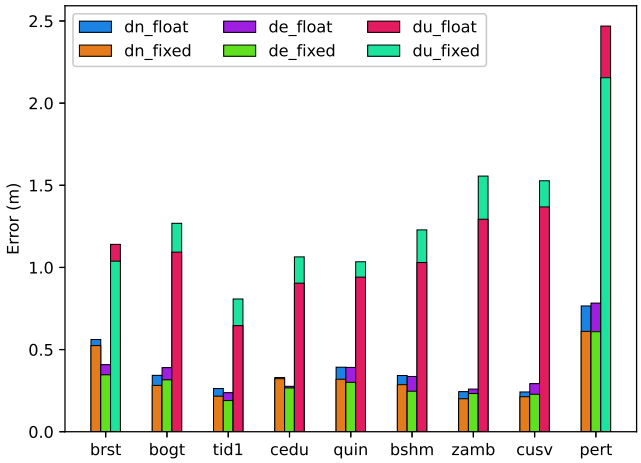

Figure 5.23: *The 68th percentile of GPS L1/L2/L5 + Galileo E1/E5a/E5b/E6 ambiguity-float and ambiguity-fixed single-epoch errors at the selected stations on 01/05/2021*

As presented in the last section, the distribution of the positioning errors over the ten testing days for all stations is presented in Figure 5.24, which shows that both of the north and east errors of fixed solutions are more aggregated around zero and have higher peak. From Table 5.6, the accuracy of the north and east components after AR can reach 32 cm and 31 cm (68th percentile) improved by 13% and 16% respectively. The height accuracy degrades as found in Figure 5.23. As discussed in Figure 5.15, appropriate code and phase standard deviation for specific stations when using the BIE estimator could improve the results further. At the same time, more precise ionospheric information would also benefit the single-epoch solution since there is no convergence process.

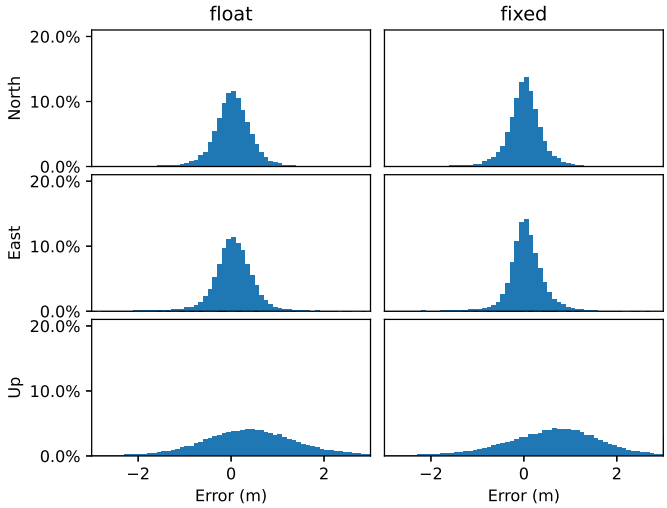

Figure 5.24: *Histogram of GPS L1/L2/L5 + Galileo E1/E5a/E5b/E6 single-epoch float (left) and widelane fixed (right) solutions at the selected stations from 01/05/2021 to 10/05/2021*

Table 5.6: The 68th percentile of GPS L1/L2/L5 + Galileo E1/E5a/E5b/E6 single-epoch positioning errors at all the testing stations from 01/05/2021 to 10/05/2021 (unit: m).

Model	North	East	Up
Float	0.37	0.37	1.11
Fixed	0.32	0.31	1.27

5.4 Summary

This chapter presents the GPS/Galileo ionosphere-free and ionosphere-estimated PPP results using CNES uncombined bias products. It has been demonstrated that the uncombined code and phase bias products can be applied to ionosphere-free and ionosphere-estimated models and the combined phase ambiguity or its uncombined form still have the integer property conserved, thus allowing for integer ambiguity resolution. This chapter proves the flexibility of these uncombined biases for ambiguity resolution of different PPP models from a user side.

Based on the in-house software POINT, the GPS/Galileo zero-difference PPP AR performance using the uncombined biases are highlighted as following:

The dual-frequency ionosphere-free ambiguity-fixed kinematic PPP can achieve an accuracy of 0.82, 0.96, 3.04 cm on average in the north, east and up direc-

tion respectively (68th percentile). In particular the east component obtains a significant improvement of 45% compared to the float solutions. In terms of the convergence, PPP is accelerated by 23% after AR for 3D error below 5 cm. In the multi-frequency case, the ionosphere-estimated ambiguity-fixed solution can achieve an accuracy of 1.16, 0.98 and 4.44 *cm* in the north, east and up direction respectively (68th percentile). A significant improvement of 63% on the east component is obtained with respect to the ambiguity-float solution. The PPP convergence requires 29.2 min on average to be below 5 cm horizontally after AR with an acceleration of 17%. Regarding the instantaneous positioning capability of the multi-frequency model, an accuracy of 32 and 31 *cm* for north and east components (68th percentile) can be obtained after WAR improved by 13% and 16% respectively relative to the code-only solution. The N_1 and N_{E1} AR was deactivated in our single-epoch test as their estimated precisions could still be larger than one cycle and not sufficient for resolution.

With the use of additional measurements from other constellations, more strengthened geometry would further benefit the multi-frequency PPP solution and it is anticipated that full ambiguity resolution would be more reliable at an instant even without external ionospheric correction. CNES now also issues the uncombined satellite code and phase bias products for the Chinese BeiDou satellite navigation system, the positioning performance of GPS/Galile/BeiDou multi-frequency PPP is to be investigated, especially using this widelane-nested model.

Further investigation would also be required for the validation of the fixed solutions and proper weighting between code and phase observation especially when using the BIE estimator. A procedure of hypothesis test about the empirical measurement standard deviation to determine proper measurement weights for the BIE estimator should also be investigated.

Moreover, the performance of multi-frequency ionosphere-free PPP is also to be studied, especially its single-epoch positioning ability.

Chapter 6

PPP integration with Inertial Navigation System (INS)

6.1 Introduction

In the previous chapters, it is clearly shown that GNSS PPP is capable of achieving centimeter-level positioning accuracy. However, this high-accuracy capability would be deteriorated severely when frequent signal blockages happen in navigation. The Inertial Navigation System (INS) is an autonomous system that does not require measurements to external signals. It provides high-accuracy short-term position, velocity and attitude at a high data rate. The integration of PPP and INS is expected to achieve better positioning performance, especially in the harsh GNSS signal reception environment. In this chapter, the integration models between GPS/Galileo PPP using CNES uncombined bias products and INS are formulated including both loosely coupled integration (LCI) and tightly coupled integration (TCI).The organization is as follows: Section 6.2 presents the INS principle and reviews the PPP/INS integration architecture especially for the TCI; Section 6.3 gives the PPP/INS integration models used in this study, which is presented in the form of Kalman filter implementation; Section 6.4 briefly summarises this chapter.

6.2 Background

6.2.1 INS principle

Inertial Navigation System (INS) is an autonomous, dead-reckoning system using accelerometer and gyro measurements. It can provides precise velocity, position and attitudes solutions in a short term. Due to the error accumulation in integral, INS solution will drift over the measuring time span. The INS principle including basic frame transformation, navigation equation and error dynamics are presented in the following.

Frame transformation

- Earth frame e to local navigation frame n

$$\begin{aligned} C_e^n &= R_y(-\varphi - \pi/2)R_z(\lambda) \\ C_n^e &= (C_e^n)^T \end{aligned} \tag{6.1}$$

  where C is called Direction Cosine Matrix (DCM) which is derived from rotation matrix R. φ and λ are geodetic latitude and longitude.

- Local navigation frame n to body frame b

$$\begin{aligned} C_n^b &= R_x(\phi)R_y(\theta)R_z(\psi) \\ C_b^n &= (C_n^b)^T \end{aligned} \tag{6.2}$$

  where ψ ,θ and ϕ are body's yaw, pitch and roll angles with respect to the local frame, which are also called Euler angles. Note that this angle relationship can also be described by quaternion and the conversion between quaternion and Euler angles is commonly used in INS algorithms.

- The earth rotation rate vector

$$\begin{aligned} \omega_{ie}^e &= [\ 0 \ \ 0 \ \ \omega_e\ ]^T \\ \omega_{ie}^n &= C_e^n \omega_{ie}^e \end{aligned} \tag{6.3}$$

where ω_e is the earth rotation rate.

- The transport rate vector The transport rate ω_{en}^n describes the rotation of local frame with respect to the earth frame. It is related to the rate of geodetic latitude and longitude as follows:

$$\begin{aligned} \dot{\varphi} &= v_N/(RN+h) \\ \dot{\lambda} &= v_E/(RE+h) \end{aligned} \tag{6.4}$$

where RN, RE are radii of curvature in the meridian and prime vertical. And we can also get:

$$\omega_{in}^n = \omega_{ie}^n + \omega_{en}^n \tag{6.5}$$

INS navigation equation

The inertial navigation equation refers to the time derivatives of position, velocity and attitude or quaternion as following:

$$\dot{r}^n = \begin{bmatrix} \dot{\varphi} \\ \dot{\lambda} \\ \dot{h} \end{bmatrix} = \begin{bmatrix} \frac{1}{(RN+h)} & 0 & 0 \\ 0 & \frac{1}{(RE+h)cos\varphi} & 0 \\ 0 & 0 & -1 \end{bmatrix} \begin{bmatrix} v_N \\ v_E \\ v_D \end{bmatrix}$$

$$\dot{v}^n = C_b^n f^b - (2\omega_{ie}^n + \omega_{en}^n) \times v^n + g^n$$

$$\dot{q} = \Omega q = \frac{1}{2} \begin{bmatrix} 0 & -\omega_x & -\omega_y & -\omega_z \\ \omega_x & 0 & \omega_z & -\omega_y \\ \omega_y & -\omega_z & 0 & \omega_x \\ \omega_z & \omega_y & -\omega_x & 0 \end{bmatrix} \begin{bmatrix} q_0 \\ q_1 \\ q_2 \\ q_3 \end{bmatrix} = \frac{1}{2} \begin{bmatrix} -q_1 & -q_2 & -q_3 \\ q_0 & -q_3 & q_2 \\ q_3 & q_0 & -q_1 \\ -q_2 & q_3 & q_0 \end{bmatrix} \begin{bmatrix} \omega_x \\ \omega_y \\ \omega_z \end{bmatrix} \tag{6.6}$$

where $r^n = [\, \varphi \, \lambda \, h \,]^T$ is the curvilinear position; $v^n = [\, v_N \, v_E \, v_D]^T$ is the body velocity (with respect to the earth) resolved in the navigation frame; f^b is the accelerometer measurements (in the body b frame); ω_{ie}^n is the earth rotation rate resolved in the navigation frame; ω_{en}^n is the transport rate, which describes the rotation of local frame with respect to the earth frame; $\omega^b = [\, \omega_x \, \omega_y \, \omega_z \,]^T$ denotes the gyroscope measurements with respect to a local navigation frame; $q = [\, q_0 \, q_1 \, q_2 \, q_3 \,]^T$ is the attitude quaternion for conversion between body

and navigation frame; g^n is the gravity vector in the navigation frame and in POINT it is approximated using the normal gravity γ_h at hegiht h above the WGS84 ellipsoid (Heiskanen and Moritz, 1967). The 2nd-order Runge-Kutta method is used in POINT to solve Equation 7.3 and navigation solution are finally obtained.

INS error dynamics

when the coordinate transformation matrix and Euler angles represent a small angle perturbation for which the small angle approximation is valid, the coordinate transformation matrix becomes

$$C_n^b \approx \begin{bmatrix} 1 & \psi & -\theta \\ -\psi & 1 & \phi \\ \theta & -\phi & 1 \end{bmatrix} = I - [\ \Psi\ \times\ ] \tag{6.7}$$

where $[\Psi\ \times\ ]$ denotes the skew-symmetric matrix of the Euler angles. This expression is frequently used in the derivation of the position, velocity and attitude error derivatives as below:

$$\begin{aligned} \delta\dot{r}^n &= F_{rr}\delta r^n + F_{rv}\delta v^n \\ \delta\dot{v}^n &= F_{vr}\delta r^n + F_{vv}\delta v^n + (f^n\times)\epsilon^n + C_b^n\delta f^b \\ \dot{\epsilon}^n &= F_{er}\delta r^n + F_{ev}\delta v^n - (\omega_{in}^n\times)\epsilon^n - C_b^n\delta\omega_{ib}^b \end{aligned} \tag{6.8}$$

Where δr^n and δv^n are the error states of position and velocity respectively; $\delta r^n = [\delta\varphi\ \delta\lambda\ \delta h]^T$, $\delta v^n = [\delta v_N\ \delta v_E\ \delta v_D]^T$; ϵ is attitude error in the form of Euler angle and $\epsilon = [\epsilon_N\ \epsilon_E\ \epsilon_D]^T$. F stands for partial derivative and the exact expressions for $F_{rr}, F_{rv}, F_{vr}, F_{vv}.F_{er}, F_{ev}$ can be found in many textbooks like Groves (2013) and Shin (2001). The attitude error components ϵ_N, ϵ_E and ϵ_D correspond to pitch, roll and yaw angles respectively.

6.2.2 Review of PPP/INS integration

Loosely coupled architecture

The LCI of PPP or RTK and INS is in the domain of solutions (Scherzinger, 2000; Shin, 2001). As summarised in Gautier (2003), in LCI the GNSS receiver

can be treated as a "black box". However, if there is a GPS outage, the GPS stops providing processsed measurements and the inertial sensor calibration from the GPS/INS filter stops as well. Elsheikh et al. (2018) studies the positioning performance of single-frequency loosely coupled PPP/INS integration and show that sub-meter accuracy can be achieved with good satellite observability.

The architechture of LCI could be depicted as in Figure 6.1. The INS data rate is usually much higher than the GNSS sampling and an alignment is required at first. Then the kalman filter integrates the position and velocity solutions by making differences to estimate the error states and corrects the sensors with updated solutions.

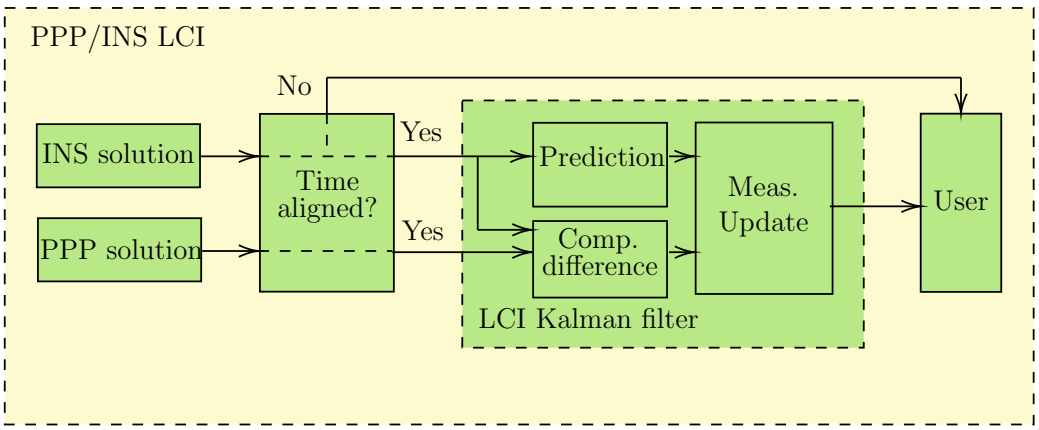

Figure 6.1: *Architecture of loosely coupled integration between INS and PPP*

Tightly coupled architecture

The TCI is in the GNSS measurements domain. A TCI structure limits the problems due to satellite signal blockage and benefits from GNSS measurement updates even if there are less than four satellites available for a complete GPS navigation solution (Gautier, 2003). It is then possible for a TCI system to remain high positioning accuracy in harsh GNSS reception environment.

The development of the PPP technique leads to a great variety of PPP/INS TCI models. Zhang and Gao (2008) first proposed the model of tightly coupled GPS dual-frequency ionosphere-free PPP and INS integration. It is an undifferened PPP model as in Héroux and Kouba (2001); Kouba (2009) but

the phase ambiguities are real-valued. Roesler and Martell (2009) assesses the implementation of tightly coupled GPS PPP/INS filter in an airborne environment and their results show an significant improvement during periods of poor satellite geometry or after losses of lock. Du and Gao (2012) uses inertial data to estimate the phase (range) variation between adjacent epochs to determine the phase cycle slips in comparison with the computed phase measurement time difference. Their results indicate this INS-based method can effectively identify cycle slips and improve the performance of GPS PPP/INS integrated system. Muhammad (2014) incorporated GLONASS into PPP and assess the GPS/GLONASS PPP with loose and tight integration of low cost inertial sensors in vehicular urban navigation. Their results show that the inclusion of GLONASS measurements yields great improvement and an accuracy of about 20 meters in position, about 2 m/s in velocity, about 2-3 degrees in roll/pitch angles and about 25 degrees in azimuth can be obtained. But they also explained that the TCI suffers more of the blunders issue and the LCI has the best results in this scenario. Abd Rabbou and El-Rabbany (2015) investigate GPS PPP/ Micro-Electro-Mechanical System (MEMS) IMU TCI and show that the between-satellite single-difference (BSSD) system performs better in general than the undifference model. Gao et al. (2017b) study the performance of GPS/GLONASS/BeiDou PPP tightly integrated with the MEMS IMU and show that the additional satnavs significantly improve the positioning accuracy. The benefits of multi-GNSS on PPP/INS convergence and results during signal outage are also demonstrated. Gao et al. (2017a) evaluates the results of tightly coupled integration of GPS/BeiDou PPP and four different grades of INS using an ionosphere-estimated model and the and the apriori constraints on the slant ionospheric delays are from the IGS Global Ionosphere Maps (GIM) products. Vana et al. (2019) assesses the tightly coupled GPS/GLONASS/Galileo/BeiDou PPP/MEMS IMU integration. The dual-frequency ionosphere-free model is used and it is shown that the integrated solution offers less than meter-level accuracy when there is a GNSS

signal outage for half a minute.

As PPP with ambiguity resolution (AR) is increasing studied since around 2008, PPP/INS integration with AR also becomes popular. Han et al. (2016) and Liu et al. (2016) study the GPS PPP/INS TCI with AR. The between-satellite single-difference PPP model is used and the CNES WSB and 'integer' phase clock products are applied for phase bias correction, which can actually used directly in undifferend model. Both studies report significant accuracy improvement after AR. Zhang et al. (2018) also studied the ambiguity-fixed GPS PPP/INS TCI. The UPD products are used for AR and their model is also single-differenecd and ionosphere-free. Their results show that for the navigation- and tactical-grade IMU, significant improvement is obtained when the outage duration is less than 10 s. Recently, undifferenced and uncombined PPP model for integrated navigation is also demonstrated (Gu et al., 2021, 2022; Li et al., 2021, 2022b). Besides the additional bias correction, external atmospheric information including tropospheric and ionospheric corrections are also disseminated to user side, which is also referred as PPP-RTK. Li et al. (2021, 2022b) show that PPP-RTK can converge almost instantaneously and achieve centimeter-level accuracy when integrated with IMU and camera. However their bias correction is still based on the conventional combined WL and NL form instead of the uncombined observable-specific form.

Figure 6.2 is a general PPP/INS TCI structure.

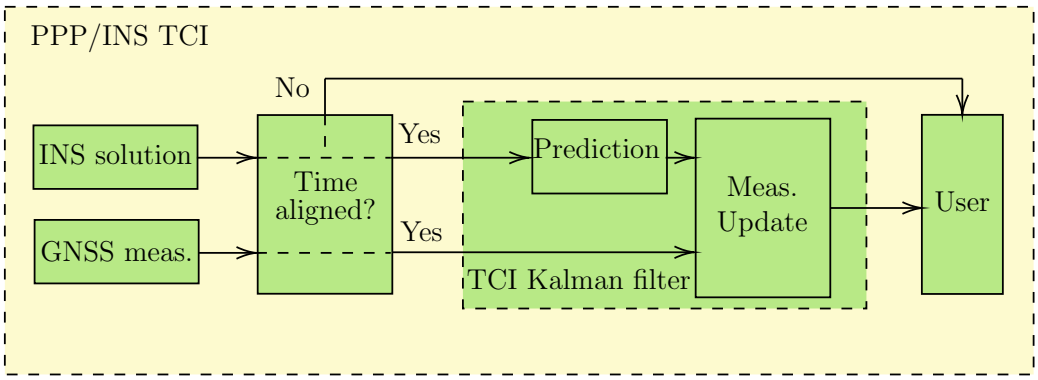

Figure 6.2: *Architecture of tightly coupled integration between INS and PPP*

For the ultra-tightly coupled integration, the INS outputs of position, velocity and attitude, used as external inputs to a GNSS receiver, aid in the pre-positioning calculations for faster signal acquisition and inteference rejection during signal tracking (Gautier, 2003). This type of integration is in the receiver hardware level and more description on this can be found in Groves (2013) and Morton et al. (2020).

6.3 PPP/INS integration using uncombined bias products

This section presents mathematical models for PPP/INS integration with the application of CNES uncombined bias products in a local navigation frame n. The GPS/Galileo dual-frequency ionosphere-free PPP model is used, see Section 3.7.2. These models are given in the form of Kalman filter implementation.

6.3.1 Loosely-coupled integration

Prediction

The discrete Kalman filter prediction step is presented in Section 3.4. For LCI the estimated states may be expressed as:

$$x = \begin{bmatrix} \delta r^n & \delta v^n & \epsilon^n & b_a & b_g & s_a & s_g \end{bmatrix}^T \tag{6.9}$$

where b stands for biases of IMU sensors; $b_a = [b_{a_X}\ b_{a_Y}\ b_{a_Z}]^T$ is the IMU accelerometer bias vector in the IMU XYZ frame; $b_g = [b_{g_X}\ b_{g_Y}\ b_{g_Z}]^T$ is the IMU gyro bias vector in the IMU axis tripod; s stands for scale factor of IMU sensors.

The state transition matrix is not identity but comprises the contribution from the IMU error dynamics. The dynamic matrix is formed as :

$$F = \begin{bmatrix} F_{rr} & F_{rv} & 0_{3\times3} & 0_{3\times3} & 0_{3\times3} & 0_{3\times3} & 0_{3\times3} \\ F_{vr} & F_{vv} & (f^n\times) & C_b^n & 0_{3\times3} & C_b^n f^b & 0_{3\times3} \\ F_{er} & F_{ev} & (-\omega_{in}^n\times) & 0_{3\times3} & C_b^n & 0_{3\times3} & C_b^n \omega_{nb}^b \\ 0_{3\times3} & 0_{3\times3} & 0_{3\times3} & \beta_{b_a} & 0_{3\times3} & 0_{3\times3} & 0_{3\times3} \\ 0_{3\times3} & 0_{3\times3} & 0_{3\times3} & 0_{3\times3} & \beta_{b_g} & 0_{3\times3} & 0_{3\times3} \\ 0_{3\times3} & 0_{3\times3} & 0_{3\times3} & 0_{3\times3} & 0_{3\times3} & \beta_{s_a} & 0_{3\times3} \\ 0_{3\times3} & 0_{3\times3} & 0_{3\times3} & 0_{3\times3} & 0_{3\times3} & 0_{3\times3} & \beta_{s_g} \end{bmatrix} \tag{6.10}$$

where β is the self-correlation time matrix for IMU sensor bias and scale factor parameters. Then The state transition matrix Φ is computed according to Equation (3.14). The spectral density matrix is defined as:

$$Q = diag\{n_a \quad n_g \quad \sigma_{b_a}^2 \quad \sigma_{b_g}^2 \quad \sigma_{s_a}^2 \quad \sigma_{s_g}^2\} \tag{6.11}$$

where n_a and n_g are IMU sensors noises and σ is spectral density. And the disturbance mapping matrix is as below:

$$G = \begin{bmatrix} 0_{3\times3} & 0_{3\times3} & 0_{3\times3} & 0_{3\times3} & 0_{3\times3} & 0_{3\times3} \\ C_b^n & 0_{3\times3} & 0_{3\times3} & 0_{3\times3} & 0_{3\times3} & 0_{3\times3} \\ 0_{3\times3} & C_b^n & 0_{3\times3} & 0_{3\times3} & 0_{3\times3} & 0_{3\times3} \\ 0_{3\times3} & 0_{3\times3} & I_{3\times3} & 0_{3\times3} & 0_{3\times3} & 0_{3\times3} \\ 0_{3\times3} & 0_{3\times3} & 0_{3\times3} & I_{3\times3} & 0_{3\times3} & 0_{3\times3} \\ 0_{3\times3} & 0_{3\times3} & 0_{3\times3} & 0_{3\times3} & I_{3\times3} & 0_{3\times3} \\ 0_{3\times3} & 0_{3\times3} & 0_{3\times3} & 0_{3\times3} & 0_{3\times3} & I_{3\times3} \end{bmatrix} \tag{6.12}$$

Then the process noise matrix can be computed using Equation (3.16). And the computation of the predicted states and covariance matrix follows Equation (3.13) and Equation (3.15).

Measurements update

The measurements in LCI are the position and velocity difference between PPP and INS, which can be expressed as:

$$z = \begin{bmatrix} S(r^n_{PPP} - r^n_{INS}) - C^n_b l^b \\ v^n_{Doppler} - v^n_{INS} - C^n_b(\omega^b_{nb}\times)l^b \end{bmatrix} \tag{6.13}$$

where l^b is the lever arm from IMU center to the antenna phase center; S is a scale matrix to convert radian to meter:

$$S = \begin{bmatrix} RN + h & 0 & 0 \\ 0 & (RE + h)cos\varphi & 0 \\ 0 & 0 & 1 \end{bmatrix} \tag{6.14}$$

This conversion avoids numerical instabilities in the computation of Kalman gain. The design matrix is then formed as:

$$H = \begin{bmatrix} S & 0_{3\times3} & 0_{3\times3} & 0_{3\times3} & 0_{3\times3} & 0_{3\times3} & 0_{3\times3} \\ 0_{3\times3} & I_{3\times3} & 0_{3\times3} & 0_{3\times3} & 0_{3\times3} & 0_{3\times3} & 0_{3\times3} \end{bmatrix} \tag{6.15}$$

The measurements noise matrix can be expressed as:

$$R = diag\{\sigma^2_{r^n_{PPP}} \quad \sigma^2_{v^n_{Doppler}}\} \tag{6.16}$$

where the $\sigma^2_{r^n_{PPP}} \quad \sigma^2_{v^n_{Doppler}}$ can be the precision of the estimated position and velocity from PPP solutions using the CNES bias products and doppler measurements.

The update procedure follows Equation (3.18) and Equation (3.20).

6.3.2 Tightly-coupled integration

Prediction

For the tight integration of GPS/Galileo dual-frequency ionosphere-free PPP using CNES bias products and INS the states to be estimated could be:

$$x = \begin{bmatrix} \delta r^n & \delta v^n & \epsilon^n & b_a & b_g & s_a & s_g & ZTD & dt_P^G & dt_L^G & \dot{dt}^G & dt_C^E & dt_L^E & \dot{dt}^E \\ N_{IF}^{p1} & ... & N_{IF}^{pm} & N_{IF_{E_1E_{5a}}}^{q1} & ... & N_{IF_{E_1E_{5a}}}^{qn} \end{bmatrix}^T \tag{6.17}$$

where m GPS satellites (p1, ..., p2) and n Galileo satellites (q1, ..., qn) are assumed to be used. The dynamic matrix in this TCI case is formed as:

$$F_{TCI} = \begin{bmatrix} \mathbf{F} & \mathbf{0} \\ \mathbf{0} & \mathbf{0} \end{bmatrix} \tag{6.18}$$

where **F** is the same as Equation (6.10). The spectral density matrix is formed as:

$$\begin{aligned} Q = diag\{ & n_a \quad n_g \quad \sigma_{b_a}^2 \quad \sigma_{b_g}^2 \quad \sigma_{s_a}^2 \quad \sigma_{s_g}^2 \quad \sigma_{ZTD}^2 \quad \sigma_{dt_P^G}^2 \quad \sigma_{dt_L^G}^2 \\ & \sigma_{\dot{dt}^G}^2 \quad \sigma_{\dot{dt}^E}^2 \quad \sigma_{dt_C^E}^2 \quad \sigma_{dt_L^E}^2 \quad \mathbf{0} \} \end{aligned} \tag{6.19}$$

where the spectral densities of all the ambiguities are set to zero. The disturbance mapping matrix is :

$$G_{TCI} = \begin{bmatrix} \mathbf{G} & \mathbf{0} \\ \mathbf{0} & \mathbf{I} \end{bmatrix} \tag{6.20}$$

where **G** is equal to Equation (6.12).

Measurements update

Assume the measurement vector is arranged as:

$$\begin{aligned} z = \begin{bmatrix} P_{IF}^{p1} & \lambda_{IF} L_{IF}^{p1} & \lambda_{L_1} D_{L_1}^{p1} & ... & P_{IF}^{pm} & \lambda_{IF} L_{IF}^{pm} & \lambda_{L_1} D_{L_1}^{pm} \\ C_{IF_{E_1E_{5a}}}^{q1} & \lambda_{IF_{E_1E_{5a}}} L_{IF_{E_1E_{5a}}}^{q1} & \lambda_{E_1} D_{E_1}^{q1} & ... & C_{IF_{E_1E_{5a}}}^{qn} & \lambda_{IF_{E_1E_{5a}}} L_{IF_{E_1E_{5a}}}^{qn} & \lambda_{E_1} D_{E_1}^{qn} \end{bmatrix}^T \end{aligned} \tag{6.21}$$

and the design matrix will be:

$$H = \begin{bmatrix} H_{r,v}^{p1} & \mathbf{0} & H_{T}^{p1} & H_{clk}^{p1} & \mathbf{0} & H_{amb}^{p1} & \dots & \mathbf{0} & \mathbf{0} & \mathbf{0} & \mathbf{0} \\ \vdots & \vdots & \vdots & \vdots & \vdots & \vdots & \vdots & \vdots & \vdots & \vdots & \vdots \\ H_{r,v}^{pm} & \mathbf{0} & H_{T}^{pm} & H_{clk}^{pm} & \mathbf{0} & \mathbf{0} & \dots & H_{amb}^{pm} & \mathbf{0} & \mathbf{0} & \mathbf{0} \\ H_{r,v}^{q1} & \mathbf{0} & H_{T}^{q1} & \mathbf{0} & H_{clk}^{q1} & \mathbf{0} & \mathbf{0} & \mathbf{0} & H_{amb}^{q1} & \dots & \dots \\ \vdots & & \vdots & \vdots & \vdots & \vdots & \vdots & \vdots & \vdots & \vdots & \vdots \\ H_{r,v}^{qn} & \mathbf{0} & H_{T}^{qn} & \mathbf{0} & H_{clk}^{qn} & \mathbf{0} & \mathbf{0} & \mathbf{0} & \dots & \dots & H_{amb}^{qn} \end{bmatrix} \tag{6.22}$$

with

$$H_{r,v}^{p} = \begin{bmatrix} H_{\varphi}^{p} & H_{\lambda}^{p} & H_{h}^{p} & 0 & 0 & 0 \\ H_{\varphi}^{p} & H_{\lambda}^{p} & H_{h}^{p} & 0 & 0 & 0 \\ 0 & 0 & 0 & H_{v_N}^{p} & H_{v_E}^{p} & H_{v_U}^{p} \end{bmatrix} \tag{6.23}$$

where $[H_{v_N}^{p}\ H_{v_E}^{p}\ H_{v_U}^{p}]^T$ is the line of sight of vector in a local frame (also see Equation (3.44)), which are the coefficients for the velocity parameters. H_T consists of the coefficients for ZTD and is a column vector with same elements for all range measurements lines. The measurement weight or noise matrix are set as Section 3.7.2.

6.4 Summary

The integration models of PPP and INS is presented in this chapter. The GPS/Galileo dual-frequency ionosphere-free PPP model using CNES uncombined bias products is used for integration. The selected PPP model is undifferenced but allows for phase ambiguity resolution. For the INS part both of the IMU biases and scale factors are estimated in the states. The integration models are based on forward filtering, thus are suited for real-time navigation scenario.

This study uses dual-frequency ionosphere-free PPP for the integration. It requires more investigation to evaluate the multi-frequency ionosphere-free PPP/INS integration using CNES bias products.

Chapter 7

Methodology for PPP/INS integration

7.1 Introduction

The integration of GNSS Precise Point Positioning (PPP) and Inertial Navigation System (INS) in the software level is a Kalman filtering process. Both the loosely-coupled integration (LCI) and the tightly-coupled integration (TCI) use INS error dynamics in Kalman prediction.The GNSS solutions and measurements are used for LCI and TCI measurement update respectively. This integration is realised using our internal software POINT.

This chapter is organised as follows: Section 7.2 presents the INS mechanization module of POINT and the newly developed PPP/INS integration structure; Section 7.3 presents the test settings for PPP/INS positioning including a test train and a test van; finally this chapter is summarised in Section 7.4.

7.2 The POINT software

The POINT software (Hide et al., 2007) already contains a module for INS. Multiple types of IMU sensors are supported including Crossbow IMU440CA, Honeywell HG1700AG62, Analogue Devices ADIS16350, Samsung Galaxy Tablet, Litef LCI. A profile is defined for each of these IMUs, which gives the IMU specifications.

7.2.1 INS implementation in POINT

Figure 7.1 shows the INS mechanization in a local frame inside the POINT software.

Initialization

The Initialization module provides the initial position, velocity and attitude of body frame. The initial position and velocity values can be from GNSS or other sensors. The determination of initial attitude is also called alignment, which aligns the initial body frame with respect to a local navigation frame. There are different types of alignment methods including static alignment and dynamic alignment. The coarse alignment and fine alignment are usually used for static alignment. The dynamic alignment is usually achieved using a Kalman filter Hide (2003).

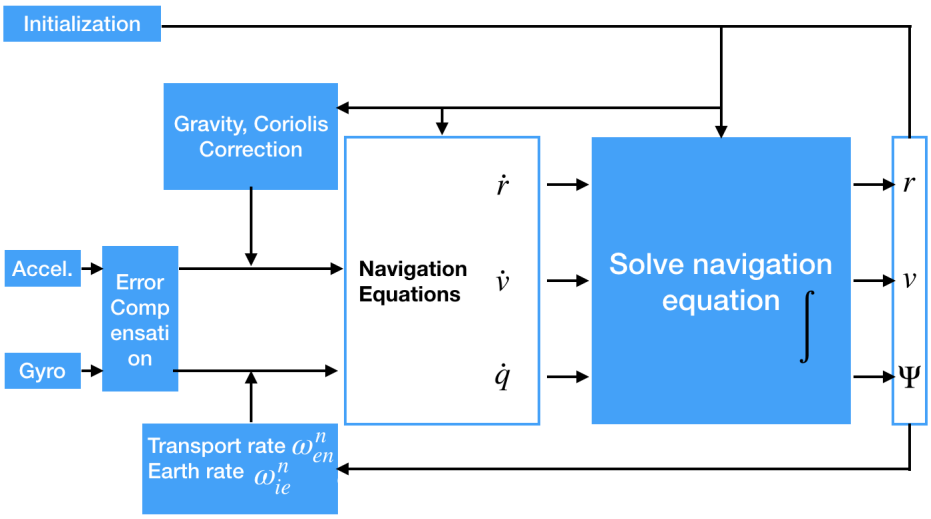

Figure 7.1: *INS mechanization in local frame*

A coarse alignment for the initial roll and pitch angles by comparing the accelerometers measurements with the modeled gravity vector can be computed as:

$$\begin{aligned} \phi &= atan2(-f_y, f_x) \\ \theta &= atan2(f_x, \sqrt{f_y^2 + f_z^2}) \end{aligned} \tag{7.1}$$

where the acceleromter measurement vector is denoted as $f^b = [f_x\ f_y\ f_z]^T$. If the gyro measurements are also used, the DCM matrix between navigation

frame and vehicle body frame can be determined in a static mode with (Shin, 2001):

$$C_b^n = \begin{bmatrix} \frac{-tan\varphi}{\gamma} & \frac{1}{\omega_e cos\varphi} & 0 \\ 0 & 0 & \frac{-1}{\gamma\omega_e cos\varphi} \\ \frac{-1}{\gamma} & 0 & 0 \end{bmatrix} \begin{bmatrix} (f^b)^T \\ (\omega_{ib}^b)^T \\ (f^b \times \omega_{ib}^b)^T \end{bmatrix} \tag{7.2}$$

where γ is the normal gravity vector. Then by transforming the DCM matrix to the Euler angles, the vehicle attitude can be determined as

$$\begin{aligned} \phi &= atan2(c_{32}, c_{33}) \\ \theta &= -tan^{-1}(\frac{c_{31}}{\sqrt{1-c_{31}^2}}) \\ \psi &= atan2(c_{21}, c_{11}) \end{aligned} \tag{7.3}$$

where $c_{i,j}$ with i,j = 1,2,3 is the element of C_b^n.

For low-cost IMU sensors the earth rate cannot be detected and external yaw solution from a compass output or a dual-antenna GPS receiver needs to be used.

Gravity model

The normal gravity on the reference ellipsoid surface is computed as:

$$\gamma = \gamma_a \frac{1 + \frac{b\gamma_b - a\gamma_a}{a\gamma_b} sin^2\varphi}{\sqrt{1 - \frac{a^2-b^2}{a^2} sin^2\varphi}} \tag{7.4}$$

where φ denotes the geodetic latitude; γ_a and γ_b are the gravity at the equator and the pole. a and b are the semi-major and semi-minor axes of the ellipsoid. The gravity γ_h above the ellipsoid with height h is expressed as:

$$\gamma_h = \gamma[1 - \frac{2}{a}(1 + f + m - 2fsin^2\varphi)h + \frac{3}{a^2}h^2] \tag{7.5}$$

where f is the ellipsoid flattening; m is a ratio between the centrifugal force at equator and the gravity at equator. For more explanations on the normal gravity, readers are directed to Heiskanen and Moritz (1967). The POINT software computes the gravity using the WGS84 ellipsoid parameters.

Error compensation

The POINT software uses a closed-loop INS error compensation. The gyro accelerometer measurements are compensated as:

$$\begin{bmatrix}\omega_x\\ \omega_y\\ \omega_z\end{bmatrix} = \begin{bmatrix}s_{g_x} & 0 & 0\\ 0 & s_{g_y} & 0\\ 0 & 0 & s_{g_z}\end{bmatrix}\begin{bmatrix}\omega_x\\ \omega_y\\ \omega_z\end{bmatrix} + \begin{bmatrix}b_{g_x}\\ b_{g_y}\\ b_{g_z}\end{bmatrix} \tag{7.6}$$

$$\begin{bmatrix}f_x\\ f_y\\ f_z\end{bmatrix} = \begin{bmatrix}s_{ax} & 0 & 0\\ 0 & s_{ay} & 0\\ 0 & 0 & s_{az}\end{bmatrix}\begin{bmatrix}f_x\\ f_y\\ f_z\end{bmatrix} + \begin{bmatrix}b_{ax}\\ b_{ay}\\ b_{az}\end{bmatrix} \tag{7.7}$$

where the subscripts x, y and z indicate the components along the IMU axes. At each epoch the errors of the accelerometer and gyro biases are estimated in the filter and corrected to the bias values before next epoch. The scale factor estimation has the same procedure.

Conversion of attitude expression

The attitude in POINT is represented in both cosine direction matrix (DCM) or coordinate transformation matrix and quaternion. The DCM is mainly used in the computation of reference frame transformation while the attitude quaternion form is used in the navigation euqations. The conversion between the two attitude representations is as follows:

$$\begin{aligned} q_0 &= \frac{1}{2}\sqrt{1 + C_{1,1} + C_{2,2} + C_{3,3}}, & q_1 &= \frac{C_{2,3} - C_{3,2}}{4q_0}\\ q_2 &= \frac{C_{3,1} - C_{1,3}}{4q_0}, & q_3 &= \frac{C_{1,2} - C_{2,1}}{4q_0} \end{aligned} \tag{7.8}$$

$$\begin{aligned} &C_{1,1} = q_0^2 + q_1^2 - q_2^2 - q_3^2,\ C_{2,2} = q_0^2 - q_1^2 + q_2^2 - q_3^2,\ C_{3,3} = q_0^2 - q_1^2 - q_2^2 + q_3^2\\ &C_{1,2} = 2(q_1q_2 + q_3q_0),\ C_{2,1} = 2(q_1q_2 - q_3q_0)\\ &C_{1,3} = 2(q_1q_3 - q_2q_0),\ C_{1,3} = 2(q_1q_3 + q_2q_0)\\ &C_{2,3} = 2(q_2q_3 + q_1q_0),\ C_{3,2} = 2(q_2q_3 - q_1q_0) \end{aligned} \tag{7.9}$$

Numerical solutions of navigation equations

The INS navigation equations of Equation (7.3) are solved using the 2nd-order Runge-Kutta Methods. More examples of this numerical method can be found in Chapter 25 of Chapra and Canale (2014).

7.2.2 Newly developed features

Thanks to the well-implemented INS module in POINT, the integration of INS and PPP can be achieved easily. For both tight and loose integration the PPP model with uncombined bias correction is used, which allows for the ambiguity resolution in zero-differenced form.

PPP/INS loosely coupled integration

The PPP/INS LCI diagram in POINT is showed in Figure 7.2. The aligned INS and PPP solutions are integrated in the LCI module, which estimates the error states using Kalman filter. At the user end, three types of solutions are available: INS, PPP, and PPP/INS LCI. The PPP module can output the ambiguity-fixed solutions and thus LCI also supports the integration with the ambiguity resolution.

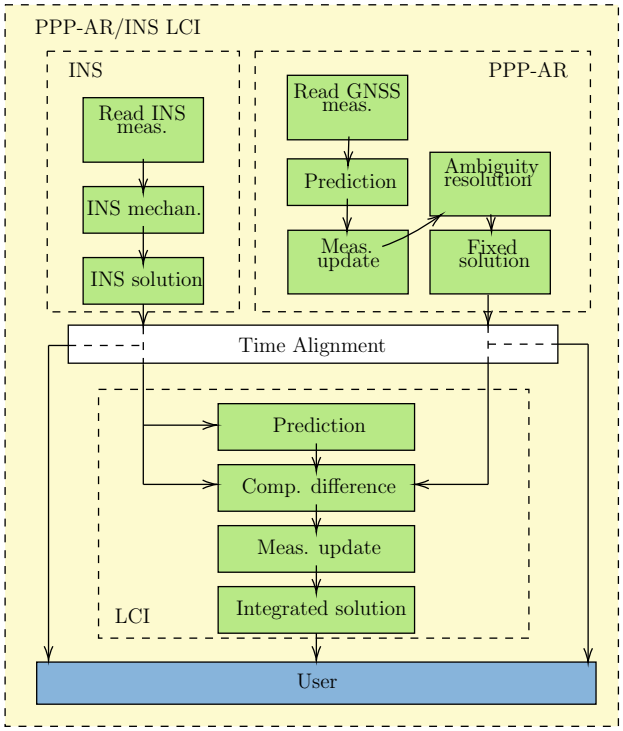

Figure 7.2: *The structure of PPP/INS loosely-coupled integration in POINT*

PPP/INS tightly coupled integration

The PPP/INS TCI structure is presented in Figure 7.3. When the GNSS measurements are aligned with the INS solutions, TCI predicts the states using the INS solutions. The linearization of satellite-receiver geometric distance is also evaluated at the predicted position with the correction of IMU center to the antenna lever arm. AR is also supported after measurement update. At the user side, INS-only and TCI solutions are available.

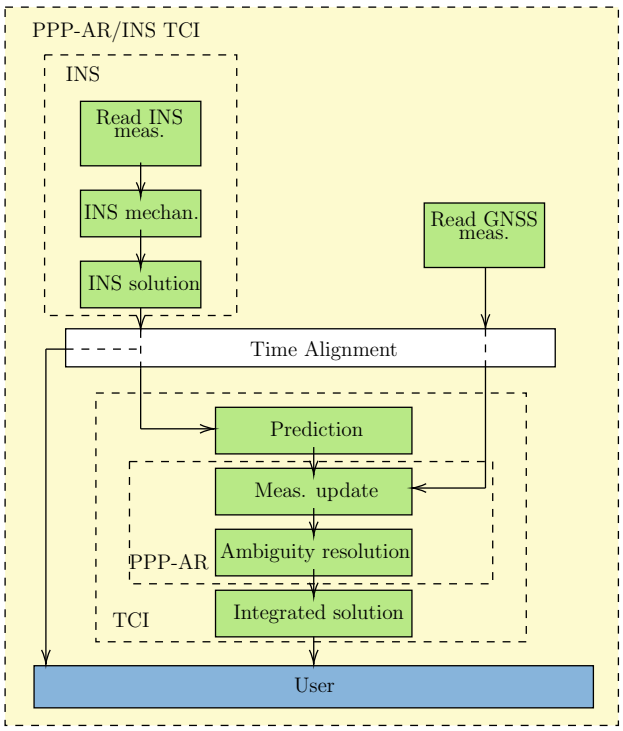

Figure 7.3: *The structure of PPP/INS tightly-coupled integration in POINT*

7.3 Data sources and test setting

7.3.1 NGI test train

An electric train that runs on the roof of Nottingham Geospatial Building (NGB) is a specially designed teaching and research facility at Nottingham Geospatial Institute (NGI) for precise positioning test. The left of Figure 7.4 gives a view of the train and the right is a plan of the track of the train. The triangles in the plan are a series of precisely measured control points, among which the NGB2 permanent station with known coordinates is used as base for computing RTK (Real-Time Kinematic) reference solutions.

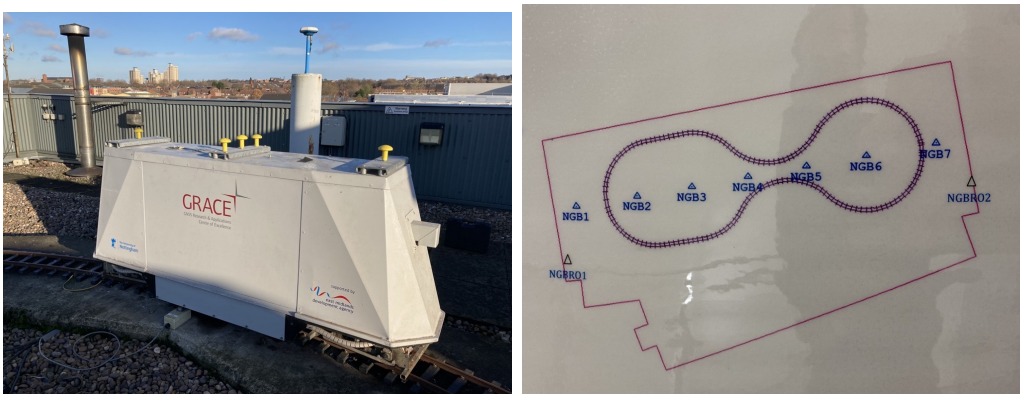

(a) *train* **(b)** *train track*

Figure 7.4: *NGI train facility*

Sensor configuration

The LEICA GS10 (Leica-Geosystems-AG, 2016) GNSS receiver is used for collecting GNSS measurements. It can track GPS L1/L2/L5 and Galileo E1/E5a/E5b signals. The Novatel SPAN UIMU-LCI (Novatel-SPAN-UIMU-LCI, 2014) is used for measuring acceleration and rotation, which is a tactical grade IMU. The installation of these sensors is shown in Figure 7.5. The GNSS signal from the LEICA AS10 antenna is split into two routes: one is connected to the LEICA GS10 and the other to the SPAN GNSS receiver, which is also connected to the IMU. This connection synchronizes the GNSS and inertial measurements to the GPS time frame. The purpose of the signal split is to enable the SPAN IMU integration with external GNSS receiver e.g. LEICA GS10, instead of using its internal GNSS receiver, , so that various advanced algorithm could be tested.

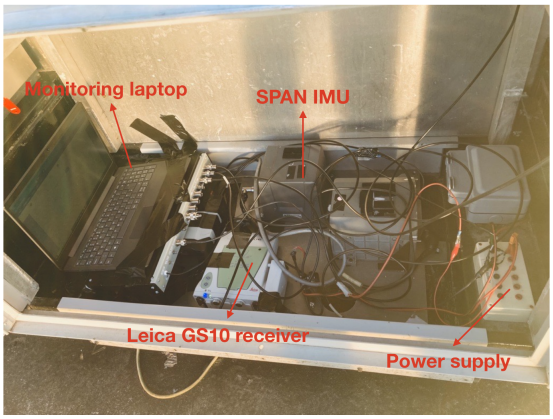

Figure 7.5: *Sensor installation*

Table 7.1 lists the sensor sampling rates, lever arm and installation angle. The installation angle is applied to the raw inertial measurements to align the IMU axes to the train frame. After alignment, the lever arm which is measured in the train frame is applied to correct the reference point from IMU origin to the GNSS antenna center. The train Y-axis is towards its front and the Z-axis towards up and the X-axis forms the right-hand rule. Table 7.2 is the technical specifications of IMU sensors.

Table 7.1: Sensor sampling rates, lever arm and installation angles of train test

GNSS data rate	10 Hz
IMU data rate	200 Hz
Installation angle	180 ° (roll), 0 ° (pitch), 0 ° (yaw) from IMU frame to vehicle frame
Lever arm	0.783 m, 0.156 m, -1.011 m

Table 7.2: Specifications of IMU sensors

Gyro rate bias	$0.5°/hr$
Angular random walk	$0.15°/\sqrt{hr}$
Gyro rate scale factor	100 ppm
Accel. bias	$<$1.0 mg
Accel. scale factor	250 ppm

7.3.2 NGI test van

A survey van as shown in Figure 7.6 is another teaching and research facility at Nottingham Geospatial Institute (NGI) supporting the collection of different types of data such like GNSS, INS, wheel sensor and camera. GNSS antennas can be attached on the top frame.

Figure 7.6: *NGI survey van*

Sensor configuration

The LEICA GS10 and Novatel SPAN UIMU-LCI are used to collect GNSS and IMU data respectively as in Chapter 8. A spliter is also used for the time synchronization of the two sensors. The IMU data is saved on board of the SPAN GNSS receiver as shown in Figure 7.7:

(a) *Novatel SPAN receiver* **(b)** *Novatel SPAN UIMU-LCI*

Figure 7.7: *Sensor instellation*

Table 7.3 lists the sensor sampling rates, lever arm and installation angle.

Table 7.3: Sensor sampling rates, lever arm and installation angles of van test

GNSS data rate	1 Hz
IMU data rate	200 Hz
Installation angle	180 ° (roll), 0 ° (pitch), 0 ° (yaw) from IMU frame to vehicle frame
Lever arm	-0.626 m, 0.307 m, -0.543 m

7.3.3 Reference software

RTKLIB

The post-processed relative positioning solutions with base the NGB2 station (see Figure 7.4) and rover the LEICA GS10 on board of either train or van are used to provide the reference solution, which was computed using the open-source RTKLIB software (Takasu, 2009) with basic settings as listed in Table 7.4:

Table 7.4: RTKLIB setting for reference computation

Ephemeride	IGS GNSS Broadcast ephemeris
Constellation	GPS, Galileo
Frequency	L1+L2
Ionosphere	OFF
Troposphere	OFF
Filter	Forward & Backward combined
Antenna PCO/PCV	igs14_2188.atx For both satellites and base and rover antennas

Inertial Explorer

The Inertial Explorer (IE) is a commercial software that is developed by the NovAtel company. It can compute GNSS solutions including differential positioning and PPP, LCI and TCI. For each positioning mode, it also supports forward and backward smoothing. The IE solutions have different quality state as shown in Figure 7.8.

GNSS Quality Number Description

Quality	Color	Description	3D Accuracy (m)
1	Green	Fixed integer	0.00 – 0.15
2	Cyan	Converged float or noisy fixed integer	0.05 – 0.40
3	Blue	Converging float	0.20 – 1.00
4	Purple	Converging float	0.50 – 2.00
5	Magenta	DGPS	1.00 – 5.00
6	Red	DGPS	2.00 – 10.00
Unprocessed	Grey	Has not been processed	N/A

Figure 7.8: *Inertial Explorer solution quality state number indication. Source: NovAtel (2022)*

7.3.4 Results evaluation

The POINT computed solutions and the reference solutions are transformed to a local NEU frame similar to Chapter 4. Then positioning errors are obtained by making the difference of the computed and the interpolated reference solutions.

The error RMS is computed for accuracy evaluation instead of the 68th percentile as the number of test sessions is very limited compared to Chapter 4. See Figure 8.9 for an example. The 68th-percentile errors are also computed. See Table 8.2, Table 8.3 and Table 8.4.

7.4 Summary

This chapter presents the software tool POINT and test settings for PPP/INS LCI and TCI positioning test. Based on our internal software POINT which is originally for RTK/INS integration, the new feature for PPP/INS integration is developed. Our PPP model uses uncombined bias products allowing carrier-phase ambiguity resolution in the fusion with INS. The positioning tests use a test train and a test van with LEICA geodetic receiver and tactical IMU sensors onboard.

Chapter 8

Train positioning test

8.1 Introduction

This chapter investigates the real-time positioning performance of GPS/Galileo Precise Point Positioning (PPP) integrated with Inertial Navigation System (INS) through a train positioning test. Six positioning modes including PPP, PPP/INS loosely-coupled integration (LCI), PPP/INS tightly-coupled integration (TCI), PPP with ambiguity resolution (AR), PPP-AR/INS LCI and PPP-AR/INS TCI are evaluated. In particular, the real-time uncombined bias products from CNES are used for PPP ionosphere-free AR. This train positioning test has a good observability of GNSS satellites and could be able to achieve centimeter-level accuracy. Simulated GNSS signal gaps are also inserted in the data processing to show the benefit of the use of IMU measurements in the case of signal blockage.

This chapter is organized as follows: Section 8.2 gives an overview of the observation data. Section 8.3 presents a preliminary comparison between three reference solutions. Section 8.4 presents the PPP/INS integrated results. Section 8.5 shows the positioning performance with GNSS signal gaps. Finally the evaluation test is summarized in Section 8.6.

8.2 Observation data overview

8.2.1 Reference and trajectory

The train positioning test was conducted from 16:49 to 18:30 on 7 March in 2022. Figure 8.1 shows the trajectory of the reference solutions computed by RTKLIB (see 7.3.3) on the Google earth. The reference solutions uses a post-processed forward-backward combined differential positioning with the base NGB2 (see 7.3.1). 96.6% of the solutions are phase ambiguity-fixed.

Figure 8.1: *Reference solutions on Google Earth. Green, yellow and red points standard for fixed, float and single solutions respectively.*

Figure 8.2 is the time line of train state during the test. It takes about one minute for the train to complete a cycle along its track.

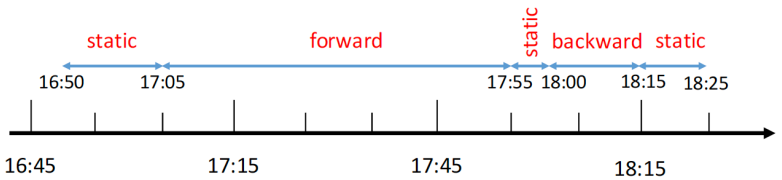

Figure 8.2: *Time line of train positioning test on 07/03/2022*

8.2.2 Satellite visibility and raw inertial data

Figure 8.3 shows that about 12 GPS/Galileo satellites are available during the test period. This satellite visibility suggests that high precision GNSS-only solutions should be available. Figure 8.4 is the decoded raw IMU data.

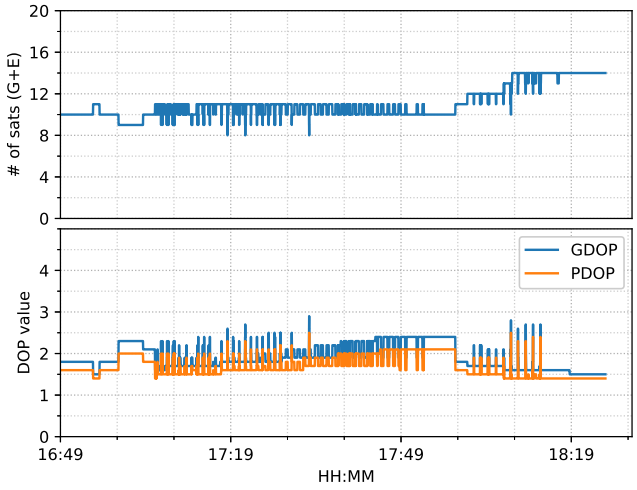

Figure 8.3: *GNSS satellite information of train test on 07/03/2022*

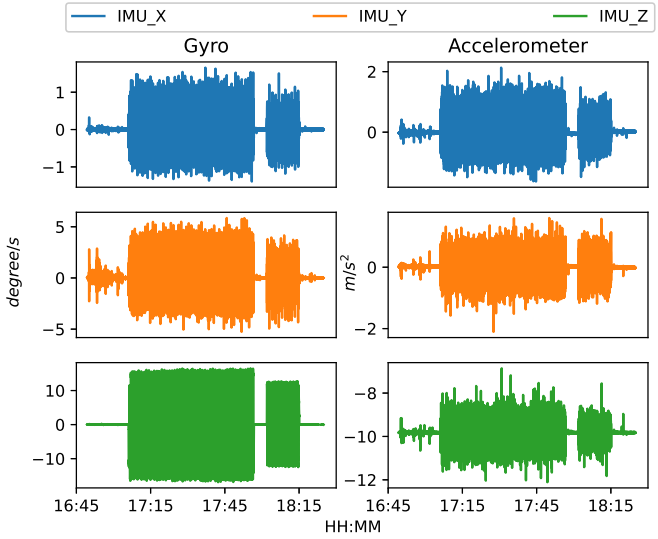

Figure 8.4: *Raw IMU measurements of train test on 07/03/2022*

8.3 Comparison of reference solutions

This section compares the data processing results from three sources: RTKLIB, Inertial Explorer (IE) and a PPP online service prior to the integration of PPP and INS.

The commercial IE software is used to generate smoothed GNSS differential positioning solutions and TCI solutions. The open-source software RTKLIB is also used to generate differential results. The RTK (Real-time kinematic)is simply used to refer to this precise differential positioning technique in spite of post-processing. From Figure 8.5, it can be seen that during the static periods, IE RTK solutions are consistent well with the IE TCI results, of which the difference is within 1 *cm*; while the difference becomes noisy as the train moves, which is around 3 *cm*. The RTKLIB RTK solutions are more aggregated in the kinematic states with respect to IE RTK, of which the major difference is around 2 *cm*.

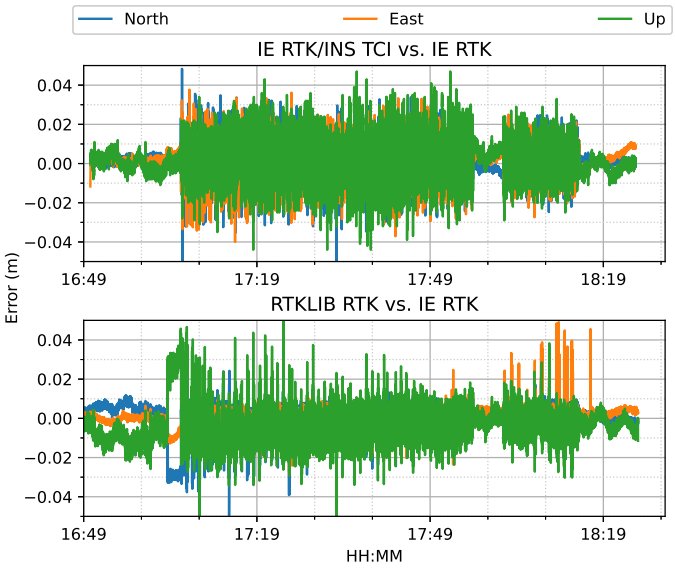

Figure 8.5: *Comparison of reference solutions*

The measured train data is also processed by using the CNES online PPP service (Laurichesse, 2010). Its PPP service can provide post-processed PPP solutions with AR in a NMEA output format. Figure 8.6 is PPP accuracy with respect to the RTKLIB RTK solutions. It shows that the north and up error

components clearly are biased from the middle static period by more than 10 *cm* but recover to high accuracy at the end. This abnormal drift still needs further investigation as the detailed data processing strategy is not provided in the online PPP service.

Figure 8.7 shows that the estimated receiver clock bias fluctuate upwardly from around 17:55.

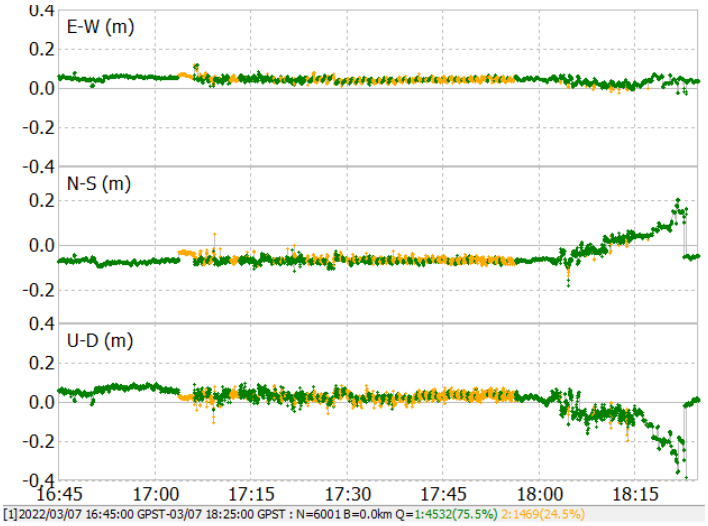

Figure 8.6: *Train positioning results processed by CNES online PPP service. Generated by RTKLIB*

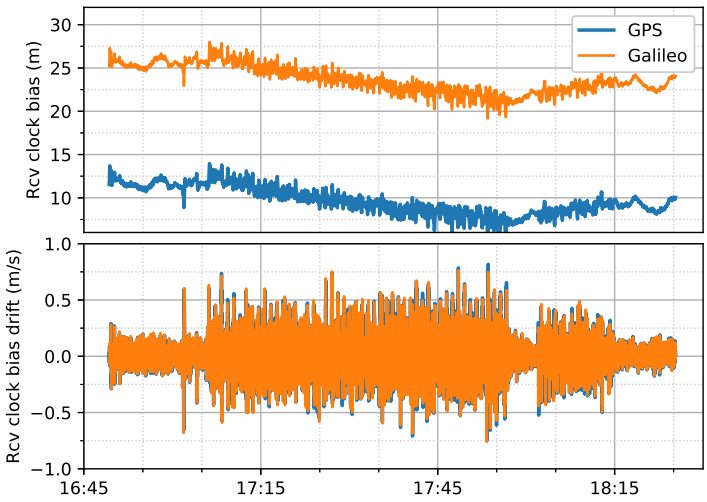

Figure 8.7: *Estimated GPS/Galileo receiver clock bias and drift of train positioning test on 07/03/2022 by POINT*

8.4 PPP/INS results

This section presents the real-time GPS/Galileo PPP/INS integrated results with the measured train data. The ionosphere-free PPP model is selected for the integration as the unknown ionospheric could cause difficulty in tuning the Kalman filter to obtain the optimal integrated solutions. The GPS and Galileo doppler measurements on the L1/E1 frequency are used for velocity estimation with the noise of 5 cm/s. The CNES real-time uncombined bias products are applied to the GNSS code and phase measurements before forming the dual-frequency ionosphere-free combination to enable the estimation of integer phase ambiguities.

The Bootstrapping method is used for phase ambiguity resolution (AR). This method starts fixing the ambiguity with the minimal variance first and then updates the float solutions and fixes the remaining ambiguities iteratively. The ambiguity-fixing conditions for the estimated float widelane (WL) and narrowlane (NL) ambiguities are listed in Table 8.1. Only the ambiguities with conditions in Table 8.1 satisfied are fixed, therefore partial ambiguity resolution (PAR) is enabled in the results. To mitigate the effect of wrong ambiguity fixing, the ambiguities are resolved independently at each epoch.

Table 8.1: Ambiguity-fixing conditions for train test on 07/03/2022

Minimal time of tracking	WL: 1 min, NL: 25 min
Maximal ambiguity precision	0.25 $cycles$
Maximal ambiguity residual	0.25 $cycles$

8.4.1 Positioning accuracy evaluation

The positioning results of six positioning modes are demonstrated in Figure 8.8.

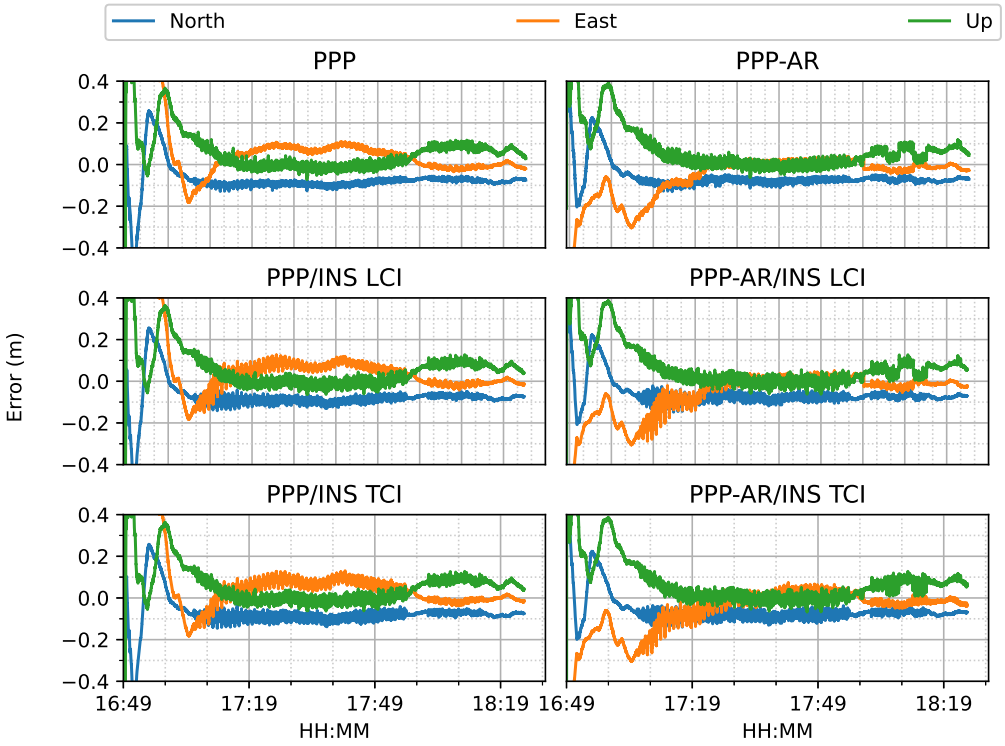

Figure 8.8: *PPP/INS results of the train positioning test on 07/03/2022 with respect to IE RTK solutions*

It can be seen that for both ambiguity-float (left column) and ambiguity-fixed (right column) solutions, the integrated results conform well with the PPP-only solutions. The converged PPP results maintain high positioning accuracy of within 10 *cm* during the test period mainly because of the good satellites visibility as indicated in Figure 8.3. With phase ambiguity resolution the east component of the three fixed solutions achieves noticeable improvement compared with the related left part. However all the solutions still require approximately 25 *min* to obtain converged solutions. There is no substantial improvement in convergence time in the integrated solutions in this case.

The positioning error RMS of each mode is given in Figure 8.9. It clearly shows that the ambiguity-fixed solutions has higher accuracy in all directions than the ambiguity-float results. The ambiguity-float LCI and TCI solutions are almost identical to the PPP accuracy; PPP-AR outperforms the ambiguity-fixed LCI and TCI but it has smaller sample size.

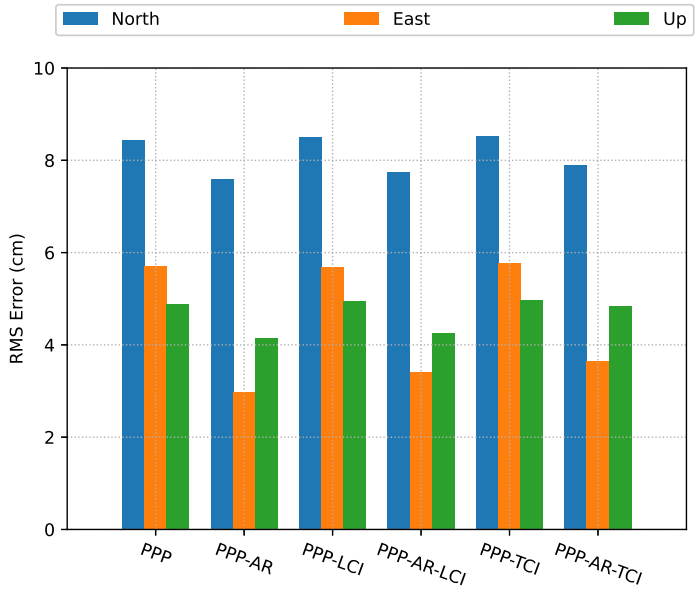

Figure 8.9: *PPP/INS positioning error RMS of the train test on 07/03/2022 with respect to IE RTK solutions*

The detalied statistics of the six modes solutions are listed in Table 8.2, Table 8.3 and Table 8.4. All the PPP/INS solutions obtain an accuracy below 10 *cm* in each direction. After AR, all the solutions achieve significant improvements in all components, which are around 9%, 9% and 7% for the North component, 47%, 40% and 38% for the East component and 14%. 12% and 4% for the height component, for PPP-AR, PPP-AR/INS LCI and PPP- AR/INS TCI respectively. In this open-sky environment, the accuracy of PPP/INS loose and tight integration is indeed close. The relatively low improvement of the TCI could be caused by the improper setting of the weighing scheme for code and phase measurements as well as the IMU sensor profile (e.g. gyro random walk noise) when tightly integrating the inertial data. It was found that this setting could greatly affect the integrated results. As a consequence, multiple tuning of Kalman filter stochastic modelling is required to obtain optimal solutions, which would hamper real-time applications. More investigation is required for the weighting scheme in TCI with AR.

Table 8.2: Statistics of GPS/Galileo PPP and PPP-AR results of the train test on 07/03/2022. Unit: *cm*

Statistics	PPP			PPP-AR		
	N	E	U	N	E	U
RMS	8.4	5.7	4.9	7.6	3.0	4.2
Mean	-8.4	4.0	2.6	-7.5	-0.8	2.6
Std.	1.2	4.1	4.1	0.9	2.9	3.3
68th Percentile	9.1	6.9	5.6	7.9	2.2	3.6

Table 8.3: Statistics of GPS/Galileo PPP/INS LCI and PPP-AR/INS LCI results of the train test on 07/03/2022. Unit: *cm*

Statistics	PPP/INS LCI			PPP-AR/INS LCI		
	N	E	U	N	E	U
RMS	8.5	5.7	4.9	7.7	3.4	4.3
Mean	-8.4	3.9	2.6	-7.6	-1.0	2.6
Std.	1.3	4.1	4.2	1.3	3.3	3.4
68th Percentile	9.0	6.8	5.7	8.1	2.3	3.9

Table 8.4: Statistics of GPS/Galileo PPP/INS TCI and PPP-AR/INS TCI results of the train test on 07/03/2022. Unit: *cm*

Statistics	PPP/INS TCI			PPP-AR/INS TCI		
	N	E	U	N	E	U
RMS	8.5	5.8	5.0	7.9	3.6	4.8
Mean	-8.4	4.0	2.6	-7.8	-1.2	2.9
Std.	1.5	4.2	4.2	1.4	3.4	3.8
68th Percentile	9.0	6.7	5.7	8.3	3.1	5.1

8.4.2 Ambiguity fixing status

Figure 8.10 shows the status of ambiguity fixing for each observed satellite during the train test. The IF ambiguity fixing starts after 25 *min*. More GPS satellites have fixed IF ambiguities while only 2 Galileo satellites have IF ambiguities fixed. The fixed ambiguities are not spread continuously along the tracking time, which is mainly caused by the fluctuation of the float NL ambiguities. This is demonstrated in Figure 8.11 and Figure 8.12.

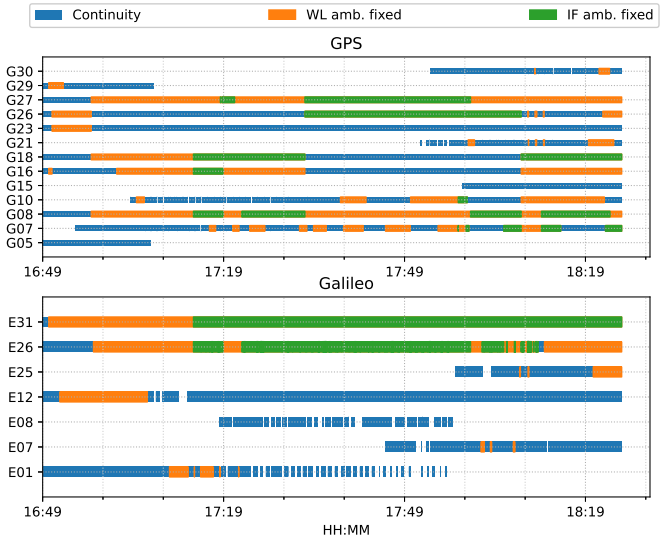

Figure 8.10: *Time span of observed satellites and the ambiguity fixing states of PPP-AR train positioning test on 07/03/2022*

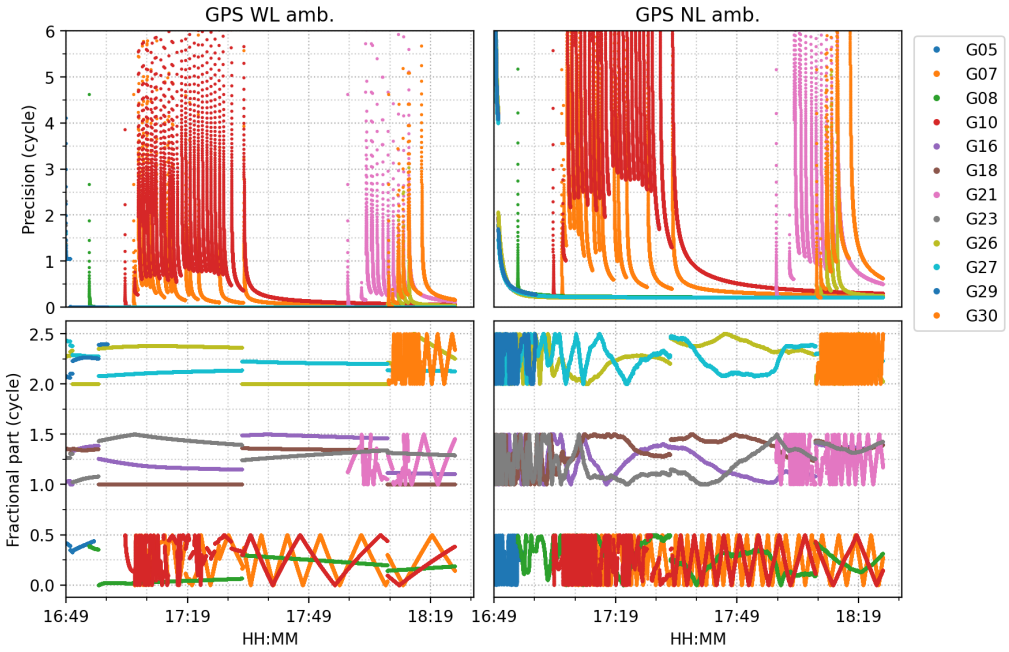

Figure 8.11: *Precision and fractional parts of estimated GPS WL and NL ambiguities of PPP-AR train positioning test on 07/03/2022*

It can be seen that the NL ambiguities requires longer time to converge than that of WL due to the shorter wavelength. As the ambiguities converge, the precision also becomes higher. The fixing criteria of these two factors are listed in 8.1.

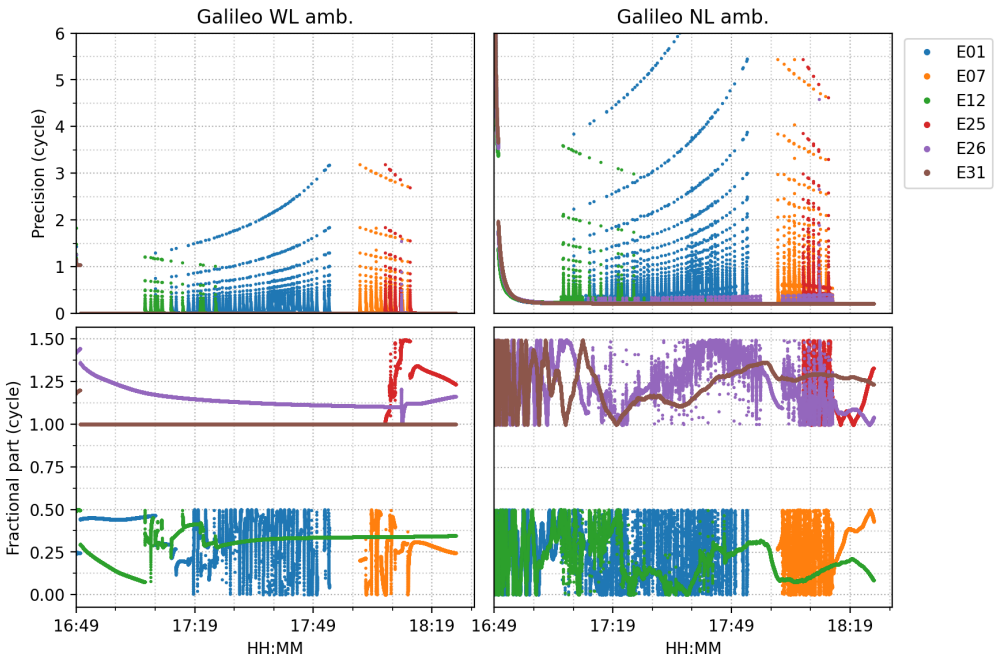

Figure 8.12: *Precision and fractional parts of estimated Galileo WL and NL ambiguities of PPP-AR train positioning test on 07/03/2022*

8.4.3 Velocity and attitude accuracy evaluation

Figure 8.13 shows the estimated velocity values. It can be seen that the velocities from doppler estimation are much more noisy than that of the integrated solution. The integrated velocity results have higher accuracy with nearly all components below 5 cm/s in Figure 8.14. It also shows that PPP AR slightly degrades the solutions which needs to be further studied.

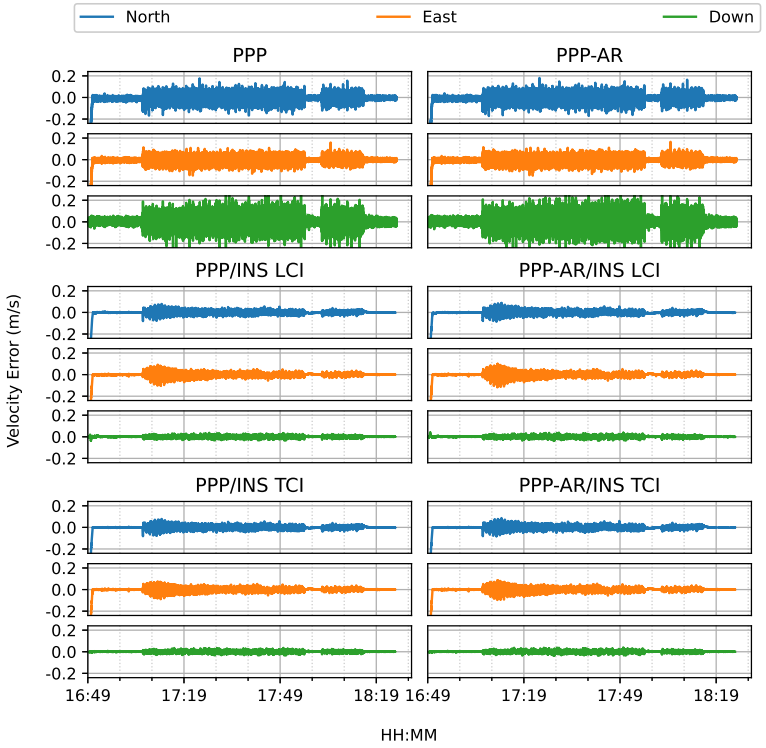

Figure 8.13: *Velocity errors of PPP/INS train positioning test on 07/03/2022 with respect to IE TCI*

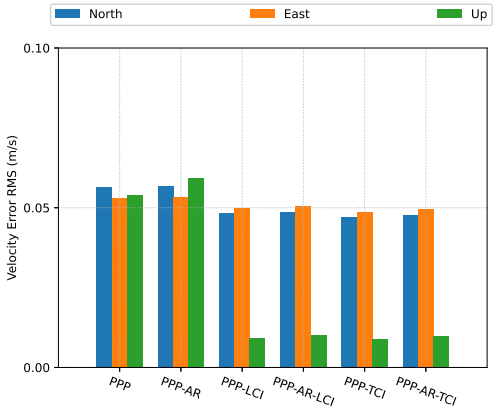

Figure 8.14: *PPP/INS positioning velocity error RMS of the train test on 07/03/2022 with respect to IE TCI solutions*

The heading direction in Figure 8.15 shows frequent spikes because the heading angles of the train contain dramatic changes in the movement along the curved path and the interpolated results will be also affected when comparing with the reference. The accurate heading determination requires additional alignment for this PPP/INS system. The roll and pitch errors are below 0.1 ° in Figure 8.16.

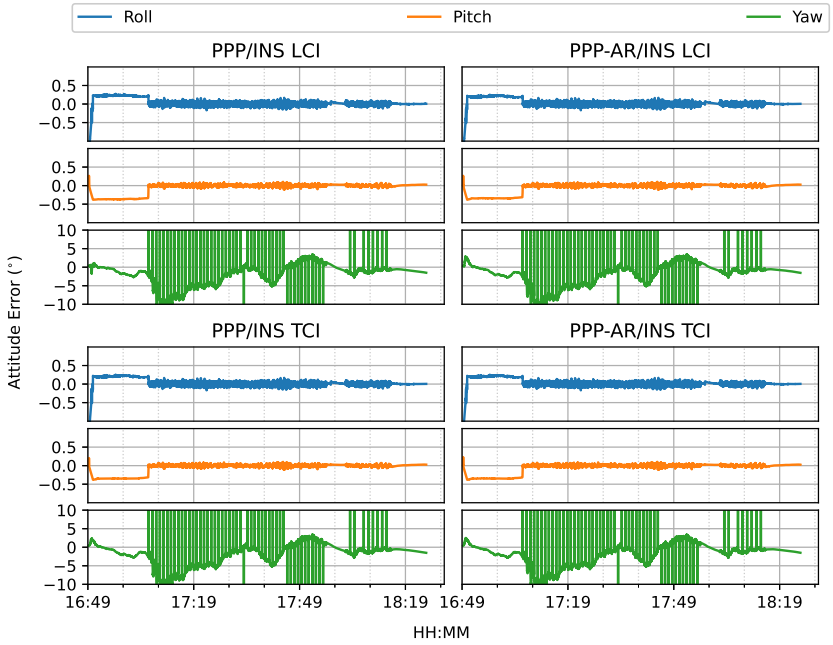

Figure 8.15: *Attitude errors of PPP/INS train positioning test on 07/03/2022 with respect to IE TCI*

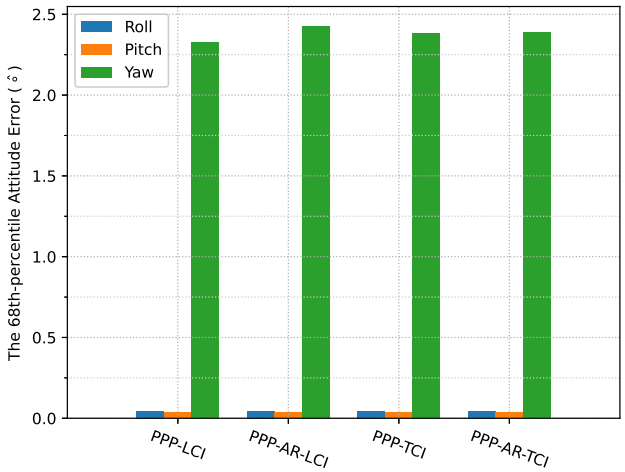

Figure 8.16: *PPP/INS positioning attitude error RMS of the train test on 07/03/2022 with respect to IE TCI solutions*

8.4.4 Estimates of IMU sensor biases and scale factors

Figure 8.17 and Figure 8.18 are the estimated biases of three gyros and three accelerometers, which indicate the performance of a typical tactical grade IMU.

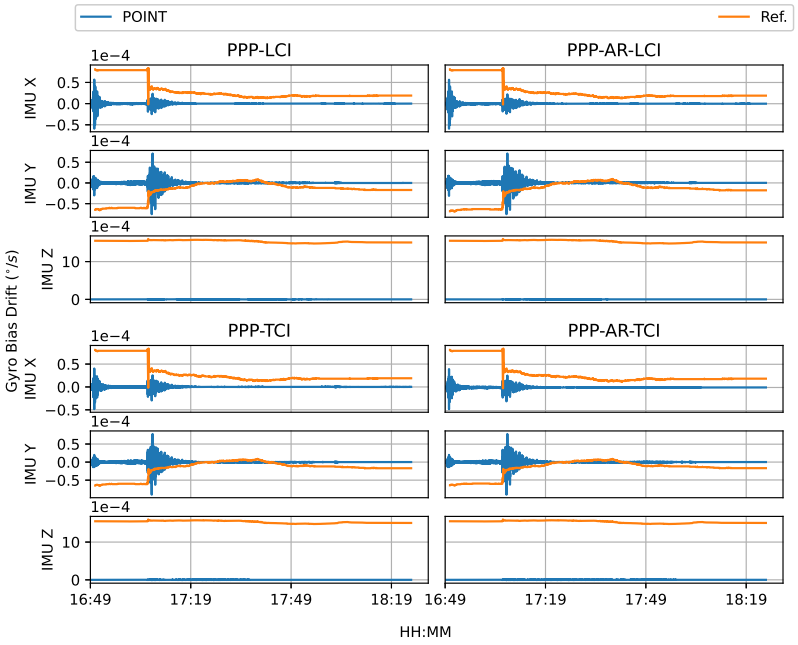

Figure 8.17: *Estimated gyro bias drift of PPP/INS train positioning test on 07/03/2022*

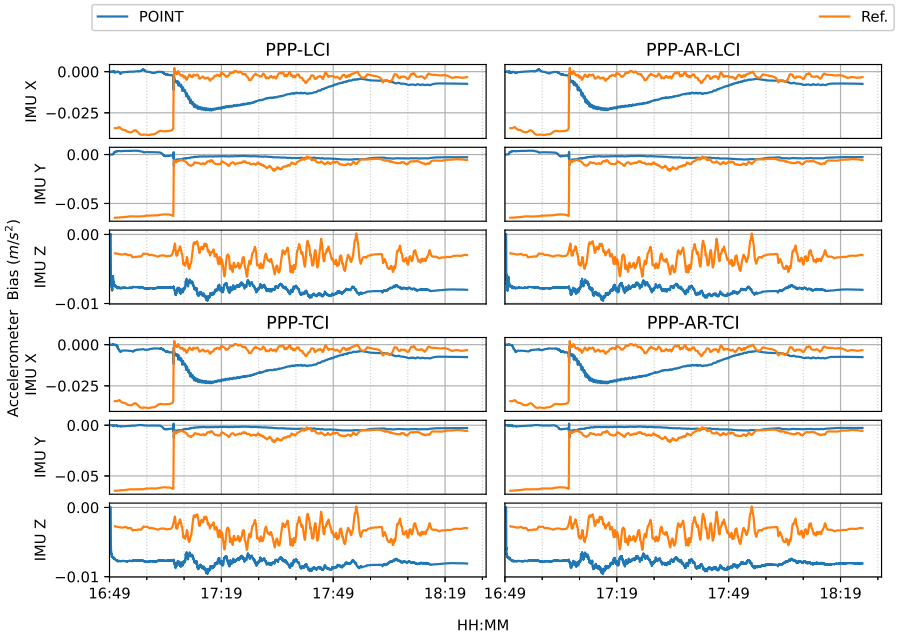

Figure 8.18: *Estimated accelerometer bias of PPP/INS train positioning test on 07/03/2022*

Figure 8.19 and Figure 8.20 are the estimated scale factor of the three gyros and three accelerometers. These parameters are in the vicinity of value one and optional for the navigation of tactical grade IMU. Groves (2013) stated that the lowest-cost sensors can exhibit significant scale factor asymmetry.

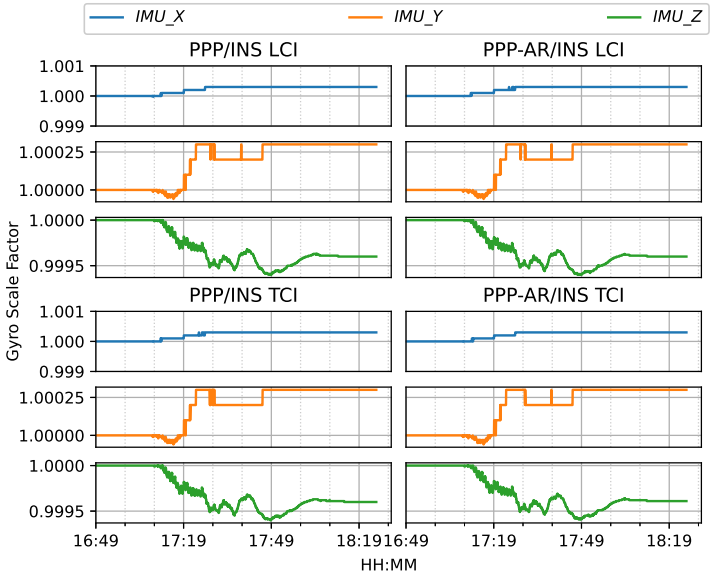

Figure 8.19: *Estimated gyro scale factor of PPP/INS train positioning test on 07/03/2022*

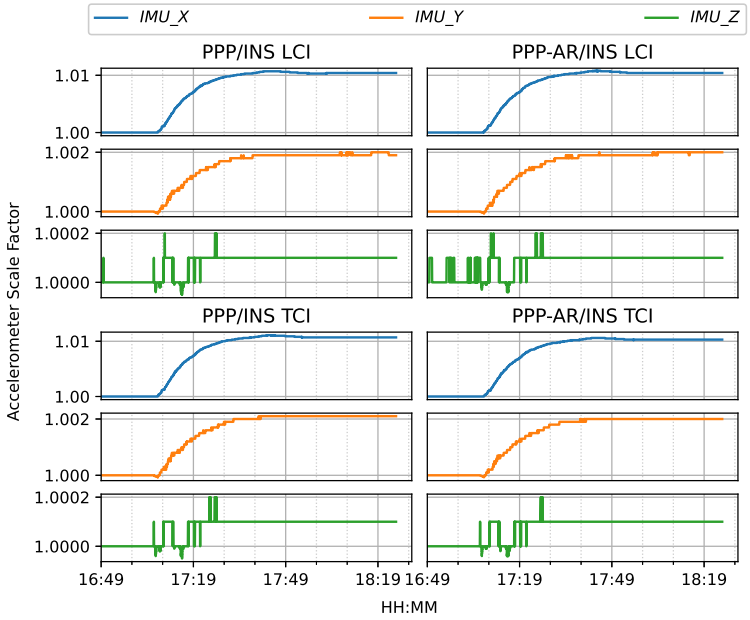

Figure 8.20: *Estimated accelerometer scale factor of PPP/INS train positioning test on 07/03/2022*

8.5 PPP/INS gap analysis

In this section, simulated GNSS signal gaps are inserted in the train measured data and the performance of the PPP/INS LCI and TCI modes are investigated during these gaps. Two gaps are added during the forward period, one gap for backward and one gap for static The gap length is set to one minute.

The Kalman measurement update is skipped during the gap and only the predicted solutions are output.

Figure 8.21 shows the positioning performance with the four inserted gaps. It can be seen that after each gap the solution has a reconvergence process due to the reset of all phase ambiguities. When the ambiguities remain the original state after gap, the solution can reconverge instantaneously. However this only works providing that no phase cycle slips occur during the gap.

Scaling up to the gap duration, the absolute positioning errors within each gap are presented in Figure 8.22. These solutions are Kalman predicted solutions after INS mechanization and the raw IMU measurements are corrected by the predicted gyro and accelerometer biases. It shows that the positioning drift during a one-minute gap in kinematic state can be more than 15 m in the north direction (e.g. gap3) while in static mode the horizontal drifts are around 2.5 m (e.g. gap4). It also suggests that within the first 10 seconds INS-only solution in a kinematic state can still remain high-accuracy results and in the static case this high-accuracy period can even be extended to more than 20 seconds.

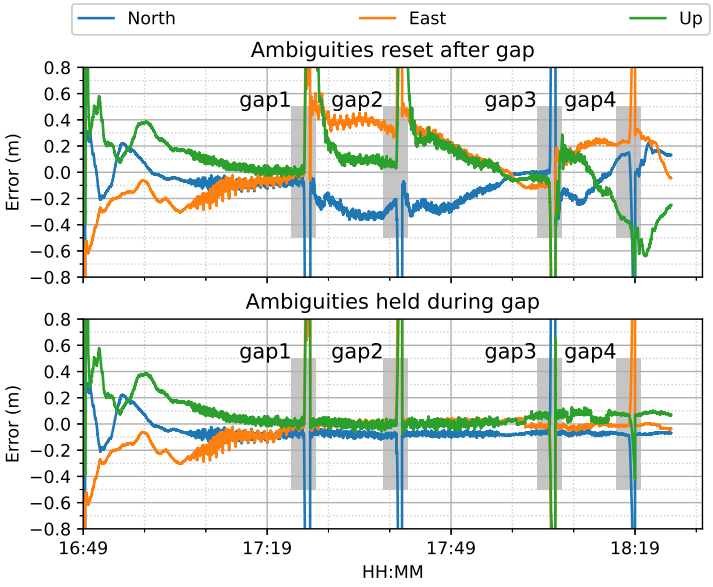

Figure 8.21: *PPP-AR/INS LCI performance of train test with different handling of phase ambiguities after each gap. The gap period is marked with grey shading.*

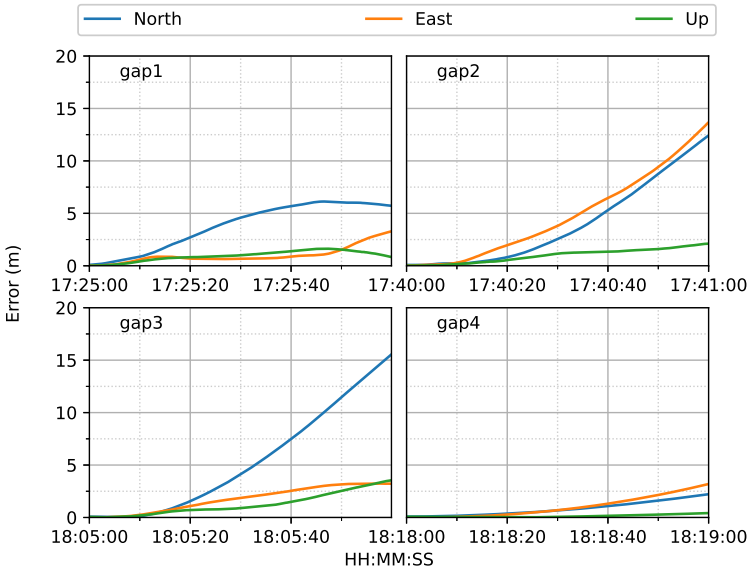

Figure 8.22: *Positioning results during four gaps*

The predicted accelerometer and gyro biases during the four gaps are depicted Figure 8.23 and Figure 8.24 respectively. It shows that the predicted accelerometer biases are constant within the four gaps but the reference bias values are varied except the static gap4 case. The reference gyro bias has non-zero constant drift in the IMU-Z axis direction during the gaps.

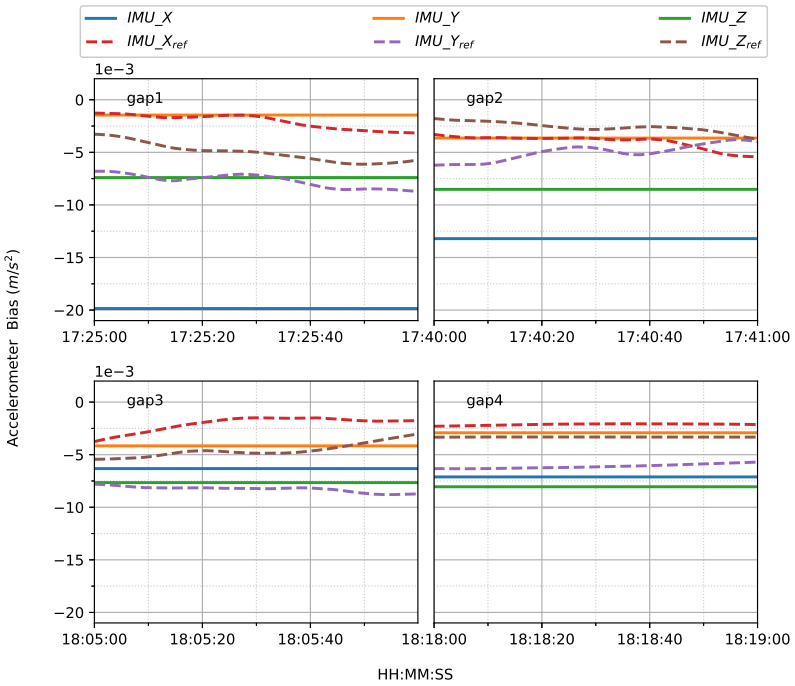

Figure 8.23: *Predicted accelerometer biases during GNSS measurement gaps*

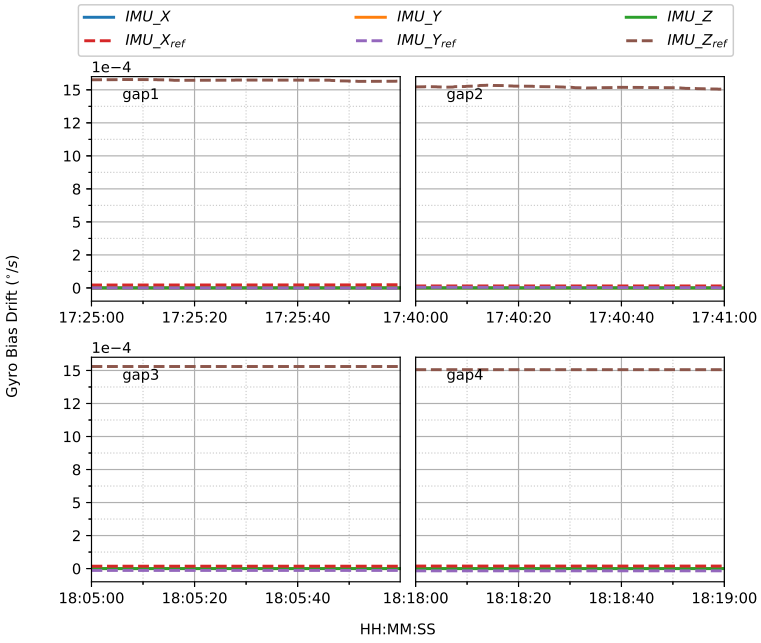

Figure 8.24: *Predicted gyro biases during GNSS measurement gaps*

Figure 8.25 shows the positioning performance with partial satellites available for each gap. It can be seen that the positioning errors are substantially reduced with the increased number of satellites. When scaling up to 1 m error threshold of y-axis in Figure 8.26, it is clear that the initial high-precision period can be extended longer with more satellites. The gap2 shows that the positioning errors are within nearly half meter over the 1-min gap after adding three satellites.

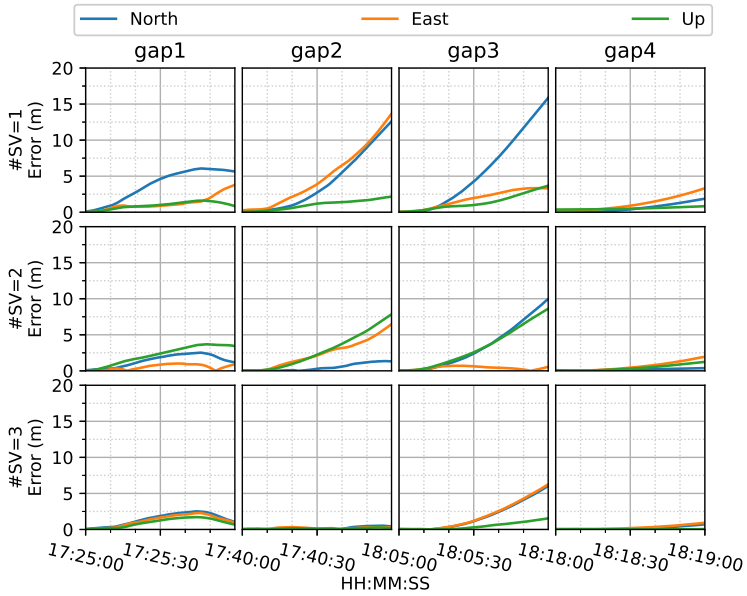

Figure 8.25: *PPP/INS TCI positioning performance with partial satellites available for all four gaps. Y limit is set to 20 m*

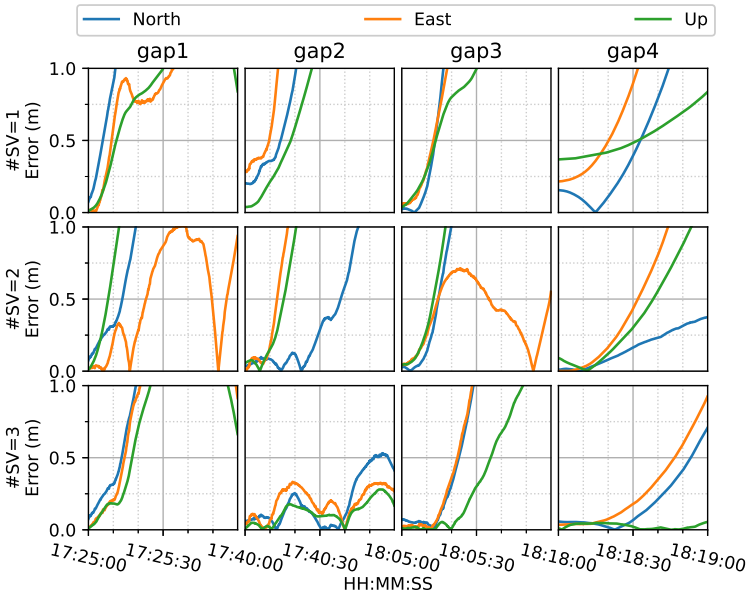

Figure 8.26: *PPP/INS TCI positioning performance with partial satellites available for all four gaps. Y limit is set to 1 m*

Figure 8.27 and Figure 8.28 show the changes of estimated gyro and accelerometer biases by the partial satellites measurements update. Only the static gap4 biases has marginally variations.

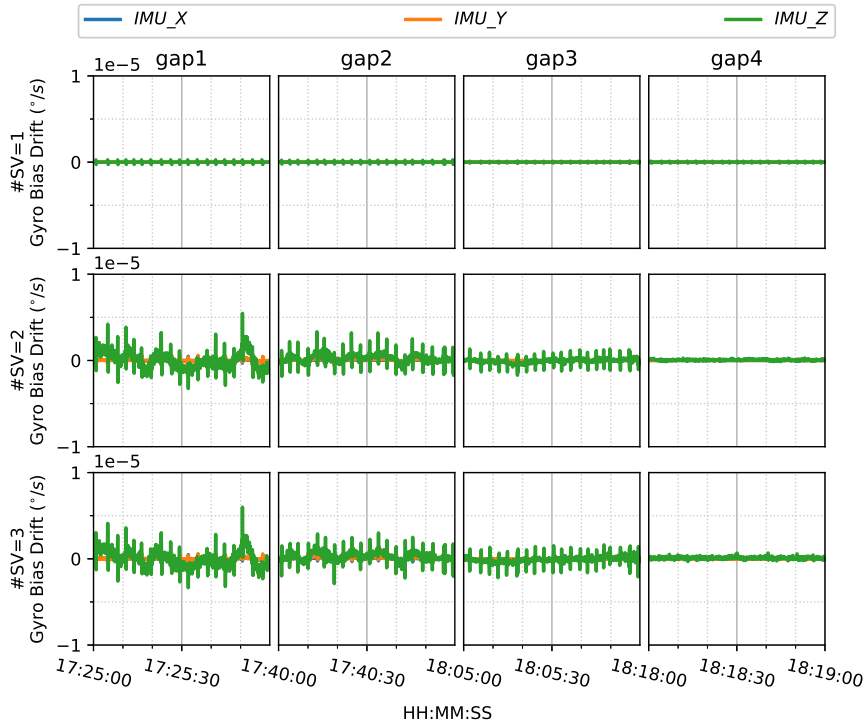

Figure 8.27: *Estimated gyro biases during gaps with partial satellites available*

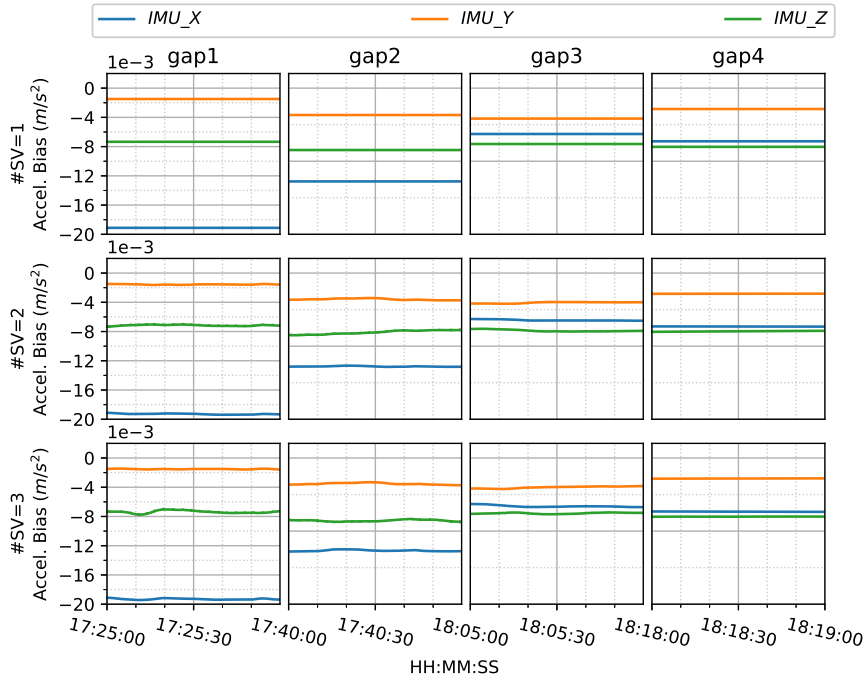

Figure 8.28: *Estimated accelerometer biases during gaps with partial satellites available*

8.6 Summary

This chapter highlights the application of uncombined bias products to PPP integrated with INS. we present real-time GPS/Galileo PPP/INS positioning results through a testing train in an open sky environment. The CNES real-time orbit, clock and bias products are used for PPP and PPP with ambiguity resolution (AR). The dual-frequency ionosphere-free PPP model is selected for the integration with the inertial data. Based on our internal software POINT, results of six positioning modes are presented with respect to the Inertial Explorer TCI solutions. It is found that ambiguity-float PPP has almost identical performance with LCI and TCI, which can reach an accuracy of 8.5, 5.7 and 4.9 *cm* in the north, east and up direction respectively. After AR, all the solutions achieve significant improvements in all components, which are around 9%, 9% and 7% for the North component, 47%, 40% and 38% for the East component and 14%. 12% and 4% for the height component, for PPP-AR, PPP-AR/INS LCI and PPP- AR/INS TCI respectively.

The GNSS signal has good continuity during the train test and about 12 GPS/Galileo satellites are visible. Under this good observation condition, the benefit of additional inertial measurements to the positioning results is not significant. So, four simulated one-minute gaps are inserted in the GNSS data to investigate the positioning drift. The results show that in kinematic state the drift can be more than 15 m in the north direction while in static mode the horizontal drifts are around 2.5 m. Within the first 10 seconds INS-only solution in a kinematic state can still remain a high accuracy of around 30 *cm* and in the static case this high-accuracy period can be as long as more than 20 seconds. With the increased number of satellites, the positioning errors are substantially reduced. In kinematic state, positioning errors could be nearly within half meter over the 1-min gap after adding three satellites.

It is also found that in PPP-AR/INS TCI the weighting scheme of code and phase measurements can have non-negligible impact on the positioning er-

rors, which requires further investigation. Also the real-time PPP results are expected to have further improvement when precise external information(e.g ionosphere) is added which needs to be assessed, especially with the integration of INS.

Chapter 9

Van positioning test

9.1 Introduction

This chapter investigates the real-time GPS/Galileo Precise Point Positioning (PPP) integrated with Inertial Navigation System (INS) through a van positioning test around city center streets and complex road layouts. Unlike the good GNSS observability in the train test in Chapter 8, frequent signal blockages occur in this van positioning test due to vegetation, bridges and city canyon. As a consequence of the signal interruption or low satellite availability, the PPP solution filter could have frequent reconvergences, which will degrade the positioning accuracy significantly. With the aiding of INS, either loosely-coupled integration (LCI) or tightly-coupled integration (TCI), the PPP divergence in the gap could be mitigated, and better positioning results would be expected. Like the previous chapter, six positioning modes: PPP, PPP/INS LCI, PPP/INS TCI, PPP with ambiguity resolution (AR), PPP-AR/INS LCI and PPP-AR/INS TCI are evaluated.

This chapter is organized as follows: Section 9.2 presents a brief description of the test. Section 9.3 and Section 9.4 present the PPP/INS testing results in the complex road and city center respectively. Section 9.5 summarises the positioning performance of this chapter.

9.2 Test description

9.2.1 Reference and trajectory

Two van positioning tests were carried out, on a city-express road with fly-over bridges from 15:20 to 17:19 on 27 January 2022, and in the Nottingham city center from 10:30 to 11:30 on 11 February 2022. The commercial software Inertial Explorer (IE) is used to compute reference RTK/INS TCI solution with base the NGB2 station (see Figure 7.4) and rover the LEICA GS10 on the van. The maximum baseline length during the van movement is around 3 km. Figure 9.1 is the trajectory of the reference solutions of the two tests on the Google earth.

(a) *Complex road test*

(b) *City center test*

Figure 9.1: *Trajectories of two van positioning tests*

9.2.2 Satellite visibility and raw inertial data

The PPP/INS measurements basic information are provided in this section, for the two different test environments.

Complex road test

Figure 9.2 shows that the number of observed satellites has a lot of drops. Nevertheless, approximate 12 satellites can still be recovered rapidly after these sudden drops. Figure 9.3 is the decoded raw IMU data from three accelerometers and three gyros.

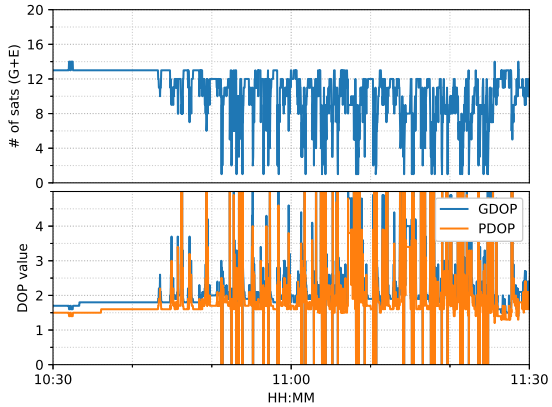

Figure 9.2: *GNSS satellite information of road bridges test on 11/02/2022*

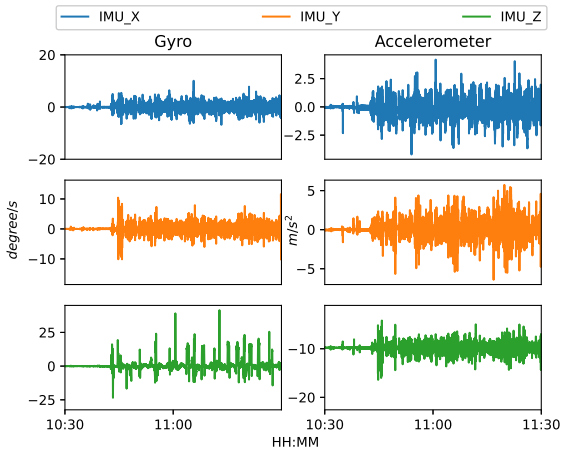

Figure 9.3: *Raw IMU measurements of road bridges test on 11/02/2022*

City center test

Figure 9.4 shows that the number of tracked satellites has significant decrease at around 16:00 and 16:30 and requires more time to recover peak values

compared to Figure 9.2, which indicates harsh signal reception environment in the city center. The inertial measurements in Figure 9.5 have more spikes than Figure 9.3.

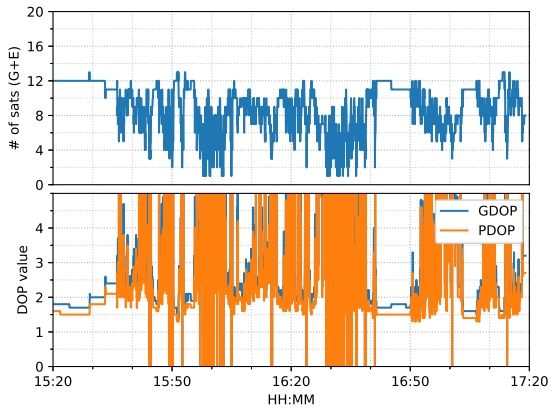

Figure 9.4: *GNSS satellite information of city center test on 27/01/2022*

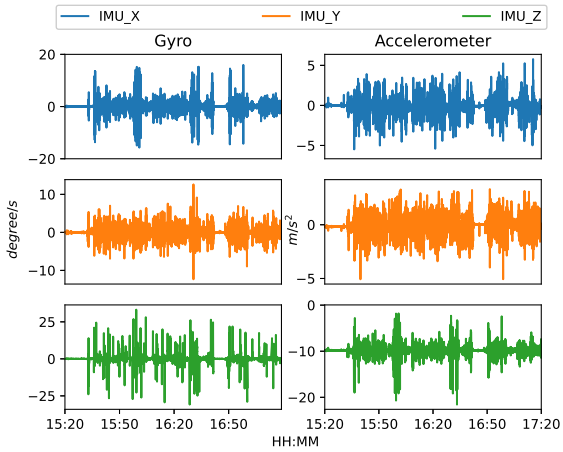

Figure 9.5: *Raw IMU measurements of van test on 27/01/2022*

9.3 Complex road positioning test

This section presents the real-time GPS/Galileo PPP/INS integrated results on the complex road. The real-time satellite orbit, clock and uncombined bias products are from French CNES analysis center. The Bootstrapping method is used for ambiguity resolution (see Section 8.4).

9.3.1 Positioning performance evaluation

Phase ambiguity status

Figure 9.6 shows that only G24 and E01 have fixed ionosphere-free (IF) or narrow-lane (NL) ambiguities and only for a short period of time. These two IF ambiguities are actually fixed as datum but the remaining ambiguities cannot be fixed due to the frequent interruptions and the conditions in Table 8.1 are not satisfied. Single WL ambiguity resolution (AR) is not beneficial to the solution because the WL ambiguity is estimated from the geometry-free MW combination in this dual-frequency setting. The van starts moving at around 10:45.

Figure 9.6: *Phase ambiguity status of road bridge test on 11/02/2022*

PPP/INS results

Since only datum IF ambiguities and WL ambiguities can be fixed, the PPP-AR results will be equivalent to PPP only with uncombined bias correction and without AR. New notation 'PPP+bias' to indicate this condition of near-zero IF ambiguity fixing rate. Figure 9.7 shows the six modes of positioning results. 79.6% of the reference IE solutions are ambiguity-fixed with quality flag 1, which is usually corresponding to epochs with good satellite visibility and has higher accuracy of 3D < 15 *cm* as shown in Figure 7.8. The quality flag

2 or 3 of reference solution usually have poor observation conditions e.g. under bridges and lower accuracy. The van starts moving at around 10:45. It can be seen that PPP or PPP+bias solutions suffer from frequent noisy divergence in all directions during the movement but can still re-converge rapidly. The solution divergence is caused by a drastic drop of observed satellite number or even data gaps as the van passes through a bridge. When no cycle slip occurs during a short signal outage, the previous converged ambiguity could continue to be applied to the re-captured phase measurements to compute new innovations for measurement update of kalman filter. As a result, PPP can converge almost instantaneously as shown in Figure 8.21. The PPP/INS integrated results for both LCI and TCI can effectively eliminate the noisy spikes and conserve high accuracy throughout the test. The INS acts as a good complement during short GNSS signal blockage. Moreover, the TCI solutions achieve the best accuracy. In particular, the additional uncombined bias correction can improve the related PPP, LCI and TCI further especially on the up component. Figure 9.8 shows the ionosphere-free code residuals after filtering. It can be seen that the code residuals with bias correction are more aggregated for both GPS and Galileo system.

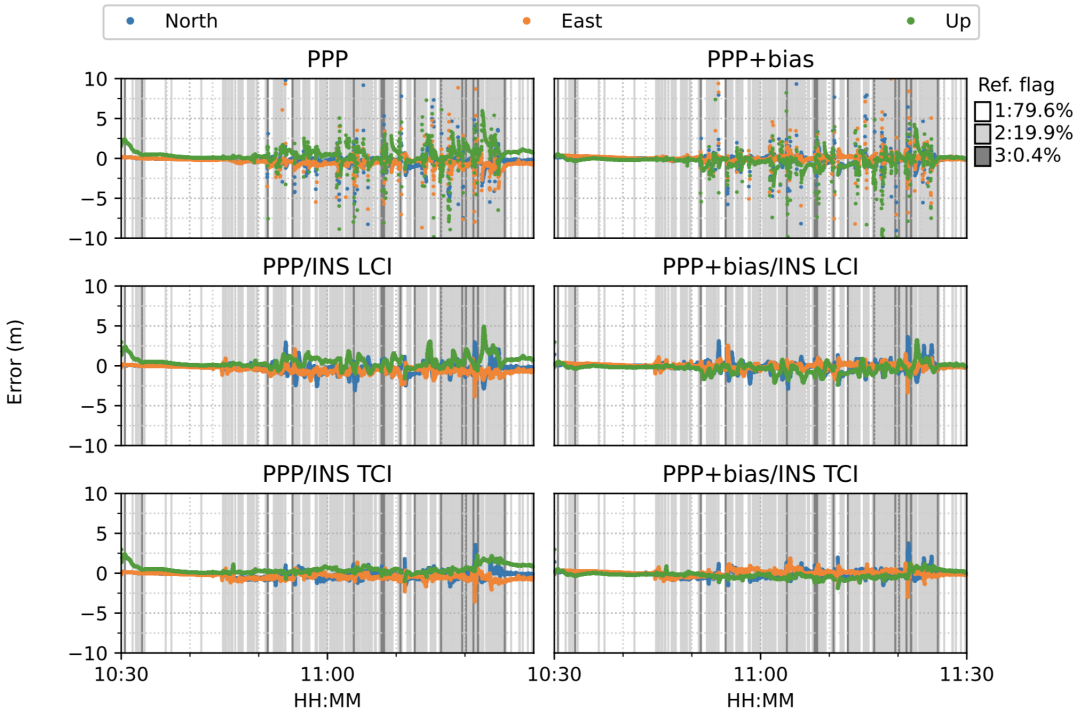

Figure 9.7: *GPS/Galileo PPP/INS results of road bridge test on 11/02/2022 with respect to IE RTK/INS TCI solutions. The notation 'PPP+bias' means low ambiguity-fixing rate only with bias correction instead of the full AR of 'PPP-AR' in Figure 8.8. (The same below). The background color indicates different quality flags of reference solutions as in Figure 7.8*

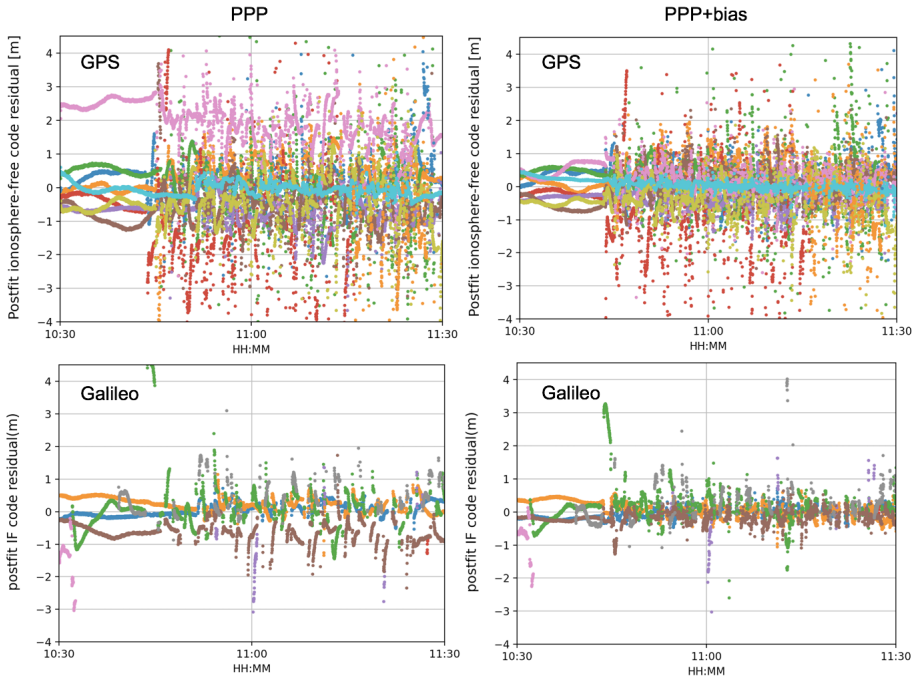

Figure 9.8: *Postfit code residuals of GPS/Galileo PPP of road bridge test on 11/02/2022*

Re-convergence examples

Figure 9.9 is a two-minute example with signal outage due to bridges from Figure 9.7. It clearly shows that after each bridge epoch(red vertical line) PPP converges rapidly within a couple of seconds. The LCI and TCI solutions maintain high precision (decimeter level) horizontally and TCI obtains more accurate and steady height solutions. With the real-time uncombined bias correction, all solutions are more aggregated, especially for the height component, and TCI achieves the highest accuracy. Nevertheless, PPP+bias can also converge to comparable high accuracy at the end of the session. It is also shown that at the forth red-line epoch (10:53:50) TCL and LCI solutions have significant drift. TCI uses around 6 seconds to recover steady solutions and about 12 seconds for LCI to be below 1 m. TCI solutions also maintain higher accuracy of nearly less than 1 m in all directions during the drift. This drift is caused by a 4-s data gap when the van travels through a tunnel instead of a short bridges, which is illustrated in Figure 9.10. It can be seen that PPP solutions are drifted severely after entering the tunnel while the TCI solutions are consistent well with the reference solutions. It is also noted that the reference solution quality status in Figure 9.10 becomes yellow or number 2 (lower accuracy) from entering the tunnel and changes to number 1 (highest accuracy) as the van leaves the tunnel gradually which also shows the difficulty of positioning during longer GNSS data gaps.

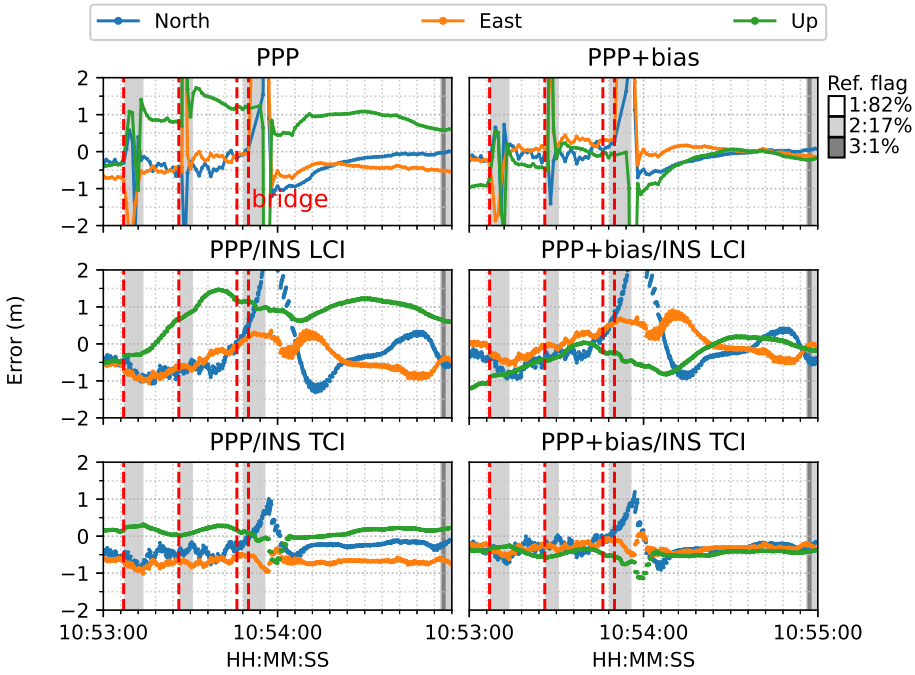

Figure 9.9: *Re-convergence example 1. The red lines indicate the epochs through bridges (The same below).*

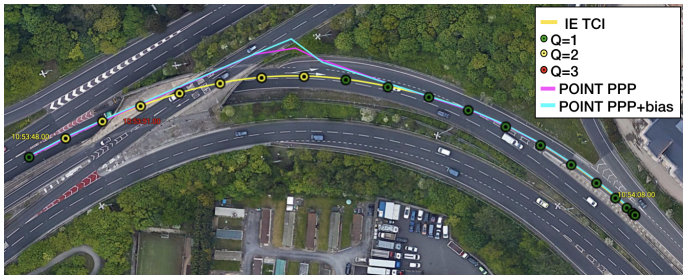

(a) *POINT PPP solutions*

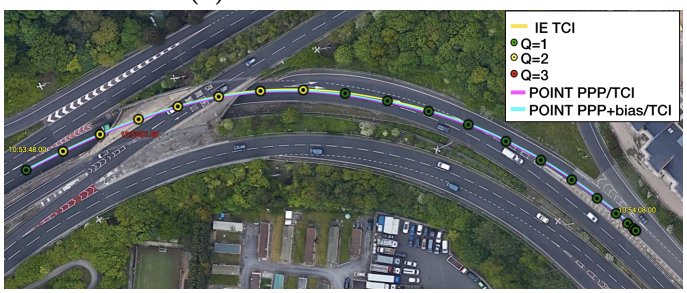

(b) *POINT PPP/INS TCI solutions*

Figure 9.10: *Re-convergence example 1 on Google earth. The red epoch 10:53:51 signifies the van is in a tunnel. IE stands for the reference software: Inertial Explorer (The same below)*

Figure 9.11 gives another example of PPP re-convergence after bridge epochs. In this case the additional uncombined bias correction accelerates the PPP convergence to a few seconds horizontally and also improves PPP, LCI and

TCI positioning accuracy. TCI as expected achieves the best performance and preserve a decimeter-level accuracy during the session. Figure 9.12 is the related satellite view of the first two bridge epochs. As in example 1, PPP-only solutions show large drift under bridge at 11:15:26 while TCI solutions gives the best consistency with the reference.

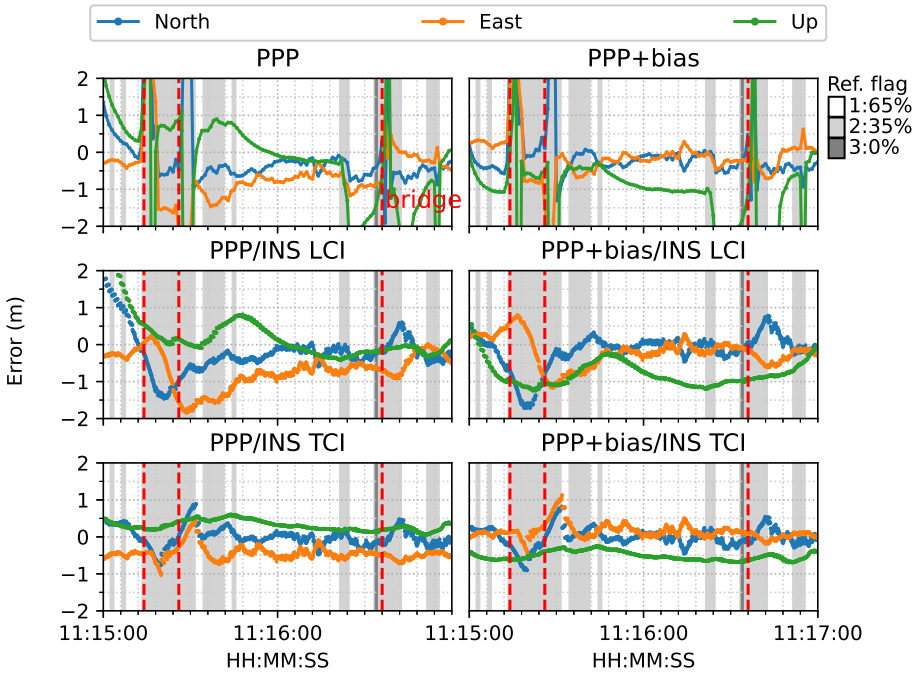

Figure 9.11: *Re-convergence example 2. The red epochs 11:15:14 and 11:1526 signify the van is under bridge.*

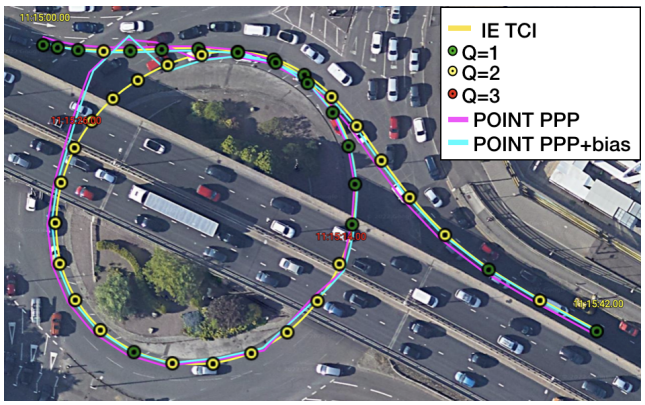

(a) *POINT PPP solutions*

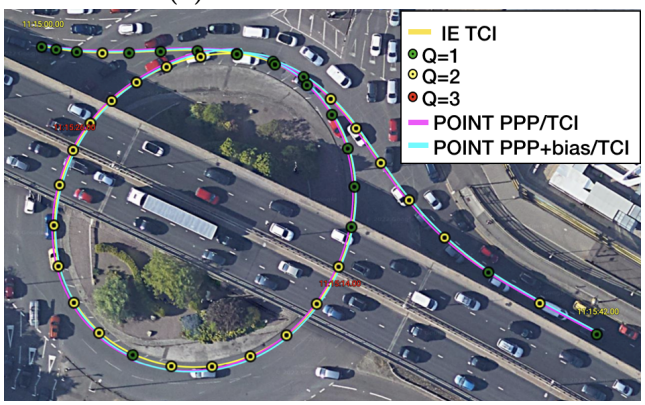

(b) *POINT PPP/INS TCI solutions*

Figure 9.12: *Re-convergence example 2 on Google earth*

In order to measure the re-convergence time when the van passes a bridge or has short signal blockage statistically. The positioning solutions are divided into multiple sessions where a data gap starts or the number of satellites is less than 2 at the beginning . In total, there are 61 sessions generated but it is found that only parts of the sessions can converge to be less than 50 *cm* horizontally, which are shown in Figure 9.13. A convergence time is computed when the converged solutions are consecutive for more than 10 epochs. It can be seen that TCI with bias correction has most samples that are converged and the 68th-percentile convergence time is only 4.7s, which is improved by 94% compared to PPP-alone solutions. INS can aid PPP to converge rapidly for both LCI and TCI. Bias correction can accelerate the convergence further.

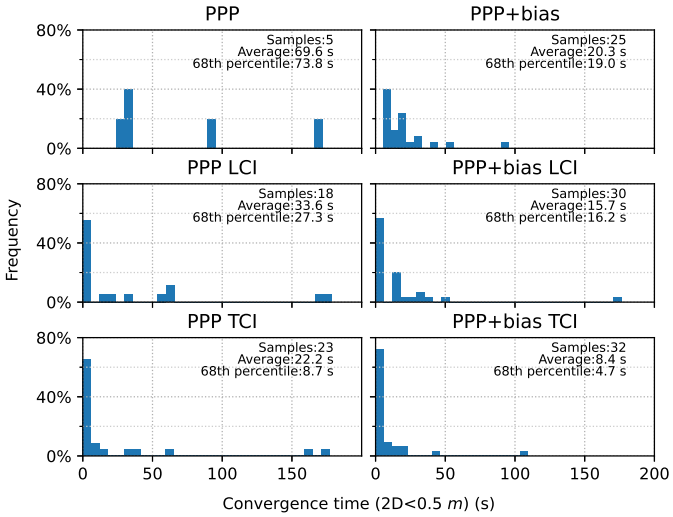

Figure 9.13: *Histogram of convergence time when passing through bridges. 61 sessions are analysed.*

Error statistics

Figure 9.14 shows the overall error RMS of each positioning mode. The comparison is divided by the quality of the reference solutions e.g. Ref. state 1 and 2 in the figure. For quality 1, without bias correction, TCI achieves the best accuracy in the north, east and up direction, which is 38, 48 and 67 *cm* and has an improvement of 25%, 21% and 32% respectively compared to PPP of 51, 61, 99 *cm*. After applying the uncombined biases to PPP, LCI and TCI, higher positioning accuracy is obtained in comparison with the uncorrected solutions. TCI still gives the highest accuracy of 32, 29, 41 *cm* for the N E U component, which is improved by 18%, 40%, and 39% respectively compared with uncorrected TCI and by 37%, 52% and 59% with PPP-only solutions. The east accuracy after bias correction is almost identical for the three modes and the up component is improved most. The LCI performance is in the middle of PPP and TCI. For quality 2, the integrated solutions have substantial improvement, especially for the height component, which can be 94%. The horizontal accuracy is improved from around 2.5 *m* to decimeter level. LCI and TCI have comparable accuracy and bias correction can improve the results further.

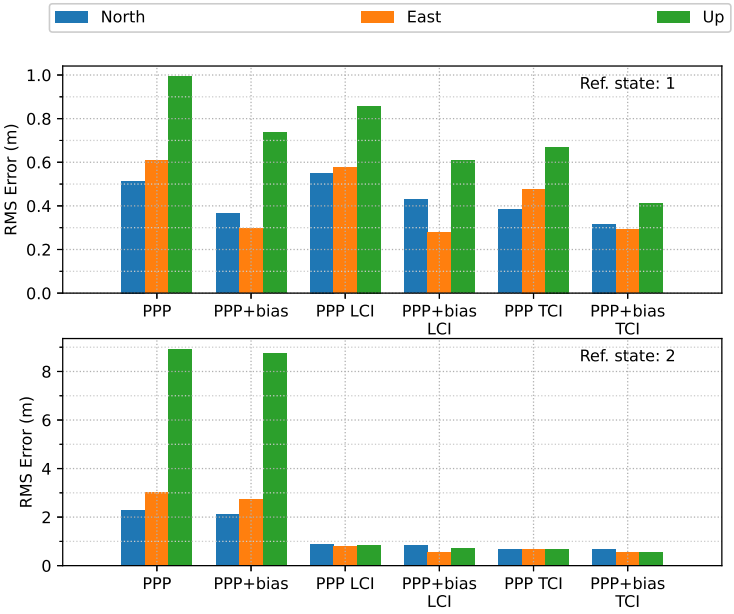

Figure 9.14: *Error RMS of real-time GPS/Galileo PPP/INS results of road bridge test on 11/02/2022*

9.3.2 Velocity and Attitude errors

Figure 9.15 shows the estimated velocity errors of GNSS antenna. It is noted that the lever arm is needed to transfer the IMU velocity to the antenna reference point (ARP). It is clear that the integrated solutions are more aggregated than doppler estimation. The effect of bias correction is not significant. As shown in Figure 9.16, the PPP or doppler velocity accuracy is 0.31, 0.42, 3.39 m/s in the N E U direction respectively and 0.15, 0.11, 0.03 m/s for that of LCI. The TCI results are nearly identical to LCI. The integrated solution achieves an improvement of 52%, 74% and 99%.

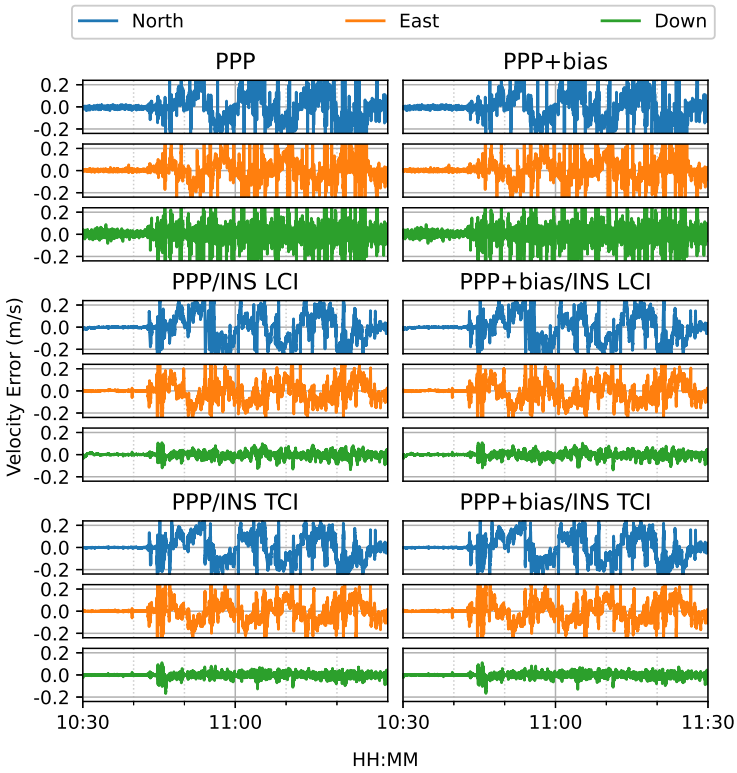

Figure 9.15: *GPS/Galileo PPP/INS velocity results of road bridge test on 11/02/2022 with respect to IE RTK/INS TCI solutions*

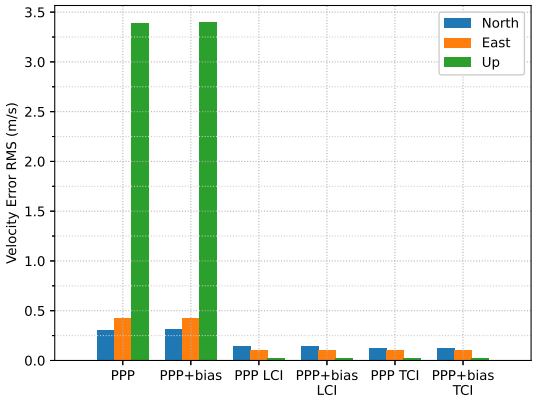

Figure 9.16: *Velocity error RMS of real-time GPS/Galileo PPP/INS results of road bridge test on 11/02/2022*

Figure 9.17 shows the attitude errors. The yaw (heading) errors have many spikes similar to Figure 8.15 in the train positionig test which is caused by dramatic change of heading during the movement. The bias correction is also not significant. The LCI attitude accuracy as shown in Figure 9.18 is 0.06, 0.05, and 1.89 ° for roll, pitch and yaw angles respectively. The TCI attitudes have an improvement of 10% in the heading accuracy. The effect of the bias

correction is still negligible.

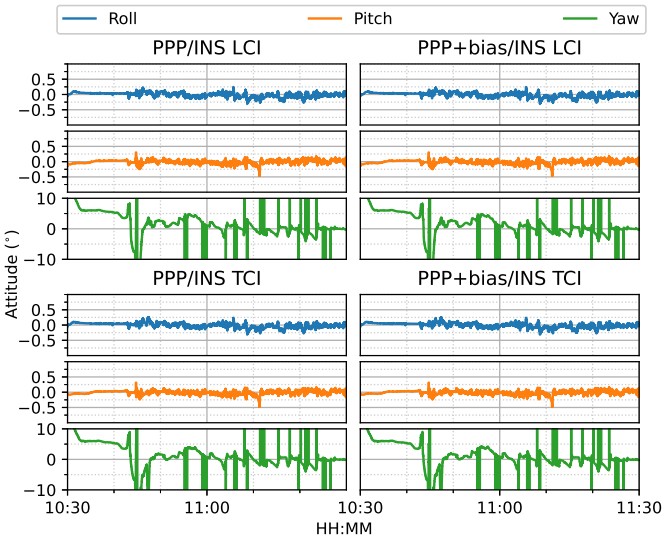

Figure 9.17: *GPS/Galileo PPP/INS attitude results of road bridge test on 11/02/2022 with respect to IE RTK/INS TCI solutions*

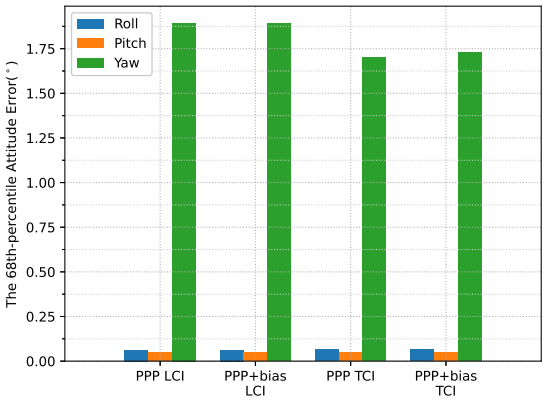

Figure 9.18: *Attitude error RMS of real-time GPS/Galileo PPP/INS results of road bridge test on 11/02/2022*

9.3.3 Estimates of IMU biases and scale factors

The gyro and accelerometer biases are critical to correct the raw IMU measurements before INS mechanization. In Figure 9.19, the reference gyro bias drift varies after around 11:00 in all directions while the POINT computed values are close to zero indicating a constant gyro bias. The accelerometer biases of reference estimates in Figure 9.20 are also not constant. These difference could be caused by the applied bias spectral densities in the configuration file or profile. The clear shift in the IMU Z direction could result from different gravity models.

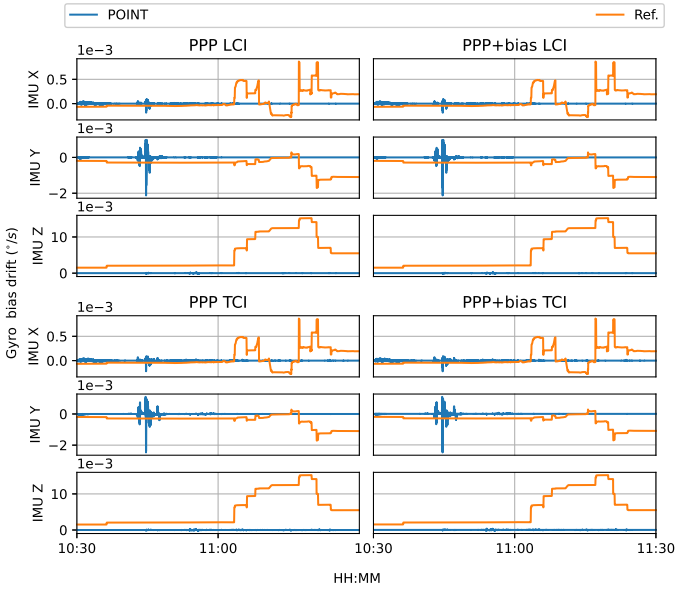

Figure 9.19: *Estimated gyro bias results of road bridge test on 11/02/2022 with respect to IE RTK/INS TCI solutions*

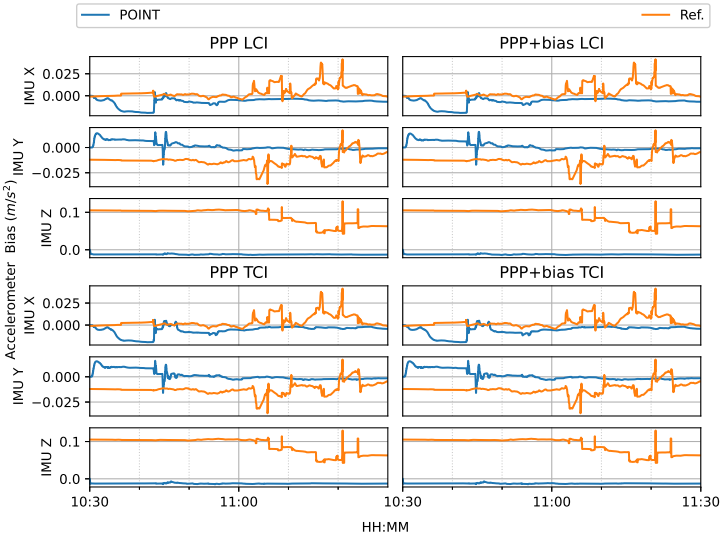

Figure 9.20: *Estimated accelerometer bias results of road bridge test on 11/02/2022 with respect to IE RTK/INS TCI solutions*

For tactical IMU sensors, the scale factor error estimation is optional because they should be close to 1 as shown in Figure 9.21 and Figure 9.22.

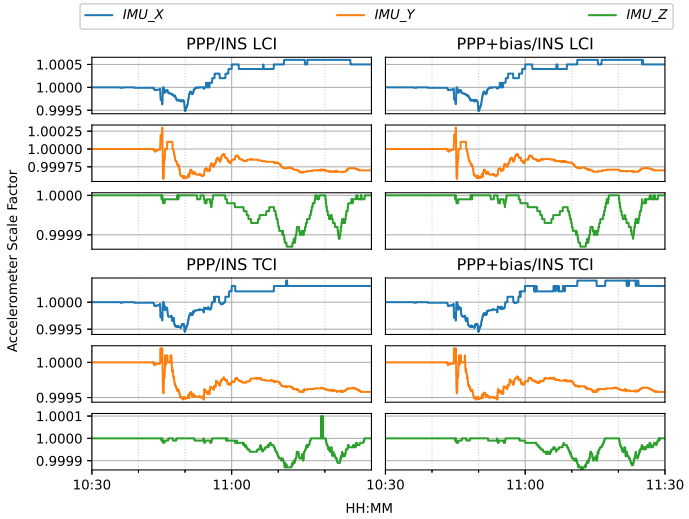

Figure 9.21: *Estimated gyro scale factor results of road bridge test on 11/02/2022 with respect to IE RTK/INS TCI solutions*

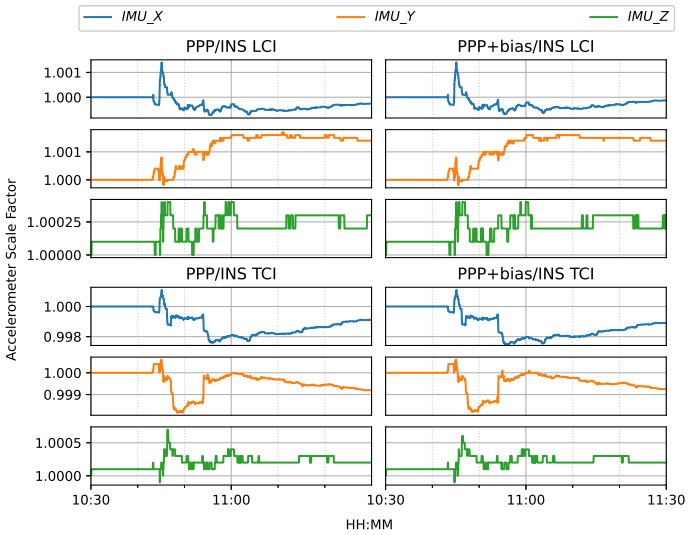

Figure 9.22: *Estimated accelerometer scale factor results of road bridge test on 11/02/2022 with respect to IE RTK/INS TCI solutions*

9.4 City center positioning test

This section provides the real-time PPP/INS results from the Nottingham city center test.

9.4.1 Positioning performance evaluation

Ambiguity status

Due to vegetation and highrise canyons, GNSS signal blockage or gap can occur more frequently during the city center positioning test. As in Figure 9.23,

the ambiguities of the tracked satellites are not consecutive and has many interruptions, which makes it difficult to fix the IF or NL ambiguities as in Figure 9.6. Only two datum IF ambiguities can be fixed G25 and E30. As a result, PPP-AR solutions are just corrected with biases and no IF ambiguity resolution contributes to the results. The . notation 'PPP+bias' is again used to indicate this type of solution.

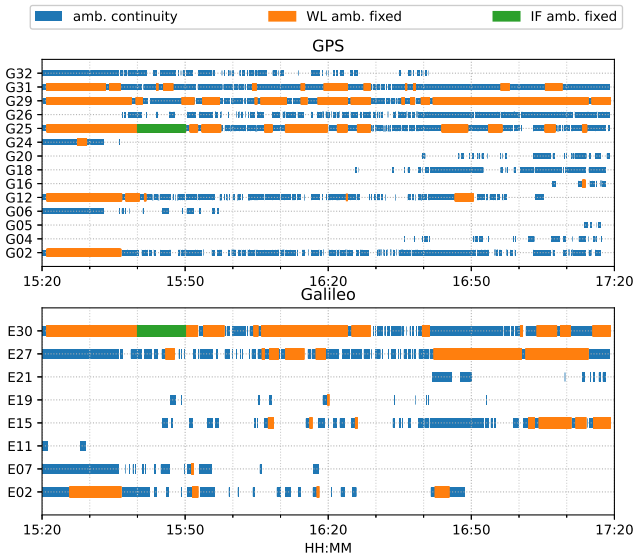

Figure 9.23: *Phase ambiguity status of city center test on 27/01/2022*

PPP/INS results

The van starts moving at around 15:35 and stops for about 15 *min* from around 16:35. It can be seen in Figure 9.24 that the PPP solutions re-converge significantly several times during the movement where solutions diverge severely along with large positioning errors. PPP+bias improves the results in some degree (e.g. at around 17:10) but still suffers from frequent re-convergence. The LCI solution mitigates the noisy spikes of PPP but the improvement is marginal. The bias correction adds more aggregation in the up component. The TCI solutions however eliminates the divergence effectively and obtains the best performance of the test. TCI with bias correction can improve the results further especially for the up component.

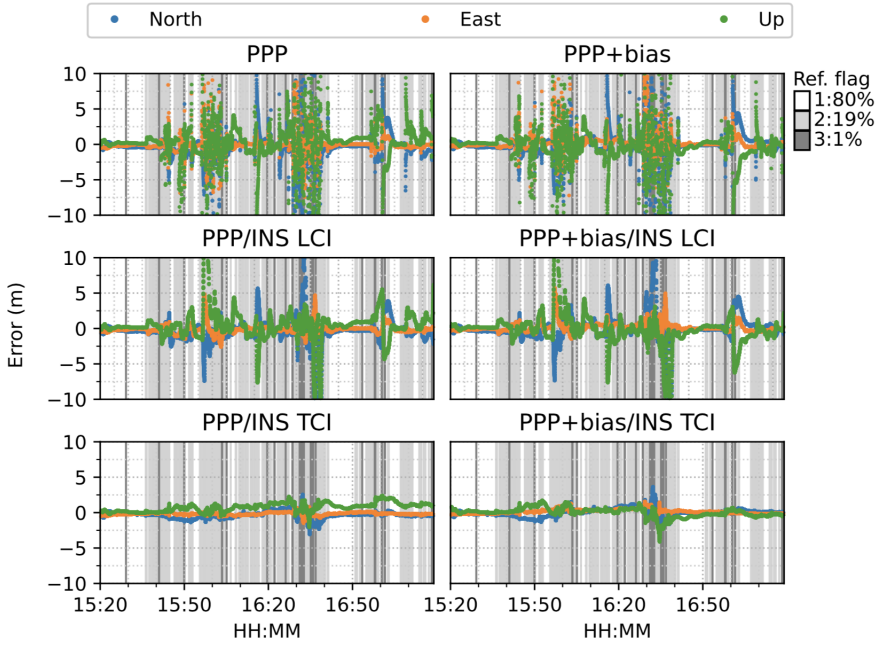

Figure 9.24: *Real-time GPS/Galileo PPP/INS results of city center test on 27/01/2022 with respect to IE RTK/INS TCI solutions*

Examples on Google earth

Two time periods at around 15:56 and around 16:30 have the worst accuracy in Figure 9.24, where significant drops of satellite number are also observed in Figure 9.4. This poor satellite visibility is mainly caused by the trees and buildings along the road in city center. Figure 9.25 is a two-minute example from 15:56:00. The majority of reference solutions is in yellow state. It can be seen that the PPP solutions show irregularities at two regions where a building canyon (right of subfigure (a)) and dense vegetation(upper left of subfigure (a)) are observed on the map. The LCI solutions also show clear drift after the building canyon. TCI solutions are closely adherent to the reference trajectory.

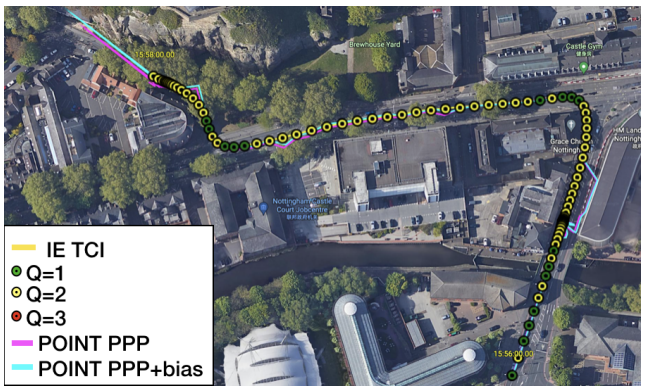

(a) *POINT PPP solutions*

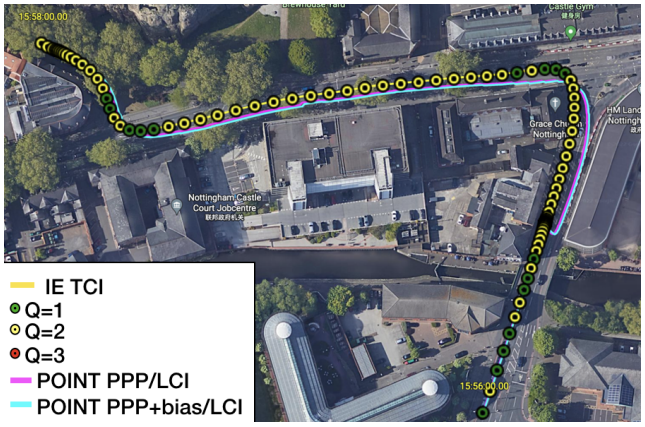

(b) *POINT PPP/INS LCI solutions*

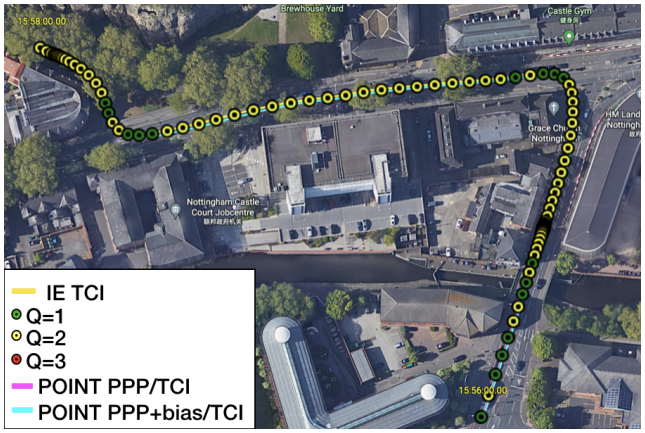

(c) *POINT PPP/INS TCI solutions*

Figure 9.25: *Example 2 of city center test on Google earth*

Figure 9.26 is another example from 16:31:02 to 16:32:52. Vegetation is clustered along the curved path and the reference solutions show a lot of red states indicating a challenging signal reception environment. As expected the the PPP solutions as well as as the bias corrected solutions have large inconsistency along the path. The LCI solutions are better yet still have clear shift from the reference. The TCI solutions again gives the best consistency.

(a) *POINT PPP solutions*

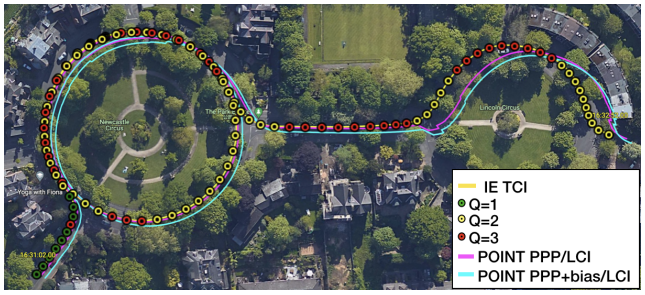

(b) *POINT PPP/INS LCI solutions*

(c) *POINT PPP/INS TCI solutions*

Figure 9.26: *Example 1 of city center test on Google earth*

Error statistics

In terms of overall error RMS as shown in Figure 9.27, the contribution of bias correction is mainly on the up component and the horizontal accuracy is almost equivalent to the solutions without biases for PPP, LCI and TCI. With respect to reference state or quality 1 solutions, TCI achieves the best performance with an accuracy of 47, 26 and 55 *cm* in the N E U direction respectively, which improves the up component most by 43% after bias correction. The bias-corrected LCI has an accuracy of 118, 49 and 179 *cm* on the N E U component and PPP of 183, 51 and 242 *cm*. Though the reference state 2 solutions may be only as precise as decimeter -level, the echelon form is still clear from PPP, LCI and TCI solutions.

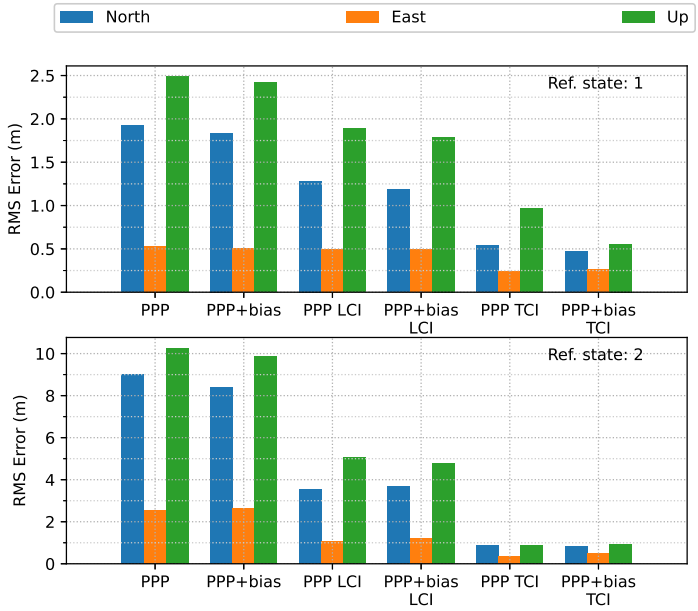

Figure 9.27: *Error RMS of real-time GPS/Galileo PPP/INS results of city center test on 27/01/2022 with respect to IE RTK/INS TCI solutions*

9.4.2 Velocity and Attitude errors

From Figure 9.28, the integrated solutions has higher accuracy than doppler estimation in all directions. As in Figure 9.29, the doppler velocity accuracy is 0.97, 0.29, 0.97 m/s. The TCI velocity accuracy is 0.04, 0.04, 0.02 m/s with an improvement of 96%, 86% and 98%. The LCI solution has slightly poorer accuracy in the up direction compared to TCI.

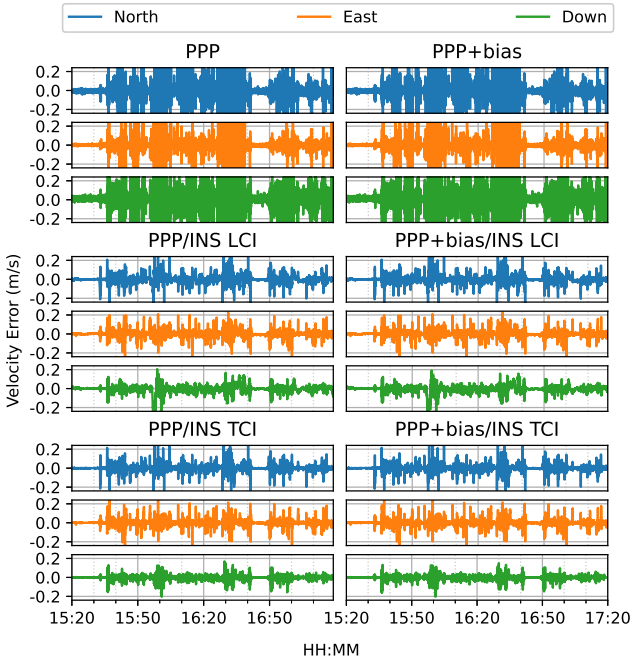

Figure 9.28: *Real-time GPS/Galileo PPP/INS velocity errors of city center test on 27/01/2022 with respect to IE RTK/INS TCI solutions*

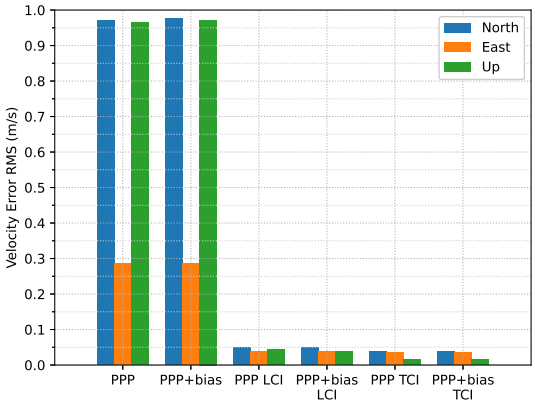

Figure 9.29: *Velocity error RMS of real-time GPS/Galileo PPP/INS positioning of city center test on 27/01/2022 with respect to IE RTK/INS TCI solutions*

The attitude heading errors also show many spikes in Figure 9.31. This is caused by small time offset after INS and GNSS time synchronization, which is illustrated in Figure 9.30. It can be seen that the reference and computed yaw angles are not strictly synchronized and interpolation will cause spikes when there are dramatic changes in the heading direction.

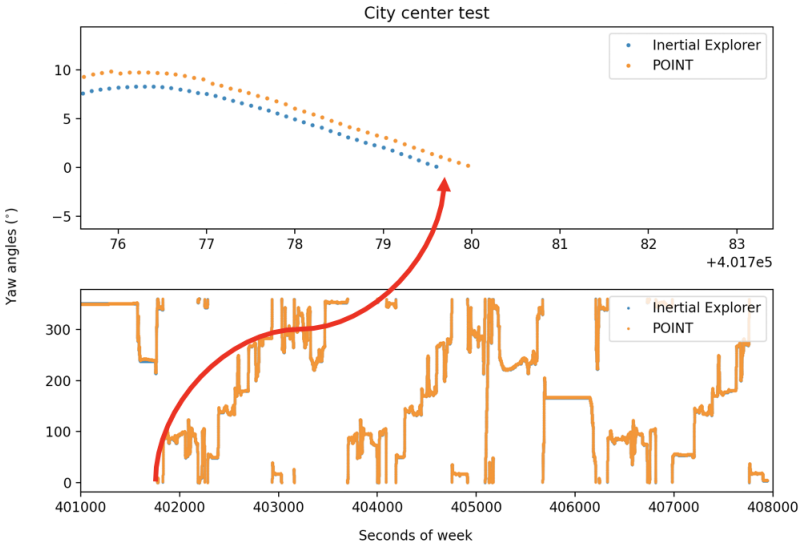

Figure 9.30: *Reference (Inertial Explorer) and computed (POINT) yaw angles of city center test on 27/01/2022. The lower panel is the two superimposed heading solutions. The upper panel is a scale-up view of the local part indicated by the red arrow.*

The LCI and TCI solutions are almost identical. As in Figure 9.32, the attitude accuracy is 0.01, 0.01, 0.52 ° in this city center positioning test.

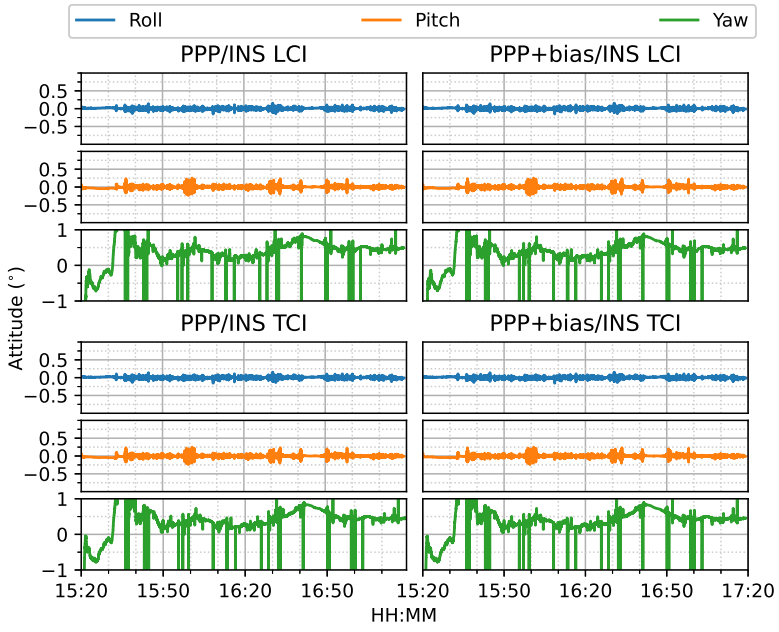

Figure 9.31: *Real-time GPS/Galileo PPP/INS attitude errors of city center test on 27/01/2022 with respect to IE RTK/INS TCI solutions*

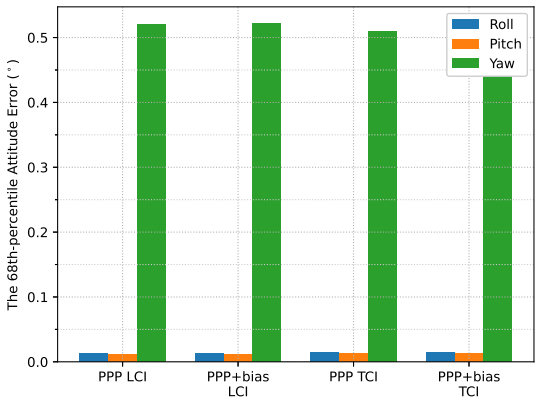

Figure 9.32: *Attitude error RMS of real-time GPS/Galileo PPP/INS positioning of city center test on 27/01/2022 with respect to IE RTK/INS TCI solutions*

9.4.3 Estimates of IMU biases and scale factors

The estimated gyro bias drifts and accelerometer biases by POINT as shown in Figure 9.33 and Figure 9.34 are in the same magnitude level with reference. The difference could still come from the different profiles that are applied.

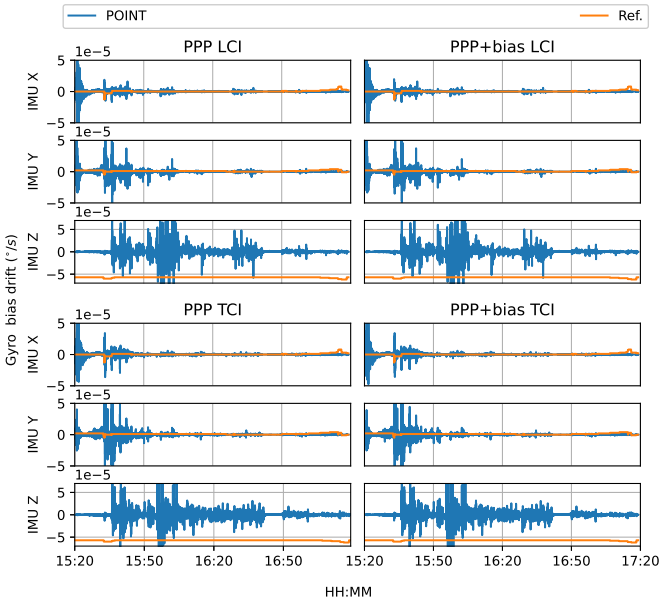

Figure 9.33: *Estimated gyro bias results of city center test on 27/01/2022 with respect to IE RTK/INS TCI solutions*

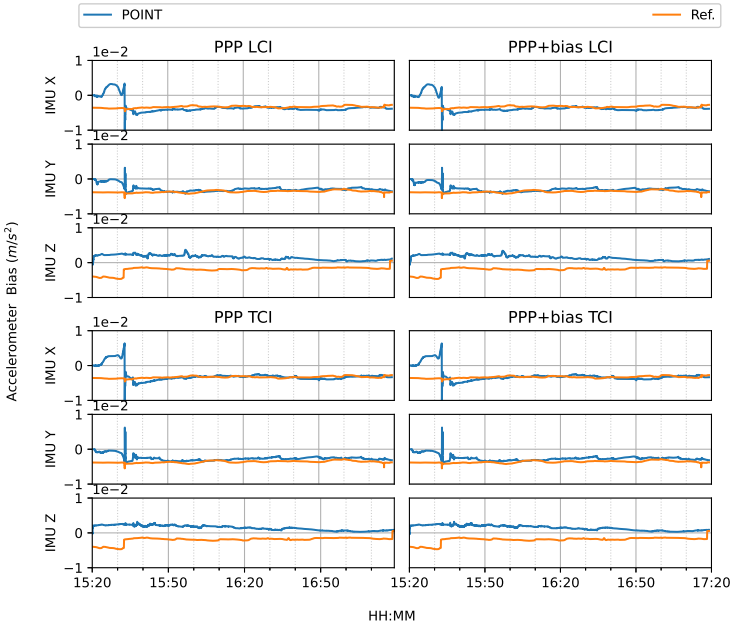

Figure 9.34: *Estimated accelerometer bias results of city center test on 27/01/2022 with respect to IE RTK/INS TCI solutions*

The estimated scale factor errors in Figure 9.35 and Figure 9.36 are also very close to one as in the previous tests.

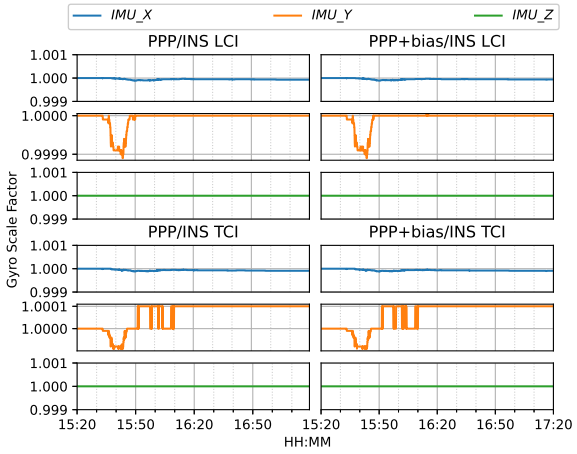

Figure 9.35: *Estimated gyro scale factor results of city center test on 27/01/2022 with respect to IE RTK/INS TCI solutions*

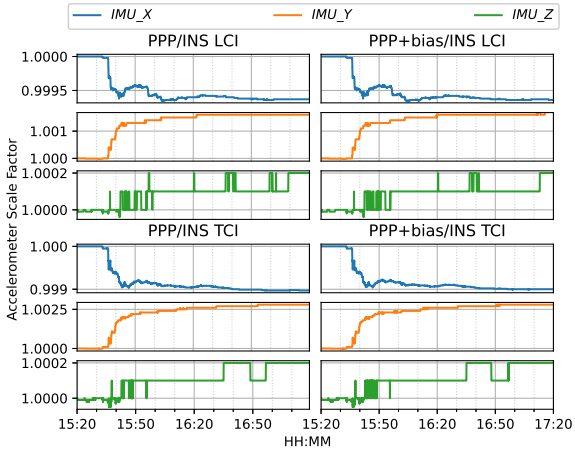

Figure 9.36: *Estimated accelerometer scale factor results of city center test on 27/01/2022 with respect to IE RTK/INS TCI solutions*

9.5 Summary

In this chapter the GPS/Galileo PPP/INS positioning performance with CNES real-time orbit, clock and bias products is evaluated through two van tests. One of the test is conducted on a city-express road where several bridges exist. The other is around Nottingham city center where dense vegetation and building canyons are spread along the path. Six positioning modes are tested. The dual-frequency ionosphere-free PPP model is used for the integration.

Frequent drops of number of visible satellites during the two tests directly cause multiple re-convergences in the PPP solutions, in which the IF AR is not feasible though phase biases are corrected. With respect to the IE RTK/INS TCI reference, in the complex road test PPP-alone has an accuracy of 51, 61, 99 *cm* in the N E U direction respectively. TCI achieves the best accuracy, which is 38, 48 and 67 *cm* with an improvement of 25%, 21% and 32% respectively compared to PPP. The LCI performance is in the middle of PPP and TCI. After applying the uncombined biases, higher positioning accuracy is obtained. TCI still gives the highest accuracy of 32, 29, 41 *cm* for the N E U component, which is improved by 18%, 40%, and 39% respectively compared with uncorrected TCI and by 37%, 52% and 59% with PPP-only solutions. In the city center test, the contribution of bias correction is mainly on the up component. The bias-corrected TCI still achieves the best performance with an accuracy

of 47, 26 and 55 cm in the N E U direction respectively, which improves the up component most by 43% after bias correction. The bias-corrected LCI solution has an accuracy of 118, 49 and 179 *cm* on the N E U component, and the PPP solution of 183, 51 and 242 cm.

PPP/INS TCI can effectively reduce solution divergence and maintain high accuracy during temporary signal blockage and short data gaps (e.g. a couple of seconds). PPP with phase cycle slip correction (CSC) can also accelerate re-convergence, and the performance of TCI with CSC, or even single-epoch PPP is to be investigated in the future.

Chapter 10

Conclusions and perspectives

10.1 Conclusions

10.1.1 General remarks

The performance of GPS/Galileo PPP integrated with Inertial Navigation System (INS) is investigated in this thesis. Both loosely coupled integration (LCI) and tightly-coupled integration (TCI) are developed and evaluated based on our in-house software POINT.

The additional layer of the bias correction for PPP uses the CNES latest uncombined bias products. This uncombined bias representation can be referenced to arbitrary clock definition and its form is closer to the physical nature of signal hardware delays. This formulation is also independent of the network estimation and user application. These uncombined bias products are directly added to the raw code and phase measurements, and the phase ambiguity or its combinations can conserve the integer nature. The CNES uncombined bias products were applied along with the corresponding precise satellite orbits and clock to two GPS/Galileo PPP models for AR : dual-frequency ionosphere-free (DFIF) model multi-frequency ionosphere-estimated (MFIE) model, which validates the flexibility of this uncombined bias products in different user modelling. Therefore users can establish positioning models at their own choice with the availability of phase AR using the same uncombined form of biases.

This assessment is the first part of this thesis and is reflected in Objective 1 & 2 in Section 1.2 .

Then the uncombined bias products are applied to the GPS/Galileo PPP/INS integrated models. The LCI integrates the INS and PPP or PPP-AR solutions by an independent Kalman filter. The LCI filter uses the difference between the PPP and INS positioning solutions as measurements to update the predicted states from INS error dynamics. When there is PPP solutions outage, LCI will only output INS solutions, which fills the GNSS solution gap but degrades over time and the quality is closely related to the grades of IMU. The TCI has the same prediction procedure as LCI, but updates the predicted solution using GNSS raw measurements, which is similar to PPP. The raw code and phase measurements are corrected with the CNES satellite uncombined biases to enable AR. When only limited number of satellites are available, TCI can still output solutions with higher accuracy than that of PPP. In general, when satellite availability is good, PPP, LCI and TCI would have similar performance, but when there is poorer satellite visibility, TCI would outperform LCI and PPP. For both TCI and LCI, ambiguity-fixed or bias-corrected solution can achieve better accuracy than the ambiguity-float solution. This is the second part of the thesis and reflected in objective 3 & 4 in Section 1.2.

10.1.2 Remarks on Objective 1 & 2

Objective 1: To implement and evaluate GPS/Galileo dual-frequency ionosphere-free PPP and PPP AR using uncombined bias products.

Experiment review: The observation data is from selected globally distributed IGS stations. The GFZ MGEX rapid satellite precise orbit and clock products are used. GPS L1/L2 and Galileo E1/E5a signals are used, and the standard dual-frequency ionosphere-free PPP model are established based on our in-house software POINT. The CNES uncombined bias products are added to the raw measurements to recover the integer nature of phase ambiguities, thus allowing for the resolution of the ionosphere-free (IF) combined ambigu-

ities. The IF ambiguity is decomposed as the widelane (WL)and narrowlane (NL) ambiguities. The WL intergers are determined by a simple integer rounding. The classical LAMBDA method is used for searching the best integer candidate validated by a simple ratio test in NL AR. The receiver coordinate parameters are assigned with a process noise of 100 m/s to simulate the kinematic case.

Conclusions: Results show that the dual-frequency ionosphere-free ambiguity-fixed kinematic PPP can achieve an accuracy of 0.82, 0.96, 3.04 cm on average in the north (N), east (E) and up (U) direction respectively (68th percentile). In particular the east component obtains a significant improvement of 45% compared to the float solutions. In terms of the convergence, PPP is accelerated by 23% after AR for 3D error below 5 cm.

Objective 2: To implement and evaluate GPS/Galileo multi-frequency ionosphere-estimated PPP and PPP AR using uncombined bias products.

Experiment review: The observation data is from selected globally distributed IGS stations. The GFZ MGEX rapid satellite precise orbit and clock products are used. GPS L1/L2/L5 and Galileo E1/E5a/E5b/E6 signals are used and the ionosphere-estimated PPP model are established based on our internal software POINT. The CNES uncombined bias products are applied to the raw measurements for AR. The original ambiguities on each frequency (except L1 and E1) are configured as combinations of a series of WL ambiguities. The best integer equivillant (BIE) is used for AR in a cascading manner according to the wavelength of the combined ambiguities. The simulated kinematic state is also configured. The ionospheric parameters are constrained using empirical values and no external ionosphere information is imposed.

Conclusions:The ionosphere-estimated ambiguity-fixed solution can achieve an accuracy of 1.16, 0.98 and 4.44 *cm* in the north, east and up direction respectively (68th percentile). A significant improvement of 63% on the east component is obtained with respect to the ambiguity-float solution. The PPP

convergence requires 29.2 min on average to be below 5 cm horizontally after AR with an acceleration of 17%. Regarding the instantaneous positioning capability of the multi-frequency model, an accuracy of 32 and 31 *cm* for north and east components (68th percentile) can be obtained after WAR improved by 13% and 16% respectively relative to the code-only solution. The N_1 and N_{E1} AR was deactivated in the single-epoch test as their estimated precisions are still larger than one cycle and not sufficient for resolution.

10.1.3 Remarks on Objective 3 & 4

Objective 3 & 4 : To implement and evaluate GPS/Galileo PPP/INS and PPP-AR/INS LCI and TCI with the uncombined bias correction for AR.

Experiment review: The PPP/INS LCI and TCI experiments are carried out in a train positioning test and two van positioning tests. A LEICA GS10 GNSS receiver and a NovAtel tactical-grade IMU are equipped in the two tests. The train test is on the roof of NGI and has good satellite observability. The van tests are on complex road and city center of the Nottingham city, where signal interruptions happen frequently. CNES real-time orbit, clock and the uncombined bias products are used. For both LCI and TCI, GPS L1/L2 and Galileo E1/E5a ionosphere-free PPP and PPP AR models are configured. Artificial signal gaps are simulated in the train test for navigation resilience investigation. The bootstrapping method is used for AR.

Conclusions: In the train positioning test, it is found that ambiguity-float PPP has almost identical performance with LCI and TCI, which can reach an accuracy of 8.5, 5.7 and 4.9 cm in the north, east and up direction respectively. After AR, all the solutions achieve significant improvements in all components, which are around 9%, 9% and 7% for the North component, 47%, 40% and 38% for the East component and 14%. 12% and 4% for the height component, for PPP-AR, PPP-AR/INS LCI and PPP- AR/INS TCI respectively. When simulated one-minute gaps are inserted, Within the first 10 seconds. INS-only solution in a kinematic state can still remain a high accuracy of around 30 *cm*

and in the static case this high-accuracy period can last as long as more than 20 seconds. With the increased number of satellites observed, the positioning errors could be substantially reduced. In kinematic state, positioning errors can be nearly within half meter over the 1-min gap of having three satellites observed.

For the two van tests, due to the frequent signal interruptions, AR is not feasible though uncombined phase biases are corrected. In the complex road test, PPP-alone has an accuracy of 51, 61, 99 *cm* in the N E U direction respectively. TCI achieves the best accuracy, which is 38, 48 and 67 *cm* with an improvement of 25%, 21% and 32% respectively compared to PPP. The LCI performance is in the middle of PPP and TCI. After applying the uncombined biases, higher positioning accuracy is obtained. TCI still gives the highest accuracy of 32, 29, 41 *cm* for the N E U component, which is improved by 18%, 40%, and 39% respectively compared with uncorrected TCI. In the city center test, the contribution of bias correction is mainly on the up component. TCI still achieves the best performance with an accuracy of 47, 26 and 55 cm in the N E U direction respectively after bias correction with an improvement of 43% on the up component. The bias-corrected LCI has an accuracy of 118, 49 and 179 *cm* on the N E U component and PPP of 183, 51 and 242 cm.

10.2 Innovation summary

This work makes contribution to the validation of the flexibility of the latest GNSS code and phase uncombined bias products, especially for the AR of an arbitrary PPP model established at a user side.

This validation is accomplished through the two following designed experiments:

- AR of two basic PPP models: the ionosphere-free and the ionosphere-estimated models with the application of the GNSS uncombined code and phase bias products.
- PPP/INS integration including LCI and TCI with AR using the uncom-

bined bias products.

It is demonstrated that the uncombined bias products could allow for AR of different PPP modelling at a user end, which would be compatible with the diverse PPP applications for better positioning accuracy. Besides, PPP/INS integration with the uncombined bias correction yield better positioning performance, which could be used as an effective technique for robust real-time air-borne or land-borne navigation.

10.3 Limitations and future work

10.3.1 Limitations

This research investigated the application of GNSS uncombined bias products on ionosphere-free and ionosphere-estimated PPP models with AR. Nevertheless, the following points are not covered in this study:

- The positioning performance of multi-frequency ionosphere-free PPP AR using uncombined bias products.
- The contribution of external precise ionospheric information to the performance of multi-frequency PPP AR with the uncombined bias correction.

10.3.2 Future work

Accordingly, these following work could be carried out in the near future based on the POINT software:

- GPS L1/L2/L5 Galileo E1/E5a/E5b/E6 ionosphere-free PPP AR using CNES real-time/post-processed uncombined bias products.
- GPS L1/L2/L5 Galileo E1/E5a/E5b/E6 ionosphere-estimated PPP AR using CNES real-time/post-processed uncombined bias products with the correction of external ionospheric information.
- GPS/GLONASS/Galileo/BeiDou multi-frequency ionodphere-free/ionosphere-estimated PPP AR using uncombiend bias products.

- The evaluation of uncombined bias products from other institutions of the above PPP models.
- Direct satellite orbit, clock and bias estimation based on the raw undifferenced and uncombined GNSS observation equations allowing for phase AR of any kind at a user side.
- The performance of the integrated INS and the above PPP models.

10.4 GNSS PPP Perspectives

GNSS multi-frequency PPP can provide a series of phase widelane combinations and the phase ambiguities of these widelane combinations can be resolved easily due to the longer wavelength (meter level) with the phase bias information. As a result, these phase combinations could be used as precise 'pseudorange' to contribute to positioning. As demonstrated in Laurichesse and Banville (2018), GNSS multi-frequency PPP is capable of instantaneous centimeter-level positioning. This single-epoch PPP feature is free of phase cycle slip detection and correction because the phase ambiguity is resolved at each epoch. It is anticipated that single-epoch PPP would be an effective alternative to the traditional RTK and greatly increase the navigation resilience especially in harsh GNSS environment.

Bibliography

Abd Rabbou M, El-Rabbany A (2015) Tightly coupled integration of GPS precise point positioning and MEMS-based inertial systems. GPS Solutions 19(4):601–609, DOI 10.1007/s10291-014-0415-3, URL http://dx.doi.org/10.1007/s10291-014-0415-3

Banville S, Langley RB (2013) Mitigating the impact of ionospheric cycle slips in GNSS observations. DOI 10.1007/s00190-012-0604-1

Banville S, Resources N, Banville S (2016) GLONASS ionosphere-free ambiguity resolution for precise point positioning. Journal of Geodesy (February), DOI 10.1007/s00190-016-0888-7

Banville S, Geng J, Loyer S, Schaer S, Springer T, Strasser S (2020) On the interoperability of IGS products for precise point positioning with ambiguity resolution. Journal of Geodesy 94(1):1–15, DOI 10.1007/s00190-019-01335-w, URL https://doi.org/10.1007/s00190-019-01335-w

Bierman GJ (1975) Measurement updating using the u-d factorization. In: 1975 IEEE Conference on Decision and Control including the 14th Symposium on Adaptive Processes, pp 337–346, DOI 10.1109/CDC.1975.270702

Bisnath S, Gao Y (2008) Current State of Precise Point Positioning and Future Prospects and Limitations, vol 133, pp 615–623. DOI 10.1007/978-3-540-85426-5_71

Blewitt G (1990) An automatic editing algorithm for gps data. Geophysical Research Letters 17:199–202

Chapra SC, Canale RP (2014) Numerical Methods for Engineers. Series of books in geology, McGraw Hill Higher Education

Cheng S, Wang J, Peng W (2017) Statistical analysis and quality control for GPS fractional cycle bias and integer recovery clock estimation with raw and combined observation models. Advances in Space Research 60(12):2648–2659, DOI 10.1016/j.asr.2017.06.053, URL https://doi.org/10.1016/j.asr.2017.06.053

Choy S, Bisnath S, Rizos C (2016) Uncovering common misconceptions in GNSS Precise Point Positioning and its future prospect. GPS Solutions DOI 10.1007/s10291-016-0545-x, URL http://link.springer.com/10.1007/s10291-016-0545-x

Collins P, Bisnath S, Lahaye F, Héroux P (2010) Undifferenced GPS Ambiguity Resolution Using the Decoupled Clock Model and Ambiguity Datum Fixing. Navigation 57(2):123–135, DOI 10.1002/j.2161-4296.2010.tb01772.x, URL http://doi.wiley.com/10.1002/j.2161-4296.2010.tb01772.x

Du S, Gao Y (2012) Inertial aided cycle slip detection and identification for integrated PPP GPS and INS. Sensors (Switzerland) 12(11):14344–14362, DOI 10.3390/s121114344

Dunn MJ (2021) Interface specification, is-gps-200m. https://www.gps.gov/technical/icwg/IS-GPS-200M.pdf, accessed: 2022-08

Duong V, Harima K, Choy S, Laurichesse D, Rizos C (2020) Assessing the performance of multi-frequency gps, galileo and beidou ppp ambiguity resolution. Journal of Spatial Science 65(1):61–78, DOI 10.1080/14498596.2019.1658652, URL https://doi.org/10.1080/14498596.2019.1658652, https://doi.org/10.1080/14498596.2019.1658652

Elsheikh M, Abdelfatah W, Wahdan A, Gao Y (2018) Low-cost PPP/INS integration for continuous and precise vehicular navigation. Proceedings of the 31st International Technical Meeting of the Satellite Division of the Institute of Navigation, ION GNSS+ 2018 (January 2019):3169–3178, DOI 10.33012/2018.15985

European Union D (2021) European gnss (galileo) open service signal-in-space interface control document. https://www.gsc-europa.eu/sites/default/files/sites/all/files/Galileo_OS_SIS_ICD_v2.0.pdf, accessed: 2022-08

Gao Z, Ge M, Shen W, Li Y, Chen Q, Zhang H, Niu X (2017a) Evaluation on the impact of IMU grades on BDS + GPS PPP/INS tightly coupled integration. Advances in Space Research 60(6):1283–1299, DOI 10.1016/j.asr.2017.06.022, URL http://dx.doi.org/10.1016/j.asr.2017.06.022

Gao Z, Zhang H, Ge M, Niu X, Shen W, Wickert J, Schuh H (2017b) Tightly coupled integration of multi-GNSS PPP and MEMS inertial measurement unit data. GPS Solutions 21(2):377–391, DOI 10.1007/s10291-016-0527-z

Gautier JD (2003) Gps/ins generalized evaluation tool (giget) for the design and testing of integrated navigation systems. PhD thesis, STANFORD UNIVERSITY

Ge M, Gendt G, Rothacher M, Shi C, Liu J (2008) Resolution of GPS carrier-phase ambiguities in Precise Point Positioning (PPP) with daily observations. Journal of Geodesy 82(7):389–399, DOI 10.1007/s00190-007-0187-4

Geng J, Guo J (2020a) Beyond three frequencies: an extendable model for single-epoch decimeter-level point positioning by exploiting Galileo and BeiDou-3 signals. Journal of Geodesy 94(1), DOI 10.1007/s00190-019-01341-y, URL https://doi.org/10.1007/s00190-019-01341-y

Geng J, Guo J (2020b) Beyond three frequencies: an extendable model for single-epoch decimeter-level point positioning by exploiting

Galileo and BeiDou-3 signals. Journal of Geodesy 94(1), DOI 10.1007/s00190-019-01341-y, URL https://doi.org/10.1007/s00190-019-01341-y

Geng J, Meng X, Dodson AH, Teferle FN (2010) Integer ambiguity resolution in precise point positioning: Method comparison. Journal of Geodesy 84(9):569–581, DOI 10.1007/s00190-010-0399-x

Geng J, Shi C, Ge M, Dodson AH, Lou Y, Zhao Q, Liu J (2012) Improving the estimation of fractional-cycle biases for ambiguity resolution in precise point positioning. Journal of Geodesy 86(8):579–589, DOI 10.1007/s00190-011-0537-0

Geng J, Guo J, Meng X, Gao K (2020) Speeding up PPP ambiguity resolution using triple-frequency GPS/BeiDou/Galileo/QZSS data. Journal of Geodesy 94(1):1–15, DOI 10.1007/s00190-019-01330-1, URL https://doi.org/10.1007/s00190-019-01330-1

Geng J, Wen Q, Zhang Q, Li G, Zhang K (2022) GNSS observable-specific phase biases for all-frequency PPP ambiguity resolution. Journal of Geodesy 96(2):1–18, DOI 10.1007/s00190-022-01602-3, URL https://doi.org/10.1007/s00190-022-01602-3

Glaner M, Weber R (2021) PPP with integer ambiguity resolution for GPS and Galileo using satellite products from different analysis centers. GPS Solutions 25(3):1–13, DOI 10.1007/s10291-021-01140-z, URL https://doi.org/10.1007/s10291-021-01140-z

Groves PD (2013) Principles of GNSS, inertial, and multisensor integrated navigation systems / Paul D. Groves., second edition. edn. GNSS technology and applications series, Artech House

Gu S, Dai C, Fang W, Zheng F, Wang Y, Zhang Q, Lou Y, Niu X (2021) Multi-GNSS PPP/INS tightly coupled integration with atmospheric augmentation and its application in urban vehicle navigation. Journal of Geodesy 95(6):1–15, DOI 10.1007/s00190-021-01514-8, URL https://doi.org/10.1007/s00190-021-01514-8

Gu S, Dai C, Mao F, Fang W (2022) Integration of Multi-GNSS PPP-RTK/INS/Vision with a Cascading Kalman Filter for Vehicle Navigation in Urban Areas. Remote Sensing 14(17), DOI 10.3390/rs14174337

Guo J, Geng J (2018) GPS satellite clock determination in case of inter-frequency clock biases for triple-frequency precise point positioning. Journal of Geodesy 92(10):1133–1142, DOI 10.1007/s00190-017-1106-y, URL https://doi.org/10.1007/s00190-017-1106-y

Gurtner W, Estey L (2006) Rinex3.05. Rinex305

Han H, Xu T, Wang J (2016) Tightly coupled integration of GPS ambiguity fixed precise point positioning and MEMS-INS through a troposphere-constrained adaptive kalman filter. Sensors (Switzerland) 16(7), DOI 10.3390/s16071057

Heiskanen W, Moritz H (1967) Physical Geodesy. Series of books in geology, W. H. Freeman, https://books.google.co.uk/books?id=Pzy4AAAAIAAJ (accessed on 20/10/2019)

Héroux P, Kouba J (2001) GPS precise point positioning using IGS orbit products. Physics and Chemistry of the Earth, Part A: Solid Earth and Geodesy 26(6-8):573–578, DOI 10.1016/S1464-1895(01)00103-X

Herrera AM, Suhandri HF, Realini E, Reguzzoni M, de Lacy MC (2016) goGPS: open-source MATLAB software. GPS Solutions 20(3):595–603, DOI 10.1007/s10291-015-0469-x

Hide C (2003) Integration of gps and low cost ins measurements. PhD thesis, The University of Nottingham

Hide C, Pinchin J, Park D (2007) Development of a low cost multiple GPS antenna attitude system. 20th International Technical Meeting of the Satellite Division of The Institute of Navigation 2007 ION GNSS 2007 1(September):88–95

Hofmann-Wellenhof B, Lichtenegger H, Collins J (2001) Global positioning system: theory and practice. Springer Vienna

Juan JM, Hernandez-Pajares M, Sanz J, Ramos-Bosch P, Aragon-Angel A, Orus R, Ochieng W, Feng S, Jofre M, Coutinho P, Samson J, Tossaint M (2012) Enhanced precise point positioning for gnss users. IEEE Transactions on Geoscience and Remote Sensing 50(10):4213–4222, DOI 10.1109/TGRS.2012.2189888

Katsigianni G, Loyer S, Perosanz F (2019a) Ppp and ppp-ar kinematic post-processed performance of gps-only, galileo-only and multi-gnss. Remote Sensing 11(21), DOI 10.3390/rs11212477, URL https://www.mdpi.com/2072-4292/11/21/2477

Katsigianni G, Perosanz F, Loyer S, Gupta M (2019b) Galileo millimeter-level kinematic precise point positioning with ambiguity resolution. Earth, Planets and Space 71(1):1–6, DOI 10.1186/s40623-019-1055-1, URL https://doi.org/10.1186/s40623-019-1055-1

Kouba J (2009) A Guide to using international GNSS Service (IGS) Products. Geodetic Survey Division Natural Resources Canada Ottawa 6:34, URL http://graypantherssf.igs.org/igscb/resource/pubs/UsingIGSProductsVer21.pdf

Laurichesse D (2010) The ppp-wizard project. http://www.ppp-wizard.net/upload.html, accessed: 2022-03

Laurichesse D (2011) The CNES Real-time PPP with undifferenced integer ambiguity resolution demonstrator. 24th International Technical Meeting of the Satellite Division of the Institute of Navigation 2011, ION GNSS 2011 1:654–662

Laurichesse D (2012) Phase biases estimation for integer ambiguity resolution. URL https://igs.bkg.bund.de/root_ftp/NTRIP/documentation/PPP-RTK2012/14_Laurichesse_Denis.pdf, accessed: 2020-10-29

Laurichesse D (2014) Phase biases for ambiguity resolution from an undifferenced to an uncombined formulation. URL http://www.ppp-wizard.net/Articles/WhitePaperL5.pdf, accessed: 2020-11-01

Laurichesse D, Banville S (2018) Innovation: Instantaneous centimeter-level multi-frequency precise point positioning. GPS World 2018(September)

Laurichesse D, Langley R (2015) Handling the biases for improved triple-frequency ppp convergence. GPS World DOI https://www.gpsworld.com/innovation-carrier-phase-ambiguity-resolution/

Laurichesse D, Privat A (2015) An open-source PPP client implementation for the CNES PPP-WIZARD demonstrator. 28th International Technical Meeting of the Satellite Division of the Institute of Navigation, ION GNSS 2015 4:2780–2789

Laurichesse D, Mercier F, Berthias JP, Broca P, Cerri L (2009) Integer ambiguity resolution on undifferenced GPS phase measurements and its application to PPP and satellite precise orbit determination. Navigation, Journal of the Institute of Navigation 56(2):135–149, DOI 10.1002/j.2161-4296.2009.tb01750.x

Leica-Geosystems-AG (2016) Leica gs10/gs15 user manual. http://www.surveyteq.com/uploads/p_C9C59E1C-40F3-A040-B287-D30E0C6B00A4-1517301551.pdf, accessed: 2021-09-30

Li P, Zhang X, Ren X, Zuo X, Pan Y (2016) Generating GPS satellite fractional cycle bias for ambiguity-fixed precise point positioning. GPS Solutions 20(4):771–782, DOI 10.1007/s10291-015-0483-z

Li P, Jiang X, Zhang X, Ge M, Schuh H (2020a) GPS + Galileo + BeiDou precise point positioning with triple-frequency ambiguity resolution. GPS Solutions 24(3):1–13, DOI 10.1007/s10291-020-00992-1, URL https://doi.org/10.1007/s10291-020-00992-1

Li X, Zhang X, Ge M (2011) Regional reference network augmented precise point positioning for instantaneous ambiguity resolution. Journal of Geodesy 85(3):151–158, DOI 10.1007/s00190-010-0424-0

Li X, Ge M, Zhang H (2013) A method for improving uncalibrated phase delay estimation and ambiguity-fixing in real-time precise point positioning. Journal of Geodesy pp 405–416, DOI 10.1007/s00190-013-0611-x

Li X, Zhang X, Ren X, Fritsche M, Wickert J, Schuh H (2015) Precise positioning with current multi-constellation global navigation satellite systems: Gps, glonass, galileo and beidou. Scientific reports 5:8328, DOI 10.1038/srep08328

Li X, Li X, Yuan Y, Zhang K, Zhang X, Wickert J (2018) Multi-GNSS phase delay estimation and PPP ambiguity resolution: GPS, BDS, GLONASS, Galileo. Journal of Geodesy 92(6):579–608, DOI 10.1007/s00190-017-1081-3

Li X, Li X, Liu G, Feng G, Yuan Y, Zhang K, Ren X (2019) Triple-frequency PPP ambiguity resolution with multi-constellation GNSS: BDS and Galileo. Journal of Geodesy 93(8):1105–1122, DOI 10.1007/s00190-019-01229-x, URL https://doi.org/10.1007/s00190-019-01229-x

Li X, Liu G, Li X, Zhou F, Feng G, Yuan Y, Zhang K (2020b) Galileo PPP rapid ambiguity resolution with five-frequency observations. GPS Solutions 24(1):1–13, DOI 10.1007/s10291-019-0930-3, URL https://doi.org/10.1007/s10291-019-0930-3

Li X, Li X, Huang J, Shen Z, Wang B, Yuan Y, Zhang K (2021) Improving PPP–RTK in urban environment by tightly coupled integration of GNSS and INS. Journal of Geodesy 95(12):1–18, DOI 10.1007/s00190-021-01578-6, URL https://doi.org/10.1007/s00190-021-01578-6

Li X, Li X, Jiang Z, Xia C, Shen Z, Wu J (2022a) A unified model of GNSS phase/code bias calibration for PPP ambiguity resolution with GPS, BDS, Galileo and GLONASS multi-frequency observations. GPS Solutions 26(3):1–16, DOI 10.1007/s10291-022-01269-5, URL https://doi.org/10.1007/s10291-022-01269-5

Li X, Li X, Li S, Zhou Y, Sun M, Xu Q, Xu Z (2022b) Centimeter-accurate vehicle navigation in urban environments with a tightly integrated PPP-RTK/MEMS/vision system. GPS Solutions 26(4), DOI 10.1007/s10291-022-01306-3

Liu S, Sun F, Zhang L, Li W, Zhu X (2016) Tight integration of ambiguity-fixed PPP and INS: model description and initial results. GPS Solutions 20(1):39–49, DOI 10.1007/s10291-015-0464-2

Liu T, Jiang W, Laurichesse D, Chen H, Liu X, Wang J (2020) Assessing GPS/Galileo real-time precise point positioning with ambiguity resolution based on phase biases from CNES. Advances in Space Research DOI 10.1016/j.asr.2020.04.054, URL https://doi.org/10.1016/j.asr.2020.04.054

Liu Z (2011) A new automated cycle slip detection and repair method for a single dual-frequency GPS receiver. Journal of Geodesy 85(3):171–183, DOI 10.1007/s00190-010-0426-y

Loyer S, Perosanz F, Mercier F, Capdeville H, Marty JC (2012) Zero-difference GPS ambiguity resolution at CNES-CLS IGS Analysis Center. Journal of Geodesy 86(11):991–1003, DOI 10.1007/s00190-012-0559-2

Melbourne W (1985) The case for ranging in gps-based geodetic systems. In: Proceedings of 1st International Symposium on Precise Positioning with the Global Positioning System, Rockville, MD, USA, p 373–386

Montenbruck O, Etal (2014) IGS-MGEX Preparing the Ground for Multi-COnstellation GNSS Science. Inside GNSS (January/February):42–49, URL http://www.insidegnss.com/auto/janfeb14-MONTENBRUCK.pdf

Montenbruck O, Hugentobler U, Dach R, Steigenberger P, Hauschild A (2012) Apparent clock variations of the Block IIF-1 (SVN62) GPS satellite. GPS Solutions 16(3):303–313, DOI 10.1007/s10291-011-0232-x

Montenbruck O, Steigenberger P, Hauschild A (2015) Broadcast versus precise ephemerides: a multi-GNSS perspective. GPS Solutions 19(2):321–333, DOI 10.1007/s10291-014-0390-8

Morton YTJ, van Diggelen F, Jr JJS, Parkinson BW, Lo S, Gao G (2020) Position, Navigation, and Timing Technologies in the 21st Century: Integrated Satellite Navigation, Sensor Systems, and Civil Applications. Wiley-IEEE Press

Muhammad S (2014) GNSS / INS Integration in Urban Areas. ION GNSS 2010 – Session D3 – Portland, OR – Sept 21-24, 2010 (April):1–8

Nadarajah N, Khodabandeh A, Wang K, Choudhury M, Teunissen PJ (2018) Multi-GNSS PPP-RTK: From large- to Small-Scale networks. Sensors (Switzerland) 18(4):1–18, DOI 10.3390/s18041078

NovAtel (2022) Inertial explorer show map window, waypoint user documentation. https://docs.novatel.com/Waypoint/Content/GrafNav/Show_Map_Window.htm, accessed: 2022-Oct

Novatel-SPAN-UIMU-LCI (2014) Tactical grade, low noise imu delivers 3d position, velocity and attitude solution as part of span technology. http://www.canalgeomatics.com/product_files/novatel-uimu-lci-datasheet_372.pdf, accessed: 2021-09-30

Odolinski R, Teunissen PJ (2020) Best integer equivariant estimation: performance analysis using real data collected by low-cost, single- and dual-frequency, multi-GNSS receivers for short- to long-baseline RTK positioning. Journal of Geodesy 94(9):1–17, DOI 10.1007/s00190-020-01423-2, URL https://doi.org/10.1007/s00190-020-01423-2

Pan L, Zhang X, Li X, Liu J, Li X (2017) Characteristics of inter-frequency clock bias for Block IIF satellites and its effect on triple-frequency GPS precise point positioning. GPS Solutions 21(2):811–822, DOI 10.1007/s10291-016-0571-8

Pan L, Zhang X, Guo F, Liu J (2019) GPS inter-frequency clock bias estimation for both uncombined and ionospheric-free combined triple-frequency precise point positioning. Journal of Geodesy 93(4):473–487, DOI 10.1007/s00190-018-1176-5, URL https://doi.org/10.1007/s00190-018-1176-5

Roesler G, Martell H (2009) Tightly coupled processing of precise point position (PPP) and INS data. 22nd International Technical Meeting of the Satellite Division of the Institute of Navigation 2009, ION GNSS 2009 3:1740–1747

Schaer S (2016) Sinex bias—solution (software/technique) inde- pendent exchange format for gnss biases version 1.00. http://ftp.aiub.unibe.ch/bcwg/format/draft/sinex_bias_100_feb07.pdf, accessed: 2022-08

Scherzinger BM (2000) Precise robust positioning with inertial/gps rtk

Shi J, Gao Y (2014) A comparison of three PPP integer ambiguity resolution methods. GPS Solutions 18(4):519–528, DOI 10.1007/s10291-013-0348-2

Shin EH (2001) Accuracy improvement of low cost ins/gps for land applications. Master's thesis, university of Calgary

Steigenberger P, Montenbruck O, Weber R, Hugentobler U (2013) Status and Perspective of the IGS Multi-GNSS Experiment (MGEX). In: EGU General Assembly Conference Abstracts, EGU General Assembly Conference Abstracts, pp EGU2013–2558

Strasser S, Mayer-Gürr T, Zehentner N (2019) Processing of GNSS constellations and ground station networks using the raw observation approach. Journal of Geodesy 93(7):1045–1057, DOI 10.1007/s00190-018-1223-2, URL https://doi.org/10.1007/s00190-018-1223-2

Subirana JS, Zornoza JJ, Hernández-Pajares M (2013) GNSS DATA PROCESSING. ESA Communications, https://gssc.esa.int/navipedia/GNSS_Book/ESA_GNSS-Book_TM-23_Vol_I.pdf (accessed on 20/01/2019)

Takasu T (2009) Rtklib: Open source program package for rtk-gps,. http://gpspp.sakura.ne.jp/paper2005/foss4g_2009_rtklib.pdf, accessed: 2021-09-30

Takasu T, Kasai S, Consultant T (2005) Precise Orbit Determination of GPS Satellites using Carrier Phase Measurements. Orbit An International Journal On Orbital Disorders And Facial Reconstructive Surgery (1)

Tegedor J, Liu X, Jong K, Goode M, Ovstedal O, Vigen E (2014a) Estimation of galileo uncalibrated hardware delays for ambiguity fixed precise point positioning. vol 3

Tegedor J, Øvstedal O, Vigen E (2014b) Precise orbit determination and point positioning using GPS, Glonass, Galileo and BeiDou. Journal of Geodetic Science 4(1):65–73, DOI 10.2478/jogs-2014-0008, URL http://www.degruyter.com/view/j/jogs.2014.4.issue-1/jogs-2014-0008/jogs-2014-0008.xml

Teunissen PJ (1995) The least-squares ambiguity decorrelation adjustment: a method for fast GPS integer ambiguity estimation. Journal of Geodesy 70(1-2):65–82, DOI 10.1007/BF00863419

Teunissen PJ (2003) Theory of integer equivariant estimation with application to GNSS. Journal of Geodesy 77(7-8):402–410, DOI 10.1007/s00190-003-0344-3

Teunissen PJG (1999) An optimality property of the integer least-squares estimator. Journal of Geodesy pp 587–593

Thornton CL, Bierman GJ (1975) Gram-schmidt algorithms for covariance propagation. In: 1975 IEEE Conference on Decision and Control including the 14th Symposium on Adaptive Processes, pp 489–498, DOI 10.1109/CDC.1975.270739

Vana S, Naciri N, Bisnath S (2019) Low-cost, dual-frequency PPP GNSS and MEMS-IMU integration performance in obstructed environments. Proceedings of the 32nd International Technical Meeting of the Satellite Division of the Institute of Navigation, ION GNSS+ 2019 pp 3005–3018, DOI 10.33012/2019.16966

Verhagen S, Li B, Teunissen PJG (2013) Computers & Geosciences Ps-LAMBDA : Ambiguity success rate evaluation software for interferometric applications. Computers and Geosciences 54:361–376, DOI 10.1016/j.cageo.2013.01.014, URL http://dx.doi.org/10.1016/j.cageo.2013.01.014

Wabbena G, Schmitz M, Bagge A (2005) Ppp-rtk: Precise point positioning using state-space representation in rtk networks

Wang J, Huang G, Yang Y, Zhang Q, Gao Y, Xiao G (2019) FCB estimation with three different PPP models: equivalence analysis and experiment tests. GPS Solutions 23(4):1–14, DOI 10.1007/s10291-019-0887-2, URL https://doi.org/10.1007/s10291-019-0887-2

Wu JT, Wu SC, Hajj GA, Bertiger WI, Lichten SM (1993) Effects of antenna orientation on gps carrier phase. Manuscripta Geodaetica 18(2):91–98, URL www.scopus.com

Wübbena G (1985) Software developments for geodetic positioning with gps using ti-4100 code and carrier measurements. In: 1st international symposium on precise positioning with the global positioning system, Rockville, MD, USA, p 403–412

Zhang X, Zhu F, Zhang Y, Mohamed F, Zhou W (2018) The improvement in integer ambiguity resolution with INS aiding for kinematic precise point positioning. Journal of Geodesy DOI 10.1007/s00190-018-1222-3, URL https://doi.org/10.1007/s00190-018-1222-3

Zhang Y, Gao Y (2008) Integration of INS and un-differenced GPS measurements for precise position and attitude determination. Journal of Navigation 61(1):87–97, DOI 10.1017/S0373463307004432

Zhao L, Blunt P, Yang L (2022) Performance Analysis of Zero-Difference GPS L1 / L2 / L5 and Galileo E1 / E5a / E5b / E6 Point Positioning Using CNES Uncombined Bias Products. Remote Sensing pp 1–17

Zumberge J, Heflin M, Jefferson D, Watkins M, Webb F (1997) Precise point positioning for the efficient and robust analysis of gps data from large networks. Journal of Geophysical Research 102, DOI 10.1029/96JB03860

Appendix A

Basic classes in POINT

The variables in GNSS positioning can be receiver-related like receiver coordinateds, satellite-related like satellite orbits and receiver- and satellite-related such like phase ambiguity. These variables are handled mainly by three classes in POINT: *stateManager*, *SpectralDensityManager* and *AmbiguityStateManager*. With these classes, a variable in POINT can be configured and accessed conveniently. In the following, each of the class is presented according to three C++ language properties for *class*, which are *Private members*, *User Interface* and *Inheritance relationship*.

A.1 The *stateManager* class

The private arrays inside the *stateManager* class map a variable name or ID, which is usually assigned by users and has been registered within POINT, to a unique index number and make it easy to access a variable merely through its name without concern about its actual index for a user.

- Private members

  The *stateManager* basically consists of two private arrays: n and $value$.

Table A.1: Basic elements in *stateManager*

Element	Explanation
n	Indices and their related variable names
$value$	Values of variables

For example $n[X] = 0$ means that the X component of a point in the Cartesian coordinate system has an index number 0. $value[X] = 3850179.38$ could be interpreted that the value of the X component of a point in the Cartesian coordinate system is 3850179.38 m.

- User Interface

  External users can access the n and $value$ arrays through the methods as below:

Table A.2: Interface for user in *stateManager*

Operation	Explanation
sn	Returns the index of a variable
get_value	Get the value of a variable
add_state	Add a new variable
remove	Remove an existing variable

For example $add\_state(X, 3850179.38)$ adds a new state X with value 3850179.38 into the the n and *value* arrays in Table A.1. When adding a new variable, the value of n will be incremented in order. If a variable is removed by the *remove* method, the associated n value is assigned to be -1. POINT uses this negative indicator to check if a variable is in the current states list.

- Inheritance relationship

  The *stateManager* class is not an independent class but derived from four base classes as shown in Figure A.1.

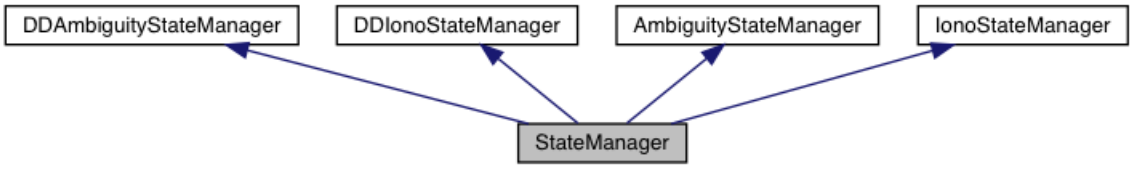

Figure A.1: *Inheritance diagram for stateManager. Generated by Doxygen.*

The *AmbiguityStateManager* and *IonoStateManager* are two specific data structure in POINT for managing the phase ambiguity and ionospheric delay parameters, see *AmbiguityStateManager* in the following. The prefix DD is for double-differencing modeling. A *pure virtual method* (C++ syntax) *newStateNo* is defined in all the four base classes and implemented in the *stateManager*, which extends the size of states. This function together with the *remove* method makes the length of the estimated states grow dynamically instead of a fixed size and increases the flexibility of POINT in dealing with parameters.

A.2 The *SpectralDensityManager* class

The *SpectralDensityManager* class handles the spectral density or the empirical standard deviation of a stochastic variable to be estimated. This value is used to compute the related process noise in the Kalman filter.

- Private members

  Similar to the *stateManager* structure, the *SpectralDensityManager* is mainly made up of two arrays n and q which save the indices and the values respectively of spectral densities. As an example, the command $add\_position\_n(std)$, see Table A.3, adds a new element into n and assigns a new value *std* to q with the same index, thus the standard deviation of the north component of a point in a local frame is stored.

- User Interface

  Users have to employ the variable-specific function to get its index in q and then access the spectral density by calling *get_value*(*index*). Table A.3 just lists an example for the north error variable. The compound command *get_value*(*position_n*()) then returns the spectral density of the north component of a point in a local frame.

Table A.3: Interface for user in *SpectralDensityManager*

Operation	Explanation
add_position_n	Add a spectral density for north error
position_n	Get the index of the spectral density for north error
get_value	Get a spectral density
remove	Remove an existing spectral density

- Inheritance relationship

  This class is also derived from the same base classes as in Figure A.1:

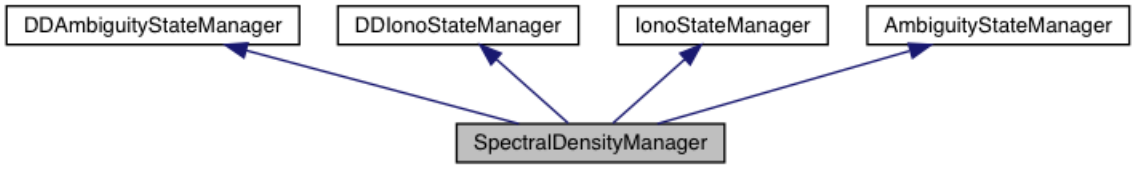

Figure A.2: *Inheritance diagram for SpectralDensityManager. Generated by Doxygen*

The *newStateNo* and the *remove* methods are also realized within the *stateManager*. Noted that when adding or removing a variable in POINT, both the *stateManager* and the *SpectralDensityManager* should be configured coordinately. The inconsistency of the indices within these two structure will cause severe mistake in the subsequent Kalman filter. However the size of states in *stateManager* may not be equal to the number of spectral densities in *SpectralDensityManager*. For example when predicting the error states in INS, the disturbing forces or the noises of gyro and accelerometer have to be mapped into the prediction which are not in the error states.

A.3 The *AmbiguityStateManager* class

The *AmbiguityStateManager* managers the GNSS phase ambiguity parameter and is one of the major characteristics of the POINT software.

- Private member

  This class manipulates a collection of ambiguity data. The ambiguity data in POINT mainly consists of the following elements:

Table A.4: The ambiguity data in POINT

Element	Explanation
Time	Time tag expressed in GPS week and seconds of week.
Constellation	GPS, Galileo, GLONASS, BeiDou (Currently supported)
Satellite ID	Satellite PRN number
Receiver ID	Receiver name
Frequency	The Frequency of ambiguity
Value	The value of ambiguity
Fix indicator	Fixed or not

- User Interface

  The *AmbiguityStateManager* primarily supports the following operations on a specific ambiguity:

Table A.5: Interface for user in *AmbiguityStateManager*

Operation	Explanation
add_ambiguity	Add a new ambiguity
ambiguity_sn	Get the index of a ambiguity in the states list
ambiguity_delete	Delete an existing ambiguity
get_ambiguity	Get a specific ambiguity

- Inheritance relationship

  The *AmbiguityStateManager* is a base class as shown in Figure A.1, see more in Figure A.1 and Figure A.2.

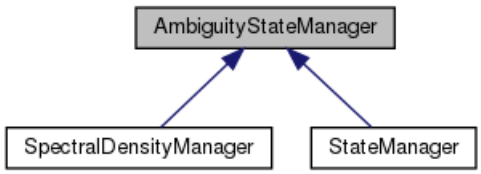

Figure A.3: *Inheritance diagram for AmbiguityStateManager. Generated by Doxygen*

The stored values in *stateManager* are kept synchronized with the actually estimated states in Kalman filter through two methods: *updateStateVector* and *updateStateCovariance*.

The *updateStateVector* method updates the states in Kalman filter with the latest values in *stateManager*. This typically happens when the states including position, velocity and attitudes in *stateManager* are corrected by INS update at a new epoch before entering the Kalman filter.

The *updateStateCovariance* uses the lastest states from Kalman filter to update the *stateManager*. This operation is required after each time Kalman filter is performed. POINT prints out the estimated products from the *stateManager* instead of directly from the Kalman filter.

Appendix B

POINT global PPP results of tested stations

This chapter gives a fairly full demonstration of PPP results of the selected global stations in Chapter 5.
The organization is as follows: first the dual-frequency ionosphere-free (DFIF) PPP results are presented, followed by the multi-frequency ionosphere-estimated (MFIE) results.

B.1 Dual-frequency ionosphere-free test

This section presents the DFIF PPP results. The superimposed positioning errors of each station for each testing days are given first; then the errors of multiple stations on each of the three days are depicted; last, the error values of all sessions of each station during the testing days are listed.

B.1.1 Superimposed results

Figure B.1 to Figure B.24 show the superimposed PPP errors of all sessions from the ambiguity-float and ambiguity-fixed solutions. It can be seen that for some ambiguity-fixed results e.g. Figure B.3 spike errors occur. This is mainly caused by wrong ambiguity fixing at these epochs and can be mitigated by using more strict fixing criteria. Effective validation methods for ambiguity-fixed solutions could also improve the results and this kind of technique needs further investigations.

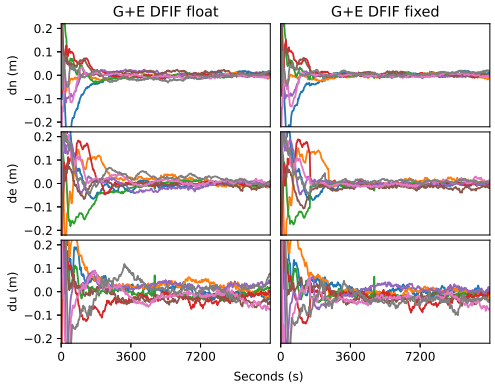

Figure B.1: *GPS L1/L2 and Galileo E1/E5a ionosphere-free float (left) and fixed (right) PPP results on 19/05/2020 at station BOGT. (Different color represents different session; dN, dE dU stand for positioning error in the north, east and up direction respectively; G and E denote for GPS and Galileo; DFIF is dual-frequency ionosphere-free, the same below*

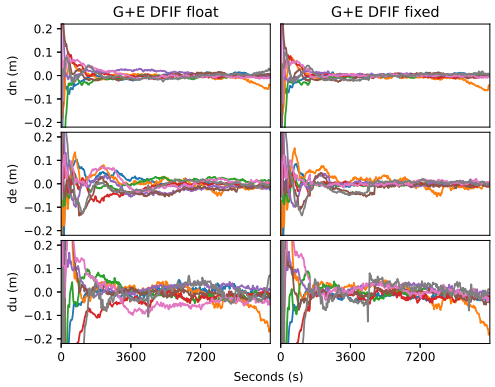

Figure B.2: *GPS L1/L2 and Galileo E1/E5a ionosphere-free float (left) and fixed (right) PPP results on 20/05/2020 at station BOGT.*

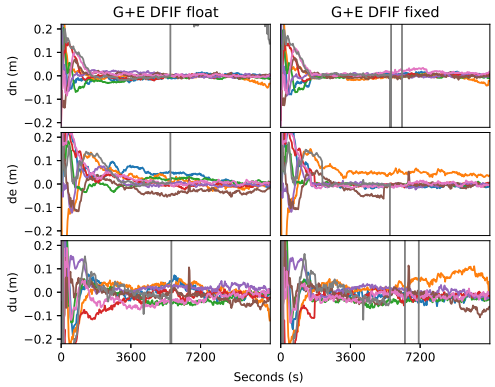

Figure B.3: *GPS L1/L2 and Galileo E1/E5a ionosphere-free float (left) and fixed (right) PPP results on 21/05/2020 at station BOGT.*

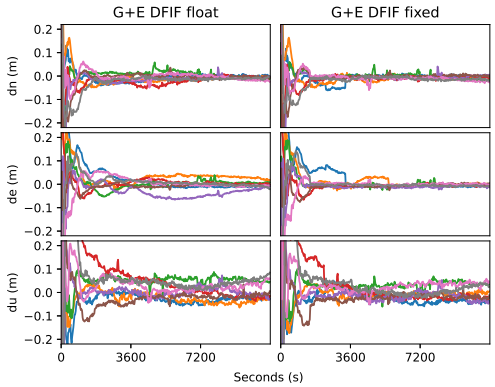

Figure B.4: *GPS L1/L2 and Galileo E1/E5a ionosphere-free float (left) and fixed (right) PPP results on 19/05/2020 at station BRST.*

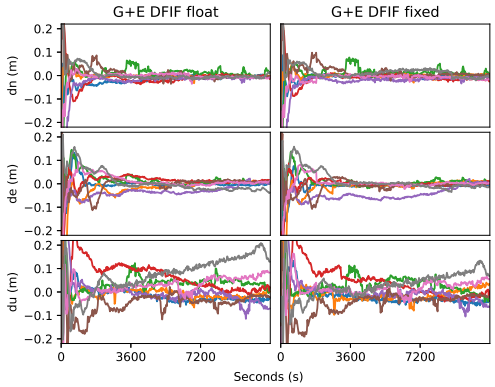

Figure B.5: *GPS L1/L2 and Galileo E1/E5a ionosphere-free float (left) and fixed (right) PPP results on 20/05/2020 at station BRST.*

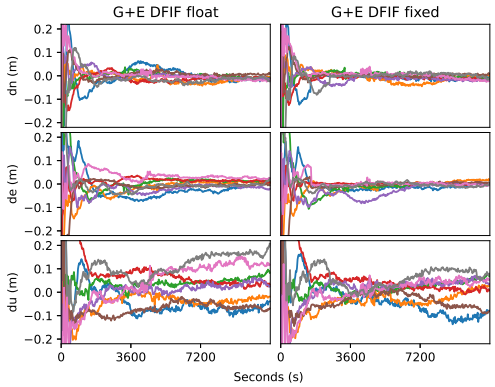

Figure B.6: *GPS L1/L2 and Galileo E1/E5a ionosphere-free float (left) and fixed (right) PPP results on 21/05/2020 at station BRST.*

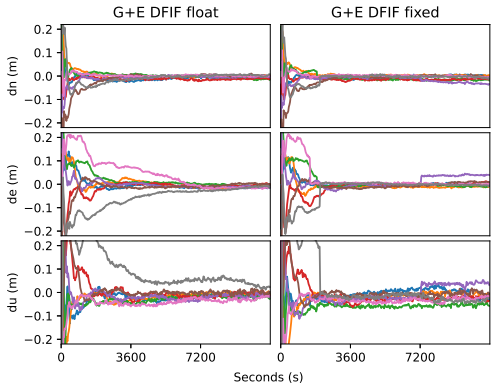

Figure B.7: *GPS L1/L2 and Galileo E1/E5a ionosphere-free float (left) and fixed (right) PPP results on 19/05/2020 at station BSHM.*

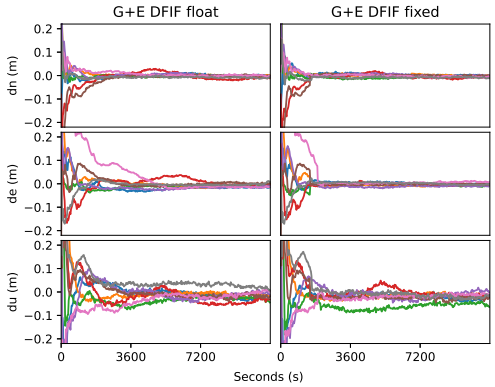

Figure B.8: *GPS L1/L2 and Galileo E1/E5a ionosphere-free float (left) and fixed (right) PPP results on 20/05/2020 at station BSHM.*

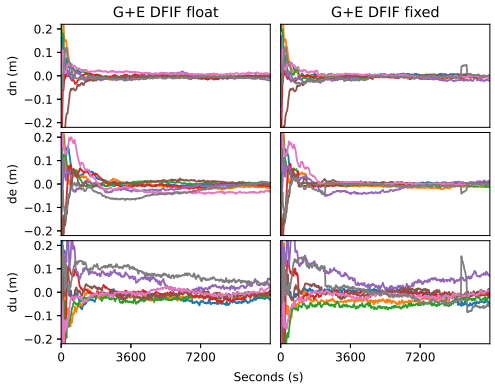

Figure B.9: *GPS L1/L2 and Galileo E1/E5a ionosphere-free float (left) and fixed (right) PPP results on 21/05/2020 at station BSHM.*

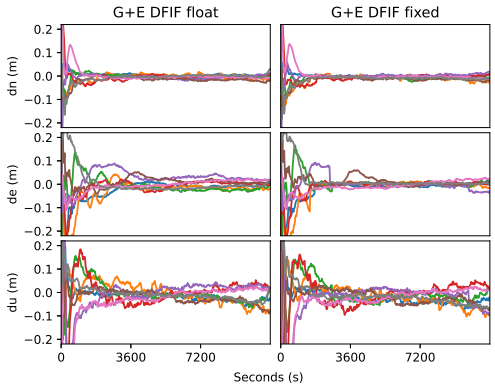

Figure B.10: *GPS L1/L2 and Galileo E1/E5a ionosphere-free float (left) and fixed (right) PPP results on 19/05/2020 at station CUSV.*

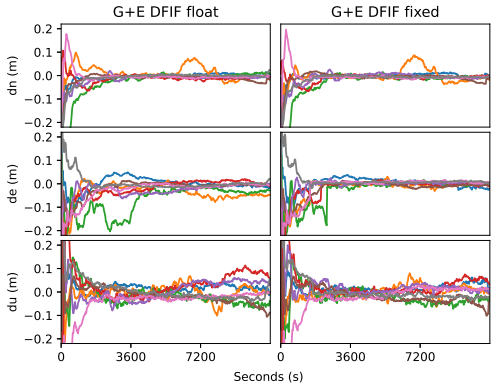

Figure B.11: *GPS L1/L2 and Galileo E1/E5a ionosphere-free float (left) and fixed (right) PPP results on 20/05/2020 at station CUSV.*

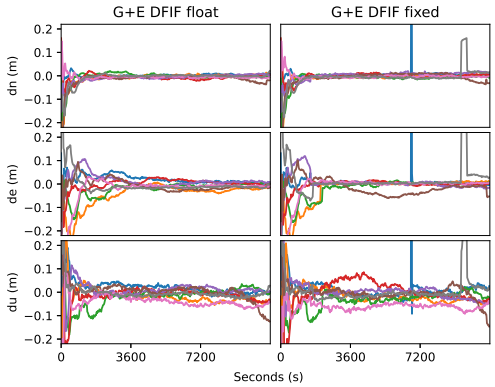

Figure B.12: *GPS L1/L2 and Galileo E1/E5a ionosphere-free float (left) and fixed (right) PPP results on 21/05/2020 at station CUSV.*

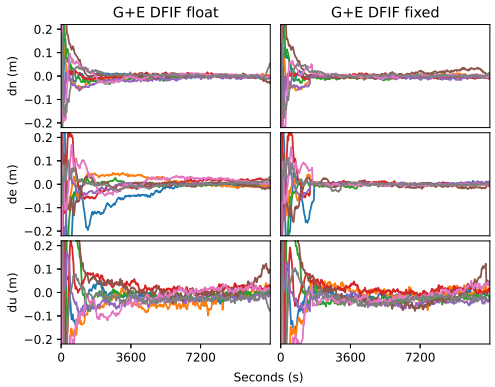

Figure B.13: *GPS L1/L2 and Galileo E1/E5a ionosphere-free float (left) and fixed (right) PPP results on 19/05/2020 at station PERT.*

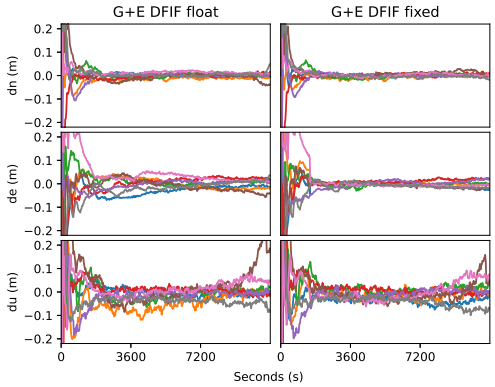

Figure B.14: *GPS L1/L2 and Galileo E1/E5a ionosphere-free float (left) and fixed (right) PPP results on 20/05/2020 at station PERT.*

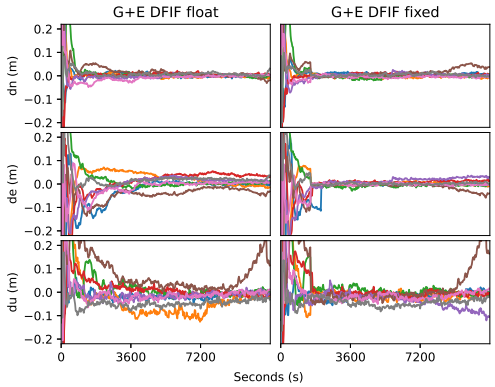

Figure B.15: *GPS L1/L2 and Galileo E1/E5a ionosphere-free float (left) and fixed (right) PPP results on 21/05/2020 at station PERT.*

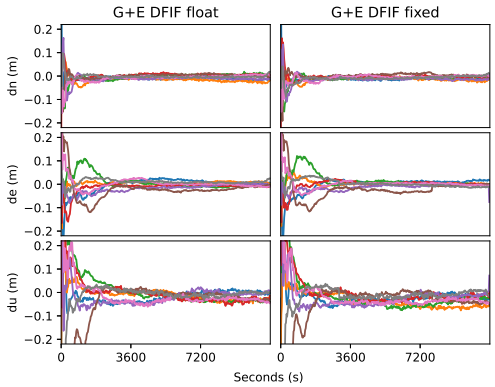

Figure B.16: *GPS L1/L2 and Galileo E1/E5a ionosphere-free float (left) and fixed (right) PPP results on 19/05/2020 at station POL2.*

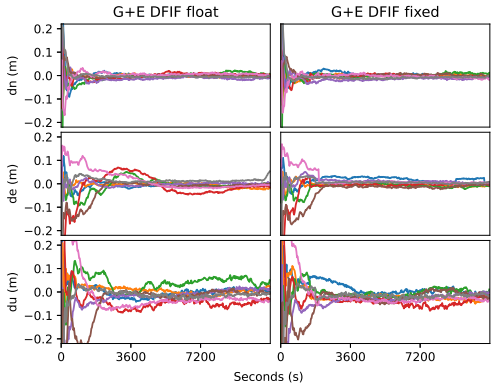

Figure B.17: *GPS L1/L2 and Galileo E1/E5a ionosphere-free float (left) and fixed (right) PPP results on 20/05/2020 at station POL2.*

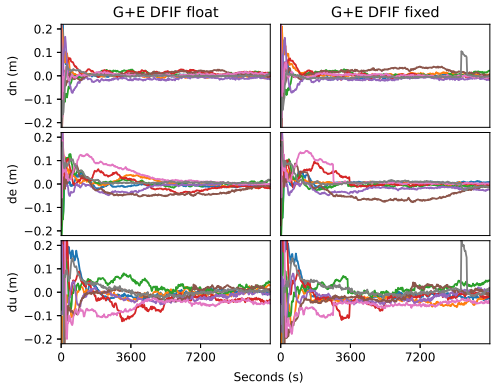

Figure B.18: *GPS L1/L2 and Galileo E1/E5a ionosphere-free float (left) and fixed (right) PPP results on 21/05/2020 at station POL2.*

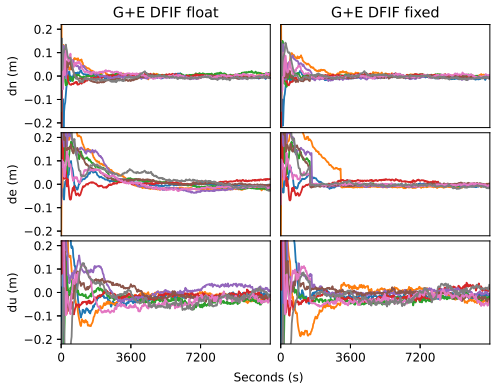

Figure B.19: *GPS L1/L2 and Galileo E1/E5a ionosphere-free float (left) and fixed (right) PPP results on 19/05/2020 at station QUIN.*

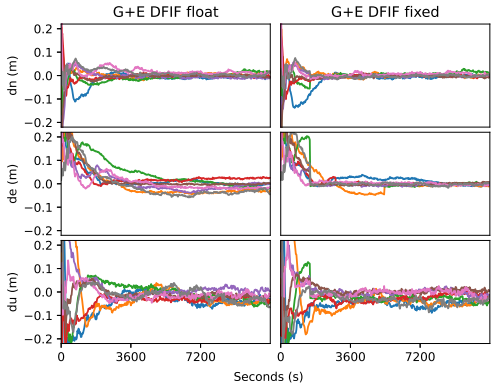

Figure B.20: *GPS L1/L2 and Galileo E1/E5a ionosphere-free float (left) and fixed (right) PPP results on 20/05/2020 at station QUIN.*

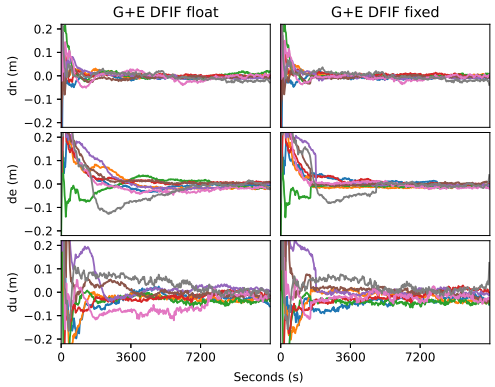

Figure B.21: *GPS L1/L2 and Galileo E1/E5a ionosphere-free float (left) and fixed (right) PPP results on 21/05/2020 at station QUIN.*

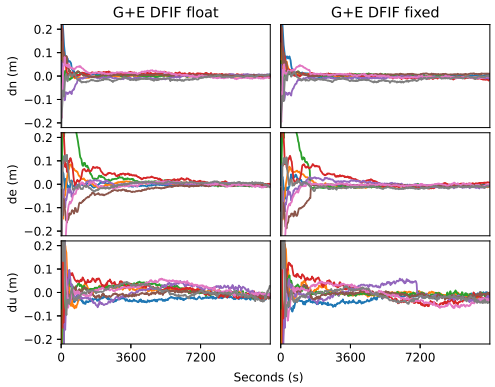

Figure B.22: *GPS L1/L2 and Galileo E1/E5a ionosphere-free float (left) and fixed (right) PPP results on 19/05/2020 at station ZAMB.*

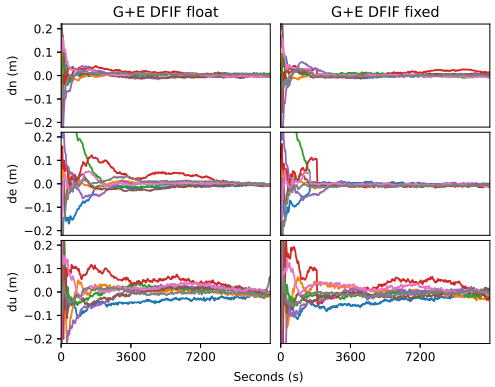

Figure B.23: *GPS L1/L2 and Galileo E1/E5a ionosphere-free float (left) and fixed (right) PPP results on 20/05/2020 at station ZAMB.*

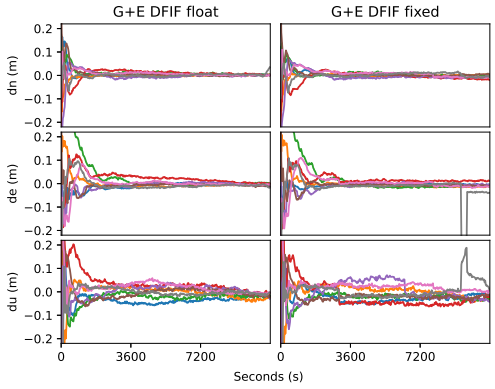

Figure B.24: *GPS L1/L2 and Galileo E1/E5a ionosphere-free float (left) and fixed (right) PPP results on 21/05/2020 at station ZAMB.*

B.1.2 Multi-station demonstration

Figure B.25 to Figure B.27 show the multi-station statistical errors for the three days. The 68-percentile is used for error representation. It can be seen that the ambiguity-fixed errors of some stations are degraded compared to the float errors, which could be caused by improper setting of ambiguity-fixing conditions and need to be further studied.

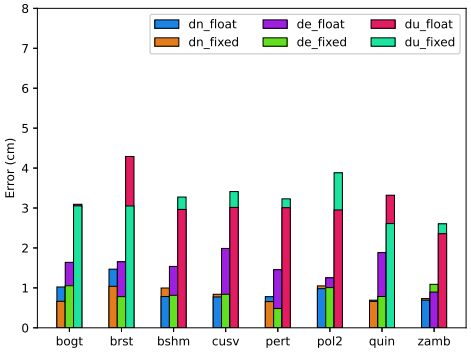

Figure B.25: *The 68th percentile of GPS/Galileo DFIF PPP solutions from selected stations on 19/05/2020*

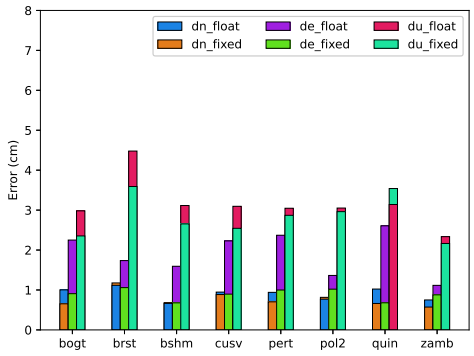

Figure B.26: *The 68th percentile of GPS/Galileo DFIF PPP solutions from selected stations on 20/05/2020*

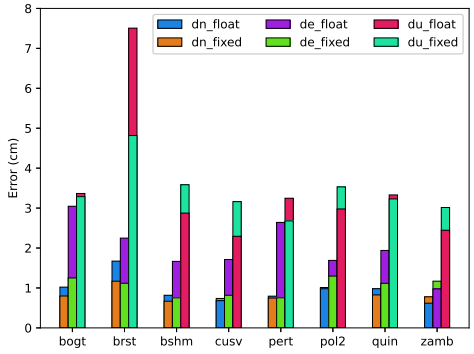

Figure B.27: *The 68th percentile of GPS/Galileo DFIF PPP solutions from selected stations on 21/05/2020*

B.1.3 Error values of all sessions

Table B.1 to Table B.8 list the error values of all sessions of the stations during the three days. The 68th percentile is still used to measure the error of each session.

Table B.1: The 68th percentiles of positioning errors in all sessions of GPS/Galileo DFIF PPP solutions at station BOGT during the three testing days

Station: BOGT Unit: m							
		Float			Fixed		
Date	Session	North	East	Up	North	East	Up
19/05/2020	0	0.0109	0.0119	0.0205	0.0098	0.0102	0.0146
	1	0.0064	0.0212	0.0338	0.0075	0.0109	0.0139
	2	0.0078	0.0114	0.0175	0.0052	0.0052	0.0215
	3	0.0051	0.006	0.0395	0.0049	0.0049	0.0328
	4	0.0135	0.0199	0.0296	0.0039	0.0058	0.0242
	5	0.014	0.009	0.0367	0.008	0.0201	0.0339
	6	0.0074	0.0124	0.0321	0.0053	0.0104	0.0381
	7	0.0171	0.0298	0.0288	0.0104	0.0124	0.042
20/05/2020	0	0.0089	0.0154	0.018	0.0055	0.0054	0.0232
	1	0.0103	0.0195	0.0353	0.0116	0.0231	0.0362
	2	0.0085	0.0189	0.027	0.0049	0.0058	0.0139
	3	0.0065	0.0138	0.0323	0.006	0.0058	0.0235
	4	0.0176	0.0312	0.0249	0.0045	0.0061	0.0249
	5	0.0093	0.034	0.0144	0.0097	0.0166	0.0168
	6	0.0094	0.0194	0.0571	0.004	0.0083	0.0181
	7	0.0119	0.0166	0.034	0.0092	0.0125	0.0363
21/05/2020	0	0.0109	0.0471	0.0239	0.0089	0.0109	0.0211
	1	0.0055	0.0263	0.0326	0.0099	0.0512	0.0568
	2	0.011	0.0204	0.0402	0.0052	0.0045	0.0377
	3	0.0072	0.0109	0.0246	0.0041	0.0042	0.0167
	4	0.012	0.0075	0.0233	0.0056	0.0056	0.0184
	5	0.0067	0.0365	0.0261	0.0068	0.0185	0.0373
	6	0.0055	0.0137	0.0419	0.0145	0.0097	0.0263
	7	0.5158	5.8792	5.3431	27.8479	30.653	54.8159

Table B.2: The 68th percentiles of positioning errors in all sessions of GPS/Galileo DFIF PPP solutions at station BRST during the three testing days

Station: BRST Unit: m							
		Float			Fixed		
Date	Session	North	East	Up	North	East	Up
19/05/2020	0	0.0144	0.013	0.0343	0.0051	0.0105	0.0384
	1	0.0172	0.0345	0.0381	0.0143	0.0093	0.0124
	2	0.0144	0.0112	0.0601	0.0096	0.0059	0.0371
	3	0.0248	0.0089	0.0532	0.0096	0.0069	0.0258
	4	0.0147	0.0491	0.016	0.0078	0.0128	0.0266
	5	0.0065	0.0079	0.0257	0.0058	0.0065	0.0257
	6	0.0129	0.0106	0.0368	0.0134	0.0037	0.0349
	7	0.0151	0.0095	0.0515	0.0147	0.0061	0.0265
20/05/2020	0	0.0161	0.0061	0.0325	0.006	0.0093	0.0379
	1	0.0052	0.0143	0.0173	0.0057	0.0106	0.0277
	2	0.0178	0.0099	0.0462	0.015	0.0082	0.0471
	3	0.0159	0.0202	0.0904	0.0112	0.006	0.05
	4	0.0148	0.0364	0.0238	0.0193	0.0578	0.0178
	5	0.0109	0.0128	0.0449	0.0084	0.0112	0.0354
	6	0.0079	0.0082	0.0527	0.0074	0.0042	0.033
	7	0.0089	0.023	0.1258	0.0177	0.0118	0.06
21/05/2020	0	0.0269	0.045	0.0765	0.0101	0.0208	0.0855
	1	0.0248	0.0119	0.0388	0.0224	0.0153	0.0435
	2	0.0092	0.0161	0.0484	0.0111	0.0112	0.0375
	3	0.0198	0.018	0.0724	0.0111	0.0032	0.0446
	4	0.0111	0.0195	0.0273	0.018	0.0398	0.0413
	5	0.0108	0.0123	0.0763	0.0055	0.0066	0.0558
	6	0.013	0.0341	0.1105	0.0111	0.0054	0.0409
	7	0.0209	0.0115	0.1574	0.0085	0.0101	0.089

Table B.3: The 68th percentiles of positioning errors in all sessions of GPS/Galileo DFIF PPP solutions at station BSHM during the three testing days

Station: BSHM Unit: m							
		Float			Fixed		
Date	Session	North	East	Up	North	East	Up
19/05/2020	0	0.0149	0.0162	0.0226	0.0061	0.0042	0.02
	1	0.0033	0.014	0.0184	0.0033	0.0119	0.018
	2	0.0086	0.0078	0.0298	0.0155	0.0072	0.0594
	3	0.0145	0.0076	0.0157	0.016	0.0038	0.0309
	4	0.0057	0.0106	0.0241	0.0219	0.0348	0.0367
	5	0.0044	0.0118	0.008	0.0048	0.0122	0.0104
	6	0.0029	0.0476	0.046	0.004	0.0051	0.0374
	7	0.0072	0.0428	0.06	0.0038	0.0037	0.029
20/05/2020	0	0.0051	0.022	0.0236	0.0049	0.0056	0.0251
	1	0.0029	0.0121	0.0169	0.0038	0.0082	0.0221
	2	0.0039	0.0107	0.0401	0.0105	0.0055	0.0692
	3	0.0156	0.0147	0.0463	0.0098	0.0056	0.0187
	4	0.0056	0.0203	0.0242	0.0051	0.0129	0.0213
	5	0.0039	0.0073	0.0181	0.0033	0.0036	0.0277
	6	0.0047	0.0195	0.0315	0.0049	0.0063	0.0231
	7	0.0087	0.0057	0.036	0.0089	0.0052	0.0159
21/05/2020	0	0.0045	0.0077	0.0377	0.0048	0.0043	0.014
	1	0.0045	0.0158	0.0223	0.0034	0.0126	0.0385
	2	0.0049	0.0073	0.0288	0.0074	0.0078	0.0588
	3	0.0073	0.0099	0.0181	0.0087	0.004	0.01
	4	0.01	0.023	0.0532	0.0164	0.0319	0.0624
	5	0.0063	0.0112	0.0163	0.0034	0.0061	0.0117
	6	0.0121	0.0364	0.0107	0.0047	0.0037	0.0167
	7	0.0114	0.0445	0.0786	0.0083	0.0076	0.0424

Table B.4: The 68th percentiles of positioning errors in all sessions of GPS/Galileo DFIF PPP solutions at station CUSV during the three testing days

Station: CUSV Unit: m							
		Float			Fixed		
Date	Session	North	East	Up	North	East	Up
19/05/2020	0	0.0057	0.0096	0.0263	0.006	0.0087	0.0411
	1	0.008	0.0195	0.0419	0.0102	0.0065	0.0366
	2	0.0058	0.0242	0.0267	0.0102	0.0066	0.0321
	3	0.0074	0.0117	0.0343	0.0056	0.0057	0.0379
	4	0.0089	0.0347	0.0274	0.0046	0.0079	0.0123
	5	0.0165	0.0205	0.0356	0.0142	0.0101	0.0378
	6	0.0074	0.0142	0.0272	0.0051	0.0166	0.0306
	7	0.0047	0.0182	0.0193	0.0097	0.0046	0.0326
20/05/2020	0	0.0076	0.0148	0.0256	0.0078	0.0195	0.0193
	1	0.0184	0.0477	0.0246	0.0223	0.0073	0.0225
	2	0.0107	0.0436	0.0408	0.0105	0.0093	0.0395
	3	0.0134	0.0223	0.0406	0.0063	0.0059	0.0183
	4	0.0085	0.0326	0.0449	0.0089	0.0047	0.0218
	5	0.0074	0.0072	0.0278	0.0082	0.01	0.0355
	6	0.0075	0.0139	0.0275	0.0089	0.0096	0.0227
	7	0.0038	0.0112	0.0235	0.007	0.0083	0.0189
21/05/2020	0	0.0058	0.0211	0.0256	0.0046	0.0063	0.0216
	1	0.0047	0.0297	0.0332	0.0064	0.0076	0.0345
	2	0.0064	0.0098	0.0157	0.0065	0.0073	0.03
	3	0.0094	0.0143	0.0155	0.0055	0.0065	0.0378
	4	0.0077	0.0119	0.0135	0.0106	0.0088	0.0176
	5	0.0091	0.0224	0.0202	0.01	0.0383	0.0159
	6	0.0075	0.0112	0.0508	0.0051	0.0055	0.0655
	7	0.0027	0.0167	0.0143	0.0103	0.0056	0.0199

Table B.5: The 68th percentiles of positioning errors in all sessions of GPS/Galileo DFIF PPP solutions at station PERT during the three testing days

Station: PERT Unit: m							
		Float			Fixed		
Date	Session	North	East	Up	North	East	Up
19/05/2020	0	0.0052	0.0428	0.0242	0.0064	0.0038	0.0185
	1	0.006	0.0284	0.0525	0.0056	0.0043	0.0202
	2	0.0099	0.0063	0.013	0.0067	0.0046	0.0343
	3	0.0085	0.0178	0.0276	0.0068	0.0055	0.0156
	4	0.016	0.0058	0.0336	0.0072	0.0047	0.0439
	5	0.0051	0.0075	0.0242	0.0154	0.0112	0.0448
	6	0.008	0.0262	0.0296	0.0046	0.0034	0.0321
	7	0.0057	0.0088	0.0312	0.0046	0.0037	0.0352
20/05/2020	0	0.0068	0.0378	0.0161	0.0044	0.0099	0.0425
	1	0.0143	0.0243	0.0634	0.0095	0.0042	0.0173
	2	0.0074	0.0098	0.0253	0.0082	0.0067	0.0185
	3	0.0084	0.0237	0.0134	0.0069	0.0157	0.0142
	4	0.0045	0.0131	0.0142	0.0055	0.0146	0.0134
	5	0.0132	0.0288	0.046	0.0113	0.0111	0.0342
	6	0.015	0.0321	0.0265	0.0065	0.008	0.037
	7	0.0057	0.0198	0.0419	0.0063	0.0152	0.0454
21/05/2020	0	0.008	0.01	0.0215	0.0092	0.0037	0.0151
	1	0.0057	0.0426	0.0831	0.0056	0.0061	0.0197
	2	0.0059	0.0076	0.0133	0.0064	0.0083	0.0124
	3	0.01	0.0391	0.015	0.0078	0.0115	0.0111
	4	0.0057	0.022	0.0198	0.0072	0.0224	0.0484
	5	0.0153	0.0426	0.054	0.0151	0.0085	0.0286
	6	0.0072	0.0082	0.0198	0.0062	0.0042	0.0272
	7	0.0082	0.0223	0.0527	0.0061	0.0043	0.0526

Table B.6: The 68th percentiles of positioning errors in all sessions of GPS/Galileo DFIF PPP solutions at station POL2 during the three testing days

Station: POL2 Unit: m							
		Float			Fixed		
Date	Session	North	East	Up	North	East	Up
19/05/2020	0	0.012	0.0154	0.0334	0.0134	0.0125	0.0338
	1	0.0186	0.0086	0.0261	0.014	0.0043	0.0594
	2	0.0075	0.0094	0.0327	0.0095	0.0089	0.0488
	3	0.0073	0.0075	0.0289	0.0056	0.0077	0.028
	4	0.0118	0.0156	0.0369	0.0143	0.0104	0.0463
	5	0.0064	0.0253	0.0167	0.0069	0.0297	0.0298
	6	0.0062	0.0085	0.0368	0.0047	0.005	0.0435
	7	0.0052	0.011	0.0138	0.0101	0.0102	0.0199
20/05/2020	0	0.0046	0.0089	0.0162	0.0064	0.0262	0.0147
	1	0.0055	0.0061	0.0149	0.0029	0.0066	0.0287
	2	0.0093	0.0143	0.0512	0.007	0.0095	0.0168
	3	0.0101	0.0415	0.0584	0.0065	0.0058	0.0488
	4	0.0155	0.0053	0.0178	0.0173	0.0114	0.033
	5	0.0043	0.009	0.0111	0.0052	0.0148	0.026
	6	0.0071	0.0175	0.0471	0.0068	0.0065	0.0371
	7	0.0065	0.0135	0.0166	0.0106	0.0058	0.0204
21/05/2020	0	0.0025	0.0095	0.0134	0.0071	0.0081	0.026
	1	0.0042	0.0133	0.0144	0.0064	0.0054	0.04
	2	0.0135	0.0077	0.0341	0.0101	0.0095	0.0285
	3	0.016	0.0279	0.0429	0.0071	0.007	0.0305
	4	0.0145	0.0104	0.0303	0.0157	0.0256	0.0351
	5	0.0141	0.0451	0.021	0.0279	0.0655	0.0294
	6	0.0077	0.0266	0.053	0.0052	0.0055	0.055
	7	0.0024	0.0067	0.0131	0.0072	0.0104	0.0131

Table B.7: The 68th percentiles of positioning errors in all sessions of GPS/Galileo DFIF PPP solutions at station QUIN during the three testing days

Station: QUIN Unit: m							
		Float			Fixed		
Date	Session	North	East	Up	North	East	Up
19/05/2020	0	0.0044	0.0074	0.0246	0.0077	0.0071	0.0196
	1	0.0041	0.0206	0.0277	0.0076	0.0131	0.031
	2	0.008	0.0173	0.0407	0.0041	0.0045	0.0379
	3	0.0044	0.0112	0.0163	0.0048	0.0145	0.0257
	4	0.0066	0.0251	0.0281	0.0099	0.0072	0.0083
	5	0.0079	0.0152	0.0257	0.0068	0.0045	0.0134
	6	0.0077	0.0194	0.0561	0.0054	0.0042	0.0385
	7	0.0108	0.037	0.0447	0.0074	0.0082	0.03
20/05/2020	0	0.0097	0.0066	0.0462	0.0079	0.0226	0.057
	1	0.0093	0.036	0.0483	0.0062	0.012	0.0566
	2	0.0153	0.0343	0.0302	0.0079	0.0058	0.0315
	3	0.0057	0.022	0.0329	0.0045	0.0038	0.0336
	4	0.0088	0.0234	0.016	0.0057	0.0068	0.0101
	5	0.0039	0.0032	0.0189	0.0051	0.0039	0.0094
	6	0.018	0.019	0.0253	0.0087	0.0057	0.0126
	7	0.0088	0.0412	0.0293	0.0061	0.0053	0.0406
21/05/2020	0	0.0101	0.011	0.0308	0.0113	0.0109	0.0459
	1	0.0057	0.0196	0.0294	0.0039	0.0152	0.0206
	2	0.0101	0.0178	0.0399	0.0041	0.0104	0.046
	3	0.0042	0.0086	0.0263	0.0067	0.009	0.0267
	4	0.009	0.0181	0.0196	0.0083	0.0043	0.0086
	5	0.0092	0.0108	0.018	0.0071	0.0041	0.016
	6	0.015	0.0297	0.0802	0.0098	0.0135	0.0264
	7	0.0172	0.0601	0.0537	0.0164	0.0379	0.0383

Table B.8: The 68th percentiles of positioning errors in all sessions of GPS/Galileo DFIF PPP solutions at station ZAMB during the three testing days

Station: ZAMB	Unit: m						
		Float			Fixed		
Date	Session	North	East	Up	North	East	Up
19/05/2020	0	0.0042	0.0052	0.0294	0.0034	0.0048	0.0311
	1	0.0031	0.0048	0.0157	0.0034	0.0111	0.0108
	2	0.0026	0.0136	0.0264	0.0062	0.011	0.0107
	3	0.0115	0.0267	0.0236	0.0082	0.0158	0.0385
	4	0.008	0.0053	0.0273	0.0083	0.0128	0.0324
	5	0.0046	0.0177	0.0111	0.0079	0.0053	0.0136
	6	0.0128	0.009	0.0307	0.0065	0.0038	0.042
	7	0.0144	0.0081	0.0203	0.019	0.0156	0.0258
20/05/2020	0	0.008	0.0129	0.0398	0.0051	0.004	0.05
	1	0.0042	0.0065	0.0135	0.0036	0.0095	0.0199
	2	0.0067	0.0088	0.0178	0.0077	0.0102	0.0149
	3	0.0148	0.0424	0.0521	0.0169	0.0106	0.0427
	4	0.0078	0.0079	0.021	0.0057	0.0062	0.0093
	5	0.0073	0.0213	0.0175	0.0068	0.0076	0.0181
	6	0.0061	0.0039	0.0216	0.0047	0.0049	0.0247
	7	0.0077	0.0111	0.01	0.0034	0.0099	0.0113
21/05/2020	0	0.0037	0.0048	0.0436	0.0029	0.0039	0.0374
	1	0.0026	0.0096	0.0205	0.0033	0.0129	0.0229
	2	0.0104	0.0059	0.0208	0.006	0.0143	0.0236
	3	0.0155	0.0256	0.0294	0.0122	0.0136	0.0513
	4	0.0071	0.0069	0.0211	0.0099	0.0065	0.0452
	5	0.0033	0.0085	0.016	0.0031	0.0072	0.0249
	6	0.0072	0.0051	0.0286	0.0104	0.0116	0.0275
	7	0.0048	0.0149	0.0117	0.0089	0.0123	0.0212

B.2 Multi-frequency ionosphere-estimated test

This section presents the MFIE PPP results. The superimposed positioning errors of each station for each testing days are given first; then the errors of multiple stations on each of the ten days are depicted; last, the error values of all sessions of each station during the testing days are listed.

B.2.1 Superimposed results

Figure B.28 to Figure B.117 show the superimposed PPP errors of all sessions from the ambiguity-float and ambiguity-fixed solutions. It shows that spike errors happen at some testing sessions e.g. Figure B.29, which results from wrong ambiguity fixing. But the overall comparison between float and fixed solutions can still demonstrate the advantage of ambiguity resolution in positioning accuracy i.e. Figure 5.18 and acceleration of convergence time i.e. Figure 5.19. Effective validation methods for ambiguity-fixed solutions needs further investigations.

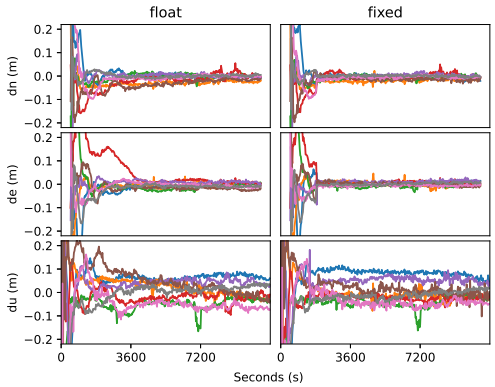

Figure B.28: *GPS L1/L2/L5 and Galileo E1/E5a/E5b/E6 ionosphere-estimated float (left) and fixed (right) PPP results on 01/05/2021 at station BRST.*

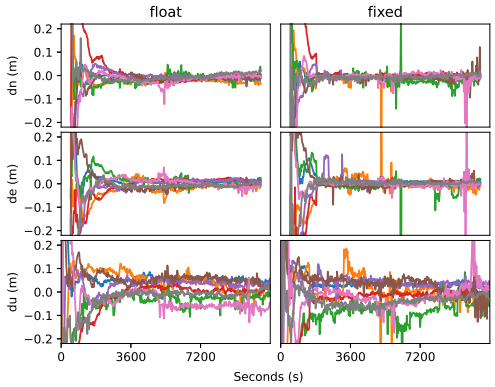

Figure B.29: *GPS L1/L2/L5 and Galileo E1/E5a/E5b/E6 ionosphere-estimated float (left) and fixed (right) PPP results on 02/05/2021 at station BRST.*

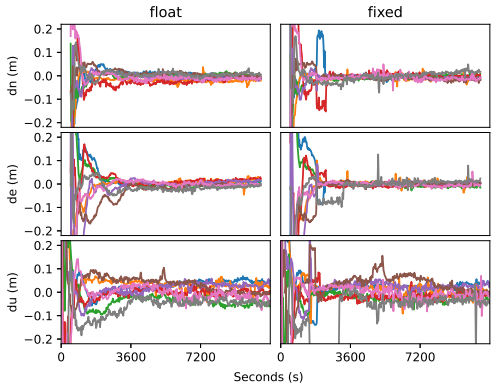

Figure B.30: *GPS L1/L2/L5 and Galileo E1/E5a/E5b/E6 ionosphere-estimated float (left) and fixed (right) PPP results on 03/05/2021 at station BRST.*

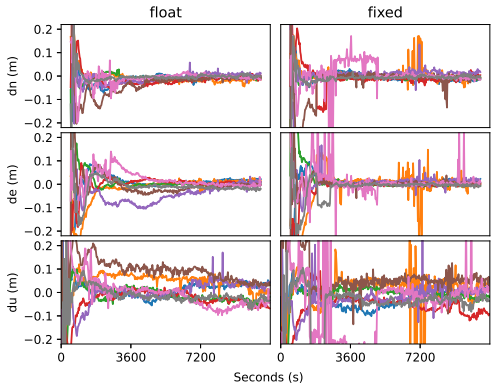

Figure B.31: *GPS L1/L2/L5 and Galileo E1/E5a/E5b/E6 ionosphere-estimated float (left) and fixed (right) PPP results on 04/05/2021 at station BRST.*

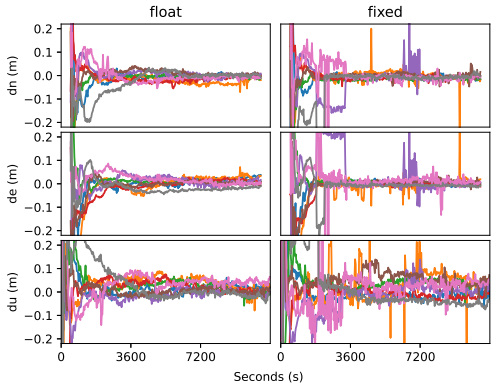

Figure B.32: *GPS L1/L2/L5 and Galileo E1/E5a/E5b/E6 ionosphere-estimated float (left) and fixed (right) PPP results on 05/05/2021 at station BRST.*

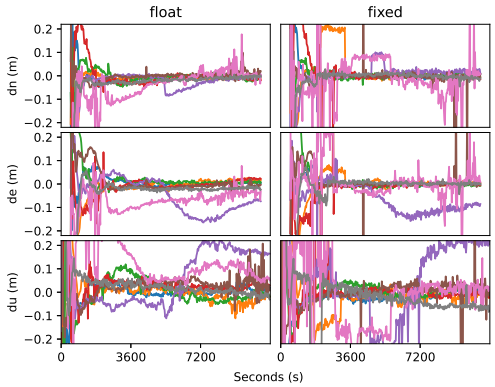

Figure B.33: *GPS L1/L2/L5 and Galileo E1/E5a/E5b/E6 ionosphere-estimated float (left) and fixed (right) PPP results on 06/05/2021 at station BRST.*

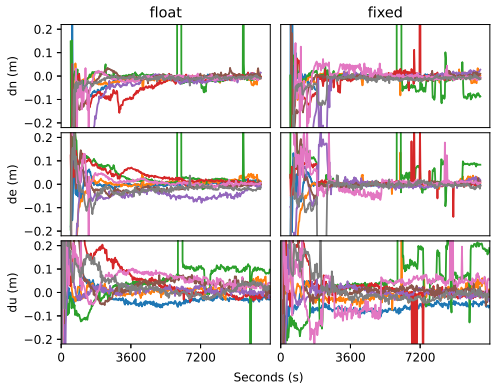

Figure B.34: *GPS L1/L2/L5 and Galileo E1/E5a/E5b/E6 ionosphere-estimated float (left) and fixed (right) PPP results on 07/05/2021 at station BRST.*

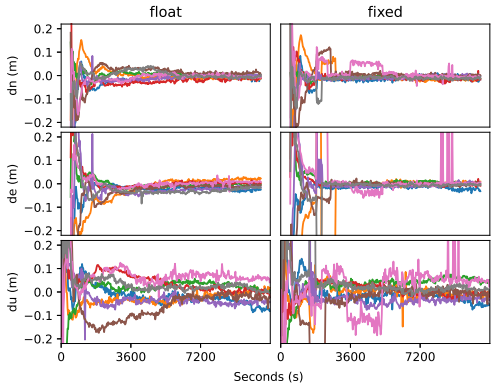

Figure B.35: *GPS L1/L2/L5 and Galileo E1/E5a/E5b/E6 ionosphere-estimated float (left) and fixed (right) PPP results on 08/05/2021 at station BRST.*

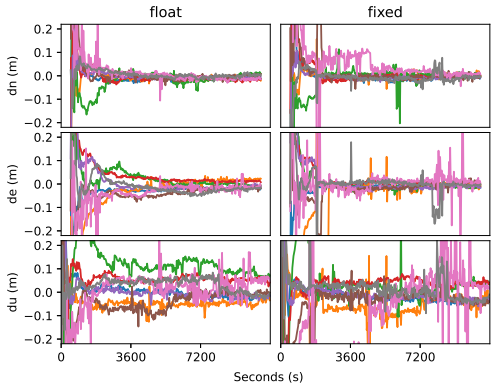

Figure B.36: *GPS L1/L2/L5 and Galileo E1/E5a/E5b/E6 ionosphere-estimated float (left) and fixed (right) PPP results on 09/05/2021 at station BRST.*

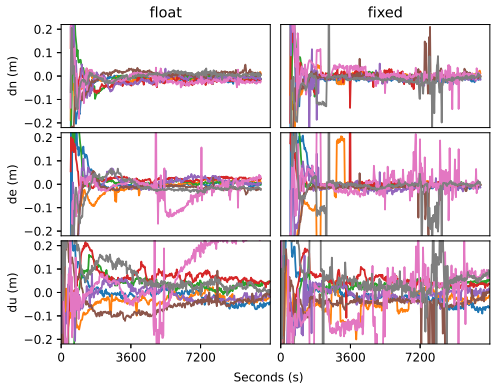

Figure B.37: *GPS L1/L2/L5 and Galileo E1/E5a/E5b/E6 ionosphere-estimated float (left) and fixed (right) PPP results on 10/05/2021 at station BRST.*

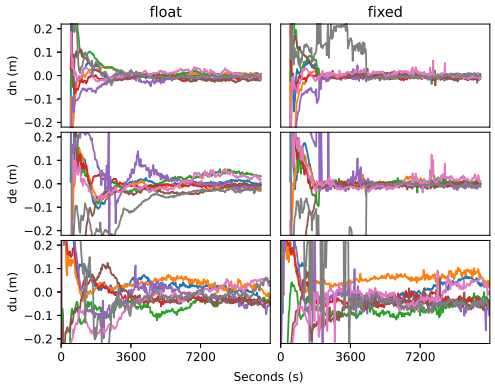

Figure B.38: *GPS L1/L2/L5 and Galileo E1/E5a/E5b/E6 ionosphere-estimated float (left) and fixed (right) PPP results on 01/05/2021 at station BOGT.*

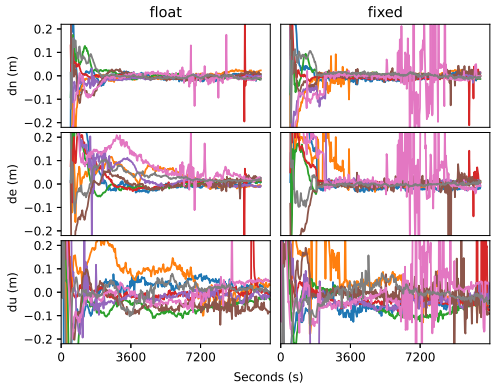

Figure B.39: *GPS L1/L2/L5 and Galileo E1/E5a/E5b/E6 ionosphere-estimated float (left) and fixed (right) PPP results on 02/05/2021 at station BOGT.*

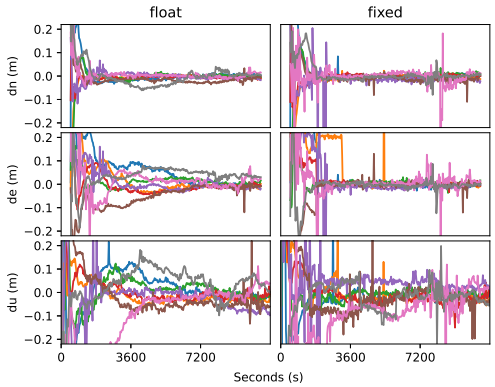

Figure B.40: *GPS L1/L2/L5 and Galileo E1/E5a/E5b/E6 ionosphere-estimated float (left) and fixed (right) PPP results on 03/05/2021 at station BOGT.*

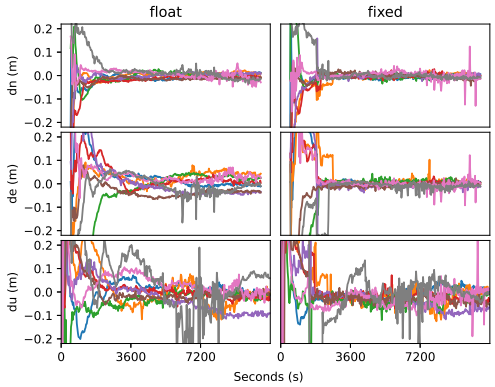

Figure B.41: *GPS L1/L2/L5 and Galileo E1/E5a/E5b/E6 ionosphere-estimated float (left) and fixed (right) PPP results on 04/05/2021 at station BOGT.*

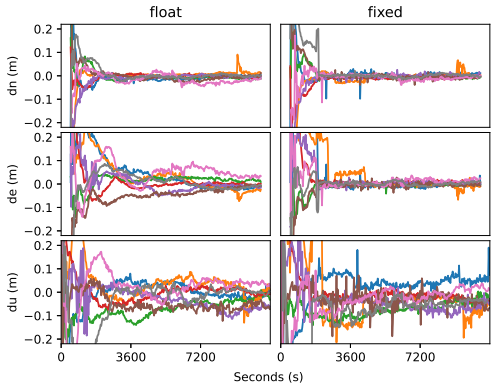

Figure B.42: *GPS L1/L2/L5 and Galileo E1/E5a/E5b/E6 ionosphere-estimated float (left) and fixed (right) PPP results on 05/05/2021 at station BOGT.*

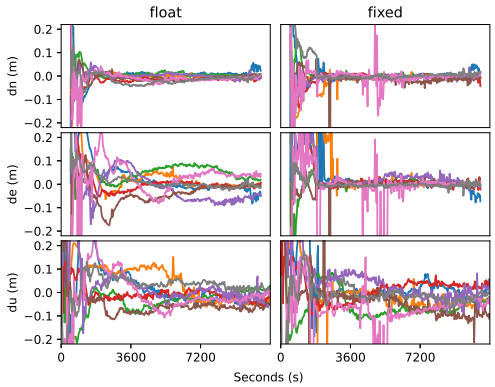

Figure B.43: *GPS L1/L2/L5 and Galileo E1/E5a/E5b/E6 ionosphere-estimated float (left) and fixed (right) PPP results on 06/05/2021 at station BOGT.*

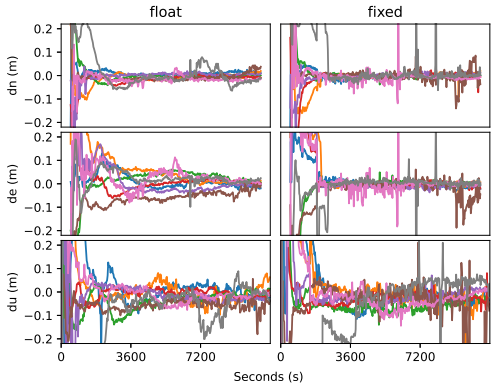

Figure B.44: *GPS L1/L2/L5 and Galileo E1/E5a/E5b/E6 ionosphere-estimated float (left) and fixed (right) PPP results on 07/05/2021 at station BOGT.*

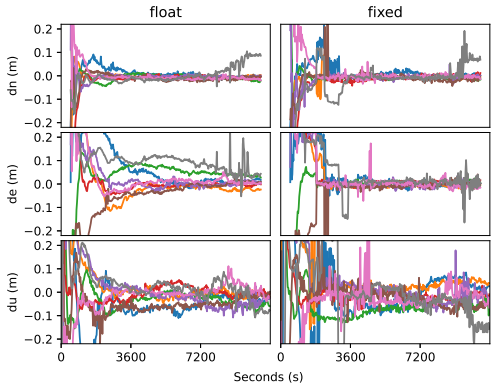

Figure B.45: *GPS L1/L2/L5 and Galileo E1/E5a/E5b/E6 ionosphere-estimated float (left) and fixed (right) PPP results on 08/05/2021 at station BOGT.*

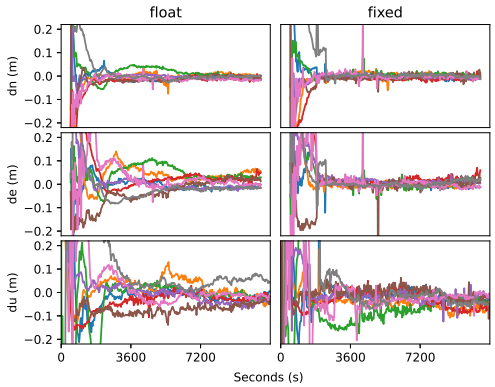

Figure B.46: *GPS L1/L2/L5 and Galileo E1/E5a/E5b/E6 ionosphere-estimated float (left) and fixed (right) PPP results on 09/05/2021 at station BOGT.*

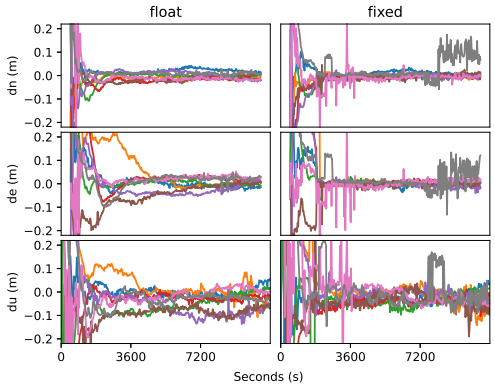

Figure B.47: *GPS L1/L2/L5 and Galileo E1/E5a/E5b/E6 ionosphere-estimated float (left) and fixed (right) PPP results on 10/05/2021 at station BOGT.*

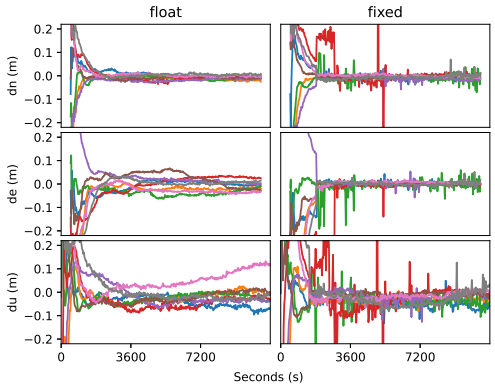

Figure B.48: *GPS L1/L2/L5 and Galileo E1/E5a/E5b/E6 ionosphere-estimated float (left) and fixed (right) PPP results on 01/05/2021 at station TID1.*

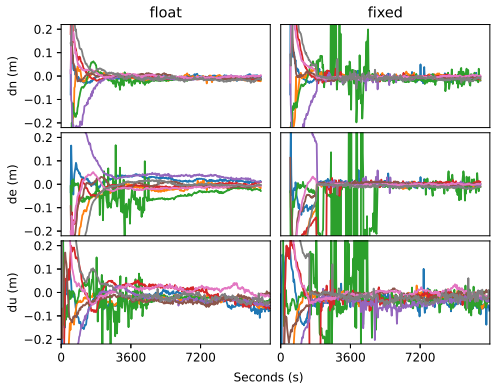

Figure B.49: *GPS L1/L2/L5 and Galileo E1/E5a/E5b/E6 ionosphere-estimated float (left) and fixed (right) PPP results on 02/05/2021 at station TID1.*

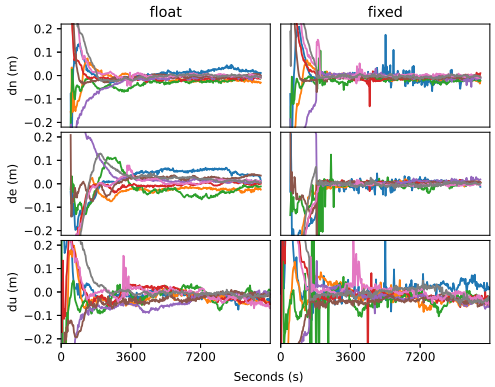

Figure B.50: *GPS L1/L2/L5 and Galileo E1/E5a/E5b/E6 ionosphere-estimated float (left) and fixed (right) PPP results on 03/05/2021 at station TID1.*

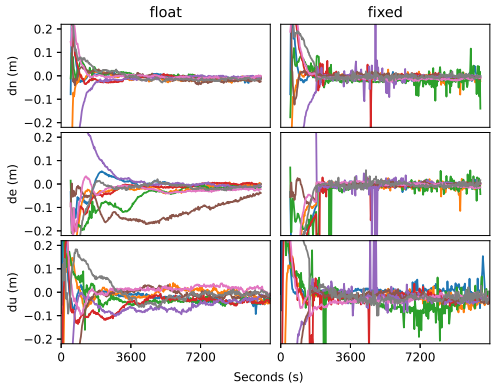

Figure B.51: *GPS L1/L2/L5 and Galileo E1/E5a/E5b/E6 ionosphere-estimated float (left) and fixed (right) PPP results on 04/05/2021 at station TID1.*

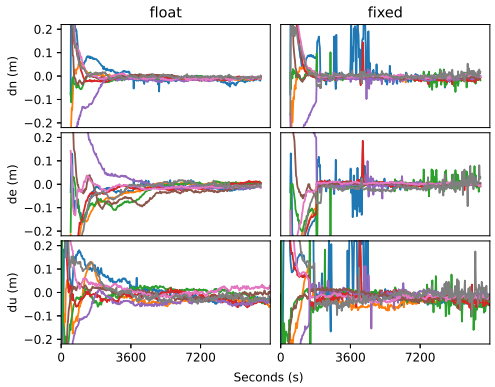

Figure B.52: *GPS L1/L2/L5 and Galileo E1/E5a/E5b/E6 ionosphere-estimated float (left) and fixed (right) PPP results on 05/05/2021 at station TID1.*

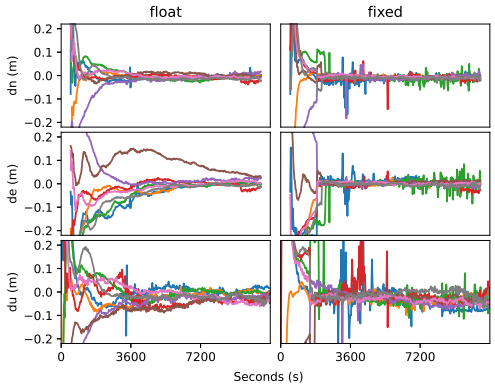

Figure B.53: *GPS L1/L2/L5 and Galileo E1/E5a/E5b/E6 ionosphere-estimated float (left) and fixed (right) PPP results on 06/05/2021 at station TID1.*

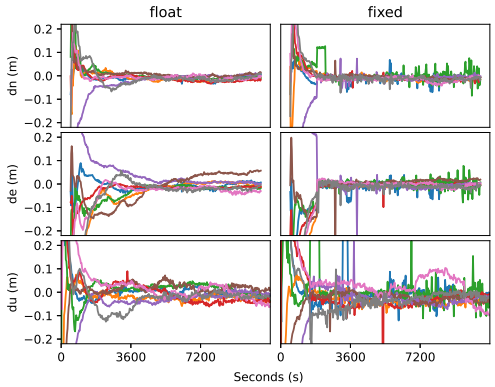

Figure B.54: *GPS L1/L2/L5 and Galileo E1/E5a/E5b/E6 ionosphere-estimated float (left) and fixed (right) PPP results on 07/05/2021 at station TID1.*

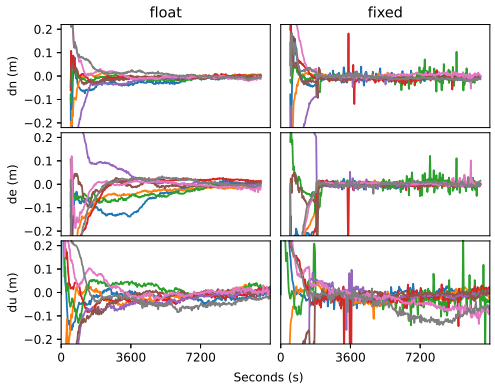

Figure B.55: *GPS L1/L2/L5 and Galileo E1/E5a/E5b/E6 ionosphere-estimated float (left) and fixed (right) PPP results on 08/05/2021 at station TID1.*

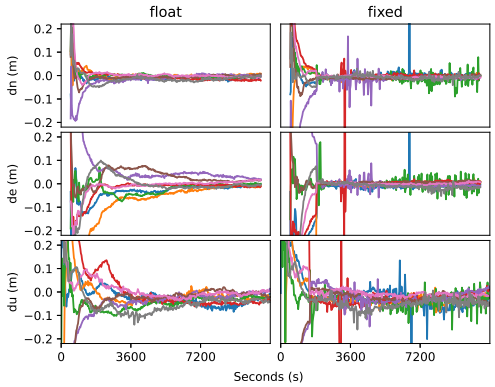

Figure B.56: *GPS L1/L2/L5 and Galileo E1/E5a/E5b/E6 ionosphere-estimated float (left) and fixed (right) PPP results on 09/05/2021 at station TID1.*

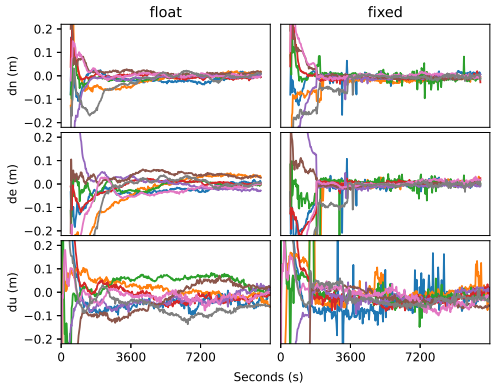

Figure B.57: *GPS L1/L2/L5 and Galileo E1/E5a/E5b/E6 ionosphere-estimated float (left) and fixed (right) PPP results on 10/05/2021 at station TID1.*

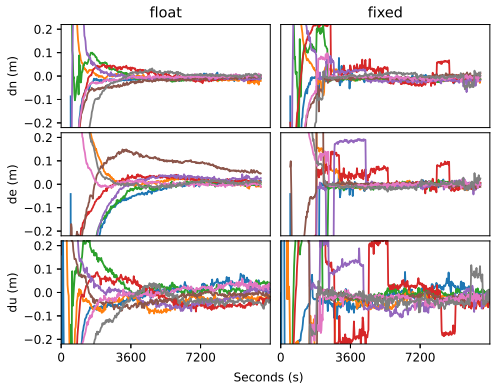

Figure B.58: *GPS L1/L2/L5 and Galileo E1/E5a/E5b/E6 ionosphere-estimated float (left) and fixed (right) PPP results on 01/05/2021 at station CEDU.*

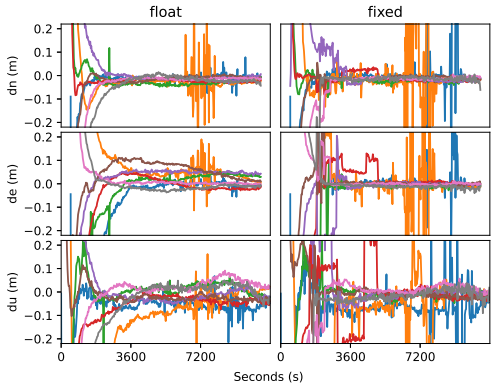

Figure B.59: *GPS L1/L2/L5 and Galileo E1/E5a/E5b/E6 ionosphere-estimated float (left) and fixed (right) PPP results on 02/05/2021 at station CEDU.*

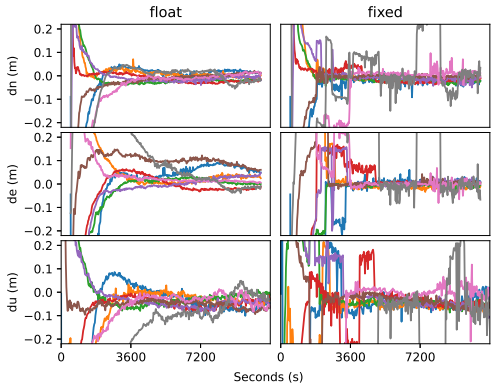

Figure B.60: *GPS L1/L2/L5 and Galileo E1/E5a/E5b/E6 ionosphere-estimated float (left) and fixed (right) PPP results on 03/05/2021 at station CEDU.*

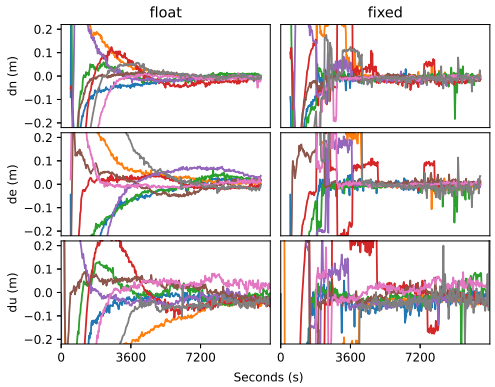

Figure B.61: *GPS L1/L2/L5 and Galileo E1/E5a/E5b/E6 ionosphere-estimated float (left) and fixed (right) PPP results on 04/05/2021 at station CEDU.*

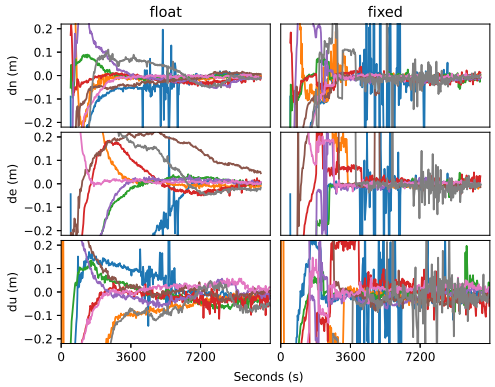

Figure B.62: *GPS L1/L2/L5 and Galileo E1/E5a/E5b/E6 ionosphere-estimated float (left) and fixed (right) PPP results on 05/05/2021 at station CEDU.*

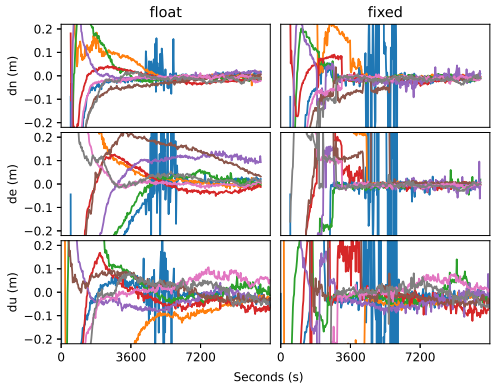

Figure B.63: *GPS L1/L2/L5 and Galileo E1/E5a/E5b/E6 ionosphere-estimated float (left) and fixed (right) PPP results on 06/05/2021 at station CEDU.*

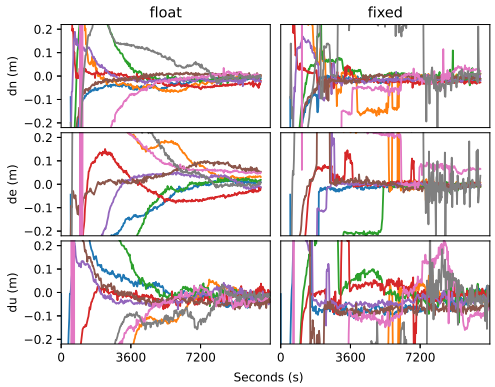

Figure B.64: *GPS L1/L2/L5 and Galileo E1/E5a/E5b/E6 ionosphere-estimated float (left) and fixed (right) PPP results on 07/05/2021 at station CEDU.*

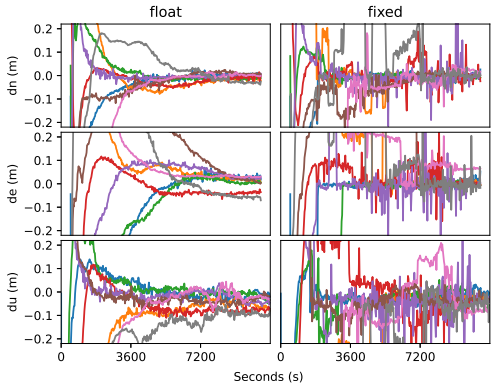

Figure B.65: *GPS L1/L2/L5 and Galileo E1/E5a/E5b/E6 ionosphere-estimated float (left) and fixed (right) PPP results on 08/05/2021 at station CEDU.*

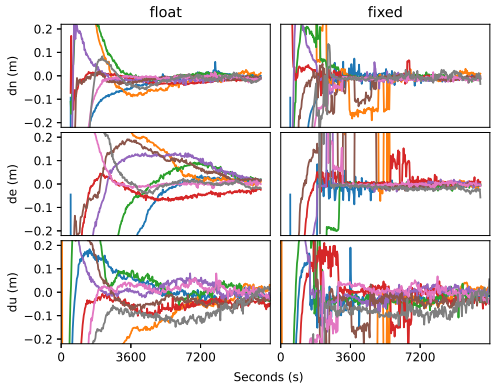

Figure B.66: *GPS L1/L2/L5 and Galileo E1/E5a/E5b/E6 ionosphere-estimated float (left) and fixed (right) PPP results on 09/05/2021 at station CEDU.*

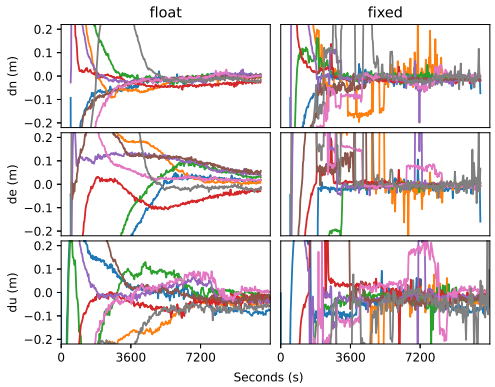

Figure B.67: *GPS L1/L2/L5 and Galileo E1/E5a/E5b/E6 ionosphere-estimated float (left) and fixed (right) PPP results on 10/05/2021 at station CEDU.*

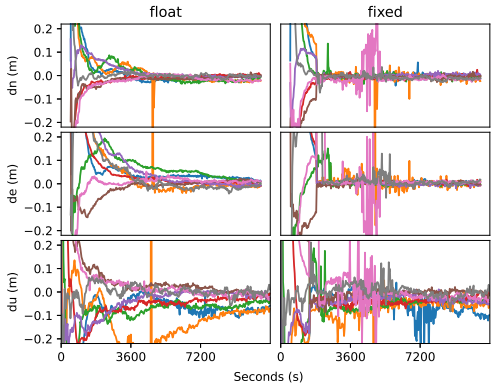

Figure B.68: *GPS L1/L2/L5 and Galileo E1/E5a/E5b/E6 ionosphere-estimated float (left) and fixed (right) PPP results on 01/05/2021 at station QUIN.*

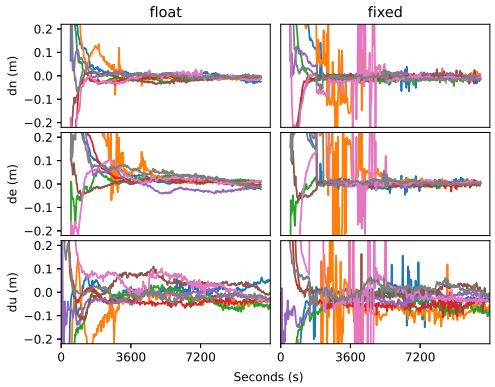

Figure B.69: *GPS L1/L2/L5 and Galileo E1/E5a/E5b/E6 ionosphere-estimated float (left) and fixed (right) PPP results on 02/05/2021 at station QUIN.*

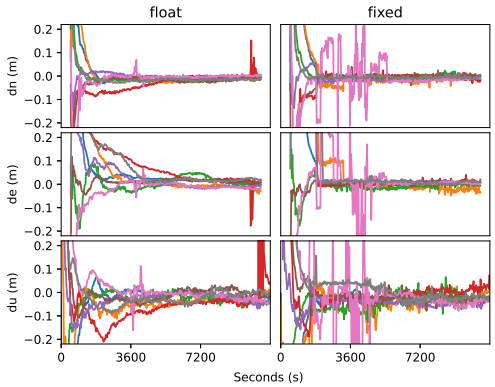

Figure B.70: *GPS L1/L2/L5 and Galileo E1/E5a/E5b/E6 ionosphere-estimated float (left) and fixed (right) PPP results on 03/05/2021 at station QUIN.*

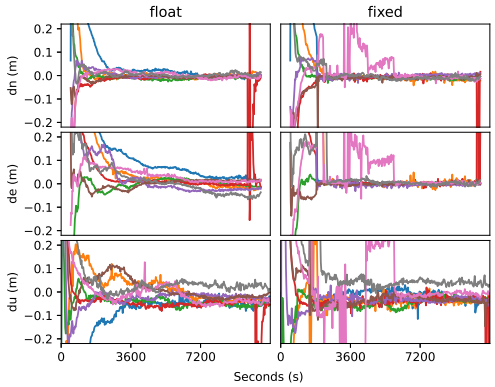

Figure B.71: *GPS L1/L2/L5 and Galileo E1/E5a/E5b/E6 ionosphere-estimated float (left) and fixed (right) PPP results on 04/05/2021 at station QUIN.*

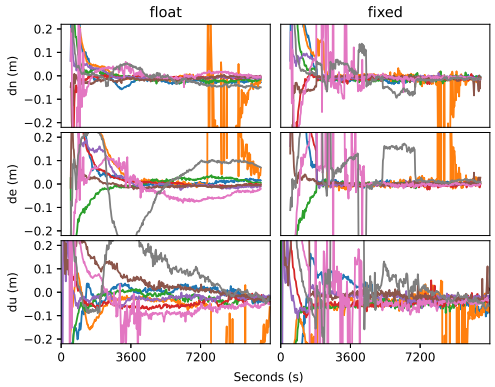

Figure B.72: *GPS L1/L2/L5 and Galileo E1/E5a/E5b/E6 ionosphere-estimated float (left) and fixed (right) PPP results on 05/05/2021 at station QUIN.*

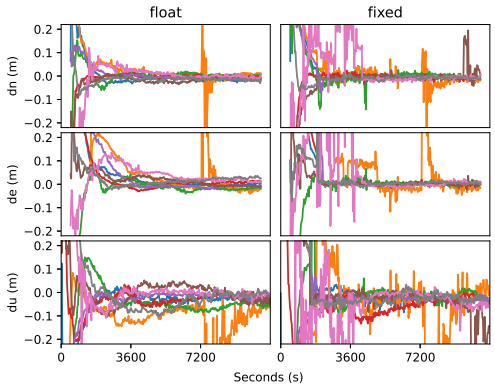

Figure B.73: *GPS L1/L2/L5 and Galileo E1/E5a/E5b/E6 ionosphere-estimated float (left) and fixed (right) PPP results on 06/05/2021 at station QUIN.*

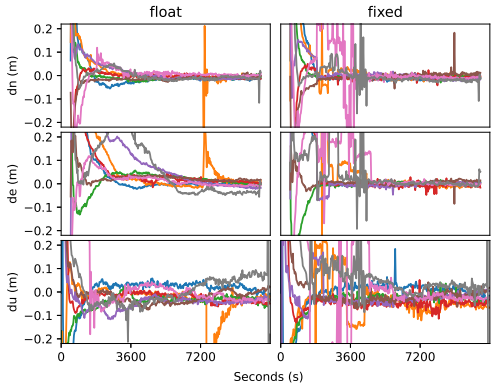

Figure B.74: *GPS L1/L2/L5 and Galileo E1/E5a/E5b/E6 ionosphere-estimated float (left) and fixed (right) PPP results on 07/05/2021 at station QUIN.*

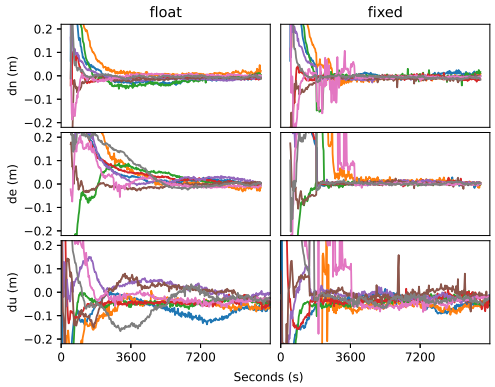

Figure B.75: *GPS L1/L2/L5 and Galileo E1/E5a/E5b/E6 ionosphere-estimated float (left) and fixed (right) PPP results on 08/05/2021 at station QUIN.*

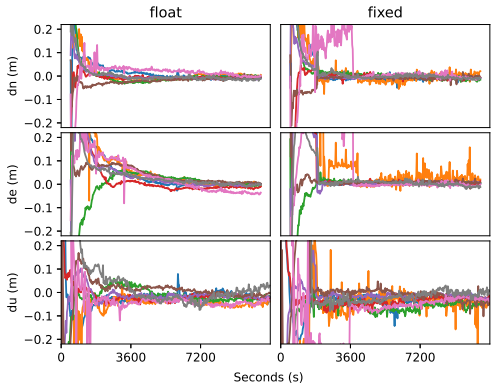

Figure B.76: *GPS L1/L2/L5 and Galileo E1/E5a/E5b/E6 ionosphere-estimated float (left) and fixed (right) PPP results on 09/05/2021 at station QUIN.*

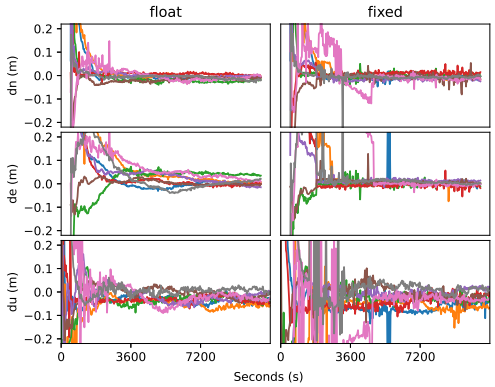

Figure B.77: *GPS L1/L2/L5 and Galileo E1/E5a/E5b/E6 ionosphere-estimated float (left) and fixed (right) PPP results on 10/05/2021 at station QUIN.*

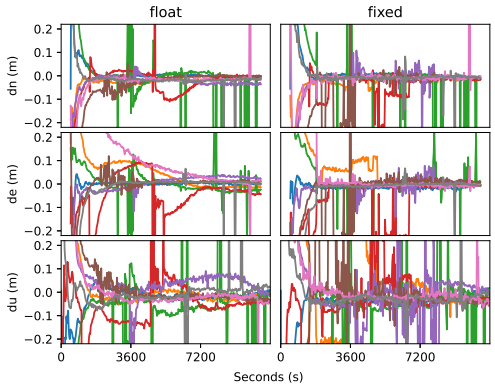

Figure B.78: *GPS L1/L2/L5 and Galileo E1/E5a/E5b/E6 ionosphere-estimated float (left) and fixed (right) PPP results on 01/05/2021 at station BSHM.*

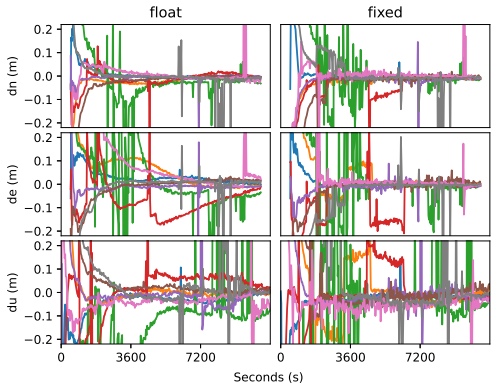

Figure B.79: *GPS L1/L2/L5 and Galileo E1/E5a/E5b/E6 ionosphere-estimated float (left) and fixed (right) PPP results on 02/05/2021 at station BSHM.*

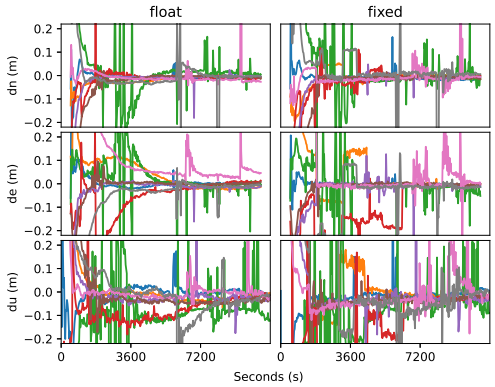

Figure B.80: *GPS L1/L2/L5 and Galileo E1/E5a/E5b/E6 ionosphere-estimated float (left) and fixed (right) PPP results on 03/05/2021 at station BSHM.*

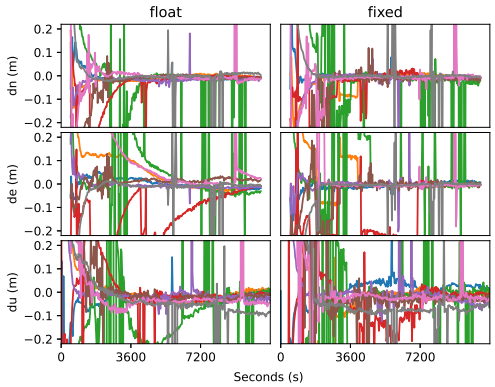

Figure B.81: *GPS L1/L2/L5 and Galileo E1/E5a/E5b/E6 ionosphere-estimated float (left) and fixed (right) PPP results on 04/05/2021 at station BSHM.*

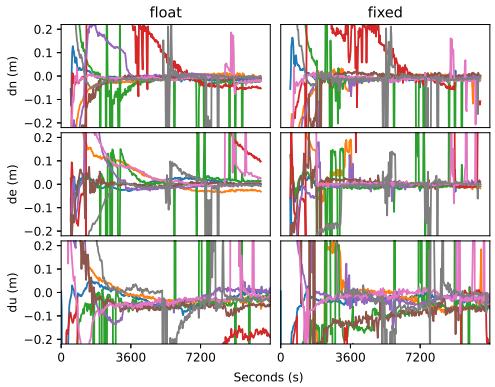

Figure B.82: *GPS L1/L2/L5 and Galileo E1/E5a/E5b/E6 ionosphere-estimated float (left) and fixed (right) PPP results on 05/05/2021 at station BSHM.*

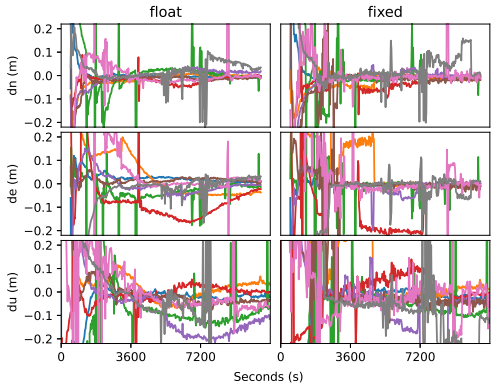

Figure B.83: *GPS L1/L2/L5 and Galileo E1/E5a/E5b/E6 ionosphere-estimated float (left) and fixed (right) PPP results on 06/05/2021 at station BSHM.*

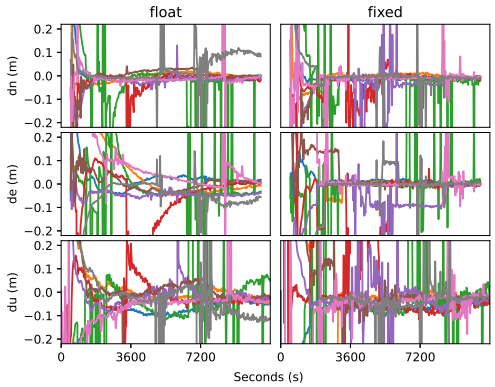

Figure B.84: *GPS L1/L2/L5 and Galileo E1/E5a/E5b/E6 ionosphere-estimated float (left) and fixed (right) PPP results on 07/05/2021 at station BSHM.*

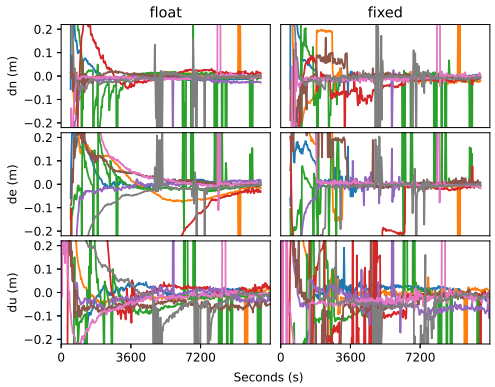

Figure B.85: *GPS L1/L2/L5 and Galileo E1/E5a/E5b/E6 ionosphere-estimated float (left) and fixed (right) PPP results on 08/05/2021 at station BSHM.*

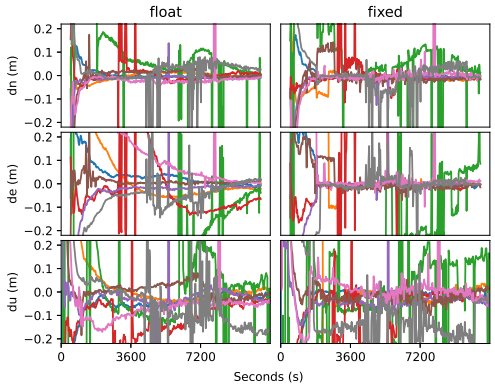

Figure B.86: *GPS L1/L2/L5 and Galileo E1/E5a/E5b/E6 ionosphere-estimated float (left) and fixed (right) PPP results on 09/05/2021 at station BSHM.*

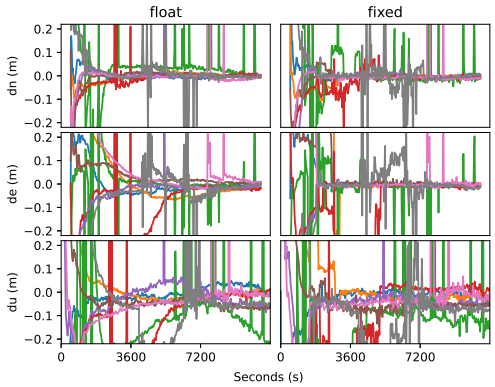

Figure B.87: *GPS L1/L2/L5 and Galileo E1/E5a/E5b/E6 ionosphere-estimated float (left) and fixed (right) PPP results on 10/05/2021 at station BSHM.*

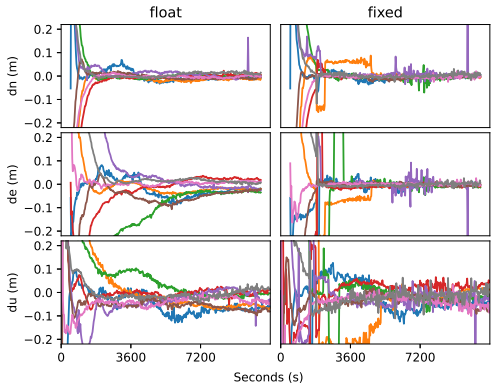

Figure B.88: *GPS L1/L2/L5 and Galileo E1/E5a/E5b/E6 ionosphere-estimated float (left) and fixed (right) PPP results on 01/05/2021 at station ZAMB.*

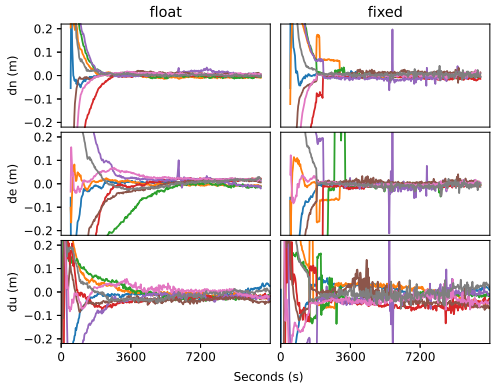

Figure B.89: *GPS L1/L2/L5 and Galileo E1/E5a/E5b/E6 ionosphere-estimated float (left) and fixed (right) PPP results on 02/05/2021 at station ZAMB.*

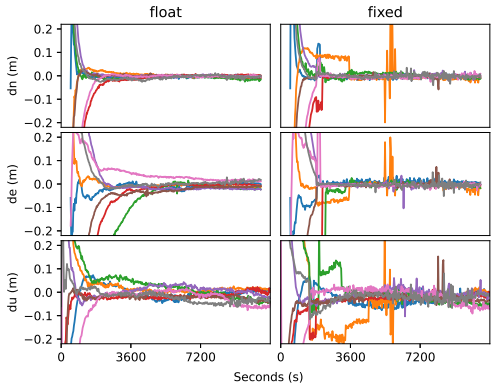

Figure B.90: *GPS L1/L2/L5 and Galileo E1/E5a/E5b/E6 ionosphere-estimated float (left) and fixed (right) PPP results on 03/05/2021 at station ZAMB.*

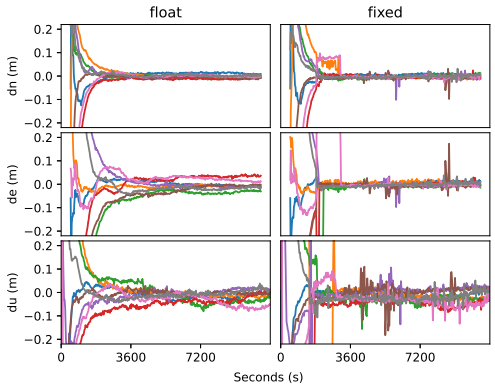

Figure B.91: *GPS L1/L2/L5 and Galileo E1/E5a/E5b/E6 ionosphere-estimated float (left) and fixed (right) PPP results on 04/05/2021 at station ZAMB.*

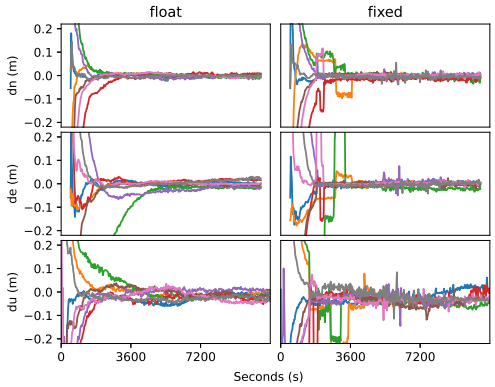

Figure B.92: *GPS L1/L2/L5 and Galileo E1/E5a/E5b/E6 ionosphere-estimated float (left) and fixed (right) PPP results on 05/05/2021 at station ZAMB.*

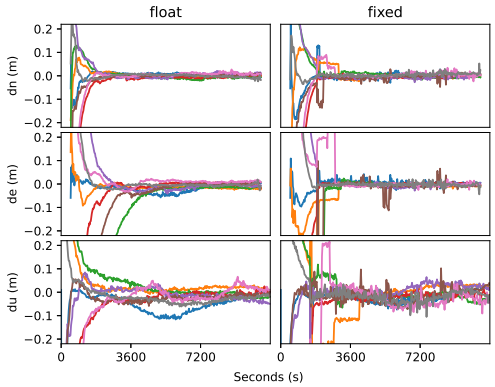

Figure B.93: *GPS L1/L2/L5 and Galileo E1/E5a/E5b/E6 ionosphere-estimated float (left) and fixed (right) PPP results on 06/05/2021 at station ZAMB.*

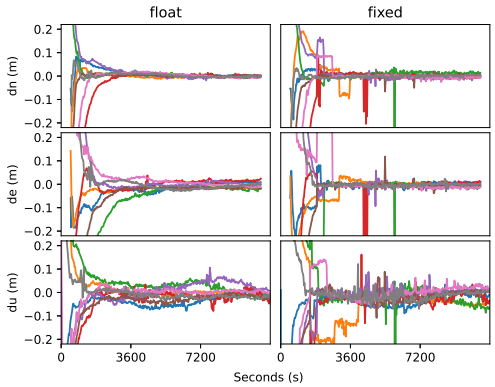

Figure B.94: *GPS L1/L2/L5 and Galileo E1/E5a/E5b/E6 ionosphere-estimated float (left) and fixed (right) PPP results on 07/05/2021 at station ZAMB.*

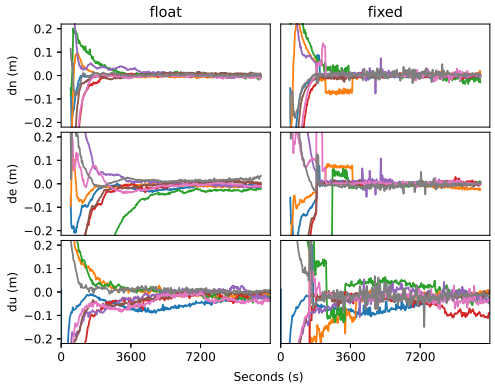

Figure B.95: *GPS L1/L2/L5 and Galileo E1/E5a/E5b/E6 ionosphere-estimated float (left) and fixed (right) PPP results on 08/05/2021 at station ZAMB.*

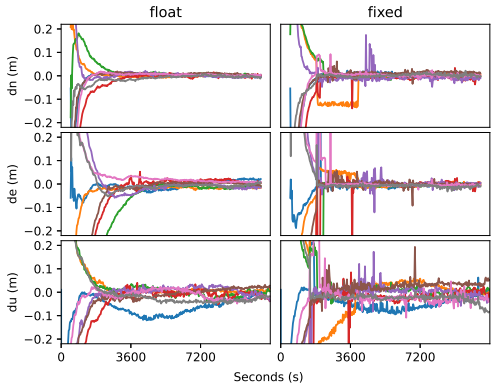

Figure B.96: *GPS L1/L2/L5 and Galileo E1/E5a/E5b/E6 ionosphere-estimated float (left) and fixed (right) PPP results on 09/05/2021 at station ZAMB.*

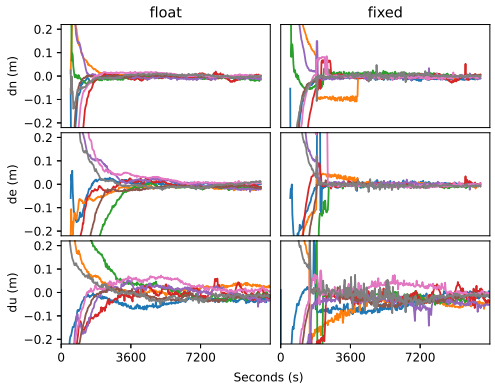

Figure B.97: *GPS L1/L2/L5 and Galileo E1/E5a/E5b/E6 ionosphere-estimated float (left) and fixed (right) PPP results on 10/05/2021 at station ZAMB.*

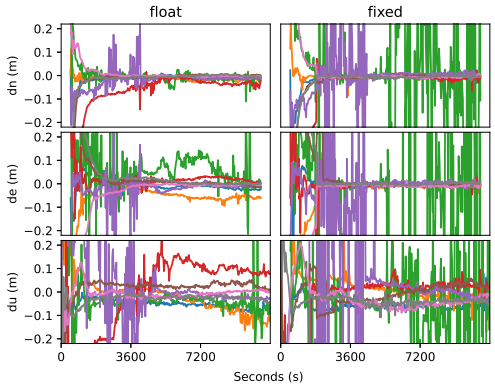

Figure B.98: *GPS L1/L2/L5 and Galileo E1/E5a/E5b/E6 ionosphere-estimated float (left) and fixed (right) PPP results on 01/05/2021 at station CUSV.*

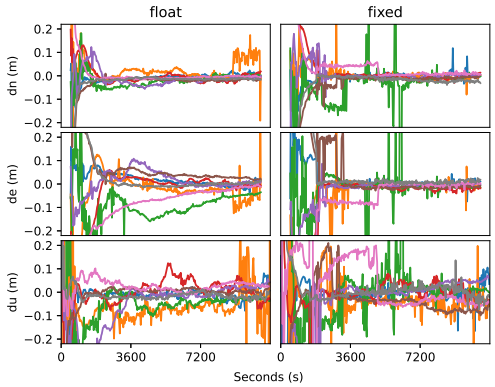

Figure B.99: *GPS L1/L2/L5 and Galileo E1/E5a/E5b/E6 ionosphere-estimated float (left) and fixed (right) PPP results on 02/05/2021 at station CUSV.*

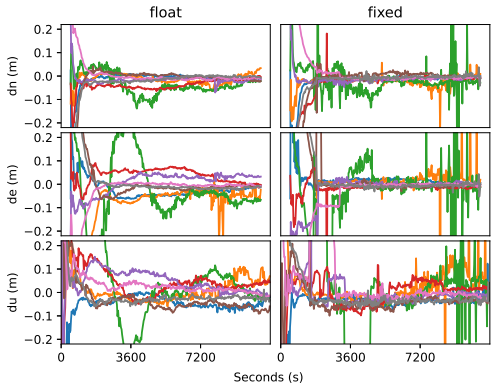

Figure B.100: *GPS L1/L2/L5 and Galileo E1/E5a/E5b/E6 ionosphere-estimated float (left) and fixed (right) PPP results on 03/05/2021 at station CUSV.*

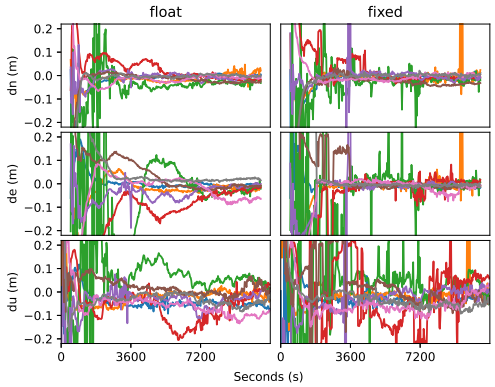

Figure B.101: *GPS L1/L2/L5 and Galileo E1/E5a/E5b/E6 ionosphere-estimated float (left) and fixed (right) PPP results on 04/05/2021 at station CUSV.*

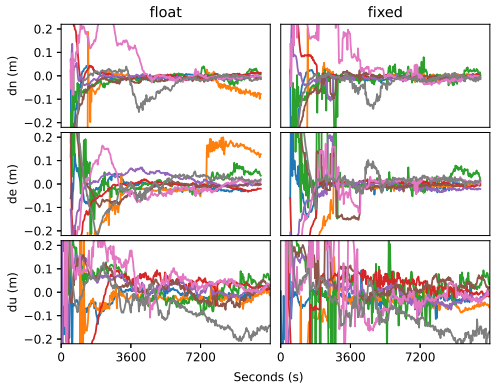

Figure B.102: *GPS L1/L2/L5 and Galileo E1/E5a/E5b/E6 ionosphere-estimated float (left) and fixed (right) PPP results on 05/05/2021 at station CUSV.*

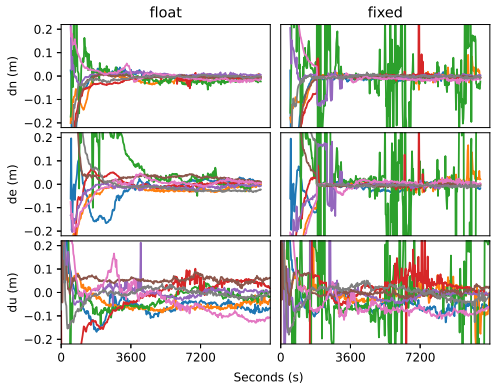

Figure B.103: *GPS L1/L2/L5 and Galileo E1/E5a/E5b/E6 ionosphere-estimated float (left) and fixed (right) PPP results on 06/05/2021 at station CUSV.*

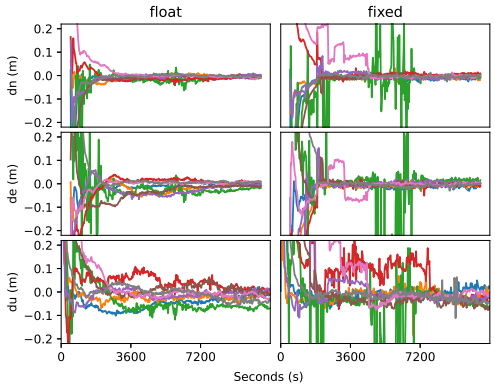

Figure B.104: *GPS L1/L2/L5 and Galileo E1/E5a/E5b/E6 ionosphere-estimated float (left) and fixed (right) PPP results on 07/05/2021 at station CUSV.*

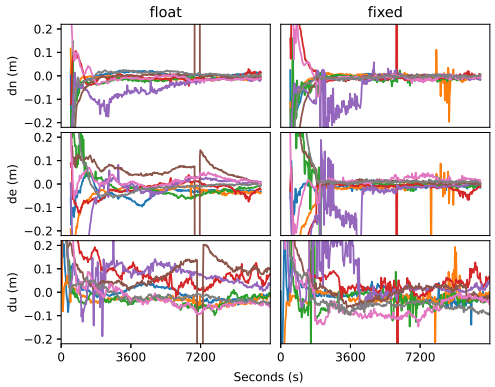

Figure B.105: *GPS L1/L2/L5 and Galileo E1/E5a/E5b/E6 ionosphere-estimated float (left) and fixed (right) PPP results on 08/05/2021 at station CUSV.*

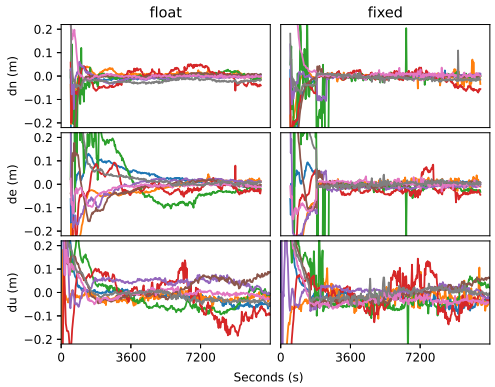

Figure B.106: *GPS L1/L2/L5 and Galileo E1/E5a/E5b/E6 ionosphere-estimated float (left) and fixed (right) PPP results on 09/05/2021 at station CUSV.*

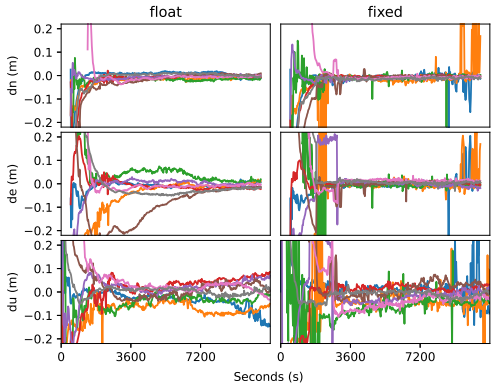

Figure B.107: *GPS L1/L2/L5 and Galileo E1/E5a/E5b/E6 ionosphere-estimated float (left) and fixed (right) PPP results on 10/05/2021 at station CUSV.*

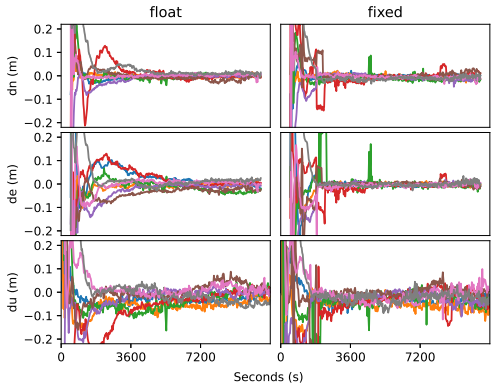

Figure B.108: *GPS L1/L2/L5 and Galileo E1/E5a/E5b/E6 ionosphere-estimated float (left) and fixed (right) PPP results on 01/05/2021 at station PERT.*

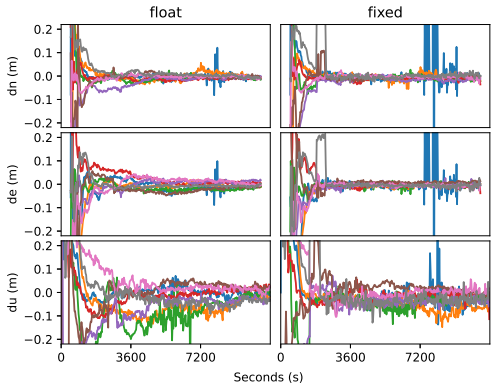

Figure B.109: *GPS L1/L2/L5 and Galileo E1/E5a/E5b/E6 ionosphere-estimated float (left) and fixed (right) PPP results on 02/05/2021 at station PERT.*

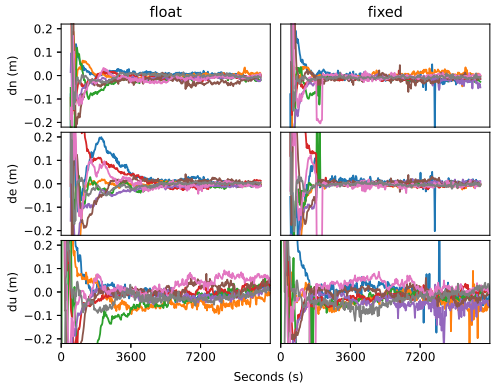

Figure B.110: *GPS L1/L2/L5 and Galileo E1/E5a/E5b/E6 ionosphere-estimated float (left) and fixed (right) PPP results on 03/05/2021 at station PERT.*

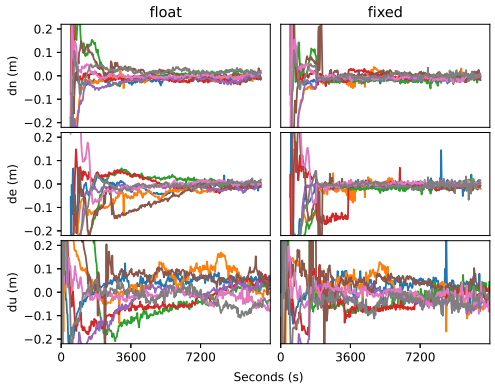

Figure B.111: *GPS L1/L2/L5 and Galileo E1/E5a/E5b/E6 ionosphere-estimated float (left) and fixed (right) PPP results on 04/05/2021 at station PERT.*

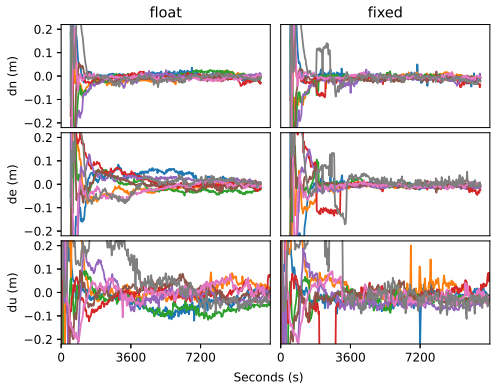

Figure B.112: *GPS L1/L2/L5 and Galileo E1/E5a/E5b/E6 ionosphere-estimated float (left) and fixed (right) PPP results on 05/05/2021 at station PERT.*

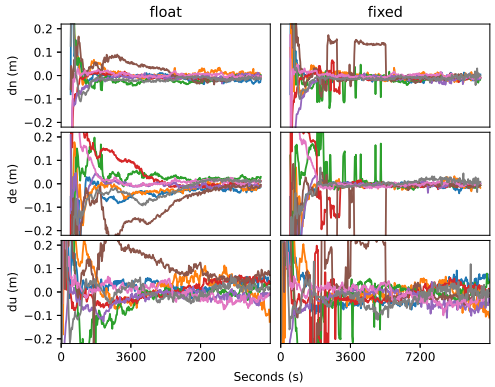

Figure B.113: *GPS L1/L2/L5 and Galileo E1/E5a/E5b/E6 ionosphere-estimated float (left) and fixed (right) PPP results on 06/05/2021 at station PERT.*

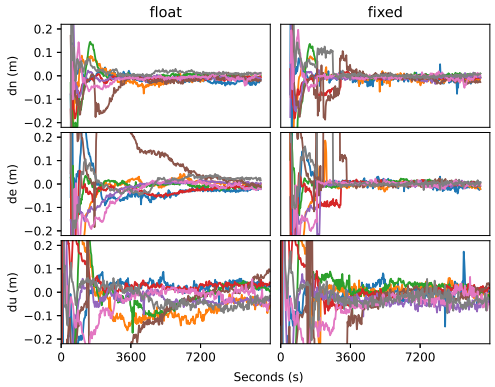

Figure B.114: *GPS L1/L2/L5 and Galileo E1/E5a/E5b/E6 ionosphere-estimated float (left) and fixed (right) PPP results on 07/05/2021 at station PERT.*

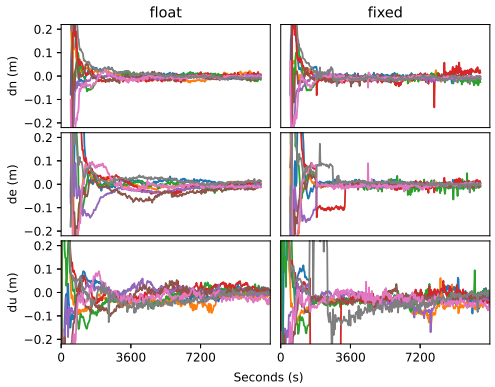

Figure B.115: *GPS L1/L2/L5 and Galileo E1/E5a/E5b/E6 ionosphere-estimated float (left) and fixed (right) PPP results on 08/05/2021 at station PERT.*

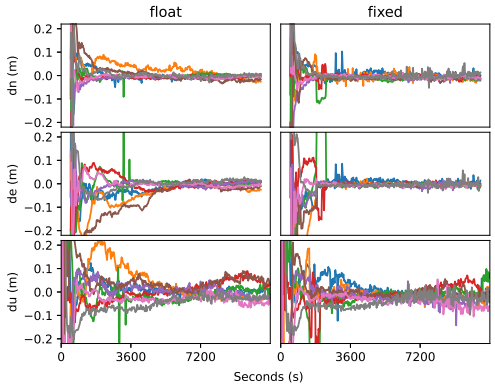

Figure B.116: *GPS L1/L2/L5 and Galileo E1/E5a/E5b/E6 ionosphere-estimated float (left) and fixed (right) PPP results on 09/05/2021 at station PERT.*

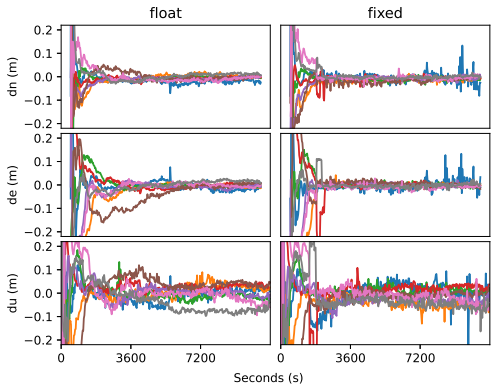

Figure B.117: *GPS L1/L2/L5 and Galileo E1/E5a/E5b/E6 ionosphere-estimated float (left) and fixed (right) PPP results on 10/05/2021 at station PERT.*

B.2.2 Multi-station demonstration

Figure B.118 to Figure B.127 show the multi-station statistical errors for the ten days. The 68-percentile is used for error representation. It shows that the ambiguity-fixed height solutions of some stations are degraded compared to the float solutions, which could be caused by improper setting of ionospheric modelling as the empirical values are applied for all the testing stations. It also clearly shows the significant improvement in the horizontal direction for most of the stations.

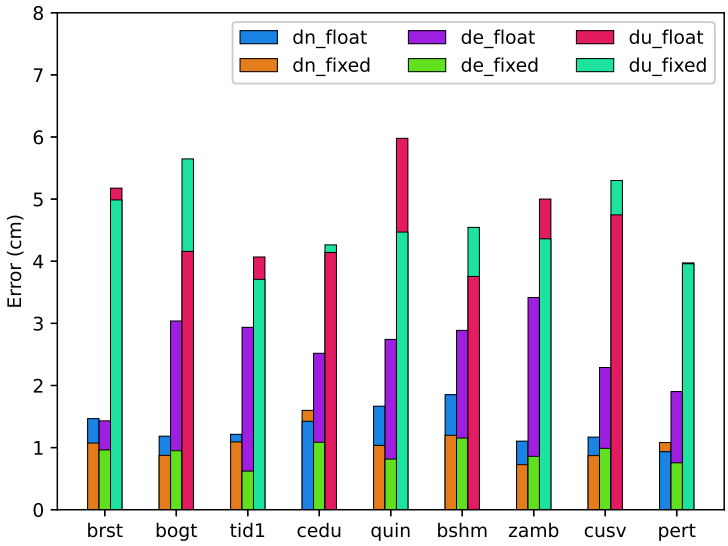

Figure B.118: *The 68th percentile of GPS L1/L2/L5 + Galileo E1/E5a/E5b/E6 ambiguity-float and ambiguity-fixed PPP solution errors at all the selected stations on 01/05/2021*

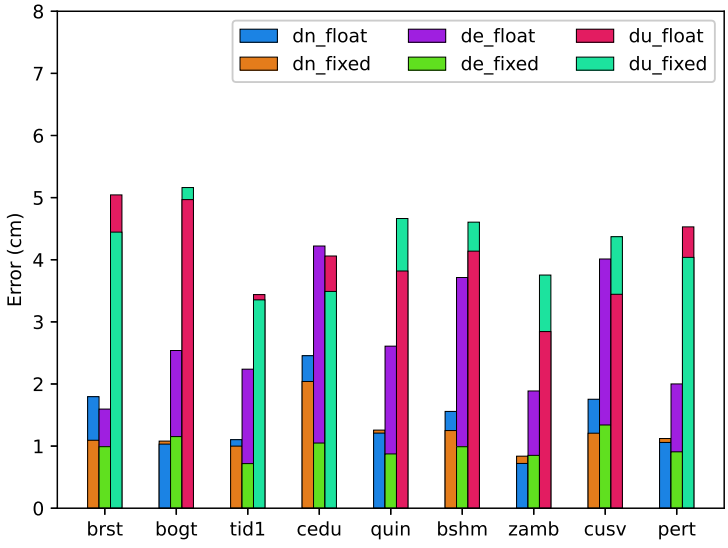

Figure B.119: *The 68th percentile of GPS L1/L2/L5 + Galileo E1/E5a/E5b/E6 ambiguity-float and ambiguity-fixed PPP solution errors at all the selected stations on 02/05/2021*

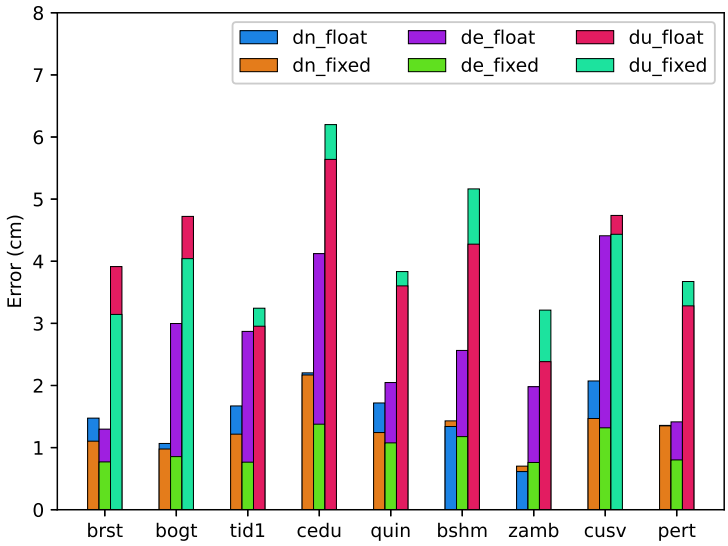

Figure B.120: *The 68th percentile of GPS L1/L2/L5 + Galileo E1/E5a/E5b/E6 ambiguity-float and ambiguity-fixed PPP solution errors at all the selected stations on 03/05/2021*

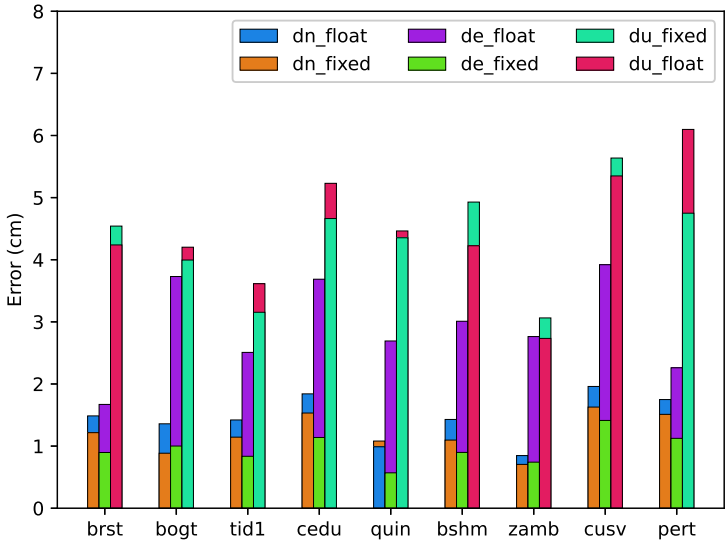

Figure B.121: *The 68th percentile of GPS L1/L2/L5 + Galileo E1/E5a/E5b/E6 ambiguity-float and ambiguity-fixed PPP solution errors at all the selected stations on 04/05/2021*

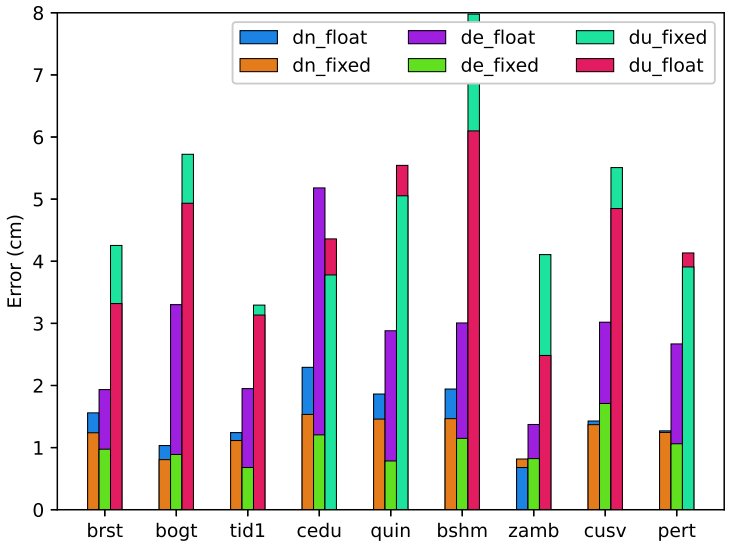

Figure B.122: *The 68th percentile of GPS L1/L2/L5 + Galileo E1/E5a/E5b/E6 ambiguity-float and ambiguity-fixed PPP solution errors at all the selected stations on 05/05/2021*

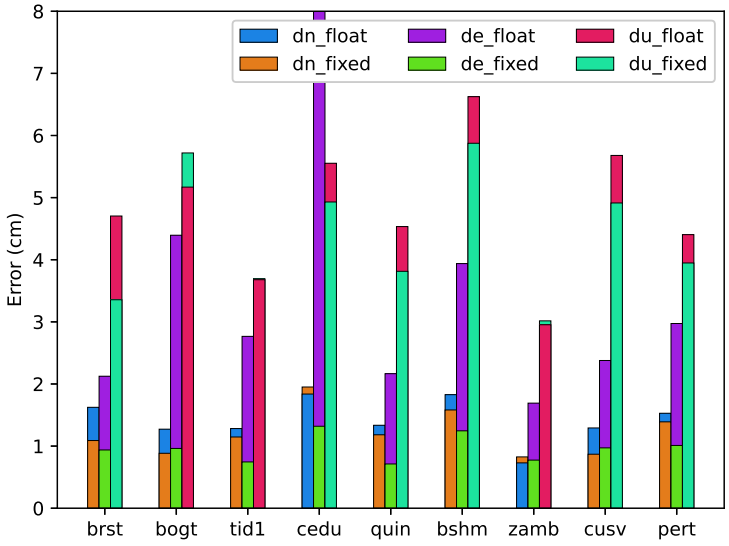

Figure B.123: *The 68th percentile of GPS L1/L2/L5 + Galileo E1/E5a/E5b/E6 ambiguity-float and ambiguity-fixed PPP solution errors at all the selected stations on 06/05/2021*

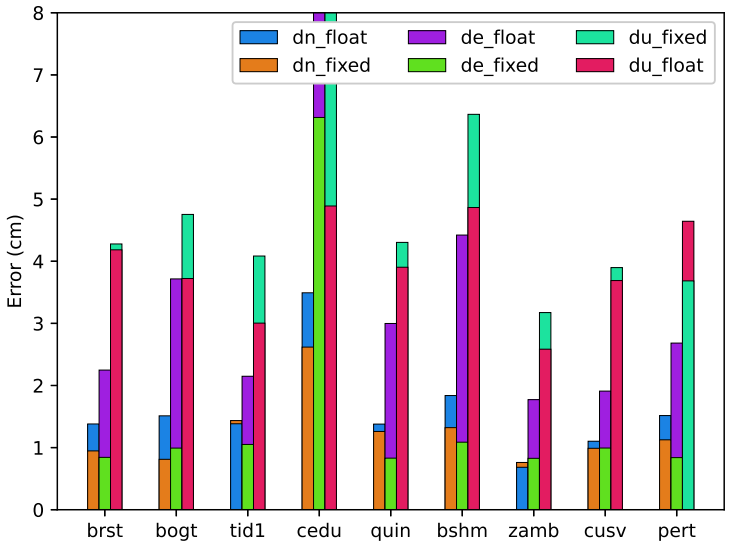

Figure B.124: *The 68th percentile of GPS L1/L2/L5 + Galileo E1/E5a/E5b/E6 ambiguity-float and ambiguity-fixed PPP solution errors at all the selected stations on 07/05/2021*

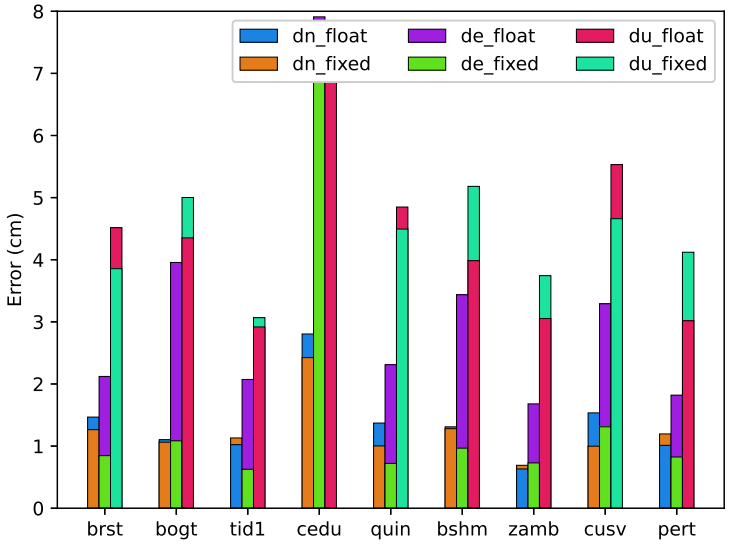

Figure B.125: *The 68th percentile of GPS L1/L2/L5 + Galileo E1/E5a/E5b/E6 ambiguity-float and ambiguity-fixed PPP solution errors at all the selected stations on 08/05/2021*

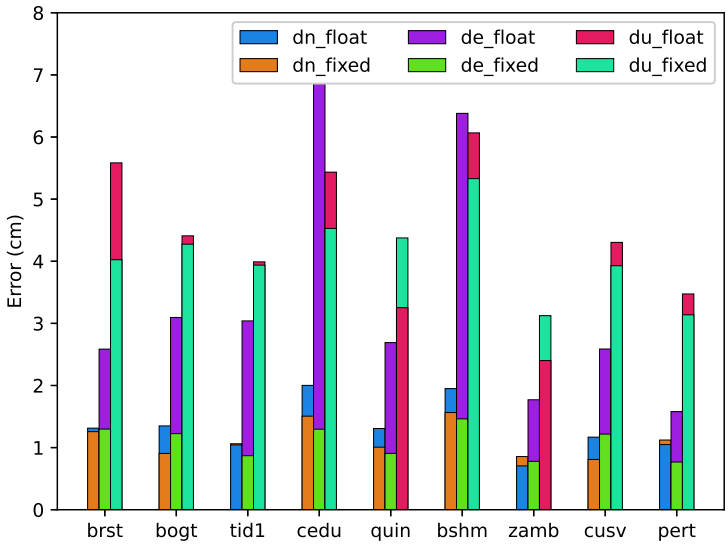

Figure B.126: *The 68th percentile of GPS L1/L2/L5 + Galileo E1/E5a/E5b/E6 ambiguity-float and ambiguity-fixed PPP solution errors at all the selected stations on 09/05/2021*

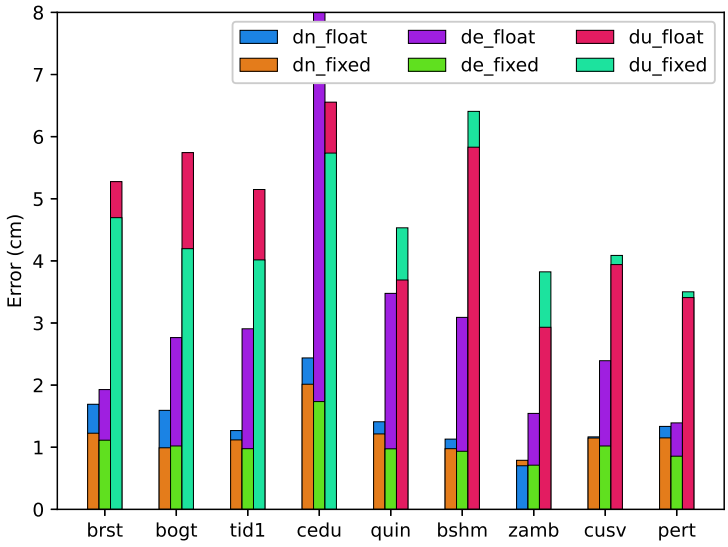

Figure B.127: *The 68th percentile of GPS L1/L2/L5 + Galileo E1/E5a/E5b/E6 ambiguity-float and ambiguity-fixed PPP solution errors at all the selected stations on 10/05/2021*

B.2.3 Error values of all sessions

Table B.9 to Table B.17 list the error values of all sessions of the stations during the ten days. The 68th percentile is still used to measure the error of each session.

Table B.9: The 68th percentiles of positioning errors in all sessions of GPS/Galileo MFIE PPP solutions at station BRST during the ten testing days

Station: BRST	Unit: m						
		Float			Fixed		
Date	Session	North	East	Up	North	East	Up
01/05/2021	0	0.0068	0.0078	0.0705	0.0071	0.01	0.1023
	1	0.0326	0.0093	0.0396	0.0223	0.0104	0.0199
	2	0.0096	0.0179	0.0551	0.0087	0.0096	0.0497
	3	0.0206	0.0181	0.0291	0.0112	0.0091	0.0322
	4	0.0075	0.0111	0.0484	0.0075	0.0156	0.0672
	5	0.0308	0.0229	0.0487	0.0142	0.0078	0.0167
	6	0.0085	0.0078	0.0596	0.0088	0.0074	0.0518
	7	0.0056	0.0123	0.0238	0.0044	0.0069	0.0202
02/05/2021	0	0.0163	0.0104	0.0567	0.0082	0.0109	0.0344
	1	0.0273	0.0253	0.0621	0.0132	0.0191	0.0312
	2	0.0254	0.0136	0.0353	0.0249	0.0112	0.0881
	3	0.0205	0.0191	0.0195	0.006	0.0061	0.0175
	4	0.0068	0.0159	0.0439	0.0097	0.0075	0.0449
	5	0.0149	0.0161	0.0614	0.0138	0.0108	0.049
	6	0.0207	0.0167	0.0615	0.0099	0.0075	0.0372
	7	0.0165	0.012	0.0139	0.0095	0.0069	0.0496
03/05/2021	0	0.0105	0.007	0.0442	0.0074	0.0054	0.0282
	1	0.0225	0.0108	0.0408	0.0103	0.0076	0.0233
	2	0.0067	0.0109	0.0469	0.012	0.009	0.0293
	3	0.0286	0.017	0.0127	0.0077	0.0093	0.0236
	4	0.0108	0.0121	0.0316	0.0088	0.0063	0.0333
	5	0.0098	0.0143	0.0491	0.0131	0.0051	0.055
	6	0.0148	0.0097	0.0263	0.0135	0.0081	0.0231
	7	0.0118	0.0228	0.0513	0.0166	0.0131	0.049
04/05/2021	0	0.0129	0.0166	0.0303	0.0173	0.0114	0.0525
	1	0.0185	0.0144	0.0665	0.0083	0.0166	0.0456
	2	0.0073	0.0043	0.0296	0.0096	0.0051	0.0173
	3	0.0275	0.0121	0.0304	0.0143	0.0045	0.0649
	4	0.0196	0.0698	0.0307	0.0157	0.0142	0.0327
	5	0.022	0.027	0.1025	0.0082	0.0064	0.0563
	6	0.0099	0.0179	0.0518	0.0209	0.0098	0.1909
	7	0.0069	0.0161	0.027	0.0082	0.0057	0.0433
05/05/2021	0	0.0075	0.0182	0.0202	0.0081	0.008	0.0235
	1	0.0304	0.0264	0.0542	0.0148	0.0115	0.0623
	2	0.0072	0.0126	0.0317	0.0172	0.0086	0.042
	3	0.0212	0.0166	0.0395	0.0123	0.0055	0.0245
	4	0.0113	0.0215	0.0192	0.0144	0.0156	0.0231
	5	0.0176	0.006	0.0152	0.0073	0.0092	0.0669
	6	0.0168	0.0229	0.0522	0.0159	0.0186	0.0502
	7	0.0191	0.0278	0.0255	0.0094	0.0093	0.0441
06/05/2021	0	0.0098	0.0065	0.0148	0.0082	0.0061	0.0228
	1	0.0127	0.0167	0.0241	0.0089	0.0086	0.0263
	2	0.0132	0.0104	0.0455	0.0081	0.0066	0.0239
	3	0.0211	0.0138	0.0364	0.0084	0.0069	0.0141
	4	0.0198	0.1062	0.1733	0.0196	0.1115	0.2041
	5	0.0075	0.0152	0.0437	0.0065	0.0044	0.0243
	6	0.0393	0.0791	0.1182	0.0747	0.0331	0.1539
	7	0.022	0.0226	0.0256	0.0081	0.0067	0.0563
07/05/2021	0	0.0104	0.0083	0.0399	0.0069	0.0056	0.072
	1	0.016	0.0128	0.0157	0.006	0.0064	0.0287
	2	0.015	0.0227	0.0985	0.0411	0.0234	0.097
	3	0.0441	0.033	0.0486	0.0102	0.0066	0.021
	4	0.025	0.0531	0.0138	0.0091	0.0117	0.0142
	5	0.0088	0.0203	0.0451	0.0075	0.0067	0.0135
	6	0.0115	0.0099	0.0727	0.0137	0.0187	0.0689
	7	0.0104	0.0248	0.0286	0.0126	0.009	0.0249
08/05/2021	0	0.0127	0.023	0.0358	0.0154	0.0173	0.0268
	1	0.0127	0.0213	0.0358	0.0164	0.0071	0.0167
	2	0.0086	0.0098	0.0353	0.01	0.0059	0.0495
	3	0.0283	0.0092	0.0546	0.0143	0.006	0.0294
	4	0.0137	0.031	0.0471	0.0114	0.0102	0.0406
	5	0.0266	0.0179	0.0921	0.007	0.005	0.0206
	6	0.0076	0.0099	0.0749	0.0123	0.0105	0.0859
	7	0.0142	0.036	0.0274	0.0131	0.0073	0.0215
09/05/2021	0	0.0161	0.0258	0.019	0.0133	0.0092	0.0327
	1	0.0117	0.022	0.0527	0.0069	0.0148	0.0759
	2	0.0174	0.0217	0.1229	0.0111	0.0137	0.0315
	3	0.0157	0.0238	0.0608	0.0118	0.0061	0.0472
	4	0.0087	0.0194	0.0157	0.0103	0.0148	0.0276
	5	0.0128	0.044	0.0604	0.008	0.0175	0.0317
	6	0.0144	0.0316	0.0484	0.0343	0.0231	0.2384
	7	0.008	0.0296	0.0525	0.0159	0.0079	0.0334
10/05/2021	0	0.0152	0.0087	0.0265	0.0178	0.0063	0.0338
	1	0.0131	0.0164	0.034	0.008	0.0109	0.0526
	2	0.0075	0.0108	0.043	0.0064	0.005	0.0386
	3	0.0252	0.025	0.0718	0.0105	0.0061	0.0526
	4	0.0169	0.0196	0.0323	0.0135	0.0193	0.021
	5	0.0158	0.0174	0.0823	0.0065	0.0137	0.0462
	6	0.0253	0.0313	0.2162	0.0188	0.032	0.1021
	7	0.0121	0.0241	0.048	0.0174	0.0099	0.0613

Table B.10: The 68th percentiles of positioning errors in all sessions of GPS/Galileo MFIE PPP solutions at station BOGT during the ten testing days

Station: BOGT Unit: m

		Float			Fixed		
Date	Session	North	East	Up	North	East	Up
01/05/2021	0	0.0071	0.01	0.0288	0.0058	0.0048	0.0349
	1	0.0085	0.0185	0.0412	0.0037	0.0074	0.065
	2	0.0078	0.0384	0.0679	0.0079	0.0076	0.0908
	3	0.0147	0.0102	0.0356	0.0102	0.0066	0.0422
	4	0.0138	0.0281	0.0422	0.0088	0.0131	0.0492
	5	0.0183	0.0369	0.0443	0.0109	0.0097	0.059
	6	0.0153	0.0344	0.0452	0.0122	0.02	0.0359
	7	0.0082	0.0584	0.0318	0.0135	0.0115	0.0683
02/05/2021	0	0.011	0.0146	0.0437	0.015	0.0202	0.0593
	1	0.0129	0.0572	0.0957	0.0124	0.0095	0.0511
	2	0.0091	0.015	0.0779	0.008	0.0084	0.0897
	3	0.008	0.0176	0.0175	0.0125	0.0074	0.0456
	4	0.0095	0.0185	0.027	0.0048	0.0104	0.0554
	5	0.0131	0.0204	0.0716	0.009	0.0136	0.0247
	6	0.0121	0.0825	0.0433	0.0202	0.0286	0.0601
	7	0.0087	0.0355	0.0314	0.0096	0.005	0.0291
03/05/2021	0	0.012	0.0656	0.0525	0.0059	0.0079	0.0247
	1	0.0062	0.0198	0.0344	0.0058	0.0067	0.0288
	2	0.0067	0.0195	0.035	0.0076	0.0084	0.0111
	3	0.0073	0.0256	0.0286	0.0046	0.0066	0.0366
	4	0.0098	0.0176	0.0317	0.0163	0.0143	0.0505
	5	0.0225	0.0503	0.0586	0.0155	0.0066	0.0546
	6	0.0069	0.0251	0.0435	0.015	0.0139	0.0908
	7	0.0306	0.0538	0.0756	0.0091	0.0077	0.0449
04/05/2021	0	0.0111	0.0267	0.027	0.01	0.0074	0.0282
	1	0.0106	0.0442	0.0548	0.008	0.0125	0.0418
	2	0.0149	0.0359	0.0313	0.0085	0.0119	0.0473
	3	0.014	0.0205	0.0202	0.0063	0.006	0.0243
	4	0.0098	0.0395	0.0738	0.0054	0.0121	0.0599
	5	0.0141	0.0498	0.0239	0.0103	0.0102	0.0373
	6	0.0165	0.0325	0.0508	0.0123	0.0104	0.058
	7	0.0184	0.0389	0.1082	0.0102	0.0114	0.062
05/05/2021	0	0.0126	0.0307	0.0338	0.0082	0.0115	0.0559
	1	0.008	0.0339	0.0446	0.0095	0.0126	0.0845
	2	0.0113	0.0255	0.0809	0.0077	0.0062	0.0898
	3	0.0054	0.0079	0.0242	0.0087	0.0079	0.022
	4	0.0069	0.0296	0.0594	0.0058	0.0069	0.0654
	5	0.0133	0.0472	0.068	0.0085	0.0082	0.042
	6	0.0276	0.0638	0.0433	0.0117	0.0152	0.0347
	7	0.0066	0.0255	0.0211	0.0057	0.0085	0.0653
06/05/2021	0	0.0099	0.0219	0.0444	0.0091	0.0092	0.0177
	1	0.0045	0.0305	0.0914	0.0094	0.0079	0.0487
	2	0.0089	0.071	0.0299	0.0066	0.0088	0.0816
	3	0.0161	0.0121	0.0214	0.0057	0.0105	0.0406
	4	0.007	0.071	0.0342	0.009	0.0247	0.0505
	5	0.0148	0.0532	0.0736	0.0169	0.0072	0.0804
	6	0.0152	0.052	0.0532	0.0093	0.0119	0.0842
	7	0.026	0.0143	0.0441	0.0075	0.0066	0.0253
07/05/2021	0	0.0116	0.0158	0.0318	0.0094	0.0118	0.0478
	1	0.0119	0.053	0.0387	0.0075	0.0067	0.0318
	2	0.0059	0.0404	0.04	0.0052	0.0065	0.0707
	3	0.0148	0.0151	0.0159	0.0057	0.0043	0.0384
	4	0.0068	0.0302	0.031	0.0065	0.0149	0.0342
	5	0.0166	0.0634	0.065	0.0122	0.0151	0.0451
	6	0.0209	0.0374	0.0261	0.0132	0.0121	0.0488
	7	0.0311	0.0257	0.0538	0.0115	0.0099	0.0597
08/05/2021	0	0.0106	0.0402	0.0657	0.0098	0.0126	0.0678
	1	0.0065	0.0269	0.0176	0.0073	0.0097	0.0349
	2	0.011	0.0659	0.0481	0.0119	0.0083	0.0835
	3	0.0088	0.0083	0.0288	0.0142	0.0097	0.0238
	4	0.0051	0.0109	0.0464	0.0075	0.0094	0.0335
	5	0.0158	0.0352	0.0641	0.0139	0.0106	0.0518
	6	0.0121	0.0177	0.017	0.0078	0.0113	0.0424
	7	0.0217	0.1068	0.0426	0.021	0.0171	0.057
09/05/2021	0	0.0143	0.0158	0.0232	0.0084	0.0093	0.0285
	1	0.0091	0.0545	0.0483	0.0093	0.0091	0.0575
	2	0.0286	0.0706	0.0259	0.0075	0.0108	0.099
	3	0.0153	0.0261	0.0335	0.013	0.0195	0.0473
	4	0.0067	0.0162	0.0382	0.0076	0.0152	0.0261
	5	0.0173	0.04	0.0808	0.0102	0.0103	0.0262
	6	0.0145	0.0199	0.0368	0.0085	0.0117	0.0381
	7	0.0087	0.0321	0.0592	0.0063	0.009	0.0477
10/05/2021	0	0.0241	0.0157	0.0202	0.0148	0.0094	0.0385
	1	0.0109	0.0257	0.0471	0.0072	0.0071	0.0224
	2	0.0076	0.0104	0.0751	0.0078	0.0064	0.0507
	3	0.0218	0.0282	0.0293	0.0055	0.0095	0.0465
	4	0.0173	0.0415	0.0934	0.0056	0.0119	0.0184
	5	0.0227	0.05	0.0939	0.0124	0.0085	0.0488
	6	0.0165	0.0273	0.0296	0.0134	0.0154	0.0391
	7	0.011	0.0291	0.0345	0.0419	0.0238	0.0494

Table B.11: The 68th percentiles of positioning errors in all sessions of GPS/Galileo MFIE PPP solutions at station TID1 during the ten testing days

Station: TID1	Unit: m						
		Float			Fixed		
Date	Session	North	East	Up	North	East	Up
01/05/2021	0	0.0115	0.0135	0.0568	0.0101	0.0054	0.053
	1	0.0155	0.0225	0.0339	0.0113	0.0045	0.0348
	2	0.0119	0.0453	0.0306	0.0137	0.0118	0.0429
	3	0.0144	0.0301	0.0638	0.0156	0.0058	0.0606
	4	0.0206	0.0227	0.0416	0.0153	0.006	0.0245
	5	0.0105	0.0481	0.0369	0.0062	0.0042	0.0101
	6	0.0057	0.0335	0.0601	0.005	0.0086	0.0237
	7	0.0067	0.0091	0.0257	0.0103	0.0058	0.051
02/05/2021	0	0.0074	0.0257	0.0459	0.0088	0.0063	0.0463
	1	0.0134	0.0207	0.0344	0.0068	0.0061	0.0322
	2	0.017	0.0602	0.0386	0.0223	0.0286	0.0573
	3	0.0103	0.0089	0.0361	0.0064	0.0072	0.0296
	4	0.0104	0.0377	0.0348	0.0108	0.0052	0.0482
	5	0.0093	0.0102	0.0387	0.0095	0.0052	0.0125
	6	0.0055	0.0179	0.0211	0.0049	0.003	0.0139
	7	0.0163	0.0086	0.0296	0.0133	0.0113	0.0293
03/05/2021	0	0.0198	0.0555	0.0216	0.0175	0.0111	0.0291
	1	0.0212	0.0272	0.0394	0.0139	0.0072	0.0428
	2	0.0309	0.0488	0.0239	0.0228	0.0087	0.0421
	3	0.0155	0.0082	0.0291	0.0127	0.0083	0.0272
	4	0.0147	0.0168	0.0572	0.0091	0.0091	0.0295
	5	0.008	0.0286	0.037	0.0115	0.0063	0.0418
	6	0.006	0.016	0.025	0.0052	0.0055	0.0218
	7	0.0062	0.029	0.0113	0.0064	0.0074	0.0209
04/05/2021	0	0.0113	0.0125	0.0312	0.0101	0.0063	0.0111
	1	0.017	0.023	0.0187	0.0093	0.0111	0.0309
	2	0.0112	0.0368	0.0439	0.0236	0.0145	0.0633
	3	0.0124	0.0111	0.0445	0.0072	0.0066	0.0275
	4	0.0099	0.012	0.0744	0.007	0.009	0.0336
	5	0.0203	0.1462	0.0179	0.0049	0.004	0.0254
	6	0.0085	0.0287	0.0187	0.0145	0.0072	0.038
	7	0.0178	0.0166	0.0272	0.0092	0.0097	0.0308
05/05/2021	0	0.0198	0.0198	0.0397	0.0124	0.0071	0.0439
	1	0.0118	0.0095	0.0378	0.0137	0.0036	0.0475
	2	0.0109	0.0131	0.0191	0.0137	0.0083	0.039
	3	0.0128	0.0189	0.0307	0.0133	0.007	0.0279
	4	0.0169	0.0184	0.0463	0.0137	0.0052	0.0113
	5	0.0077	0.0527	0.0178	0.008	0.004	0.0267
	6	0.0113	0.0157	0.0192	0.0045	0.0055	0.0257
	7	0.0066	0.0112	0.0286	0.0074	0.0211	0.034
06/05/2021	0	0.0124	0.0376	0.0191	0.0162	0.0129	0.0628
	1	0.0067	0.026	0.026	0.008	0.0056	0.0392
	2	0.0182	0.0105	0.0236	0.0159	0.0132	0.0379
	3	0.0108	0.0173	0.0507	0.0144	0.008	0.0353
	4	0.018	0.0169	0.0381	0.0125	0.0056	0.0469
	5	0.0106	0.1148	0.0713	0.0094	0.0096	0.0262
	6	0.0094	0.0141	0.041	0.0069	0.0054	0.0388
	7	0.0157	0.0251	0.0238	0.0128	0.0076	0.0173
07/05/2021	0	0.0121	0.0164	0.0167	0.0141	0.0124	0.0317
	1	0.0169	0.0151	0.03	0.0163	0.0064	0.0469
	2	0.0093	0.0193	0.0281	0.0153	0.0116	0.0157
	3	0.0215	0.0155	0.041	0.0129	0.0048	0.0493
	4	0.0119	0.0197	0.0384	0.01	0.011	0.0372
	5	0.0083	0.0527	0.0273	0.01	0.0151	0.0315
	6	0.0109	0.0257	0.0311	0.0183	0.0082	0.0554
	7	0.0209	0.0235	0.027	0.0157	0.0142	0.0461
08/05/2021	0	0.0278	0.058	0.0207	0.0117	0.0061	0.0226
	1	0.0064	0.0283	0.0273	0.009	0.005	0.0332
	2	0.0122	0.0478	0.0305	0.0116	0.0113	0.0326
	3	0.0068	0.0206	0.0333	0.0152	0.0063	0.0272
	4	0.0125	0.01	0.0428	0.0121	0.0066	0.0196
	5	0.0072	0.0086	0.0099	0.0105	0.0042	0.0096
	6	0.0108	0.0109	0.0152	0.0068	0.0059	0.0531
	7	0.0116	0.0202	0.0521	0.0117	0.0077	0.0932
09/05/2021	0	0.0124	0.0303	0.0415	0.0075	0.0114	0.0473
	1	0.0068	0.056	0.0305	0.0109	0.0063	0.0426
	2	0.0088	0.0404	0.0536	0.0152	0.0109	0.041
	3	0.0165	0.008	0.0481	0.0045	0.0081	0.038
	4	0.0126	0.0421	0.034	0.0136	0.0094	0.0373
	5	0.0077	0.0552	0.0218	0.011	0.0074	0.0274
	6	0.0047	0.0086	0.0181	0.0075	0.0035	0.0149
	7	0.0203	0.0169	0.0718	0.0106	0.0147	0.0606
10/05/2021	0	0.0218	0.0316	0.0586	0.0122	0.0089	0.0767
	1	0.0189	0.0379	0.0255	0.0209	0.0105	0.0274
	2	0.0114	0.0153	0.0642	0.0125	0.0136	0.0306
	3	0.0095	0.0129	0.035	0.0109	0.0071	0.0422
	4	0.0083	0.0241	0.0456	0.0102	0.0118	0.0311
	5	0.0152	0.0445	0.0597	0.01	0.0064	0.0413
	6	0.0063	0.0355	0.0254	0.007	0.0113	0.0372
	7	0.0182	0.0187	0.0841	0.0095	0.0082	0.046

Table B.12: The 68th percentiles of positioning errors in all sessions of GPS/Galileo MFIE PPP solutions at station CEDU during the ten testing days

Station: CEDU	Unit: m						
		Float			Fixed		
Date	Session	North	East	Up	North	East	Up
01/05/2021	0	0.0137	0.0302	0.0398	0.013	0.0075	0.0349
	1	0.0135	0.0157	0.0422	0.016	0.0095	0.0522
	2	0.0143	0.0126	0.0259	0.0154	0.0104	0.0188
	3	0.0201	0.027	0.0569	0.0326	0.0457	0.1831
	4	0.0121	0.0317	0.0435	0.0225	0.0154	0.0819
	5	0.0198	0.1056	0.039	0.0102	0.0051	0.0261
	6	0.0066	0.0067	0.026	0.0089	0.0072	0.0301
	7	0.0147	0.011	0.0439	0.0093	0.0147	0.0425
02/05/2021	0	0.0121	0.0147	0.0642	0.0108	0.0124	0.0813
	1	0.033	0.0556	0.1046	0.0332	0.0237	0.0704
	2	0.0374	0.0371	0.0296	0.0234	0.0101	0.0172
	3	0.026	0.0244	0.0449	0.0237	0.0442	0.0958
	4	0.0161	0.0517	0.0295	0.0245	0.0086	0.0245
	5	0.0157	0.0862	0.0318	0.0125	0.0066	0.0176
	6	0.0163	0.005	0.0367	0.0164	0.0041	0.0258
	7	0.0246	0.021	0.035	0.0174	0.0138	0.0297
03/05/2021	0	0.0229	0.0689	0.0639	0.0213	0.0116	0.0643
	1	0.0134	0.032	0.0376	0.0178	0.0164	0.0647
	2	0.0289	0.0212	0.0459	0.0236	0.006	0.0508
	3	0.0258	0.0264	0.0522	0.0279	0.0484	0.058
	4	0.0194	0.028	0.0547	0.0131	0.0118	0.0612
	5	0.0144	0.1093	0.0552	0.005	0.0061	0.0478
	6	0.0149	0.0206	0.0464	0.0167	0.0115	0.0234
	7	0.026	0.1104	0.1262	0.0933	0.344	0.3963
04/05/2021	0	0.0276	0.0385	0.0331	0.0115	0.007	0.0509
	1	0.0187	0.044	0.1613	0.0113	0.0176	0.0485
	2	0.017	0.0369	0.0313	0.012	0.0118	0.0295
	3	0.0409	0.0219	0.0679	0.0369	0.0791	0.1677
	4	0.0162	0.0648	0.0354	0.016	0.0069	0.0548
	5	0.0104	0.0362	0.0422	0.0111	0.0079	0.0299
	6	0.01	0.0097	0.0468	0.0118	0.0059	0.0359
	7	0.0168	0.0626	0.0669	0.0203	0.035	0.0702
05/05/2021	0	0.0508	0.227	0.0825	0.0175	0.0111	0.0334
	1	0.0116	0.0129	0.0816	0.0078	0.0128	0.0341
	2	0.0088	0.0255	0.045	0.0118	0.0084	0.0148
	3	0.0254	0.0452	0.0282	0.0214	0.0251	0.0632
	4	0.0276	0.0186	0.0337	0.0178	0.01	0.0381
	5	0.0286	0.1926	0.0203	0.0113	0.0097	0.043
	6	0.0071	0.01	0.0264	0.0075	0.0054	0.0245
	7	0.0507	0.1507	0.0902	0.0387	0.0384	0.0698
06/05/2021	0	0.0164	0.1112	0.0322	0.0158	0.0188	0.0377
	1	0.016	0.0287	0.1208	0.0126	0.0096	0.0607
	2	0.0173	0.0454	0.0395	0.0159	0.0133	0.0411
	3	0.0264	0.0391	0.0608	0.0244	0.0169	0.0759
	4	0.011	0.1149	0.0512	0.023	0.0121	0.0591
	5	0.0375	0.1689	0.0407	0.0538	0.1097	0.0458
	6	0.0115	0.0075	0.0565	0.0142	0.0085	0.0462
	7	0.0183	0.0282	0.0426	0.0184	0.0132	0.026
07/05/2021	0	0.0407	0.1066	0.0438	0.018	0.0134	0.0748
	1	0.0436	0.1745	0.123	0.0416	0.43	0.2873
	2	0.0186	0.0807	0.0325	0.0168	0.206	0.053
	3	0.0392	0.0667	0.0273	0.0274	0.0088	0.0325
	4	0.0205	0.0399	0.0365	0.0186	0.0081	0.0484
	5	0.0106	0.0719	0.0446	0.0106	0.0142	0.0796
	6	0.0382	0.1296	0.0691	0.0548	0.2229	0.1375
	7	0.1051	0.208	0.1226	0.2739	0.4911	0.3323
08/05/2021	0	0.0194	0.0532	0.0332	0.0088	0.0077	0.0317
	1	0.0462	0.0664	0.0913	0.0135	0.1895	0.2033
	2	0.0156	0.1059	0.0194	0.0099	0.0108	0.0419
	3	0.0325	0.0434	0.0805	0.025	0.0613	0.1015
	4	0.0087	0.0791	0.0235	0.0188	0.0228	0.0558
	5	0.0321	0.2933	0.0417	0.0542	0.4335	0.0532
	6	0.0209	0.0599	0.0532	0.0499	0.2094	0.1363
	7	0.0947	0.1646	0.1635	0.1301	0.3196	0.3185
09/05/2021	0	0.0249	0.0854	0.0358	0.011	0.0096	0.0333
	1	0.054	0.1748	0.1495	0.0266	0.4321	0.3221
	2	0.0126	0.0791	0.0416	0.0122	0.0082	0.0426
	3	0.0285	0.0509	0.0604	0.0135	0.0118	0.0386
	4	0.0187	0.1184	0.0275	0.0156	0.0093	0.0259
	5	0.0145	0.1274	0.0515	0.0166	0.0173	0.0476
	6	0.0098	0.009	0.0246	0.0169	0.0062	0.0285
	7	0.026	0.0173	0.1057	0.0139	0.0219	0.0907
10/05/2021	0	0.0247	0.0687	0.0787	0.0144	0.0181	0.074
	1	0.0507	0.161	0.1622	0.0339	0.2255	0.2954
	2	0.0131	0.0821	0.077	0.0139	0.0091	0.0336
	3	0.04	0.0732	0.0512	0.0199	0.0074	0.0307
	4	0.0189	0.1199	0.0334	0.0191	0.0113	0.0298
	5	0.019	0.1184	0.034	0.0184	0.0136	0.0466
	6	0.0188	0.0307	0.0472	0.0435	0.0773	0.1312
	7	0.0271	0.0269	0.1029	0.0485	0.0385	0.104

Table B.13: The 68th percentiles of positioning errors in all sessions of GPS/Galileo MFIE PPP solutions at station QUIN during the ten testing days

Station: QUIN	Unit: m						
		Float			Fixed		
Date	Session	North	East	Up	North	East	Up
01/05/2021	0	0.0165	0.0338	0.0769	0.0077	0.0096	0.0667
	1	0.0238	0.0229	0.1817	0.0119	0.0124	0.0705
	2	0.0259	0.0672	0.0706	0.0088	0.0045	0.0617
	3	0.0084	0.0201	0.0509	0.0073	0.0048	0.0431
	4	0.0091	0.0358	0.0201	0.0065	0.0053	0.0393
	5	0.0142	0.0125	0.028	0.0091	0.0084	0.01
	6	0.02	0.0143	0.0202	0.0193	0.0096	0.0362
	7	0.0063	0.0222	0.0159	0.0128	0.0111	0.0213
02/05/2021	0	0.0103	0.0223	0.0193	0.0164	0.0117	0.0242
	1	0.0122	0.0311	0.0428	0.0118	0.0418	0.0958
	2	0.0163	0.0275	0.0433	0.016	0.0059	0.0613
	3	0.01	0.0145	0.0449	0.0071	0.0063	0.0586
	4	0.0087	0.0307	0.0254	0.0083	0.0057	0.031
	5	0.02	0.0152	0.0455	0.0055	0.0071	0.0218
	6	0.0142	0.0253	0.058	0.0204	0.0102	0.0391
	7	0.0078	0.0505	0.0241	0.0134	0.011	0.0246
03/05/2021	0	0.0138	0.0233	0.0175	0.0083	0.0076	0.0248
	1	0.0218	0.012	0.0514	0.0223	0.0207	0.0446
	2	0.019	0.0254	0.0308	0.0081	0.013	0.0575
	3	0.0364	0.0643	0.0807	0.0086	0.0065	0.0284
	4	0.0066	0.0135	0.0241	0.0181	0.0126	0.0481
	5	0.0193	0.0156	0.0265	0.0057	0.0075	0.0248
	6	0.0045	0.0144	0.0229	0.0256	0.0114	0.0458
	7	0.019	0.025	0.0405	0.0086	0.013	0.0358
04/05/2021	0	0.02	0.0717	0.0593	0.009	0.0057	0.0249
	1	0.0086	0.0241	0.039	0.0119	0.0061	0.0428
	2	0.0142	0.016	0.0537	0.0113	0.0033	0.0581
	3	0.0086	0.0107	0.0545	0.01	0.0046	0.0444
	4	0.0061	0.0274	0.0243	0.007	0.0068	0.0373
	5	0.0079	0.0154	0.0286	0.0106	0.0037	0.0431
	6	0.014	0.0379	0.0423	0.021	0.0134	0.0964
	7	0.0071	0.0445	0.0317	0.0132	0.0098	0.0475
05/05/2021	0	0.0266	0.0139	0.0235	0.0185	0.0079	0.0539
	1	0.0297	0.096	0.1189	0.0152	0.0148	0.0588
	2	0.0195	0.0216	0.0281	0.0163	0.0044	0.0567
	3	0.0084	0.0089	0.0583	0.0123	0.0068	0.0528
	4	0.0101	0.0152	0.0273	0.0087	0.0052	0.0254
	5	0.0155	0.0119	0.0381	0.0086	0.0043	0.0249
	6	0.0134	0.064	0.0886	0.0142	0.0094	0.0578
	7	0.0415	0.1007	0.141	0.0482	0.1089	0.0653
06/05/2021	0	0.0192	0.0058	0.0272	0.0108	0.0032	0.0276
	1	0.0156	0.046	0.1214	0.024	0.0822	0.0966
	2	0.0086	0.0216	0.0616	0.0103	0.0068	0.0297
	3	0.0065	0.0122	0.0334	0.0104	0.0052	0.0703
	4	0.0096	0.0136	0.0227	0.0096	0.0047	0.0291
	5	0.0197	0.0204	0.0393	0.0094	0.006	0.0285
	6	0.0161	0.0497	0.0137	0.0196	0.0128	0.0546
	7	0.0147	0.021	0.0589	0.011	0.007	0.0389
07/05/2021	0	0.0189	0.0062	0.0322	0.0141	0.0044	0.0232
	1	0.0065	0.0199	0.0306	0.0123	0.0137	0.0761
	2	0.0141	0.0351	0.0372	0.0069	0.0051	0.0294
	3	0.0078	0.0253	0.0342	0.0105	0.0079	0.0533
	4	0.0144	0.0718	0.0481	0.0097	0.008	0.0373
	5	0.0149	0.027	0.042	0.01	0.0092	0.0331
	6	0.0104	0.0211	0.0318	0.0149	0.0168	0.041
	7	0.0174	0.0839	0.0552	0.0212	0.0136	0.0578
08/05/2021	0	0.0266	0.0194	0.0859	0.0093	0.0092	0.0477
	1	0.0121	0.0281	0.0587	0.0128	0.0181	0.0668
	2	0.0337	0.051	0.0501	0.0071	0.0033	0.0454
	3	0.0106	0.0337	0.0469	0.0102	0.0052	0.038
	4	0.0157	0.0261	0.0353	0.011	0.0084	0.0195
	5	0.0144	0.0114	0.0281	0.0112	0.0057	0.0187
	6	0.0056	0.0145	0.037	0.009	0.0049	0.0639
	7	0.0063	0.0301	0.0641	0.0083	0.005	0.0377
09/05/2021	0	0.0104	0.0109	0.0265	0.0127	0.0035	0.0357
	1	0.0116	0.0357	0.0488	0.0176	0.0419	0.0515
	2	0.0173	0.0305	0.0302	0.0113	0.0086	0.0656
	3	0.0084	0.0157	0.0271	0.007	0.0077	0.0447
	4	0.0103	0.019	0.0192	0.007	0.0058	0.0185
	5	0.0196	0.0414	0.0191	0.0097	0.0101	0.0173
	6	0.0256	0.0394	0.0479	0.0124	0.0076	0.0679
	7	0.0114	0.022	0.0358	0.0085	0.0104	0.0336
10/05/2021	0	0.0109	0.0133	0.0393	0.011	0.0038	0.0787
	1	0.0073	0.0345	0.0578	0.0112	0.0044	0.0647
	2	0.0252	0.0458	0.0388	0.006	0.0089	0.0299
	3	0.0091	0.0091	0.039	0.0119	0.01	0.0572
	4	0.006	0.0429	0.037	0.0177	0.014	0.0178
	5	0.0221	0.008	0.0227	0.0089	0.0092	0.0253
	6	0.0192	0.0545	0.0364	0.0245	0.1788	0.0747
	7	0.011	0.0249	0.0148	0.0092	0.0123	0.0307

Table B.14: The 68th percentiles of positioning errors in all sessions of GPS/Galileo MFIE PPP solutions at station BSHM during the ten testing days

Station: BSHM	Unit: m						
		Float			Fixed		
Date	Session	North	East	Up	North	East	Up
01/05/2021	0	0.004	0.0033	0.0205	0.0072	0.0171	0.0383
	1	0.0205	0.0625	0.029	0.0174	0.0544	0.1804
	2	0.0148	0.029	0.0724	0.0079	0.0082	0.0631
	3	0.0232	0.0756	0.0775	0.0202	0.0137	0.0583
	4	0.0311	0.0297	0.0554	0.011	0.0107	0.0569
	5	0.0114	0.0123	0.0276	0.0114	0.0151	0.0419
	6	0.0182	0.0793	0.0301	0.0107	0.0079	0.0235
	7	0.0198	0.009	0.023	0.0095	0.007	0.0363
02/05/2021	0	0.0068	0.0255	0.0323	0.0114	0.0037	0.022
	1	0.0262	0.0844	0.0118	0.012	0.0184	0.0643
	2	0.0391	0.0748	0.1422	0.02	0.0304	0.088
	3	0.0193	0.1016	0.0657	0.0113	0.0087	0.0259
	4	0.0069	0.0125	0.0217	0.0128	0.0103	0.0313
	5	0.0124	0.0166	0.0196	0.0142	0.0088	0.0354
	6	0.0119	0.0547	0.0436	0.0073	0.0089	0.0597
	7	0.008	0.0116	0.0288	0.0131	0.0059	0.0463
03/05/2021	0	0.0103	0.0073	0.017	0.0126	0.0044	0.0185
	1	0.0202	0.041	0.0266	0.0122	0.0115	0.0385
	2	0.0206	0.0326	0.115	0.0239	0.0144	0.106
	3	0.0107	0.0336	0.1062	0.0201	0.1617	0.1878
	4	0.0069	0.0145	0.033	0.0107	0.0099	0.0397
	5	0.009	0.0041	0.0441	0.0096	0.0049	0.0449
	6	0.0178	0.061	0.0181	0.0203	0.0142	0.0528
	7	0.0299	0.0264	0.0547	0.0118	0.0201	0.0834
04/05/2021	0	0.0152	0.0222	0.0411	0.0077	0.012	0.0344
	1	0.0149	0.0382	0.0284	0.0077	0.0089	0.0293
	2	0.024	0.0745	0.1885	0.0279	0.1376	0.1736
	3	0.015	0.157	0.028	0.0142	0.2164	0.0901
	4	0.0177	0.0132	0.0231	0.0086	0.0052	0.0268
	5	0.0111	0.0198	0.0265	0.0159	0.0092	0.0425
	6	0.0122	0.0582	0.0443	0.0094	0.008	0.0279
	7	0.0103	0.0099	0.0691	0.0047	0.0045	0.0797
05/05/2021	0	0.0147	0.0202	0.0493	0.0116	0.0044	0.0335
	1	0.0174	0.0332	0.0385	0.0115	0.0074	0.064
	2	0.03	0.0233	0.0554	0.0146	0.0153	0.1366
	3	0.146	1.3063	0.5492	0.1414	1.1361	0.704
	4	0.0082	0.0175	0.0529	0.0135	0.0089	0.0342
	5	0.0091	0.006	0.0655	0.0083	0.0099	0.115
	6	0.0146	0.0601	0.051	0.0171	0.0042	0.0235
	7	0.0167	0.019	0.0507	0.0154	0.0078	0.0658
06/05/2021	0	0.0045	0.0248	0.0206	0.0041	0.0067	0.0177
	1	0.0086	0.0482	0.0491	0.0195	0.0438	0.0526
	2	0.0234	0.0472	0.1146	0.0175	0.0066	0.0814
	3	0.0238	0.1255	0.0268	0.037	0.1919	0.0543
	4	0.0176	0.0299	0.168	0.0079	0.009	0.1186
	5	0.0145	0.0189	0.0429	0.0179	0.0091	0.0474
	6	0.023	0.0227	0.0631	0.0124	0.0227	0.0521
	7	0.0382	0.0209	0.2611	0.0383	0.0189	0.1548
07/05/2021	0	0.0179	0.0288	0.0838	0.0149	0.0136	0.0685
	1	0.0153	0.0422	0.0244	0.0075	0.0084	0.0254
	2	0.0233	0.0453	0.0792	0.0192	0.0104	0.0849
	3	0.0125	0.079	0.0475	0.0166	0.0135	0.0876
	4	0.0196	0.0489	0.0358	0.0345	0.0911	0.0565
	5	0.0236	0.0252	0.0262	0.0106	0.0058	0.0507
	6	0.0179	0.0563	0.046	0.0113	0.0057	0.0501
	7	0.086	0.0635	0.0925	0.0089	0.0042	0.0462
08/05/2021	0	0.0133	0.0099	0.0164	0.0084	0.0065	0.0241
	1	0.0083	0.0652	0.0265	0.0212	0.0101	0.0164
	2	0.0147	0.0216	0.0613	0.0091	0.0083	0.0916
	3	0.0237	0.4014	0.0255	0.0493	0.5191	0.1512
	4	0.0173	0.0138	0.0282	0.0085	0.0054	0.0677
	5	0.0062	0.03	0.0619	0.0083	0.0093	0.0645
	6	0.0106	0.0267	0.028	0.0133	0.0062	0.041
	7	0.0146	0.03	0.0713	0.0111	0.0083	0.0549
09/05/2021	0	0.0079	0.0323	0.0507	0.006	0.0045	0.0083
	1	0.0125	0.0491	0.0306	0.0151	0.0063	0.0369
	2	0.0751	0.3929	0.1144	0.0968	0.4673	0.14
	3	0.0166	0.1201	0.1495	0.016	0.0583	0.0406
	4	0.0092	0.0189	0.0322	0.0089	0.0039	0.0488
	5	0.0166	0.0065	0.0327	0.0186	0.0189	0.0339
	6	0.0253	0.1119	0.077	0.0107	0.0098	0.0284
	7	0.0427	0.0631	0.1325	0.0386	0.0168	0.1688
10/05/2021	0	0.0097	0.0299	0.0287	0.0054	0.005	0.0129
	1	0.0119	0.0545	0.026	0.0056	0.01	0.0341
	2	0.0379	0.0098	0.1831	0.0191	0.0131	0.1687
	3	0.0099	0.0676	0.1081	0.0169	0.1091	0.1573
	4	0.0057	0.0182	0.0493	0.0075	0.0072	0.0488
	5	0.0071	0.0184	0.0555	0.0069	0.0051	0.0631
	6	0.0079	0.0279	0.0503	0.0101	0.0067	0.0486
	7	0.0118	0.0426	0.0826	0.0174	0.0229	0.0993

Table B.15: The 68th percentiles of positioning errors in all sessions of GPS/Galileo MFIE PPP solutions at station ZAMB during the ten testing days

Station: ZAMB	Unit: m						
		Float			Fixed		
Date	Session	North	East	Up	North	East	Up
01/05/2021	0	0.0197	0.0442	0.0762	0.0104	0.0117	0.0696
	1	0.0161	0.0257	0.058	0.0148	0.0168	0.1654
	2	0.0075	0.1227	0.0595	0.0087	0.0102	0.0317
	3	0.0069	0.0275	0.0118	0.0036	0.0117	0.0357
	4	0.0114	0.03	0.0414	0.0071	0.0071	0.045
	5	0.0115	0.0642	0.0636	0.0082	0.0056	0.0399
	6	0.006	0.0098	0.0415	0.0061	0.0041	0.0406
	7	0.012	0.0169	0.0211	0.0072	0.0075	0.0335
02/05/2021	0	0.0031	0.0136	0.0203	0.0032	0.0065	0.0257
	1	0.0086	0.0078	0.0175	0.0055	0.0047	0.0365
	2	0.0064	0.0455	0.0285	0.008	0.0094	0.0274
	3	0.0047	0.0173	0.0353	0.0103	0.0117	0.0601
	4	0.0118	0.0211	0.0283	0.0136	0.0106	0.0307
	5	0.0108	0.02	0.0397	0.0129	0.0092	0.0477
	6	0.0093	0.0273	0.0208	0.0035	0.0055	0.0414
	7	0.0042	0.0168	0.0269	0.0079	0.0103	0.0217
03/05/2021	0	0.0046	0.0159	0.0244	0.0055	0.0083	0.0464
	1	0.0078	0.0115	0.0155	0.0144	0.0147	0.1035
	2	0.0114	0.0298	0.0392	0.0102	0.0092	0.0454
	3	0.0071	0.0155	0.0211	0.003	0.0066	0.0292
	4	0.0033	0.0207	0.0209	0.0045	0.0058	0.0184
	5	0.004	0.0328	0.0219	0.0045	0.0063	0.0319
	6	0.0039	0.0321	0.0162	0.0077	0.0077	0.022
	7	0.0114	0.009	0.039	0.0072	0.0078	0.0283
04/05/2021	0	0.0128	0.0118	0.0229	0.0071	0.0092	0.0206
	1	0.007	0.0101	0.0162	0.0092	0.0086	0.0237
	2	0.0061	0.0417	0.0479	0.0082	0.0096	0.0335
	3	0.0135	0.0337	0.0524	0.0069	0.0043	0.0508
	4	0.0053	0.011	0.0178	0.0053	0.0054	0.0187
	5	0.0056	0.0416	0.0098	0.0081	0.0064	0.0198
	6	0.0046	0.0291	0.0369	0.0065	0.0064	0.0445
	7	0.0049	0.0228	0.018	0.006	0.0094	0.0293
05/05/2021	0	0.0043	0.0085	0.0371	0.0047	0.0064	0.0442
	1	0.0067	0.0058	0.0146	0.007	0.0079	0.0477
	2	0.0072	0.0283	0.0242	0.0141	0.0237	0.0563
	3	0.0093	0.0162	0.0303	0.0177	0.0065	0.0288
	4	0.0092	0.0354	0.0116	0.0067	0.0089	0.0398
	5	0.0052	0.0044	0.0171	0.0065	0.0055	0.0458
	6	0.008	0.0047	0.0345	0.0038	0.0042	0.0377
	7	0.0048	0.014	0.0323	0.0081	0.0083	0.0326
06/05/2021	0	0.0077	0.029	0.0725	0.0056	0.01	0.0327
	1	0.0043	0.0165	0.0199	0.0083	0.0089	0.0314
	2	0.0091	0.0301	0.0223	0.0088	0.0076	0.0262
	3	0.0083	0.0068	0.0254	0.0088	0.0034	0.022
	4	0.009	0.0193	0.0223	0.0093	0.0075	0.0254
	5	0.004	0.0271	0.0311	0.0079	0.0095	0.03
	6	0.0086	0.0138	0.0309	0.0087	0.0075	0.0513
	7	0.0059	0.0069	0.0372	0.0076	0.0058	0.0264
07/05/2021	0	0.005	0.0233	0.049	0.0066	0.0077	0.0462
	1	0.0051	0.0168	0.0082	0.009	0.0088	0.0517
	2	0.0072	0.0309	0.0365	0.0136	0.0079	0.0309
	3	0.007	0.0181	0.0175	0.0082	0.0057	0.0303
	4	0.0093	0.0092	0.0385	0.007	0.0065	0.0136
	5	0.0038	0.0177	0.0295	0.0045	0.0092	0.0265
	6	0.0108	0.015	0.009	0.0059	0.013	0.0249
	7	0.008	0.0176	0.0207	0.0054	0.0064	0.025
08/05/2021	0	0.0033	0.0189	0.0617	0.0058	0.005	0.0717
	1	0.0058	0.0126	0.0187	0.0096	0.017	0.0298
	2	0.0088	0.0464	0.0241	0.0117	0.0113	0.044
	3	0.0036	0.0138	0.0339	0.0065	0.0041	0.0533
	4	0.0135	0.0115	0.0235	0.0075	0.0077	0.0314
	5	0.0102	0.0101	0.0268	0.0045	0.0054	0.0278
	6	0.005	0.0127	0.0479	0.0046	0.005	0.0315
	7	0.0041	0.017	0.0097	0.0097	0.01	0.0282
09/05/2021	0	0.0038	0.0197	0.0822	0.0062	0.0078	0.0632
	1	0.0035	0.0183	0.0087	0.0081	0.0126	0.0461
	2	0.01	0.0191	0.0181	0.005	0.008	0.0162
	3	0.0067	0.0163	0.0167	0.0081	0.0062	0.0209
	4	0.0074	0.0186	0.0178	0.0143	0.0061	0.0152
	5	0.0102	0.0077	0.0217	0.0151	0.0058	0.0357
	6	0.0068	0.0211	0.023	0.0064	0.006	0.0327
	7	0.0086	0.0121	0.0387	0.0055	0.0099	0.0268
10/05/2021	0	0.0035	0.0057	0.0436	0.0122	0.0058	0.0705
	1	0.0057	0.0173	0.0264	0.0082	0.0076	0.0564
	2	0.0112	0.017	0.0343	0.0106	0.0089	0.0249
	3	0.0088	0.0109	0.0213	0.0091	0.0052	0.0312
	4	0.0096	0.0194	0.0232	0.0077	0.0053	0.0457
	5	0.0036	0.0163	0.0235	0.0034	0.0073	0.0358
	6	0.0127	0.0287	0.0492	0.0057	0.0086	0.0284
	7	0.0064	0.0128	0.0243	0.0049	0.0081	0.0233

Table B.16: The 68th percentiles of positioning errors in all sessions of GPS/Galileo MFIE PPP solutions at station CUSV during the ten testing days

Station: CUSV	Unit: m						
		Float			Fixed		
Date	Session	North	East	Up	North	East	Up
01/05/2021	0	0.0097	0.0178	0.0576	0.0076	0.0049	0.0651
	1	0.0167	0.0587	0.0607	0.0072	0.009	0.0313
	2	0.013	0.0805	0.0526	0.2005	0.6151	0.1487
	3	0.0417	0.023	0.1176	0.0088	0.0113	0.028
	4	0.0153	0.0193	0.0296	0.0129	0.0152	0.056
	5	0.0052	0.0093	0.0326	0.0071	0.0077	0.039
	6	0.0034	0.0082	0.017	0.0072	0.01	0.0542
	7	0.0069	0.0169	0.0259	0.0061	0.0045	0.0431
02/05/2021	0	0.0108	0.0198	0.0198	0.0051	0.0071	0.018
	1	0.0234	0.033	0.0866	0.0106	0.0101	0.0603
	2	0.0289	0.1141	0.0498	0.0297	0.0177	0.0528
	3	0.0201	0.0193	0.0447	0.0076	0.0184	0.0316
	4	0.0282	0.0319	0.0246	0.0062	0.0093	0.0381
	5	0.0183	0.0416	0.0118	0.0126	0.0174	0.0757
	6	0.009	0.0693	0.0334	0.0381	0.0687	0.061
	7	0.0147	0.0084	0.0228	0.021	0.0108	0.0207
03/05/2021	0	0.0082	0.0456	0.0558	0.0113	0.0181	0.0403
	1	0.0236	0.0549	0.0392	0.0209	0.0194	0.0378
	2	0.0581	0.104	0.0781	0.0458	0.0508	0.0693
	3	0.0469	0.0594	0.0432	0.0142	0.014	0.0563
	4	0.0194	0.0368	0.0763	0.0165	0.0067	0.0341
	5	0.0109	0.0187	0.059	0.0088	0.0098	0.0555
	6	0.0123	0.0056	0.0247	0.0119	0.0061	0.0205
	7	0.0179	0.0161	0.0312	0.0086	0.009	0.0418
04/05/2021	0	0.0064	0.0089	0.0556	0.0059	0.0135	0.0419
	1	0.0214	0.0299	0.0221	0.0142	0.0129	0.0225
	2	0.044	0.0901	0.081	0.0307	0.0281	0.0647
	3	0.0322	0.1058	0.1015	0.0169	0.0214	0.1537
	4	0.0128	0.0434	0.0326	0.0127	0.0099	0.0303
	5	0.0242	0.0418	0.0254	0.0346	0.0175	0.0517
	6	0.0146	0.0532	0.0803	0.0174	0.0157	0.0736
	7	0.0054	0.0213	0.0426	0.0054	0.0078	0.0534
05/05/2021	0	0.0097	0.0241	0.0191	0.0146	0.0101	0.0362
	1	0.0228	0.1366	0.0292	0.0083	0.0104	0.0513
	2	0.0168	0.0314	0.0556	0.0192	0.0254	0.0489
	3	0.008	0.0123	0.0565	0.0082	0.0073	0.0538
	4	0.0102	0.0409	0.0311	0.0135	0.021	0.0385
	5	0.0159	0.014	0.0419	0.0072	0.0165	0.0459
	6	0.0167	0.039	0.0588	0.0334	0.0235	0.096
	7	0.0268	0.0339	0.1276	0.0211	0.0234	0.1465
06/05/2021	0	0.0113	0.0191	0.0721	0.0115	0.0159	0.0634
	1	0.019	0.0263	0.0669	0.0067	0.0097	0.0286
	2	0.0229	0.0421	0.052	0.0589	0.1052	0.1099
	3	0.0121	0.01	0.0509	0.0067	0.0054	0.0412
	4	0.009	0.014	0.0176	0.0048	0.0074	0.0206
	5	0.0059	0.0317	0.0559	0.0044	0.0069	0.012
	6	0.0164	0.0138	0.0931	0.0145	0.0123	0.0832
	7	0.0055	0.0266	0.0168	0.0044	0.0076	0.0274
07/05/2021	0	0.0178	0.0096	0.0561	0.0136	0.0143	0.0234
	1	0.0103	0.0236	0.029	0.0101	0.008	0.0274
	2	0.0158	0.0355	0.068	0.0148	0.0223	0.0522
	3	0.0164	0.0172	0.051	0.0084	0.0067	0.1037
	4	0.0054	0.0405	0.0162	0.0112	0.0076	0.0359
	5	0.0061	0.0357	0.0192	0.0062	0.0046	0.0447
	6	0.0059	0.0072	0.0174	0.0129	0.0077	0.0617
	7	0.0042	0.0088	0.0306	0.0049	0.0079	0.0259
08/05/2021	0	0.0119	0.0391	0.0315	0.005	0.0124	0.0293
	1	0.0149	0.0321	0.0417	0.0067	0.0149	0.0314
	2	0.0169	0.0362	0.046	0.0139	0.0074	0.0433
	3	0.0127	0.0252	0.0767	0.0138	0.0106	0.0448
	4	0.0602	0.0228	0.0934	0.0172	0.0299	0.032
	5	0.0062	0.069	0.1064	0.0086	0.0103	0.0293
	6	0.0162	0.0202	0.0532	0.0108	0.0218	0.0983
	7	0.0153	0.0177	0.032	0.0085	0.0108	0.0674
09/05/2021	0	0.0058	0.0417	0.0319	0.0045	0.0064	0.0373
	1	0.0102	0.0293	0.0298	0.0078	0.0104	0.0316
	2	0.0107	0.0802	0.0653	0.0091	0.0163	0.0569
	3	0.0351	0.0307	0.0897	0.0177	0.0375	0.0675
	4	0.0113	0.0194	0.0531	0.0051	0.0159	0.0169
	5	0.0061	0.016	0.0488	0.0054	0.0084	0.0346
	6	0.0039	0.0079	0.0123	0.0071	0.009	0.0435
	7	0.0253	0.0137	0.0325	0.0137	0.0078	0.0208
10/05/2021	0	0.0131	0.0101	0.0391	0.0095	0.0105	0.0238
	1	0.0153	0.019	0.0804	0.02	0.0127	0.0521
	2	0.017	0.0502	0.0412	0.0111	0.0086	0.079
	3	0.0062	0.0187	0.0497	0.0046	0.0063	0.0221
	4	0.0061	0.0121	0.0317	0.0102	0.0106	0.0379
	5	0.0146	0.1076	0.0311	0.008	0.0081	0.0322
	6	0.009	0.0121	0.0301	0.0119	0.0162	0.0569
	7	0.0077	0.0396	0.0149	0.0149	0.0079	0.012

Table B.17: The 68th percentiles of positioning errors in all sessions of GPS/Galileo MFIE PPP solutions at station PERT during the ten testing days

Station: PERT	Unit: m						
		Float			Fixed		
Date	Session	North	East	Up	North	East	Up
01/05/2021	0	0.0061	0.0289	0.0383	0.0045	0.0074	0.0406
	1	0.0066	0.0093	0.0593	0.0093	0.0045	0.0621
	2	0.0091	0.0303	0.0594	0.0165	0.0105	0.0449
	3	0.0143	0.0353	0.0525	0.0166	0.0143	0.0456
	4	0.0061	0.0134	0.0128	0.011	0.0065	0.0297
	5	0.0131	0.0344	0.0251	0.0074	0.006	0.0172
	6	0.0056	0.011	0.0176	0.0079	0.008	0.0335
	7	0.0182	0.0159	0.0358	0.0147	0.0074	0.0311
02/05/2021	0	0.0075	0.0238	0.018	0.0128	0.011	0.043
	1	0.0145	0.0121	0.0828	0.0112	0.0102	0.0666
	2	0.0135	0.0243	0.1101	0.0102	0.008	0.0371
	3	0.014	0.023	0.0218	0.0118	0.0096	0.0225
	4	0.0165	0.0147	0.0546	0.0174	0.0091	0.0451
	5	0.0067	0.0312	0.0378	0.0086	0.0099	0.0275
	6	0.0055	0.0216	0.0269	0.0062	0.0067	0.0186
	7	0.0091	0.0103	0.0429	0.009	0.0076	0.0435
03/05/2021	0	0.0109	0.0242	0.0196	0.0162	0.01	0.0252
	1	0.0075	0.0061	0.0598	0.0087	0.0081	0.0567
	2	0.0183	0.0124	0.0558	0.0149	0.0053	0.0325
	3	0.0103	0.0222	0.0153	0.0161	0.0089	0.0254
	4	0.0144	0.0157	0.0228	0.013	0.0076	0.0548
	5	0.0287	0.0144	0.024	0.0186	0.0089	0.0213
	6	0.0165	0.0146	0.0559	0.0077	0.0096	0.038
	7	0.0072	0.0079	0.0338	0.0097	0.0068	0.0496
04/05/2021	0	0.0177	0.0164	0.058	0.0133	0.0104	0.0447
	1	0.0154	0.0393	0.0874	0.0165	0.0145	0.0525
	2	0.0178	0.0273	0.0884	0.0222	0.0165	0.0584
	3	0.0189	0.0246	0.0627	0.016	0.0154	0.0643
	4	0.0204	0.0162	0.0321	0.0159	0.0105	0.0407
	5	0.0169	0.0739	0.0815	0.012	0.0096	0.0517
	6	0.0064	0.0132	0.0229	0.0123	0.0062	0.0212
	7	0.0232	0.0103	0.0432	0.0091	0.009	0.0472
05/05/2021	0	0.0107	0.0481	0.0598	0.0106	0.0074	0.0428
	1	0.018	0.0209	0.0296	0.0103	0.0111	0.0369
	2	0.0126	0.031	0.0751	0.008	0.0072	0.0354
	3	0.0116	0.0207	0.0219	0.0145	0.0127	0.0324
	4	0.0098	0.0253	0.0351	0.0186	0.0142	0.0572
	5	0.0135	0.0163	0.027	0.0155	0.0071	0.0268
	6	0.0122	0.0231	0.0303	0.0079	0.0089	0.0348
	7	0.0132	0.0232	0.0614	0.0168	0.0249	0.0446
06/05/2021	0	0.0184	0.0397	0.0376	0.0143	0.0073	0.0526
	1	0.0124	0.0283	0.0543	0.0121	0.0109	0.0343
	2	0.0246	0.0298	0.0253	0.0171	0.0115	0.0283
	3	0.0102	0.0209	0.0453	0.0152	0.0092	0.0351
	4	0.0093	0.0104	0.0276	0.0124	0.0065	0.0436
	5	0.0342	0.1472	0.1402	0.0263	0.017	0.0512
	6	0.0075	0.0113	0.0363	0.0072	0.0099	0.0368
	7	0.0196	0.0391	0.0274	0.014	0.0119	0.0405
07/05/2021	0	0.0247	0.0495	0.0383	0.0153	0.0127	0.0221
	1	0.0229	0.0108	0.1047	0.015	0.0089	0.0211
	2	0.0062	0.0122	0.0409	0.0067	0.01	0.0338
	3	0.0143	0.0296	0.0315	0.0111	0.0086	0.0219
	4	0.0109	0.0096	0.0399	0.011	0.0047	0.053
	5	0.0214	0.1343	0.1288	0.0226	0.0101	0.0611
	6	0.0123	0.0194	0.0253	0.0093	0.0068	0.0549
	7	0.0142	0.0294	0.0538	0.0055	0.0066	0.0407
08/05/2021	0	0.0076	0.0138	0.0328	0.0066	0.0084	0.0299
	1	0.0148	0.011	0.044	0.012	0.006	0.0525
	2	0.0088	0.0084	0.0301	0.0134	0.0129	0.042
	3	0.0154	0.026	0.0256	0.0199	0.0094	0.038
	4	0.0064	0.0259	0.0157	0.0107	0.0075	0.0422
	5	0.0123	0.0418	0.0211	0.0112	0.0062	0.0328
	6	0.0084	0.0126	0.0269	0.0083	0.0083	0.0394
	7	0.0107	0.0209	0.0401	0.0129	0.0089	0.0763
09/05/2021	0	0.0104	0.0244	0.0144	0.009	0.0106	0.0277
	1	0.0311	0.0386	0.0427	0.0133	0.0071	0.0243
	2	0.0056	0.0076	0.0281	0.0145	0.0096	0.0197
	3	0.0096	0.0224	0.041	0.0064	0.0059	0.0296
	4	0.0085	0.0099	0.0225	0.0116	0.0072	0.0345
	5	0.0189	0.0425	0.0488	0.013	0.0061	0.0174
	6	0.0067	0.0081	0.0379	0.0085	0.008	0.0446
	7	0.006	0.0149	0.0562	0.0099	0.009	0.0528
10/05/2021	0	0.0227	0.0177	0.0267	0.0138	0.0161	0.0374
	1	0.0093	0.0108	0.0302	0.0157	0.005	0.0524
	2	0.0088	0.0065	0.0203	0.0117	0.0066	0.0176
	3	0.0079	0.014	0.0338	0.009	0.0056	0.0276
	4	0.0097	0.0125	0.0185	0.0095	0.0071	0.0341
	5	0.0154	0.0482	0.05	0.0216	0.0109	0.0139
	6	0.0161	0.0094	0.0247	0.0087	0.0127	0.026
	7	0.0143	0.018	0.0748	0.0061	0.0072	0.0541